STUDY OF WELD QUALITY IN GAS METAL ARC WELDING UNDER VARIED WELDING PARAMETERS: EXPERIMENTS, ANALYSES AND OPTIMIZATION

Thesis submitted by

NABENDU GHOSH

DOCTOR OF PHILOSOPHY (ENGINEERING)

DEPARTMENT OF MECHANICAL ENGINEERING
FACULTY COUNCIL OF ENGINEERING & TECHNOLOGY
JADAVPUR UNIVERSITY
KOLKATA, INDIA

2019

JADAVPUR UNIVERSITY
KOLKATA-700032, INDIA

INDEX NO. **54/12/E**

1. Title of the Thesis:

Study of weld quality in Gas Metal Arc Welding under varied welding parameters: experiments, analyses and optimization

2. Name, Designation & Institution of the Supervisor/s:

Dr. Pradip Kumar Pal
Professor (Retired),
Department of Mechanical Engineering,
Jadavpur University, Kolkata-700032

Dr. Goutam Nandi
Associate Professor,
Department of Mechanical Engineering,
Jadavpur University, Kolkata-700032

3. List of Publication:

[i]Nabendu Ghosh, Pradip Kumar Pal and Goutam Nandi "***Parametric studies of dissimilar welding of AISI 409 ferritic stainless steel to AISI 316L austenitic stainless steel using Taguchi desirability analyses***". Journal of the Mechanical Behavior of Materials, Volume 27, 1-2 (April 2018); **DOI:** 10.1515/jmbm-2018-0008; **DE GRUYTER Publication**

[ii]Nabendu Ghosh, Pradip Kumar Pal and Goutam Nandi "***Investigation on dissimilar welding of AISI 409 ferritic stainless steel to AISI 316L austenitic stainless steel by using grey based Taguchi method***". Advances in Materials and Processing Technologies, 03/2018; **DOI:**10.1080/2374068X.2018.1451182; **Taylor & Francis Publication**

[iii]Nabendu Ghosh, Pradip Kumar Pal and Goutam Nandi "***GMAW dissimilar welding of AISI 409 ferritic stainless steel to AISI 316L austenitic stainless steel by using AISI 308 filler wire***". Engineering Science and Technology, an International Journal Volume 20/2017; Pages 1334-1341, **DOI:**10.1016/j.jestch.2017.08.002**; Elsevier Publication**

[iv]Nabendu Ghosh, Pradip Kumar Pal and Goutam Nandi "***Parametric Optimization Of Gas Metal Arc Welding Process By Using Grey Based Taguchi Method On Aisi 409 Ferritic Stainless Steel"***. 05/2016; 13(1).Technological Engineering, **DOI**: 10.2478/teen-2016-0003; **DE GRUYTER Publication**

[v] Nabendu Ghosh, Pradip Kumar Pal and Goutam Nandi "***Parametric optimization of MIG welding on 316L austenitic stainless steel by Taguchi method***". Archives of Materials Science and Engineering 05/2016; 79(1): pages27-36., **DOI:**10.5604/18972764.1227660

[vi] Nabendu Ghosh, Pradip kumar Pal and Goutam Nandi "***Experimental Investigation on Dissimilar Welding by GMAW***" Indian Journal of Science and Technology 12/2016; 9(46):pages1-3., **DOI:**10.17485/ijst/2016/v9i46/99961

4. List of Patents: NIL

5. List of Presentations in National/ International Conferences:

[i] Nabendu Ghosh, Pradip Kumar Pal, Goutam Nandi and Ramesh Rudrapati **"*Parametric Optimization of Gas metal arc welding process by PCA based Taguchi method on Austenitic Stainless Steel AISI 316L*" Materials Today: Proceedings** 5 (2018) 1620–1625, International Conference on Processing of Materials, Minerals and Energy (PMME 2016) 29th –30th July 2016, Ongole, Andhra Pradesh, India**, DOI:**10.1016/j.matpr.2017.11.255**,** Elsevier Publication

[ii]Nabendu Ghosh, Ramesh Rudrapati, Pradip Kumar Pal and Goutam Nandi" ***Parametric Optimization of Gas Metal Arc Welding Process by using Taguchi method on Ferritic Stainless Steel AISI409***"**Materials today: proceedings** ,Volume 4, Issue 2, Part A, 2017pages 2213-2221.,5th International Conference of Materials Processing and Characterization (ICMPC 2016) ,12th -13th March 2016 , Griet Hyderabad, India, **DOI:**10.1016/j.matpr.2017.02.068,, **Elsevier Publication**

[iii]Nabendu Ghosh, Pradip Kumar Pal and Goutam Nandi" ***Parametric Optimization of Gas metal arc welding process by PCA-based Taguchi method on Ferritic stainless steel AISI409"***. Materials today: proceedings volume 4 issue 9, 2017 pages 9961-9966, International Conference on Recent Trends in Engineering and Material Sciences (ICEMS-2016), March 17th -19th , 2016, Jaipur, India*,* **DOI:**10.1016/j.matpr.2017.06.302, **Elsevier Publication**

[iv]Nabendu Ghosh, Pradip Kumar Pal and Goutam Nandi "***Parametric Optimization of MIG Welding on 316L Austenitic Stainless Steel by Grey-based Taguchi Method"*.Procedia Technology,** volume25, 2016, pages1038-1048.Global Colloquium in Recent Advancement and Effectual Researches in Engineering, Science and Technology (RAEREST 2016) 22nd Apr and finish on 23rd Apr 2016, St. Joseph's College of Engineering and Technology in Kottayam, Kerala India,, **DOI:**10.1016/j.protcy.2016.08.204 **Elsevier Publication**

DEPARTMENT OF MECHANICAL ENGINEERING
FACULTY OF ENGINEERING & TECHNOLOGY
JADAVPUR UNIVERSITY
KOLKATA, INDIA

CERTIFICATE FROM THE SUPERVISORS

*This is to certify that the thesis entitled "**STUDY OF WELD QUALITY IN GAS METAL ARC WELDING UNDER VARIED WELDING PARAMETERS: EXPERIMENTS, ANALYSES AND OPTIMIZATION**" submitted by **Shri Nabendu Ghosh**, who got his name registered on **3rd September 2012** for the award of **Ph.D. (Engineering) degree** of **Jadavpur University**, is absolutely based upon his own work under the supervision of **Dr. Pradip Kumar Pal**, and **Dr. Goutam Nandi**, that neither his thesis nor any part of the thesis has been submitted for any degree/diploma or any other academic award anywhere before.*

1……
Dr. Pradip Kumar Pal
Professor (Retired),
Department of Mechanical Engineering,
Jadavpur University, Kolkata-700032
(Signature of the Supervisor and Date with Office Seal)

2…….....
Dr. Goutam Nandi
Associate Professor,
Department of Mechanical Engineering
Jadavpur University, Kolkata-700032
(Signature of the Supervisor and Date with Office Seal)

ACKNOWLEDGEMENT

The author feels pleasure in expressing his sincere gratitude to the thesis supervisors Dr. Pradip Kumar Pal, Professor (Retired), Mechanical Engineering Department, Jadavpur University and Dr. Goutam Nandi, Associate Professor, Mechanical Engineering Department, Jadavpur University, for their invaluable guidance, suggestions and encouragement provided throughout the period of this thesis work.

The author is indebted to Dr. Asish Bandyopadhyay, Professor, Mechanical Engineering Department, Jadavpur University, for their invaluable help and advice to this thesis work from time to time.

The author is very much grateful to Dr. Gautam Majumdar, Professor and Head, Mechanical Engineering Department, Jadavpur University, the author expresses special thanks to Dr. T. K. Pal , Professor (Retired), Metallurgical Engineering Department, Jadavpur University for his constant help and advices.

The author likes to thank Dr. Titas Nandi, Professor, Mechanical Engineering Department, Jadavpur University, for his immense help for this work.

The author sincerely thanks all the staff members of Blue Earth Workshop of Jadavpur University who directly or indirectly made their involment in the experimental work and testing part of this thesis work.

The author feels that the thesis, would have been incomplete without the efforts rendered by staff member of FFDA Laboratory Jadavpur University, staff member of Mechanical Engineering Department, Jadavpur University and indeed, without the co-operation and help from SKB Metallurgical Services, Salkia, Howrah-711106. The author is grateful to them.

Last, but not the least, the author gratefully recalls his parents and brother for their valuable inspiration and support from the beginning of this Doctor of Philosophy (Engineering) study. The thesis is dedicated to them.

At last, the author is thankful to all others who have assisted him directly or indirectly to accomplish this work.

NABENDU GHOSH

CONTENTS

ITEMS PAGE NUMBER

LIST OF FIGURES

LIST OF TABLES

TABLE	DESCRIPTION OF THE TABLE	PAGE

NOS. NOS.

ABSTRACT

Welding of various grades of stainless steel is still a potential area of research. In the present work investigation is carried out through welding of butt joints of i) austenitic to austenitic ii) ferritic to ferritic and iii) austenitic to ferritic stainless steels. MIG welding is used. Parametric studies have been done by planning the experiments suitably, making the butt joints as per plan, conducting visual and X-ray examinations of the welded specimens, tensile testing, hardness measurements at different zones and microstructural studies. The input parameters taken into consideration are current, gas flow rate and nozzle to plate distance. Response parameters in the context of optimization have been: ultimate tensile strength, yield strength and percentage elongation. Thickness of the material welded is 3 mm, width = 50 mm, length of each piece = 60 mm. Inert gas used is Ar+5%CO_2. Response surface methodology and Grey-Taguchi method have been applied for process optimization. Optimized conditions for each of the three sets of study have been evaluated. The results of optimization have been validated by confirmatory tests. In the process of doing so, the results of all the tests have been interpreted, discussed and analyzed. Consistency among the results of various tests has been verified. Significance of the input parameters on each of the responses has been identified. Mathematical models have been developed to relate each of the responses with the input parameters. Response surface plots and contour plots are also generated, which help predicting the response(s) at varied levels of any two input parameters, when the third parameter is held constant. The work is, principally, directed to the study of weld quality under varied welding parameters through experiments, analyses and optimization. Based on all these, some useful conclusions are made for each of the three sets of experiments mentioned in the beginning.

Chapter 1

1. INTRODUCTION

Gas metal arc welding (GMAW) is an arc welding process in which the source of heat is an arc formed between consumable metal electrode and the work piece with an externally supplied gaseous shield of gas either inert such as argon and /or helium [1].Weld quality mainly depends on features of bead geometry, mechanical-metallurgical characteristics of the weld as well as on various aspects of weld chemistry, and these features are expected to be greatly influenced by various variables such as welding geometry, groove angle, shielding type and mixture, and different input parameters: current, voltage, electrode stick-out, gas flow rate, edge preparation, position of welding, welding speed, nozzle to plate distance [2-3] etc. Moreover, the cumulative effect of various input parameters determines the extent of joint strength that should meet the functional aspects of the weld in practical field of application. Therefore, preparation of a good quality weld seems to be a challenging job. Dissimilar metal combination between Ferritic stainless steels and Austenitic stainless steels is in demand in certain applications, and, for example, it is commonly employed in $TiCl_4$ reduction retorts, because Austenitic stainless steel has good creep strength and oxidation resistance which are required in the higher temperature regions, while Ferritic stainless steel is preferred to avoid the problem of nickel leaching by molten magnesium [4].

Type AISI 316 Austenitic stainless steels are widely used in many industrial applications due to its excellent corrosion resistance, fabric ability, and they possess good mechanical properties at elevated temperatures [5-6] and their availability in the market with cheaper cost has made them popular. Typical uses of 316 stainless steels include steam generating plants as piping and super heater material. The stainless steel (SS) 316L is a chromium-nickel-molybdenum Austenitic stainless steel developed to provide improved corrosion resistance to SS 304/304L in moderately corrosive environments. Type 316L is an extra-low carbon version of Type 316 that minimizes harmful carbide precipitation due to welding. The addition of molybdenum improves general corrosion and chloride pitting resistance [7-9]. The material Austenitic stainless steel 316L is

often selected because the material contains low carbon and it has a good weldability factor. Austenitic stainless steel (ASS) such as type 316L is usually preferred over other austenitic varieties as a structural material due to its higher corrosion resistance and superior mechanical properties both at low and high temperatures.

Ferritic stainless steels (FSS) have body centered cubic crystal**,** are less ductile than Austenitic stainless steel and are not hardenable by heat treatment like Martensitic steels. Older Ferritics (i.e. AISI 430) are used mainly for household utensils and other applications not demanding in excellent anti-corrosion properties. They are the second largest selling type of stainless steels behind Austenitics. Ferritic stainless steels with 11–30% (weight percentage) chromium have been widely used in automobiles, pressure vessels, road and rail transport, power generation, mining [10-12] etc. FSS has been developed to fill the gap between stainless steels and the rust-prone carbon steels, thus providing an alternative that displays both the advantages of stainless steels and engineering properties of carbon steels. Dissimilar welding is the joining between two different materials by any welding process. Joining of dissimilar materials may significantly reduce the weight of product and minimize the cost of production as well, without compromising the safety and structural requirements. Dissimilar weld must possess sufficient tensile strength and ductility, so that the joint will not fail within the weld. Dissimilar metal joints are used in various engineering applications such as nuclear power plants, coal fired boilers, automobile manufacturing industry etc. Dissimilar materials have been joined by different welding operations which include gas metal arc welding (GMAW), gas tungsten arc welding (GTAW), submerged arc welding (SAW), fusion welding, pressure welding, explosion welding, friction welding, diffusion welding, brazing, and soldering. Among the other welding processes GMAW is a versatile process which is extensively used in manufacturing of variety of ferrous and non-ferrous metals as it greatly improves the quality characteristics of the weldment[13-15].

Ferritic to Austenitic joint is a popular dissimilar metal combination used in many applications and this joint has huge demand in industries like petrochemical industries, ship industries, nuclear power plants, pulp and paper [16-17], etc. Ferritic and Austenitic joints are normally produced using conventional welding processes such as manual metal arc (MMA), metal inert gas arc (MIG) and tungsten inert gas arc (TIG) welding . F/A dissimilar joints are based on both technical and economic aspects i.e. these dissimilar joints can provide satisfactory performance with reasonable cost savings. Joining of dissimilar Ferritic and Austenitic materials is not an easy

task; it is considered to be a challenging problem due to differences in thermal conductivities and thermal expansion which may cause crack formation. In dissimilar metal welding, base metal contributes 15% dilution from each metal while the filler metal contributes 70% to the total weld nugget composition. When welding dissimilar metals, good solid solubility is essential for sound weld properties. The trends of welding similar / dissimilar metals present considerable challenges still now. Welding of similar and dissimilar metals has attracted attention of the researchers worldwide, owing to its many advantages and challenges. There is no denial in the fact that dissimilar welded joints offer more flexibility in the design and production of the commercial and industrial components. Welding of Ferritic and Austenitic stainless steel in general and GMAW welding of such steel in particular, can well be considered as one of the areas where more extensive research may contribute, in a significant way, to the precise control of the welding process for better and acceptable quality of weldment. Weld quality mainly depends on features of bead geometry, mechanical –metallurgical characteristics of the weld as well as on various aspects of weld chemistry and these features are expected to be greatly influenced by various input parameters like current , voltage, electrode stick-out, gas flow rate, edge preparation, position of welding, welding speed and many more. The present work gives consideration of at least three of them: Welding current, Gas flow rate and Nozzle to plate distance. The purpose is to study the influence of the selected parameters on the quality of weld. The parameters are varied at several levels by planning the experiments on the basis of any one of the several techniques available like conventional design of experiments, Taguchi's Orthogonal Array, Response surface methodology (RSM). Moreover, the cumulative effect of the mentioned levels of the input parameters determines the joint strength that should meet the functional aspects of the weld in the practical field of application. Therefore, preparation of a satisfactory good quality weld seems to be a challenging job. The survey of literature has shown that, various statistical techniques such as Regression analysis, Response surface methodology (RSM) and Taguchi method have been adopted by many researchers to modeling and optimization of weld bead geometry in GMAW. The effect of process parameters on different responses can be analyzed from experimental and analytical research and modeling. Multiple linear regression and response surface methodology are two common tools available for developing mathematical models for the responses as the function of process parameters. Depending on the requirement, each quality feature is optimized (maximized or minimized) to

determine the optimal setting of the parameters. However, this method is applicable for optimizing of single objective function. In multi objective case, it is essential to convert these multiple objectives to an equivalent single objective function which has to be optimized finally. Taguchi method has been found efficient to the many researchers. The method uses a limited number of experiments through a well-balanced design called Orthogonal Array (OA) design. However, traditional Taguchi fails to solve a multi- objective problem. To overcome this, Grey relational analysis is to be adopted combined with Taguchi method. Literature survey, however, indicates that research is still being continued. It suggests there is a need of further extensive research in the area of gas metal arc welding of dissimilar steels. In so far as gas metal arc welding of Austenitic stainless steel and Ferritic stainless steel is concerned, knowledge-base is not sufficiently rich. More studies are required on various aspects of gas metal arc welding of Austenitic stainless steel to Ferritic stainless steel with the objective of achieving desired quality of weld. In doing so, parametric optimization, mathematical modeling, analysis of weld pool solidification and heat transfer, metallographic characterization, development of ANN or PNN models, analysis of joint performance etc. become important. Extensive investigation relating to all these aspects will lead to create a strong knowledge-base which will help people in practical field to use GMAW in a more predictable way, ensuring desired quality of weld. The present work takes into account some of the aspects as mentioned above in respect of welding of Austenitic stainless steel, Ferritic stainless steel and dissimilar welding between Austenitic and Ferritic stainless steels.

1.1 GAS METAL ARC WELDING

Gas metal arc welding (GMAW) is a semi-automatic or automatic arc welding process that yields coalescence of metals by heating with a welding arc between continuous filler metal (consumable) electrode and the work piece, welding being done in the protective shield of a gas or a gas mixture. The gas or gas mixture may be either inert type (helium/ argon/ mixture of them) or it may be active type (CO_2/ O_2/ mixture of them) or mixture of inert and active gases (argon + CO_2/ argon + CO_2 + O_2/ argon + He + CO_2 etc). When inert gases are used as shielding gas, this process is called Metal Inert Gas (MIG) welding and when active gases are used as shielding gases, this process is referred to as Metal Active Gas (MAG) welding. The continuous

wire electrode which is drawn from a reel by an automatic wire feeder is fed through the contact tip inside the welding torch. It is melted by the internal resistive power and heat is transferred from the welding arc. Heat is concentrated by the welding arc from the end of the melting electrode to molten weld pools and by the molten metal that is being transferred to weld pools. Molten weld pools and electrode wire are protected from contaminants of the atmosphere by a shielding gas or a gas mixture which is supplied through the gas nozzle. In figure 1.1, fundamental features of a basic GMAW process are shown.

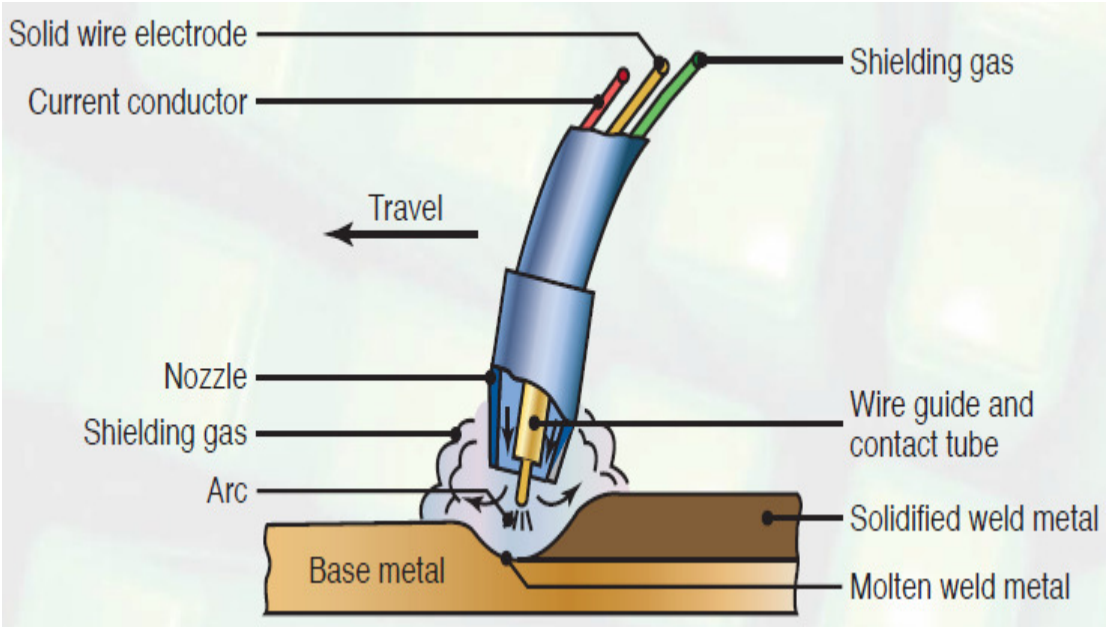

Figure 1.1 Fundamental features of a GMAW process **[18]**

1.1.1 EQUIPMENT USED IN GMAW

The basic equipment required for a semi-automatic GMAW system consists of a power source, welding gun, wire feed unit, electrode wire, shielding gas supply system, and a water cooling system, if used. Some basic features of the equipment are discussed here:

a) Power source:

In GMAW, DC with electrode positive is mostly used. It provides a stable arc with smooth metal transfer: it results in low spatter and good quality weld bead. AC is unsuitable for GMAW because, if it is used, arc extinguishes in every half cycle. That can cause partial rectification of

current and the arc may go off completely. Though DC with electrode negative provides higher deposition rate, it is not generally used because it may cause an unstable and erratic arc. It also eliminates the advantage of arc cleaning action. GMAW power sources are rated at 60% and 100% duty cycles for semi-automatic and automatic modes respectively.

Most applications of GMAW use a constant voltage or flat V-I characteristics power supply. It provides self-regulation of welding arc. Thus a wire feed unit with constant speed settings can be used, in which case the wire feed rate becomes directly related to the welding current. For fully automatic GMAW process rising V-I characteristic with thicker electrodes is used. The voltage range for such a power source is greater than that for a constant voltage power source. A constant current power source and a constant wire feed rate unit might be coupled, especially for the welding of metals with high thermal conductivities, such as aluminum. That arrangement grants the operator an additional control over the heat input into the weld.

Pulsed current GMAW is an artificial method of producing spray transfer at average currents lower than those at which spray transfer occurs naturally. P-GMAW is often used in sheet metal industries to improve joint quality and productivity. In P-GMAW, the arc current is maintained at a value high enough to permit spray transfer and for long enough to initiate the detachment of a molten droplet.

Once the droplet is transferred, the current is reduced to a relatively low value to maintain the arc. These periods of lower current, allow the average arc current to be reduced into the range suitable for positional welding, while periodic implementation of higher current pulses allows the metal to be transferred in the spray mode.

b) Welding gun and wire feed unit

The typical GMAW welding gun has a number of key parts - a control switch, a contact tip, a power cable, a gas nozzle, an electrode conduit and liner, and a gas hose etc. The control switch, or trigger, when pressed by the operator, initiates the wire feed, electric power, and the shielding gas flow, causing an electric arc to be struck.

The contact tip is made of copper and sometimes chemically treated to reduce spatter. It is connected to the welding power source through the power cable and transmits the electrical energy to the electrode while directing it to the weld area. Before arriving at the contact tip, the electrode wire is protected and guided by the electrode conduit and liner, which prevents buckling of the wire and maintains an uninterrupted wire feed. The gas nozzle is used to direct

the shielding gas into the welding zone. Larger nozzles provide greater shielding gas flow, which is useful for high current welding operations. The gas is supplied to the nozzle through a gas hose, which is connected to the tanks of shielding gas. The wire feed unit supplies the electrode to the work, driving it through the conduit and on to the contact tip. Most wire feed units provide the wire at a constant feed rate, but more advanced machines can vary the feed rate in response to the arc length and voltage.

c) Shielding gas supply

Shielding gases are supplied from gas cylinders through gas pressure regulators which are used to provide constant pressure and flow of shielding gas. The gas flow rate is controlled by a flow-meter which is calibrated in a plastic tube. The calibrations are in *l*/min. For different gases, gas flow-meters have different calibrations due to the difference in their densities. So, one flow-meter cannot be used for all gases. Special arrangements can be done to provide a gas mixture. Pressure regulators are connected to the gas nozzle of the welding gun via the welding machine and during welding the gas is supplied to the weld area.

1.1.2 MODE OF METAL TRANSFER

GMAW can be done by short-circuit, globular, spray and pulsed spray mode of metal transfer. Short-circuit mode is obtained at low wire feed rate and low voltage. This type of transfer is suitable to weld in all positions though the rate of deposition is low. Globular transfer occurs at relatively higher wire feed rate and voltage and is the most undesirable because of its tendency to produce high heat, poor weld surface and spatter. Spray mode of metal transfer is the most desirable one which occurs at a high voltage. It is well suited to welding aluminums, stainless steel etc. Due to use of high voltage and current, heat input rate is high and area of weld pool is large. So, this technique is generally used on work piece of thickness above 6.4 mm. Because of the large weld pool, it is often limited to flat and horizontal welding positions. It is not generally practical for root pass welding. In pulsed spray mode, the pulsing current melts the filler wire and allows a relatively smaller droplet to fall with each pulse. As the overall heat input is less due to lower average current, the size of the weld pool and heat-affected zone is also less, making it possible to weld thin work piece. The pulse provides a stable arc with no spatter, since no short-circuiting takes place. This also makes the process suitable for nearly all metals.

1.1.3 GMAW PROCESS PARAMETERS

Every welding process has some process parameters whose effect changes the weld attributes. To obtain desired results, it is very important to select proper parameters. In GMAW the parameters that affect weld penetration, bead geometry, and overall weld quality are arc voltage, welding current/wire feed rate, travel speed, electrode stickout, electrode-to-work angle, electrode diameter, gas flow rate, shielding gas mixture, nozzle-to-work distance, root gap, welding position etc. The role of most of these process variables is discussed below:

a) Arc voltage

With a flat characteristics power source, the arc voltage is controlled mainly by the open circuit voltage (OCV). A small difference is observed between the actual value of the arc voltage and the set value of the OCV due to the voltage drop in the cable and the slight drop in the V-I characteristics of the power source itself. The change in arc voltage leads to change in arc length that affects the bead dimension, microstructure and the mode of metal transfer. Short-circuit and globular mode of metal transfer occurs at low voltage with low and high wire feed rate respectively. Spray transfer occurs at higher arc voltage.

b) Wire current/wire feed rate

For a flat characteristics power source change in wire feed rate varies with the welding current. The relationship between them is shown in figure1.2. This relationship is linear at lower feeding rate and the curve becomes non-linear when wire feed rate increases. Short circuit mode of metal transfer occurs at lower current and lower wire feed rate. An increased welding current increases wire feed rate resulting in spray mode of metal transfer. For the same wire feed rate, increase in wire diameter necessitates increased demand for welding current, results in increased depth of penetration and weld width, increased deposition rate and increase in weld bead size at a given cross-section.

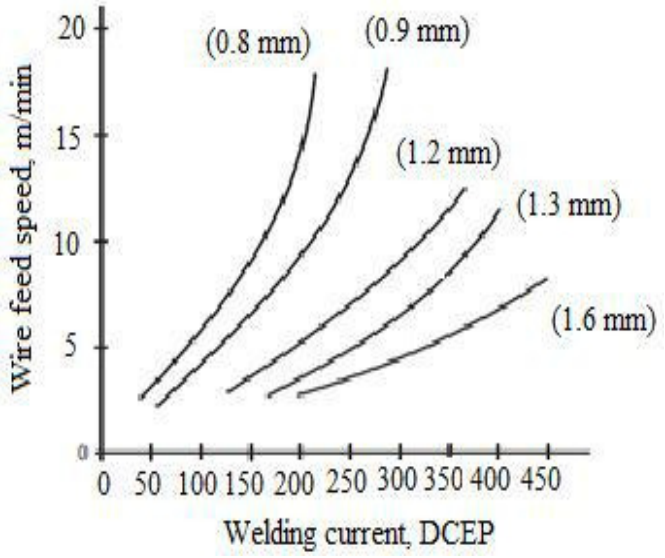

Figure 1.2 Effect of welding current on Wire feed speed for different sized electrodes **[19]**

c) Travel speed

Penetration is maximum at a particular welding speed and it decreases as the speed is varied either way. When the speed decreases bead width increases and when the speed increases bead becomes narrower. The decrease in penetration with reduction in speed is caused due to excessive molten metal sliding into the weld pool resulting in shallower weld pool. Thus the increased heat input per unit length due to reduced speed shows itself in the form of increased weld width and the reverse is true for the increase in welding speed. At higher travel speed, bead width is narrower and depth of penetration is low due to smaller heat input and lower deposition per area. Excessive high welding speed may also be accompanied by undercutting due to inadequate metal available to fill the zone melted by the arc.

d) Gas flow rate

Gas flow rate is a very important parameter affecting the weld quality. Shielding gases protect the weld pool, electrode wire, heat affected zone and the base metal from the atmosphere. At low rates, the gas cannot exclude the atmosphere properly. So the sensitive areas come in contact with atmospheric oxygen and nitrogen and get oxidized and nitrodized. At high flows, turbulence in the gas column causes mixing with the atmosphere resulting porosity at the weld bead.

e) Electrode stick-out

The distance from lower tip of the contact tube to the tip of the protruding electrode wire, as shown in figure1.3, is known as electrode stick-out. It is an important welding parameter for controlling the deposition rate and the bead geometry. With the increase in stick-out its electrical resistance increases that results in preheating of wire which leads to lower requirement of current at any given wire feed rate. If stick-out length becomes too long, excessive metal is deposited with low arc heat which leads to shallow penetration and unsatisfactory bead shape. Too short a stick-out may cause burn back resulting in damage to the contact tube. The stick-out is usually kept between 5 to 15 mm for short-circuiting transfer and 16-25 mm for other types of metal transfer.

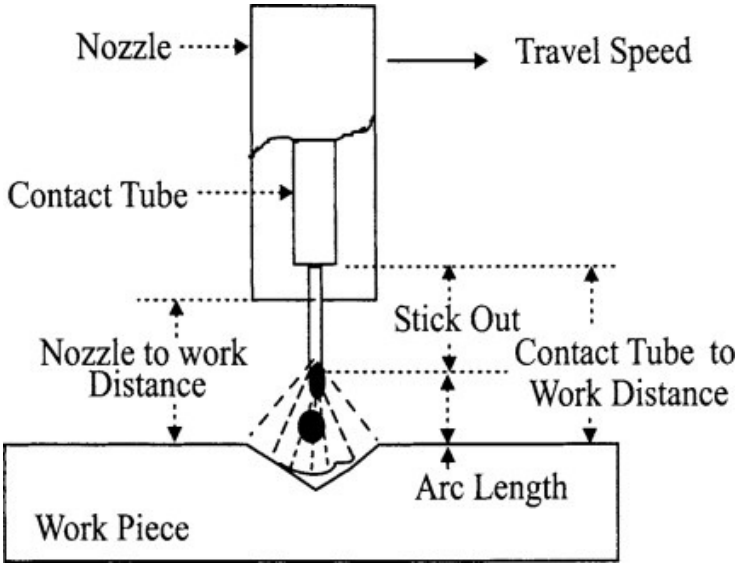

Figure1.3 Some GMAW terminology **[20]**

f) Nozzle-to-work distance

Bead shape and quality of a joint depends also on nozzle-to-work distance. A short nozzle-to-work distance damages the gas nozzle due to excessive heating and a long nozzle-to-work distance affects the shielding gas efficiency.

g) Electrode-to-work angle

Electrode-to-work angle with respect to the direction of travel may considerably affect the bead geometry. In automatic GMAW, the gun is usually held perpendicular to the work piece. In semi-automatic GMAW the gun is held in forehand or backhand position. The forehand position results in wider bead with shallow penetration. The backhand welding gives a narrower bead

with deep penetration. Backhand welding with 65° angle gives the maximum penetration, stable arc, and least spatter.

h) Electrode diameter

Electrode size also affects the penetration and bead width. For the same current, lower diameter wire gives deeper penetration while bigger diameter wire gives wider beads with shallow penetration. Smaller diameter wires provide higher deposition efficiency. Spray mode of metal transfer is easily achievable with smaller diameter wire.

i) Welding position

Weld bead geometry or weld quality is also affected by the position in which the work piece is held with respect to the welding gun. Down hand or flat welding gives the most satisfactory bead shape and all modes of metal transfer can be effectively utilized. Overhead and vertical welding positions are difficult to weld. Control of welding bead size is the major challenge by the two methods. Vertical down welding is very tough to control and is usually adopted for welding sheet metal. Vertical-up welding position is used for longitudinal pipe joints and horizontal welding is used for circumferential pipe joints.

j) Shielding gas composition

The major shielding gases used for GMAW process are argon, helium, carbon dioxide, oxygen, nitrogen, hydrogen etc. Sometimes 100% pure gas is used or sometimes a gas mixture is used for better efficiency. These shielding gases are classified into two groups viz., i) inert gases like argon and helium and ii) gases which dissolve in and react with the metal, for example, CO_2, O_2, H_2, N_2 etc. In the present study, 99% pure argon gas has been used as shielding gas.

1.2 STAINLESS STEELS

Steels are the alloys of iron and carbon in which, the carbon content is in between 0.08 and 2.0 percent. When the carbon percentage is increased beyond 2%, it is called cast iron. Commercial available steels always contain some amounts of other elements. If these elements are accidentally present without any intention, these are called impurities. However, if they are added purposely, they are called alloying elements.

Stainless steels are iron-base alloys that contain a minimum of 11- 12% Cr, the amount required to prevent the formation of rust in atmospheres (hence the designation stainless). At this

minimum level of chromium, a thin protective self-healing film of Cr_2O_3 forms spontaneously on the outer surface of steel, which acts as a barrier to protect the steel from corrosion by healing itself in the presence of oxygen.

Other elements added to improve particular characteristics include nickel, manganese, molybdenum, copper, titanium, silicon, niobium, aluminum, selenium etc. Ni addition in stainless steel improves corrosion resistance in reducing environments such as H_2SO_4. Presence of Mo increases pitting and corrosion resistance in chloride environments. Stainless steel is attractive to the architects despite its high cost, as it provides a combined effect of strength and durability.

Stainless steels are produced in cast, powder metallurgy (P/M) and wrought forms. Production of stainless steels is a two stage process involving the melting of scrap and ferroalloys in an electric-arc furnace (EAF) followed by argon oxygen decarburization (AOD) to adjust the carbon content and remove impurities. Available final product forms include plate, sheet, foil, bar, wire, billets, pipe, tube etc.

Stainless steels are used in a wide variety of applications. Most of the structural applications occur in the chemical and power engineering industries. These applications include an extremely diversified range of uses, including nuclear reactor vessels, heat exchangers, oil industry, tubular components for chemical processing and pulp and paper industries, furnace parts, boilers used in fossil fuel electric power plants etc.

a) Austenitic stainless steels

They are the most common and familiar types of stainless steels which contain up to 0.15% carbon. They have FCC crystal structure, called γ-iron. They are available in two grades, AISI 300 - series and AISI 200 - series. AISI 300- series include 301, 302, 304, 304L, 304 LN, 308, 309, 310, 316, 316 L, 316 LN, 321, 330, 347 etc and contain chromium (16- 26%) and nickel (10- 22%). AISI 200 - series include 202, 201, 205 etc and they contain chromium, nickel and manganese (5- 18%).

b) Ferritic stainless steels

They are non hardenable iron-chromium alloys. They have BCC crystal structure. They are available in AISI 400- series which include 405, 409, 430, 439, 442, 446 etc types. AISI 409 is the most commonly used Ferritic stainless steel. They contain up to 0.20% carbon and 11-18%

Cr and small amount of ferritic stabilizers, such as aluminium, niobium and titanium. These stabilizers are ferritic at all temperatures, do not transform to austenite and therefore, are not hardenable by heat treatment. Ferritic stainless steels have better engineering properties than austenitic grades, but have reduced corrosion resistance, because of the lower chromium and nickel content. They are usually less expensive than austenitic stainless steels.

c) Martensitic stainless steels

They are similar in composition to the ferritic group but contain higher carbon and lower chromium to permit hardening by heat treatment. They contain 11 to 18% Cr, up to 1.20% C and small amounts of Mn, Ni and sometimes, Mo. They transform to austenite phase on heating and, therefore, can be hardened by formation of martensite on rapid quenching. This group includes types 403, 410, 414, 416, 420, 422, 431 and 440. They are not as corrosion-resistant as the previous two classes but are extremely strong, tough and more brittle.

d) Duplex stainless steels

They have a mixed microstructure of austenite and ferrite. They solidify as 100% ferrite, but about half of the ferrite transforms to austenite during cooling through temperatures above approximately 1900°F (1040°C). This behavior is accomplished by higher chromium (19–32%) and lower nickel contents than Austenitic stainless steels. They contain molybdenum up to 5%. Nitrogen is deliberately added to speed up the rate of austenite formation during cooling. They are ferromagnetic in nature. They combine higher strength than Austenitic stainless steels with fabrication properties similar to austenitics, and with resistance to chloride stress corrosion cracking of Ferritic stainless steels. Duplex grades are characterized into groups based on their alloy content and corrosion resistance. Lean duplex refers to grades such as UNS S32101, S32304 etc. Standard duplex is 22% chromium with UNS S31803/S32205 known as 2205; it is the most widely used variety. Super duplex is by definition a duplex stainless steel with a pitting corrosion equivalent. Usually super duplex grades have 25% chromium or more and some common examples are S32760, S32750 and S32550 (Ferralium). Hyper duplex refers to duplex grades with a PRE (pitting resistance equivalent) > 48 and at the moment only UNS S32707 and S33207 are available.

e) Precipitation- hardenable stainless steels

They are chromium-nickel alloys. They provide an optimum combination of the properties of martensitic and austenitic grades. Like martensitic grades, they are known for their ability to gain

high strength through heat treatment and they also have the corrosion resistance of Austenitic stainless steel. The high tensile strength of precipitation hardening stainless steels comes after a heat treatment process that leads to precipitation hardening of a martensitic or austenitic matrix. Hardening is achieved through the addition of one or more of the elements like Copper, Aluminium, Titanium, Niobium, and Molybdenum. The advantage of precipitation hardening steels is that they can be supplied in a "solution treated" condition, which is readily machinable. After machining or another fabrication method, a single, low temperature heat treatment can be applied to increase the strength of the steel. This is known as ageing. As it is carried out at low temperature, the component undergoes no distortion. The most well-known precipitation hardening steel is 17-4 PH. The name comes from the additions of 17% Chromium and 4% Nickel. It also contains 4% Copper and 0.3% Niobium. Due to the high strength of these steels, their most applications are found in aerospace industries. They are also used in making gears, turbine blades, nuclear waste casks, valves and other engine components.

1.2.1 WELDING OF STAINLESS STEEL

Most stainless steels are considered to have good weldability, except martensitic stainless steels and may be welded by several welding processes including the arc welding processes, resistance welding, electron and laser beam welding, friction welding and brazing. Generally, welding of martensitic stainless steels is difficult. Austenitic stainless steels are also weldable, comfortably and can be welded by GTAW, GMAW and other processes. The low thermal and electrical conductivity of Austenitic stainless steel is generally beneficial in welding. They have high rate of thermal expansion when welded. The coefficient of thermal expansion for the Austenitic stainless steels is 50% greater than that of carbon steel and this must be considered to minimize distortion.

1.3 INSPECTION AND TESTING OF WELDS

To produce quality in welded joint, it is necessary to keep an eye on what is being done in three different stages in welding:

- Before welding such as cleaning, edge preparation, baking of electrode etc. are to be done to ensure quality weld joints
- During welding manipulation of heat source, selection of input parameters (gas flow rate, welding current, arc gap, welding speed, welding voltage etc.) affecting the heat input and protection of the weld pool from atmospheric condition needs to be cared for.
- After welding removal of slag peening, post welding treatment are required in many cases.

Selection of optimal method and parameters in each step and their execution in different stages of production of a welded joint determine the quality of the weld joint. Inspection is mainly carried out to assess ground realities in the work. Testing helps to access the suitability of the weld joints for a particular application and to take decision on performance parameters related with soundness. Testing methods of the welded joint are broadly classified as destructive test and non-destructive test.

1.3.1 NON-DESTRUCTIVE TESTS

Non-destructive tests as applied to weld are visual, ultrasonic, and radiographic (X-ray). All the non-destructive tests have good potential to check the flaw in weldment.

Visual inspection: Visual inspection is often the most cost-effective method, but it must take place prior to, during and after welding. Before the first welding arc is struck, materials should be examined to see if they meet specifications for quality, type, size, cleanliness. Grease, oil, oxide should be removed. The pieces to be joined should be checked for flatness, straightness and dimensional accuracy. Finally, process and procedure variables should be verified, including electrode size, equipment setting. Among the weld defects that can be recognized visually are cracking, slag inclusion, surface porosity and undercut.

Radiographic inspection: X-ray is used to determine the internal soundness of welds. Radiography is based on the ability of X-rays and gamma rays to pass through metal and other materials opaque to ordinary light, and produce photographic records of the transmitted radiant energy. All materials will absorb known amounts of this radiant energy, and therefore, X-rays and gamma rays can be used to identify discontinuities and inclusions within the opaque

material. An X-ray image of the interior of a weld may be viewed on a fluorescent screen as well as on developed film. This makes it possible to inspect parts faster and at a lower cost.

1.3.2 DESTRUCTIVE TESTS

In these testing methods, the damage of the test specimens sometimes can be up to complete fracture (like tensile and fatigue tests). Weld joints are generally subjected to destructive tests such as hardness, toughness, bend and tensile tests for developing the welding procedure.

Tensile test: Tensile properties of weld joint namely yield, and ultimate strength and ductility can be obtained depending upon the need. Tensile properties of the weld joint are obtained in taking specimen from transverse direction of weld joint. Tensile test result must be supported by respective engineering stress and strain diagram indicating modulus of elasticity, elongation at fracture, yield and ultimate strength.

Bend test: Bend test is one of the most important and commonly used destructive tests to determine ductility and soundness (porosity, inclusion, penetration) of the weld joint produced, under some given set of welding conditions. Bending of the weld joint can be done from face or root side depending upon the purpose. Bending can be performed using simple compressive or bending load and die of standard size for free and guided bending. For testing, load is kept on increasing until crack starts to appear on the face or root of the weld and angle of bend at this stage is used as a measure of ductility of weld joint. Fractured surface of the joint from the face or root side due to bending reveals the presence of internal weld discontinuities.

Hardness test: Hardness is defined as resistance to indentation and is commonly used as a measure of resistance to abrasive wear or scratching. For the formation of scratch, a relative movement is required between two bodies and out of two, one body must indent into other body. Indentation is the penetration of a pointed object into the other object under the external load. Greater the penetration of an intender at a given standard load lower is the hardness. Various methods of hardness testing can be compared on the basis of criteria such as type of intender, magnitude of load and measure of indentation. The names of the procedures are Brinell hardness test, Rockwell hardness test, Viker hardness test etc.

Toughness test: In actual practice, engineering components during service are subjected to various kinds of load, static and dynamic loads which are classified on the basis of the rate of

change in magnitude of load and direction. Dynamic loads are characterized by high rate of change in load magnitude and direction. Reverse happens in case of static loads. A material which possesses a large amount of impact resistance is said to be tough material. Toughness is the ability of a material to resist both fracture and deformation. There are two methods used for toughness testing such as Izod and Charpy tests. In Izod test the sample is held vertically on anvil as cantilever and in Charpy the sample is held horizontally on anvil as simply supported beam. Results of impact tests are expressed in terms of either amount of energy absorbed or energy absorbed per unit area.

Fatigue test: The fatigue performance of metallic components is determined either by endurance limit or number of load cycles. For plotting the stress-number of cycle (S-N) curve, fatigue test is first conducted with maximum applied tensile load corresponding to 0.9 times of yield strength of weld joint under study to determine the number of load cycles required for fracture. Then same test is repeated at 0.85, 0.8, 0.75, 0.7… times of yield strength of weld joint until endurance limit or desired fatigue life is achieved.

1.3.3 MICROSTRUCTURE ANALYSIS

Microstructure is defined as the structure of a prepared surface or thin foil of a material as revealed by microscope. The microstructure of a material can strongly influence the physical properties such as strength, toughness, ductility, hardness, corrosion resistance, wear resistance and so on. Weld metallurgy is an important subject. Weld metallurgy is evaluated by study of microstructures. Microstructures at different regions of weldments: weld region, HAZ, and base material give an idea about the quality of weld. Mechanical properties of weld depend upon the phases present in the microstructure, size of the grains, and many other features. In the present work, microstructural studies have been made up to a certain extent.

1.4 WELDING DEFECTS

A weld defect is any flaw that compromises the usefulness of a weldment. Welding defects can greatly affect weld performance and longevity. According to ASME, cause of welding defects

are broken down as follows: 45% poor process conditions, 32% operator error, 12% wrong technique, 8% incorrect consumables, 3% bad weld grooves. General welding defects are given below:

Overlap: It is caused by poor welding techniques and can generally be overcome by an improved weld procedure. The overlap can be repaired by grinding off excess weld metal and surface grinding to the base metal.

Undercut: It is an unfilled groove along the edge of the weld. The causes are usually associated with incorrect electrode angle, excessive current and travel speed. Undercutting can be avoided with careful attention during preparation of the edge and by improving the welding process.

Cracking: Cracks and planar discontinuities are some of the most dangerous defects of the weld joints, especially if they are subjected to fatigue loading condition. Longitudinal cracks run along the direction of the weld and are usually caused by a weld metal hardness problem. Cold cracking occurs after the welding when metals are completely solidified.

Lamellar tearing: Lamellar tearing is a type of defect that is most likely to occur below a welded joint at points of high stress concentration. It is created by non-metallic inclusion being rolled into the hot plate metal during fabrication. Special joint design minimizes this defect.

Porosity: Cavities or pores caused by gas and non-metallic material entrapment in molten metal during solidification are called porosity. There are many causes which include contamination; inadequate shielding, too short arc gap and poor welding technique. Porosity can be minimized by proper selection of electrode, filler material and slower speed to allow time for gasses to escape.

Misalignment: This type of geometric defects is generally caused by a set up or fit up problem, or by joining plates of different thicknesses.

Incomplete fusion: It occurs when the weld metal does not form a cohesive bond with the base metal or when the weld metal does not extend into the base metal to the required depth. This type of defects occurs due to low current, insufficient preheating, too fast welding speed, incorrect edge preparation, arc not being at the centre to the seam.

Spatter: Spatter occurs from metal drops expelled from the weld that stick to the surrounding surfaces. Spatter can be minimized by correcting the welding condition and should be eliminated by grinding when present.

Inclusions: Inclusions are generated by extraneous materials such as slag, tungsten, and sulfide and oxide inclusion. Slag inclusion not only reduces cross sectional area and thus strength of the joint but also serves as initiation point for serious cracking. This defect can be eliminated by grinding down or re-welding. Some of these defects are shown in figure 1.4

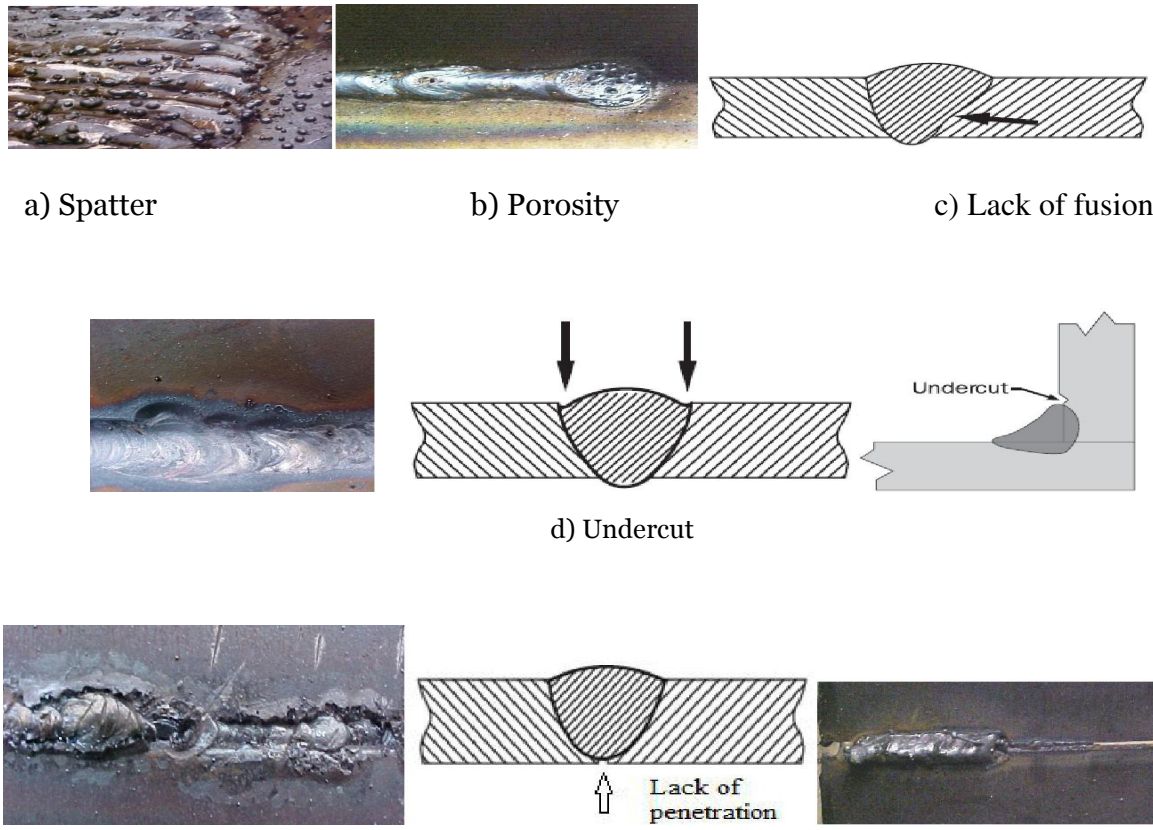

a) Spatter b) Porosity c) Lack of fusion

d) Undercut

e) Lack of penetration f) Excessive penetration

Figure 1.4 Various welding defects **[136, 142]**

1.5 WELDING OF DISSIMILAR METALS

A brief mention has been made about the importance and complexity of dissimilar welding in the beginning of this chapter. There is no doubt that welding between different materials is becoming more and more demanding, providing flexibility in design and fabrication options. Some more details are also included Scope and Objective of the present work.

1.6 LITERATURE REVIEW

Various process parameters of GMAW interact in a complicated manner and influence directly or indirectly various aspects of weld quality. Several attempts had been made by different researchers to find out the parametric influence on the desired welding characteristics. Also several works were done to develop mathematical models of heat transfer, mode of metal transfer, etc. Neural-network models had also been made to predict the influence of process parameters on the responses. Process optimization and other related aspects of GMAW had been taken into consideration by many researchers. A literature review is made on it in the context of finding scope and objective of the present work. In earlier sections, while discussing about some general features of welding, GMAW etc., some references **[1 – 20]** have already been mentioned. A literature review is made and given below with emphasis on GMA welding of stainless steels, especially Austenitic stainless steel, Ferritic stainless steel and welding of dissimilar metals, particularly dissimilar stainless steels. However, to arrive at the scope of the present work some, relevant fields are also taken into consideration other than those just mentioned above. These are welding of some other materials, optimization works done in various types of welding and on various metals, welding of dissimilar materials other than between Austenitic stainless steel and Ferritic stainless steel, etc.

B. Vijaya Sankar et al. [21] studied the effects of the welding parameters such Weld voltage, Weld Current and Gas flow rate on the weld joints AISI 310. AISI 310 stainless steels were joined by MIG welding by using AISI 310 Filler wire. Experimental procedure was derived by Design of Experiments and effects were identified through Grey relational analysis. The

significant effect of weld parameters such as weld current, weld voltage and gas flow rate was studied by Grey relational analysis and also responses under variable parameters were identified from the experimental results. The weld current was having most significant impact on weld process,

K. Srinivasan and V. Balasubramanian [22] investigated the effect of heat input on fume and their compositions during gas metal arc welding (GMAW) of AISI 316 stainless steel plates. Fume generation rate (FGR) and fume percentage were determined by ANSI/AWS F1.2 methods. Particle characterization was performed with SEM-XEDS and XRF analysis to reveal the particle morphology and chemical composition of the fume particles. The SEM analysis revealed the morphology of particles having three distinct shapes namely spherical, irregular, and agglomerated. Spherical particles were the most abundant type of individual particle. All the fume particle size fell in the range of less than 100 nm. Mechanical properties (strength, hardness and toughness) and microstructural analysis of the weld deposits were evaluated.
X. Chen et al. [23] fabricated 316L Austenitic stainless steel by gas metal arc additive manufacturing (GMA-AM) and its microstructure, and room temperature tensile properties were investigated. Results showed that in the GMA-AM 316L plate, a large number of well-aligned austenitic dendrites vertically oriented, forming large columnar grains in the middle and some microstructure of GMA-AM 316L consisted of δ, γ and σ phases. After one layer was deposited, the δ phase exhibited reticular morphology within austenitic dendrites. The δ phase was dissolved in austenite with the intermetallic σ phases forming at γ/δ interfaces under the thermal cycles influenced by the subsequent three deposition layers. And under the thermal influence after the fourth layer, both δ and σ phases turned into fine vermicular morphologies within austenitic dendrites. The tensile properties of GMA-AM 316L steel were comparable to wrought 316L and exceeded the industry requirements for 316L. Its fracture type was ductile failure due to the presence of obvious fracture surface dimples. The micro cracks initiated at the interior of σ phases and grew into large cracks leading to materials failure.
K. Abbasi et al. [24] carried out investigation on MIG welding of 10 mm thick bright drawn, mild steel. They were interested to find the effect of increase in pressure of shielding gas on penetration. The vessel was pressurized with argon-carbon dioxide mixture to an absolute pressure of 7, 14, 29, 58, 115, & 230 bars. The metal transfer modes were controlled by changing

the wire feed rates in the range of 3.81 m/min to 6.1 m/min. It was found that along with increase in pressure, the arc voltage needed to be increased in order to get good weld bead. Higher the pressure, density of fumes got increased. The investigators could carry MIG welding at a pressure was studied through variation of welding parameters like feed rate and arc voltage, on up to 230 bar.

P. Khanna and S. Maheshwari [25] investigated the effects of heat input and cooling rates on the magnitude and distribution of micro hardness values in different weld zones developed during namely; fusion zone (FZ), weld interface or fusion boundary zone (FBZ), heat affected zone (HAZ) and unaffected base metal zone. These zones experienced different rates of cooling, resulting in the formation of different microstructures. Micro-hardness study was one of the methods of testing the quality of a weld as it enabled the mechanical properties to be determined in different weld zones by corroborating the nature of microstructure constituents present therein.
B. Das et al. [26] welded EN-3A mild steel specimens by metal inert gas welding and showed the effect of various welding process parameters on its weldability. Parameters selected were welding current, arc voltage and welding speed. Butt joint was prepared and depth of penetrations was measured. Effect of welding parameters on penetration was observed with the help of surface plots.

H. H. Na et al. [27] examined the influence of welding process parameters on the weld bead geometry during fillet welding of 200 x 400 x 12 mm S400 steel plates. Neural network and mathematical equations were used for the prediction of bead geometry while Taguchi method was used for optimization of MIG welding process parameters
A. Hooda et al. [28] proposed a response surface model for the prediction of tensile strength of metal inert gas (MIG) welding of AISI 1040 medium carbon steel plates. The influence of welding process parameters like current, wire feed rate, voltage and gas flow rate was examined.
C. N. Patel and S. Chaudhary [29] investigated the effect of welding parameters like wire diameter, wire feed rate and current on weld hardness in welding of AISI 1020 carbon steel plates by MIG welding. The input welding parameters were optimized by Grey Relational Analysis (GRA) and researchers claimed that welding current was most influencing factor.
G. Kocher et al. [30] studied for the material IS 2062 E250 mild Steel and took input parameter as welding speed, variable- while arc voltage, welding current, wire feed rate, distance between

the nozzle and the plates were fixed and the purpose was to find the effect of weld speed on penetration and reinforcement. This study was also undertaken with the objective of determining the effects of weld speed on the weld profile and dilution analysis of the MIG butt welds of IS2062 E250 mild steel.

A. R. Bahman and E. Alialhosseini [31] focused on the relations between MIG welding parameters and mechanical properties of st37 joints. They searched for changes in hardness, yield strength and ultimate tensile strength with variation in input parameters.

N. Murugan and R. S. Parmar [32] used a four-factor-five level factorial technique to predict weld bead geometry (penetration, reinforcement, width and percentage dilution) in the deposition of 316L stainless steel on to structural steel IS 2062 using the GMAW process. The process parameters such as open-circuit voltage, wire feed rate, welding speed and nozzle-to-plate distance were controlled and the effect of each factor on the weld features were determined and presented graphically.

I. Z. Ibrahim et al. [33] investigated the effects of robotic GMAW process parameters on penetration, hardness and microstructural properties of mild steel weldments of 6 mm plate thickness. Arc voltage (22V, 26V, and 30V), current (90A, 150A, 210A) and welding speed (20 cm/min, 40 cm/min, and 60 cm/min) were chosen as variables. It was found that depth of penetration increased with increase in welding current. But highest hardness of the weldment was achieved at lowest current. From microstructural analysis it was found that, grain size became finer and more martensite formed at highest welding speed.

K. Sittichai et al. [34] investigated the effects of shielding gas mixture, welding current and welding speed on the ultimate tensile strength and percentage elongation of GMA welded austenitic stainless steel (AISI 304) of 3 mm thickness. Welding current was selected as 80, 90 and 100 A; travel speed was selected as 250, 300 and 350 mm/min. Three gas compositions 75% Ar + 25% CO_2, 70% Ar + 25% CO_2 + 5% O_2 and 69.5% Ar + 25% CO_2 + 5% O_2 + 0.5% He were selected as shielding gases. Shielding gas composition was found to be most influential on tensile strength. Highest UTS was found with shielding gas 70% Ar + 25% CO_2 + 5% O_2 but highest percentage elongation (47.94%) was found when welding with 69.5% Ar + 25% CO_2 + 5% O_2 + 0.5% He shielding gas at welding speed of 250 mm/min.

S. R. Patil and C. A. Waghmare [35] evaluated the process parameters of welding current, welding voltage, welding speed to investigate their influence on ultimate tensile strength (UTS)

for MIG welded specimen of mild steel by using Taguchi method. They concluded that the welding speed was most influencing parameter with 88.20% contribution followed by current of 10.76% and voltage of 0.69%.

R. Yilmaz and H. Uzun [36] compared the results obtained from destructive tests for mechanical properties of Austenitic stainless steel (AISI 304L and AISI 316L plates of 5 mm thickness) joints welded by GMAW and GTAW processes. The joints were made by GMAW process using ER 316 L Si filler metal and by GTAW process using ER 308L and ER 316L filler metals. Single V shaped groove was prepared. For GTAW process pure Argon was selected as shielding gas and the welding was carried out in double passes. In GMAW process, a mixture of 98% Ar and 2% O_2 was used and the welding was carried out in a single pass. Then the mechanical properties of the welded joints were found out by tensile, impact and Vickers micro-hardness tests. From tensile tests, it was found that better ultimate tensile strength and elongation values were obtained by GTAW process in both types of steel (304L and 316L). Impact test results showed that highest fracture energy was obtained from GTA Welding of 316L. 316L joints consumed more energy than 304L joints for both welding processes. From hardness tests it was found that, GTAW process offered better hardness values than GMAW process. It was concluded that higher tensile strength and toughness values were obtained in GTAW process due to narrower HAZ achieved in that process because of high energy concentration, thus reducing the problems of residual stress and hot cracking sensation of Austenitic stainless steel weldments. The weldments made by GMAW process suffered from low impact energy which might be due to its higher oxygen potential. Presence of more δ-ferrite in the weldments by GTAW process increased its impact energy and hardness values compared to GMAW process.

P. Khanna and S. Maheshwari [37] studied and analyzed effect of heat input on the magnitude and distribution of residual stresses developed during the MIG welding of stainless steel 409M. Stress relaxation technique of hole drilling had been used in which the elastic strain released was measured to determine the residual stresses. This method involved attaching strain gauge rosettes to the surface of weldments, drilling a hole at the centre of rosette and measuring the relieved strain with the help of suitable recording equipment. The measured strains were then related to relieved principal stresses through a series of equations. The results were analyzed by plotting the calculated residual stresses with respect to the distance from the weld centre line.

J. P. Mathew et al. [38] studied corrosion behaviour of FSS (AISI 430) weldment welded by TIG and MIG welding processes using austenitic filler metal/electrode. For analyzing the corrosion behavior of welded joints, Weight loss method and Potentio Dynamic Scanning (PDS) methods had been used. Weight loss method and PDS method were found to show similar behaviour of the corrosion rate of TIG/MIG welded joints of AISI 430 FSS in different environments. Corrosion behavior of TIG/MIG welded FSS 430 had been found to be the highest in acidic medium (H2SO4, HCl), less in marine (3.5% Nacl) and least in basic (NaOH) media. Corrosion due to sensitization was observed in acidic medium.

E. Karadeniz et al. [39] worked on the effect of process parameters on penetration in gas metal arc welding process. In the study, the effects of various welding parameters on welding penetration in *Erdemir 6842 steel* having 2.5 mm thickness welded by robotic gas metal arc welding were investigated. The welding current, arc voltage and welding speed were chosen as variable parameters. The depths of penetration were measured for each specimen after the welding operations and the effects of these parameters on penetration were researched. The welding currents chosen were 95, 105, 115 A, arc voltages considered were 22, 24, and 26 V and the welding speeds were chosen as 40, 60 and 80 cm/min for the experiments. Observation in the study was that increasing welding current increased the depth of penetration. In addition, arc voltage was another parameter in incrimination of penetration. However, its effect was not as much as current. The highest penetration was observed in 60 cm/min welding current.

A. M. Torbati et al. [40] worked for optimization of process parameters in GMAW of bimetal pipes. Autogenous gas tungsten arc welding (GTAW) and pulse rapid arc gas metal arc welding (GMAW) of butting bimetal (Bubi) pipelines were studied. GMAW was carried out from the outside of the pipe while GTAW was done from the inside to prevent lack of penetration and to promote a smooth internal weld bead surface. Current, welding speed, electrode diameter, shielding gas and orbital positions were defined as variables. The requirement for the GTA weld was to achieve 2 mm penetration depth without undercutting. The required penetration was difficult to achieve due to the outwards flow pattern in the molten pool driven by the Marangoni effect as a result of low sulphur content. It was shown that under optimized conditions, it was possible to obtain sound welds with proper geometry and defect free. The conditions needed were a combination of current of 170 A, welding speed of 200mm/min and an electrode angle of 30^0, with shielding gas protection of He–25%Ar for narrow groove welding of a J beveled pipe.

Y. Ruan et al. [41] investigated on mechanical properties and microstructures of 6082-T6 joint welded by twin wire metal inert gas arc welding with the SiO_2 flux. Twin wire MIG (metal inert gas arc welding) arc welding was employed on 6-mm thick 6082-T6 Al alloy plates partially with SiO_2 activating flux. The micro structural characteristics of the weld joint were investigated using optical, scanning microscopy and energy dispersive spectroscopy. Mechanical properties were studied with micro-hardness and tensile test. Results showed no obvious difference from the microstructures of the joints prepared with and without SiO_2 flux; the joint HAZ (heat affected zone) with SiO_2 flux was observed to be slightly wider than the one without the flux. The weld joint penetration with SiO_2 flux was about 26% deeper than without SiO_2 flux. The arc constriction and higher arc temperature were the main reasons for deeper penetration on twin wire MIG weld joint. The tensile test specimens prepared with and without the flux all showed plastic dimple fractured surfaces, SiO_2 flux did not have any obvious effect on the micro hardness and strength of the weld joint.

I .O. Oladele et al. [42] worked on wrought (6063) aluminum alloy using MIG welding .The current and voltage were used as parameters and their influences on microstructure, tensile strength, toughness and impact strength were studied. The two conditions were applied i.e. at constant voltage the current was I_1=75A and I_2=100A and at constant current the welding voltage was varied as V_1=25Vand V_2=30V.Tensile strength was more when current was at 100A. Toughness property was found to be good at V_1=25V. Hardness was more at I_1=75A and at V_2=30V.The micro structure with I_1= 75A showed that precipitation surrounding aluminum matrix led to fine particles , which were more responsible for high ultimate tensile strength and hardness. The authors concluded that as current got increased heat input increased causing better fusion of grains which gave best possible mechanical properties (ultimate tensile strength & hardness) and change in current or voltage did not affect more on impact strength.

P. J. Modenesi and R. C. de Avelar [43] had investigated the effect of variation in wire diameter characteristics in gas metal arc welding using CO_2 as shielding gas. A total of 16 samples of ER70S-6 were manufactured with little variation in mechanical strength, diameter etc. Experiments were carried out using each wire at a time. Spatter produced in each experiment was compared with the weight of the bead. The most influencing factors by variation in wire characteristic were found to be welding current, short circuit factor and transfer period.

R. Saluja and K. M. Moeed [44] studied the effect of MIG welding parameters like welding current, voltage, stick out distance of electrode and welding speed in welding of aluminium, measuring bead geometry and weld penetration using response surface methodology . They observed that the increase of welding current produced better bead geometry and deeper weld penetration up to the specific value of current.

G. Haragopal and P. V. R. Ravindrareddy [45] used Taguchi method to study the effect of gas pressure, current, groove angle and preheat on MIG welding of aluminium alloy (Al-65032).They indicated that welding current had more effect on ultimate tensile strength whereas gas pressure was the most significant parameter for proof stress, elongation and impact energy.

P. K. J. Martiikainen [46] showed the effect of different shielding gases on some mostly used steels and aluminium. It was shown that CO_2 was a preferred shielding gas for gas metal arc welding of carbon steels because it provided advantages like higher welding speeds, greater penetration and lower cost. The use of pure CO_2 was not suitable because of problems associated with spatter and element losses due to oxidation. Mixture of argon with 5–20 % carbon dioxide was referred for the welding of mild and low alloyed steels. It was claimed that increasing the amount of CO_2 in the shielding gas reduced the amount of inclusion and porosity in the weld. Inclusions in the weldment initiated and directed cracks and promoted brittle fracture. Hydrogen enhanced mixtures were not recommended for joining plain carbon steel because of detrimental effects such as under-bead cracking. Pure argon was not selected for welding stainless steel since it could not provide the desired arc stability and desired weld bead characteristics. Argon mixed with CO_2 and/or O_2 was therefore preferred. For Ferritic stainless steel it was found that increasing amount of CO_2 in shielding gas could increase the martensite content at the grain boundary. Presence of N_2 in the gas mixture increased the ductility, tensile strength, hardness and pitting corrosion resistance of the weld but amount of retained δ-ferrite reduced rapidly which further reduced the hot cracking susceptibility of the joint. Presence of H_2 in gas mixtures, increased heat input to the molten pool and provided good bead appearance but mechanical properties deteriorated. Mixture of argon and helium was found to be the most suitable gas for welding of aluminium because of more heat input, arc stability, weld puddle fluidity, reduced porosity etc.

H. Y. Huang [47] observed the effects of process parameters like current, voltage, welding speed and arc gap on penetration and weld area and optimized them using Taguchi method.

Three kinds of oxides, Fe_2O_3, SiO_2 and $MgCO_3$ were used to investigate their effect on weld bead geometry, angular distortion and mechanical properties in AISI 1020 carbon steel. For instance, welding current and welding speed had more influence on weld area, where welding current and joint gap affected weld penetration. It was found that the fluxes Fe_2O_3, SiO_2 and $MgCO_3$ increased the weld area, weld penetration and also improved the tensile strength and hardness of the GMAW joint. The angular distortion was also reduced by the flux aided GMAW.

D. S. Correia et al. [48] compared the results of response surface methodology (RSM) and genetic algorithm (GA) in gas metal arc welding optimization. A 9.5 mm thick plate of mild steel with a square-groove (1.2 mm root opening) was welded with ER 70S-6 electrode of 1.2 mm diameter. 100% CO_2 was used as shielding gas at a rate of 13 l/min. Central composite design (20 experiments, $\alpha = 1.682$) was used as design of experiments and reference voltage, wire feed rate and welding speed were selected as process variables. It was found that RSM provided good results over regular experimental regions, i.e., with no irregular points. But the problem associated with RSM was in irregular regions. If one experimental point failed, the model could not be estimated, since the matrix regarding the response values would be incomplete. D-optimal design could repair the fault but the properties of the final design would probably not compare with those of the original design and there might exist some correlation among the estimates. On the other hand GA (Genetic Algorithm) could provide good results at irregular regions also.

H. K. Lee et al. [49] investigated the effect of the wire feeding speed (WFS) and nozzle diameter on surface defects of aluminum plasma hybrid MIG welded joint using high speed imaging and metallurgical analysis. They observed that as WFS increased, the undercut size decreased and the surface defects could be completely controlled by controlling the nozzle diameter.

J. Achebo and W. E. Odinikuku [50] employed multi objective optimization technique based on ratio analysis (MOORA) and standard deviation to optimize welding parameters. Mild steel plates were joined using MIG welding. It was found that welding current of 350A, welding voltage of 22 V, and an electrode diameter of 3.2 mm and welding speed of 100 mm /s produced the weldment with the best properties.

X. Meng et al. [51] compared MIG welding and laser MIG hybrid welding methods to obtain the best method to overcome the poor weldability of invar36 alloy. They used Gauss and Cone

combined heat source for estimation. It was concluded that laser MIG hybrid welding was better than that of MIG welding for invar36 alloy.

A. Prakash and S. S. Raju [52] dealt with optimization of welding process variables by using MIG welding. In this process input variables were arc voltage (V), current (A) and welding speed(S) - with tensile properties, hardness and penetration as responses of low carbon steel (ASTM A29). Design of experiments based on Taguchi orthogonal array [L9]; and analysis of variance (ANOVA) was used to determine the impact of parameters with the optimal condition.

D. Kalita et al. [53] studied the effect of three important parameters of MIG welding; welding voltage, current and shielding gas flow rate on the tensile strength of C20 steel. An experiment was designed using Taguchi's L9 orthogonal Array with three repetitions. All welding work had been carried out using ER70S-4 electrodes. Results showed that welding voltage had significant effect, both on mean and variation of the tensile strength of the weld having 87.019% and 85.398% contribution respectively, whereas welding current had significant effect on mean only (10.807% contribution). Shielding gas flow rate had insignificant effect on the tensile strength of weld. From analysis of experimental data, the optimal setting was found to be: Welding current 200 A, Welding voltage 30V and shielding gas flow rate (CO_2) 8 l/min.

A. R. Yazdipour et al. [54] used aluminum alloy 5083 as investigating material and welding methods used were MIG and FSW (Friction Stir welding) The results considered were microstructure and mechanical properties The MIG welding was carried out at different speeds, with varying wire feed diameter. The voltage, current and heat input also were varied. FSW was carried using H13 steel tool .The microstructure by FSW was found to be of less porosity, good quality weld, with fine equiaxed and recryatallized grains as compared to that found in case of MIG welding . The microstructures varied at different zones of welded joint. But hardness was found to be more in FSW samples irrespective of weld zones. In MIG welding it was found that formation of dendrites occured during solidification. Tensile strength was greater in FSW sample as compared to MIG samples.

Investigation of fatigue property was done by **R. P. Verna and K. N. Pandey [55]** for welding of 6061 –T6 and 5083-0 aluminum alloy by manual arc welding and metal inert gas welding. In order to check fatigue, two types of loads were taken care of i.e. constant amplitude loading and with one intermediated single overload by adopting block loading method. The dimensions of materials were taken 250 x 1000 x 8 mm. Fatigue crack initiated in the HAZ and failed in case of

MIG welding, and in manual arc welding specimen, failure was at weld region. Fatigue life of 5083-0 alloy was compared to AA6061-T6 at same loading conditions of manual arc welding. For 6061-T6, fatigue life was more in MIG welding. Thus composition of alloy and method of welding both influenced the properties of material.

B. A. Prasad and P. Prassana [56] the authors made comparison of mechanical properties on AA6061 by undergoing MIG and FSW processes. MIG welding produced more porosity due to solubility of hydrogen in the molten aluminum pool. MIG welded elements were formed by columnar crystalline structure & FSW welded elements gave a fine microstructure at nugget zone and fine size of the weld nugget would generally be considered beneficial to the mechanical properties. Tensile strength of welded element was found less in case of both welding compared to that of base metal .But strength in FSW weld was found better than in MIG welding. Hardness property of FSW weld depended upon shoulder diameter and heat input. Hardness of heat affected zone (HAZ) of FSW was found to be narrower than the MIG welded joints.

J. P. Ganjigatti et al. [57] worked on Global versus cluster-wise regression analyses for prediction of bead geometry in MIG welding process. In their work, an attempt was made to establish input–output relationships in MIG welding process through regression analyses globally (i.e., one set of response equations for the entire range of the variables) as well as cluster-wise. The second approach made use of the entropy-based fuzzy clusters. The investigation was based on the data collected through full-factorial design of experiments. Results of the above two approaches were compared and some concluding remarks had been made. The cluster-wise regression analysis was found to perform in a slightly better way than the global approach in predicting weld bead-geometric parameters.

S. Pal et al. [58] investigated on artificial neural network modeling of weld joint strength prediction of a pulsed metal inert gas welding process using arc signals. This paper addressed the weld joint strength monitoring in pulsed metal inert gas welding (PMIGW) process. Response surface methodology was applied to perform welding experiments. A multi-layer neural network model had been developed to predict the ultimate tensile stress (UTS) of welded plates. Process parameters, namely pulse voltage, back-ground voltage, pulse duration, pulse frequency, wire feed rate , welding speed, and root mean square (RMS) values of welding current and voltage, are used as input variables of the model and the UTS of the welded plate was considered as the output variable. Furthermore, output obtained through multiple regression analysis was used to

compare with the developed artificial neural network (ANN) model output. It was found that the welding strength predicted by the developed ANN model was better than that based on multiple regression analysis.

K. M. Kanti and P. S. Rao [59] studied bead geometry in pulsed GMA welding using back propagation neural network, with the use of ANN. This paper presented the development of a back propagation neural network model for the prediction of weld bead geometry. The model was based on experimental data. The thickness of the plate, pulse frequency, wire feed rate, wire feed rate/travel speed ratio, and peak current were considered as the input parameters and the bead penetration depth and the convexity index of the bead as output parameters to develop the model. The developed model was then compared with experimental results and it was found that the results obtained from neural network model were accurate enough in predicting the weld bead geometry.

D. M. Arya et al. [60] had shown the influence of welding parameters like voltage, welding speed, welding current, gas flow rate and wire diameter on quality of weld. The response parameters selected for MIG welding were tensile strength, weld penetration, bead geometry and heat affected zone (HAZ) for quality target. Taguchi method followed by grey relational analysis was adopted for optimization of tensile strength and higher penetration.

N. Bhadauria and R. S. Ojha [61] adopted central composite face centered cubic design and studied GMAW process in respect of effect of process parameters on penetration depth. The authors developed mathematical models and observed that with increase in penetration weld strength increased.

A. S. Shahi and S. Pandey [62] studied the effect of some important variables such as wire feed rate, welding voltage, nozzle-to- plate distance and welding speed on dilution in GMAW process, and showed that the most significant factors on dilution were wire feed rate and welding voltage. Dilution would increase with the increase in wire feed rate and welding voltage, and decrease with the increase in welding speed and nozzle-to- plate distance.

K. Kishore et al. [63] analyzed defects in GMA process. They used Taguchi philosophy.

S. R. Meshram and N. S. Pohokar [64] investigated on the effect of MIG welding parameters like voltage, wire feed rate, welding speed, nozzle to plate distance and gas flow rate on penetration and ultimate tensile strength. With increase in welding current, values of depth of

penetration and UTS both increased. Other than that, arc voltage and welding speed were other factors that influenced the value of UTS.

B. C, Patel and J. Gandhi [65] studied the effect of MIG welding parameters: welding current, welding speed, flow rate of shielding gas and arc voltage on tensile strength.

Z. Pengcheng and L. Dasen [66] studied the free surface fluctuations in a GMAW weld pool with globular transfer mode. The transient free surface fluctuations during one droplet impingement period in a GMAW weld pool with globular transfer mode were studied to investigate the formation of ripples on weld bead surfaces. Evenly distributed fine ripples were acceptable and reduced the weld stress but coarse ripples needed to be eliminated. Capillary waves and gravity waves both were observed on the free surface of weld pools by using high-speed photography; among them the capillary waves contributed to the formation of ripples. A wave equation was established to simulate the dynamics of 3D free surface fluctuations. It was found that as the existing time of capillary waves was very short, they had small effect on the arc shape and heat input distribution mode of a GMAW arc in comparison with gravity waves.

M. M. Anzehaee and M. Haeri 67] proposed a new technique to estimate the droplet size in projected spray mode of GMAW process based on the modified force balance model. In that study, to preserve the desired transfer mode and to obtain a uniform and suitable droplet size, the melting rate and the droplet size were controlled instead of controlling the arc voltage and welding current. In that way, those variables that determine the weld geometry and the weld appearance were controlled directly. It was shown that the proposed method worked satisfactorily and helped to obtain a lower estimation error.

W. U. Chuan-song et al. [68] determined the critical transition current for metal transfer in GMAW. They developed a simple model to calculate the critical transition current based on the analysis of various forces exerted on a pendent droplet at the electrode tip. It was shown that the critical transition current from globular transfer to spray transfer decreased linearly as the stick-out length became longer, and increased with an increase in the electrode diameter.

I. S. Kim and A. Basu [69] developed an unsteady two-dimensional (2D) axisymmetric model for investigating the heat and fluid flow in weld pools and determining the weld bead geometry, velocity and temperature profiles for the GMAW process considering four driving forces for weld pool convection: electromagnetic; buoyancy; surface tension, and drag forces. The equation

was solved using a general thermo-fluid mechanics computer program, PHOENICS code, which was based on the SAMPLE algorithm.

H. Ates [70] developed an artificial neural network (ANN) model to predict gas metal arc welding parameters. The input parameters were various gas mixtures of argon, oxygen and carbon dioxide and outputs of the models were some mechanical properties such as tensile strength, elongation, impact strength and weld metal hardness. Extended delta-bar-delta learning algorithm was used to train the ANN controller. The measured and calculated data were simulated by a computer program. It was found that the model was almost accurate to predict the response.

Sreeraj et al. [71] adopted simulated annealing algorithm to analyze the effect of welding process parameters on the weld bead geometry in GMAW process. The authors used five level factorial techniques to predict four critical dimensions of bead geometry. They developed models to check for adequacy and significance. The bead geometry was predicted again using simulated annealing algorithm.

S. S. Sushant and B. S. Kumbhar [72] studied the effect of welding parameters like welding current, welding voltage, welding speed and weld plate angle on residual stresses generated in mild steel plates during welding. In their work experimental verification of temperature distribution by FEM was carried out, the verified methodology was used for parametric optimization for minimum residual stress.

S. S. Kumar et al. [73] successfully joined the rolled sheets of 3 mm thick, AISI 316L Austenitic stainless steel by friction stir welding (FSW) at different tool rotational speeds in the range from 400 rev/min to 800 rev/min with precisely selected constant values of other process parameters (welding speed of 45 mm/min, axial load of 12 kN and tool tilt angle of 1.5°). The microstructural characterization by orientation imaging microscopy (OIM) and transmission electron microscopy (TEM) revealed that discontinuous dynamic recrystallization was the dominant recrystallization mechanism in the stir zone. The grain size of the stir zone was greatly influenced by both heat generation and material strain rate. The shear bands were observed in the weld zone and the intensity of the shear bands was highly influenced by the deformation temperature. The results of the multi-spot energy dispersive spectroscopy (EDS) analysis within the narrow region of the shear bands depict the presence of tungsten traces for all the cases and, the minimal tungsten concentration was found in the weld joint made at 600 rev/min. The non-

existence of secondary phases in the weld zone was owing to lower peak temperatures in FSW . The base steel and the FSW joints depict a stable pitting potential after the activation controlled anodic region and the weld joints had marginally better pitting corrosion resistance than the base steel.

P. Bharath et al. [74] determined the influence of various welding parameters on the weld bead of AISI 316 welded joint. In this research work the ANOVA technique was used to identify the influence of the welding speed, current, electrode, root gap on the strength of the material. The result showed that speed was most influencing factor to have highest bend strength and current that was to be used was the most influencing factor to get higher tensile strength.

S. S. Kumar et al. [75] studied the influence of friction stir welding (FSW) tool material on the mechanical and microstructural properties of friction stir (FS) welded 316L stainless steel butt joints. FS welds were produced using two different tungsten based FSW tools having identical tool shoulder and pin profiles. In both the cases, the FSW experimental runs were carried out using tool rotational speed of 600 rpm, welding speed of 45 mm/min, axial force of 11 kN and tool tilt angle of 1.5°. The results of the study showed that the joints produced using the tungsten lanthanum oxide tool were having superior mechanical and microstructural properties when compared to the joints produced using tungsten heavy alloy tool. Furthermore, the tool degradation study by mass loss and photographic techniques suggested that the tungsten lanthanum oxide tool was more prone to degradation by plastic deformation, whereas the tungsten heavy alloy tool was more prone to degradation by wear.

D. Kianersi et al. [76] optimized welding parameters namely welding current and time in resistance spot welding (RSW) of the Austenitic stainless steel sheets grade AISI 316L. Afterward, effect of optimum welding parameters on the resistance spot welding properties and microstructure of AISI 316L Austenitic stainless steel sheets had been investigated. Effect of welding current at constant welding time was considered on the weld properties such as weld nugget size, tensile–shear load bearing capacity of welded materials, failure modes, failure energy, ductility, and microstructure of weld nuggets as well. Phase transformations that took place during weld thermal cycle were analyzed in more details including metallographic studies of welding of the Austenitic stainless steels. Metallographic images, mechanical properties,

electron microscopy photographs and micro-hardness measurements showed that the region between interfacial to pullout mode transition, and expulsion limit was defined as the optimum welding condition. Backscattered electron scanning microscopic images (BE-SEM) showed various types of delta ferrite in weld nuggets. Three delta ferrite morphologies consisted of skeletal, acicular and lathy delta ferrite morphologies formed in resistance spot welded regions as a result of non-equilibrium phases which could be attributed to the fast cooling rate in RSW process and consequently, prediction and explanation of the obtained morphologies based on Schaeffler, WRC-1992 and Pseudo-binary phase diagrams seemed to be a difficult task.

B. N. Zuma and J. W. van der Merwe [77] investigated the effect of Ru (Ruthenium) additions on the physical properties of 316L weld by studying the microstructural and mechanical properties of weld metal. The microstructure and mechanical properties of the welds were analyzed using optical microscope, scanning electron microscopy (SEM), EDX and Vickers hardness test respectively at 0.1%, 0.5%, 1% and 2% Ru addition. Primary ferrite (FA mode) solidification resulted in primary δ-ferrite and eutectic γ-austenite in the button welds, while hardness values increased to 198 HV with increasing Ru addition up to 2% Ru.

E. Ahmadi and A. R. Ebrahimi [78] were used four oxide fluxes (SiO2, TiO2, Cr2O3, and CaO) to investigate the effect of activating flux on the depth/width ratio and mechanical property of 316L Austenitic stainless steel. The effect of coating density of activating flux on the weld pool shape and oxygen content in the weld after the welding process was studied systematically. Experimental results indicated that the maximum depth/width ratio of stainless steel activated TIG weld was obtained when the coating density was 2.6, 1.3, 2, and 7.8 mg/cm^2 for SiO2, TiO_2, Cr_2O_3, and CaO, respectively. The certain range of oxygen content dissolved in the weld, led to a significant increase in the penetration capability of TIG welds. TIG welding with active fluxes could increase the delta-ferrite content and improved the mechanical strength of the welded joint.

M. O. H. Amuda and S. Mridha [79] investigated the effects of some input parameters by producing the welds on a 1.5mm thick plate of 16 wt% Cr FSS conforming to AISI 430 commercial grade , using TIG torch in argon environment at a heat flux between 1008W to 1584W and speed between 2.5mm/s and 3.5mm/s.

M. L. Greeef and M. D. Toit [80] investigated the susceptibility of 11-12% chromium type EN 1.4003 Ferritic stainless steel to sensitization during continuous cooling after welding at low heat input levels. It was concluded that sensitization of type En 1.4003 Ferritic stainless steel during continuous cooling after welding was possible if low heat input levels were used. Welding at low heat inputs could suppress the transformation of ferrite to austenite as the heat affected zone cooled through the (austenite+ferrite) dual phase region during welding. This resulted in largely ferritic high-temperature heat affected zones. With an increase in heat input, the cooling rate after welding was reduced, and more austenite formed in the high-temperature heat affected zones. Sensitization was prevented by the presence of enough austenite to eliminate continuous ferrite-ferrite grain boundaries.

K. Shamugam et al. [81] studied the effect of filler metals such as Austenitic stainless steel, Ferritc stainless steel and Duplex stainless steel on tensile and impact properties of the Ferritic stainless steel conforming to AISI 409M grade and concluded that the joints fabricated by Duplex stainless steel filler metal showed higher tensile strength and hardness compared to the joints fabricated by austenitic and FSS filler metals. Joints fabricated by Austenitic stainless steel filler metals exhibited higher ductility and impact toughness compared with the joints fabricated by Ferritic stainless steel filler metals.

E. Taban et al. [82] investigated the microstructural and mechanical properties of the gas metal arc welded 6 mm thick modified X2CrNi12 SS with two different heat inputs and concluded that the grain size had dominant effect on impact toughness. Grain coarsening had no adverse influence either on tensile properties or on the bend properties but the heat affected zone impact toughness for sub-zero temperature generally decreased and this was depended on the amount of grain coarsened microstructure and eventual precipitates present.

J. Rawlings et al. [83] investigated the effect of service temperature on the mechanical properties of several Ferritic P/M stainless steel grades including 410L, 409 Cb and concluded that the elevated temperature tensile properties of these ferritic P/M alloys were excellent and in most cases actually exceeded results published for wrought materials.

E. Taban et al. [84] investigated the hybrid (plasma + gas tungsten arc) welding properties of 12 mm thick modified 12% Cr Ferritic stainless steel complying with EN 1.4003 and UNS S41003 steels with a carbon content of 0.01% to improve the weldability and concluded that i) Sound joints of modified 12 Cr Ferritic stainless steel could be obtained by means of hybrid welding

since tensile and bend testing exhibited satisfactorily results. ii) In microstructural examination, some grain coarsening was observed ainly at the HAZ and fused metal at the root weld metal produced by plasma arc welding without filler metal. iii) Coarse ferrite grains did not have any adverse effect on tensile nor on bend properties but they led to relatively low impact toughness only for sub-zero temperature depending on the extent of grain coarsening.

A. K. Lakshminarayanan et al. [85] investigated the effect of welding processes such as shielded metal arc welding, gas metal arc welding and gas tungsten arc welding on tensile and impact properties of the Ferritic stainless steel conforming to AISI 409M grade on rolled plate of 4 mm thickness which was used as the base material for preparing single pass butt welded joints and authors concluded that gas tungsten arc welded joints of Ferritic stainless steel had superior tensile and impact properties compared with shielded metal arc and gas metal arc welded joints and this was mainly due to the presence of finer grains in fusion zone and heat affected zone.

A. K. Lakshminarayan et al. [86] evaluated the tensile and impact properties, micro hardness, microstructure, and fracture surface morphology of continuous current gas tungsten arc welding (CCGTAW), pulsed current gas tungsten arc welding (PCGTAW), and plasma arc welding (PAW) joints. They observed that the PAW joints of FSS showed superior tensile and impact properties when compared with CCGTAW and PCGTAW joints and this was mainly due to lower heat input, finer fusion zone grain diameter, and higher fusion zone hardness.

D. F. Filho et al. [87] investigated the influence of the shielding gas composition (pure argon and mixtures with O_2 or CO_2 on the chemical composition and microstructure of weld deposits obtained with gas metal arc welding using stabilized ferritic wires (ER430Ti and ER430LNb). The study was made comparatively to a non-stabilized wire (ER430). For each combination of gas/wire, three layers of beads were deposited. To prevent interference from base metal dilution, a UNS 43932 was used as support for the layers and only the last layer was analyzed. A special experimental approach was applied to permit more reliable comparison among different combinations of wire-shielding gas. Predicted equations for the demanded level of stabilizers in the wire were successfully applied. The results showed that the shielding gas composition played an important role in determining the final chemical composition and microstructure of the deposits, but its effect was dependent on the chemical composition of the deposit as a rule. In general, it was confirmed that the increase in CO_2 in the shielding gas augmented the carbon content (and martensite formation) in the weld metal, but wire stabilized with niobium could

prevent this detrimental effect but was not able to arrest grain coarsening. There were always losses of alloying elements due to the presence of O_2/CO_2, but the intensity depended on the amount of titanium/niobium.

M. Alizadeh-Sh et al. [88] investigated the process–microstructure–performance relationship in resistance spot welding of AISI 430 Ferritic stainless steel. The phase transformations which occured during weld thermal cycle were analyzed in details, based on the physical metallurgy of welding of Ferritic stainless steels. It was found that the microstructures of the fusion zone and the heat affected zone were influenced by different phenomena including grain growth, martensite formation and carbide precipitation. The effects of welding cycle on the mechanical properties of the spot welds in terms of peak load, energy absorption and failure mode were discussed.

G. Zhang et al. **[89]** investigated TIG welding condition of aluminum alloy by visual sensing of weld pool. For this purpose, the authors used two techniques - one was the own-developed computer-controlled variable polarity power (VPP) and the other was the composite filter technology. It was concluded that the high quality and clear images of welding pool of aluminium alloy were successfully acquired at low imaging current.

L. Yu-cheng et al. [90] developed a model of non-steady three-dimensional temperature field for red copper TIG welding with a locomotive. The temperature field of welding pool had been calculated with finite element software ANSYS. The results showed in their investigation that the heating effect of arc was evidently enhanced, with no preheating of red cooper in TIG welding. The authors also compared the experimental values with the calculated ones under different technological parameters.

A. Durgutlu [91] investigated the effect of mixing H_2 with Argon as shielding gas on TIG welding of Austenitic stainless steel. AISI 316L grade stainless steel plate with 4 mm thickness was selected as base metal. Pure Argon and Ar-5% H_2 were selected as shielding gases and then mechanical properties of the weldments were judged. Highest tensile strength and lowest hardness value were achieved with Ar- 1.5% H_2 gas mixture. The results of three point bending test showed that all samples had a bending strength of around 85 N/mm^2. It was found that penetration of the weld bead increased with increasing hydrogen content.

S. C. Juang and Y. S. Tarng [92] adopted a modified Taguchi method to analyze the effect of each TIG welding process parameters such as gas flow rate, arc gap, welding current and

welding speed on the weld pool geometry i.e. front height, back height, front width, back width and then to determine optimal combination of the process parameters associated with the optimal weld pool geometry. The base metal was AISI 304 stainless steel plates with a thickness of 1.5 mm. Experimental results showed that the front height, front width, back height, back width of the weld pool in the TIG welding of S304 stainless steel were greatly improved by using this approach.

Y. S. Tarng et al. [93] used neural network to construct the relationships between TIG welding process parameters i.e. gap, current, speed, gas flow rate, cleaning and weld pool geometry parameters i.e. front depth, back height, back width. To search for the process parameters with the optimal weld pool geometry, an optimization algorithm called simulated annealing was applied to the network. The quality of the Austenitic stainless steel welds based on the weld pool geometry was classified and verified by a fuzzy clustering technique. The membership grading obtained from fuzzy clustering algorithm corresponding to categories good (G), fair (F), and poor (P), were listed and the results showed that the membership grading for the category "good" was much higher. Therefore good weld quality could be obtained by using the optimal welding process parameters

M. Vasudevan et al. [94] used genetic algorithm (GA) to optimize the gas tungsten arc welding process parameters. Bead-on-plate welding was carried on 12 mm thick 316 LN Austenitic steel which was used in the Indian 500 MWe fast breeder reactor. An automatic GTAW machine was used with 3.2 mm thick tungsten electrode (EW Th-2) and 316L filler wire of 1.2 mm diameter. Welding current, voltage, filler wire feed rate and welding speed were used as process variables. Arc gap was maintained as 3 mm and 99.99% pure argon was selected as shielding gas. An optical microscope was used to measure the weld-bead shape parameters including bead width, depth of penetration and reinforcement height. Crossover rate was maintained at 0.65 and mutation probability was taken as 0.009; population size was selected as 100. Close agreement was achieved between weld-bead profile obtained using the genetic algorithm optimized process parameters and the target value.

R. Satish et al. [95] worked on the weldability and process parameter optimization of *dissimilar pipe joints* using GTAW. Taguchi method was used to formulate the experimental layout to rank the welding input parameters which influenced quality of weld. Results showed that lower heat

input resulted in lower tensile strength and too high heat input also resulted in reduced tensile strength.

G. Padmanaban and V. Balasubramanian [96] carried out optimization of pulsed current gas tungsten arc welding process parameters to improve tensile strength in AZ31B magnesium alloy. Result showed that maximum tensile strength of 188 MPa was obtained under the welding condition of peak current of 210 A, base current of 80A, pulse frequency of 6 Hz and pulse on time of 50%.

P. K Palani and M Saju [97] researched the effect of TIG welding process parameters on welding of Aluminium-65032. Response surface methodology was used to conduct the experiments. The parameters selected for controlling the process were welding speed, current and gas flow rate. Strength of welded joints was tested and the results were analyzed.

S. Datta et al. [98] performed a multiple response optimization in welding of mild steel specimens using submerged arc welding adopting L25 orthogonal array. Voltage, speed, stick out, and wire feed rate were taken as input welding parameters while bead width, bead height, penetration and HAZ were taken as output parameters. The process parameters were optimized using Grey-Taguchi method and welding speed was found to be the most significant factor.

K. Y. Benyounis et al. [99] developed a mathematical model using RSM to relate the failure load to the laser welding parameters i.e. laser power, focal position and welding speed. The effects of the process parameters on the failure load and the tensile-shear strength of the lap joint made of AISI 304 stainless steel with 1 mm thickness were investigated. It was found that the main factor affecting the joint strength was the welding speed and the other two factors slightly influenced the joint strength.

V. Gunaraj and N. Murugan [100] used RSM to develop mathematical models and studied the effect of important input process parameters namely the open-circuit voltage, wire feed-rate, welding speed and nozzle-to-plate distance on penetration, and percentage dilution on weld geometry in submerged arc welding (SAW) of pipes. Bead-on-plate welding was done. He concluded that the five level factorial techniques could be employed easily for developing mathematical models for predicting weld bead geometry within the workable region of control parameters in SAW of pipes.

T. Mohandas et al. **[101]** made a comparative evaluation of gas tungsten and shielded metal arc welds of AISI 430 Ferritic stainless steel. In the square butt joint titanium was added as a powder

obtained from crushed titanium sponge for grain refining and also copper was added as a foil for austenite stabilizer. Oxygen, too, was added as a 2% O_2 + 98% Ar mixture. From the investigation it was concluded that gas tungsten arc welds exhibiting equiaxed grain morphology had greater tensile and yield strength, compared to shielded metal arc welds.

A. K. Lakshminarayanan and V. Balasubramaniam [102] made a comparison between RSM and ANN in predicting tensile strength of friction stir welded AA7039 aluminium alloy joints. Author concluded that ANN model was more capable for predicting tensile strength within the range that had been trained.

B. Acherjee et al. [103] used ANN for predicting weld quality in laser transmission welding of thermoplastic; process parameters used in modeling were laser power, stand-off distance, welding speed and clamping pressure. The output parameters of the model were lap-shear strength and weld seam strength. A comparison was made between the ANN and multiple regression model analysis (MRA) for predicting laser transmission weld quality and it was found that ANN model showed better prediction, as compared to the MRA models.

B. Josefsson and U. Bergenlid [104] studied the effect of a low dose neutron irradiation on the tensile and fracture surface properties of Austenitic stainless steel. The specimens were irradiated at a temperature of about 35^0C. Irradiated tensile specimens showed a substantial radiation hardening combined with some reduction of elongations. It was concluded that there was no significant effect of the irradiation on the low cycle fatigue endurances and the irradiated tensile specimens showed a substantial radiation hardening combined with some reduction of elongation.

G. Mallaiah et al. [105] examined the influence of grain refining elements on mechanical properties of AISI 430 Ferritic stainless steel weldments by Taguchi approach. Based on Taguchi orthogonal array with regression equations, the authors developed an equation for predicting the mechanical properties of Ferritic stainless steel welds within range of grain refining elements. The authors also correlated the mechanical properties of AISI 430 Ferritic stainless steel and austenite content with microstructure and fracture features.

P. K. Palani and N. Murugan [106] proposed the use of 5% $CO_2$and 2% O_2 with Argon as gas mixture for welding of materials less than 6 mm thickness because they produced minimal spatter. For thicker materials use of higher CO_2 (u to 15%) was proposed. They found Argonex 1

(99% Ar, 1% O_2) and Argoshield 5 (95% Ar, 5% CO_2) to be suitable for welding of high alloy ferrous materials and low alloy ferrous materials (including MS and stainless steel) respectively.

J. Pasupathy and V. Ravisankar et al. [107] carried out investigations on welding of low carbon AA1050 with variation of welding current, welding speed and distance of electrode from work piece. Process optimization was done to achieve maximum joint strength.

S. R. Patil et al. [108] investigated on the material AISI 1030 mild steel welding. The input parameters were welding current, voltage, weld speed. The signal-to-noise (S\N) ratio and ANOVA (analysis of Variance) were used for optimization and it was found that tensile strength depended on welding speed. The result also showed that by increasing the welding speed and decreasing the current, strength of the welded joint increased, while voltage did not affect the weld strength.

M. Agka Khani et al. [109] studied for the material IS 2062 ES250 mild steel and took input parameter as wire feed rate, welding voltage, nozzle to plate distance, welding speed and gas flow rate and the response was the relationships between the weld dilution and the five controllable input welding parameters such as wire feed wire, welding voltage, nozzle-to-plate distance, welding speed, gas flow rate. And it was found that among main input welding parameters the effect of wire feed rate was significant. Increasing the wire feed rate and arc voltage increased the weld dilution whereas increasing the nozzle to plate distance the welding speed resulted in decrease of weld dilution and gas flow rate did not affect the weld dilution.

T. S. Kumar et al. [110] worked on influences of pulsed current tungsten inert gas welding parameters on the tensile properties of AA 6061 aluminum alloy with the use of full factorial method and ANOVA. The preferred welding process of aluminum alloy was frequently tungsten inert gas (TIG) welding due to its comparatively easier applicability and better economy. In the case of single pass TIG welding of thinner section of this alloy, the pulsed current had been found beneficial due to its advantages over the conventional continuous current process. The researchers reported that the use of pulsed current parameters improved the mechanical properties of the welds compared to those of continuous current welds of this alloy due to grain refinement occurring in the fusion zone. The authors stressed the need to carefully balance various pulse current parameters to arrive at an optimum combination. In essence, the investigation was carried out to study the influence of pulsed current TIG welding parameters on tensile properties of AA 6061 aluminum alloy weldment.

M. B. Chennaiah et al. **[111]** worked on dissimilar metals of mild steel and EN8 joined by MIG welding. The work heat input was varied from low to high with input parameters such as voltage, current and welding speed. Different response parameters like tensile strength, hardness, impact were taken for the analysis. The microstructure and mechanical properties at different zones were analyzed with or without post weld heat treatment. The properties are better when the joint was subjected to heat treatment.

S. Singh and N. Gupta [112] worked on dissimilar welded joints of stainless steel 304 and mild steel using MIG with the filler wire of stainless steel in presence of argon as shielded gas. The difference in the properties such as melting point, thermal conductivity and carbon content difference made austenite stainless steel and mild steel difficult to weld. The welding joint had more strength than mild steel (parent metal) and fracture took place in the mild steel during tensile testing. The optimum values were: current 250 A, voltage 25 V, wire feed rate 12.5 m/min and welding speed 15 cm/min to develop weld joint of maximum hardness.

R. R. Mishra et al. [113] studied on dissimilar metal joint as a structural material for various industrial applications which provided good combination of mechanical properties like strength, corrosion resistance with lower cost. In the study, stainless steel of grades 202, 304, 310 and 316 were welded with mild steel by Tungsten Inert Gas (TIG) and Metal Inert Gas (MIG) welding processes. The percentage dilutions of joints were calculated and tensile strength of dissimilar metal joints was investigated. The results were compared for different joints made by TIG and MIG welding processes and it was observed that TIG welded dissimilar metal joints have better physical properties than MIG welded joints.

V. Chauhan and R. S. Jodoun [114] optimized process parameters of MIG welding for Stainless Steel (SS-304) and low carbon steel using Taguchi design method. Three parameters of MIG welding viz. current, voltage and travel speed were taken for the analysis. The analysis for signal-to-noise ratio was done for higher-the-better quality characteristics. The significance of each parameter was studied by using the ANOVA. Finally the confirmation tests were performed to compare the predicted values with the experimental values which confirmed its effectiveness.

L. S. Kumar et al. [115] investigated for welding aspects of AISI 304 and 316 by Taguchi technique for the process of TIG and MIG welding. Mechanical properties of Austenitic stainless steel for the process of TIG and MIG welding were discussed there. The voltage was taken

constant and various characteristics such as strength, hardness, ductility, grain structure, tensile strength, HAZ width had been determined.

P. Kumar et al. [116] used Taguchi's parameter design methodology for parametric study of Gas Metal Arc Welding of Stainless Steel & Low Carbon Steel. The input process variables considered here included welding current, welding voltage and gas flow rate. Nine experimental runs were conducted using an L9 orthogonal array, and the concept of signal-to-noise ratio was adopted. Subsequently, using Analysis Of Variance (ANOVA) the significant coefficients for each input parameter on tensile strength, hardness etc. were determined.

B. Larsson and L. Berthold [117] had given detailed description of both the metallurgical properties and recommended welding procedure for joining of Ferritic and Austenitic stainless steels. Recently; joining of dissimilar materials with use of different welding processes have received more attention for producing variety of products or parts in many industrial applications

E. Taban et al. [118] investigated on several aspects of dissimilar welds between Ferritic stainless steel modified 12%cr and carbon steel.

E. M. Anawa and A. G. Olabi [119] optimized the tensile strength of dissimilar Ferritic/austenitic metal joints in laser beam welding process.

C. Ugur et al. [120] made an investigation on microstructural characteristics of dissimilar AISI 430 Ferritic and AISI 304 Austenitic stainless steel materials.

S. M. Joo et al. [121] had investigated the quality characteristics of the dissimilar welded joints between high strength steel and stainless steel in hybrid CO_2 laser GMA welding process by varying four parameters namely weld speed, welding current, laser arc distance and welding voltage.

R. Rudrapati et al. [122] had optimized process parameters of TIG welding of dissimilar mild steel and stainless steel materials.

M. Sivashanmugam et al. [123] experimented on Aluminum alloy 7075 welding by the process of GTAW using argon as inert gas and Tungsten was used as electrode. The butt joint was made using 99.99% argon as a shielding gas .The parameters considered for investigation are tensile strength, hardness and impact strength. The tensile strength got decreased with respect to parent material.

D. S. Nagesh and G. L. Datta [124] worked in the direction of prediction of weld bead geometry and penetration in shielded metal-arc welding using artificial neural networks. By

using ANN, bead geometry (bead height and width) and penetration (depth and area), the important physical characteristics of a weldment were investigated. Several welding parameters influenced the bead geometry and penetration. It was observed that high arc-travel rate or low arc-power normally produced poor fusion. Higher electrode feed rate produced higher bead width making the bead flatter. Current, voltage and arc-travel rate influenced the depth of penetration. The other factors that influenced the penetration were heat conductivity, arc-length and arc force. Longer arc-length produced shallower penetration. Too small arc-length might also give rise to poor penetration, if the arc-power was very low. Use of artificial neural networks to model the shielded metal-arc welding process was explored in this study. Back-propagation neural networks were used to associate the welding process variables with the features of the bead geometry and penetration. These networks had achieved good agreement with the training data and yielded satisfactory generalization.

D. S. Nagesh and G. L. Datta [125] examined the effect of arc power, electrode feed rate, arc voltage, arc current, arc travel rate and arc length on bead width, bead height and weld penetration. Artificial neural network was used to find out the estimated values. The experimental values were compared with the estimated values with very less error percentage. It was observed that high arc travel rate produced poor fusion and electrode high feed rate produced flatter weld bead.

K. H. Chavan et al. [126] studied single pass corner joint by Finite Element Method software using ANSYS. The analyses yielded that heat input; welding speed had significant impacts on the thermo mechanical characteristics.

I. Pires et al. [127] analyzed the influence of shielding gas mixtures on the metal transfer modes and fume formation rates. The reduction of welding fumes was necessary to improve the shop floor conditions and that could be achieved by proper selection of welding parameters. They studied the influence of 7 gas mixtures (Ar + 2% CO_2, Ar + 8% CO_2, Ar + 18% CO_2, Ar + 5% O_2, Ar + 8% O_2, Ar + 3% CO_2 + 1% O_2, Ar + 5% CO_2 + 4% O_2). When they used the binary Ar/CO_2 mixtures they found that the arc stability decreased with the increase of CO_2 content in the mixture due to high thermal conductivity of CO_2. That gave rise to more heat loss by conduction, so higher voltages were required, for same current intensity, to initiate and stabilize the arc. For mixtures with lower quantities of CO_2, the electromagnetic force changed from retention to detaching. When they used the binary Ar/O_2 mixtures they found the area of spray

transfer was larger than the area of Ar/CO_2 mixture. They also found that with the Ar + 8% O_2 mixture, the arc stabilized for lower voltages than with Ar + 5% O_2 mixture. The ternary mixtures were found to be more flexible producing short-circuit and spray transfer modes for a wide range of current intensities and voltages. It had been seen that fume formation rate increased with the increase of current intensity, and with increased CO_2 and O_2 contenst in the shielding gas both in ternary and binary mixtures. From the experiments they found that the Ar + 2% CO_2 were the one that exhibited the lowest fume formation rate.

D. Kim et al. [128] suggested the use of genetic algorithm (GA) and response surface methodology (RSM) to determine optimal welding conditions. At first a near optimal condition was determined by genetic algorithm in a relatively broad region. Then, the optimal conditions were generated over a relatively small region around this near optimal conditions by using response surface methodology. A desirability function approach was used to find different objective function values according to the positive or negative response from the set target value in the optimization problem.

A. D. Tipi [129] proposed a method to neutralize the effect of angle variation on drop detachment during automatic pipeline welding by presenting a welding current pattern. Electromagnetic force and gravitational force both had important effect on drop detachment. Due to the angle variation during welding, gravitational force varied which was neutralized by manipulating the electromagnetic force reaction. As the electromagnetic force had a direct relation with the square of the current value, the current value was adjusted to neutralize the effect of the gravity force. On the other hand to maintain the V/I ratio in all angles with varying currents, a pattern for voltage variation was presented. Again, appropriate patterns were determined for travel speed and wire feed rate also to maintain proper heat input and deposition rate all around the pipe.

P. Sathiya et al. [130] used simulated annealing to establish relationships between input parameters (heating pressure, heating time, upsetting time and upsetting pressure) and output parameters (flash thickness, flash height and flash width). The relationship between these input and output parameters were established through artificial neural network (ANN). The authors also analyzed variation between theoretical and experimental values of flash features.

M. R. Bosworth [131] studied the effect of gas composition on thermal transfer efficiency in pulse welding with (Ar + 5% CO_2) and (Ar + 18% CO_2). The use of shielding gas with low

concentration of CO_2 resulted in a considerable reduction in heat generated at the arc and received by the weld. Though, it was observed that there was not a significant difference in the thermal transfer efficiencies, however, argon with lower percentage of O_2 improved the alloy recovery. The carbide precipitation problem in welding of stainless steel was found to increase with CO_2 as shielding gas though the problem reduced when (Ar + 20% CO_2) gas mixture was used. It was found that increasing the amount of O_2 with argon in shielding gas mixture reduced the droplet size at globular and spray transfer.

P. Dutta and D. K. Prathihar [132] used conventional regression analysis and neural network to find out input-output relationships for TIG welding process. For that purpose one thousand training data for neural networks were created at random, by varying the input variables within their respective ranges and the responses were calculated for each combination of input variables by using the response equations. It was concluded that the neural network based approaches could yield predictions that were more adaptive in nature compared to those of the more conventional regression analysis approach. The authors also concluded that the Genetic Algorithm-Neural Network was found to perform better in most of the test cases.

P. Modenesi et al. [133] used a thin layer of an active flux that resulted in a great increase in weld penetration by TIG welding. The authors compared the changes in weld geometry at variations in the electrical signals from the arc and the arc shape. The authors also studied the effect of the flux on the weld microstructure. It was concluded that the simple flux used could greatly increase the penetration of the weld bead.

D. Hua-yun et al. [134] studied the heat and fluid flows in a free burning GTAW-arc under changing process conditions by a steady two-dimensional (2D) axi-symmetric model. The authors studied the temperature profiles, velocity profiles, and distribution of potential and current density of the arc. The authors established a series of response models by changing the welding process conditions, including welding current, flow rate of shielding gas, arc length and the kind of shielding gas.

Y. Chai et al. [135] investigated the fatigue behavior of the weld joints treated by TIG dressing and ultrasonic peening under variable-amplitude load. From this investigation they concluded that the effect of both TIG dressing and ultrasonic peening were to be less under variable amplitude than under constant amplitude loading. The authors also concluded that for either

constant or variable-amplitude loading, the improvement in fatigue strength of the welded joints due to ultrasonic peening was greater than that due to TIG dressing.
Some other references (136 - 142) are also found useful in the context of the present work.

1.7 SCOPE AND OBJECTIVE OF THE PRESENT WORK

GMAW/MIG has been invented in 1940's; in recent years different new welding processes have come into use but still GMA welding is one of the important welding processes for stainless steel whenever quality and productivity are concerned. Research works have indeed been done in the field of GMA welding of Austenitic stainless steel and Ferritic stainless steel. Several aspects in this context have been investigated. Literature survey, as given above, however, indicates that research is still being continued. It suggests there is a need of further extensive research in the area of gas metal arc welding. In so far as gas metal arc welding of Austenitic stainless steel and Ferritic stainless steel is concerned, knowledge-base is not sufficiently rich. More studies are required on various aspects of gas metal arc welding of Austenitic stainless steel and Ferritic stainless steel with the objective of achieving desired quality of weld. In doing so, parametric optimization, mathematical modelling, analysis of weld pool solidification and heat transfer, metallographic characterization, development of ANN or PNN models, analysis of joint performance etc. become important. Extensive investigation relating to all these aspects will lead to create a strong knowledge-base which will help people in practical field to use GMAW in a more predictable way, ensuring desired quality of weld. Further, dissimilar welding is now in demand and is used in some specific areas covering different industries. The complexity and problems exist. This provides scope of extensive research in the area of dissimilar welding. Apart from the present applications and demand of dissimilar welding, it is felt that, development in different aspects on dissimilar welding in different combinations of materials may lead to generate more useful application and demand. Ferritic/austenitic (F/A) joints are a popular dissimilar metal combination used in many applications and these joints have huge demand in industries like petrochemical industries, ship industries, nuclear power plants, pulp and paper, etc. F/A dissimilar joints are based on both technical and economic aspects i.e. these dissimilar joints can provide satisfactory performance with reasonable cost savings. Joining of dissimilar F/A materials is not an easy task; it is considered to be a challenging problem due to differences in thermal conductivities and thermal expansion which may cause crack formation at interface. In dissimilar metal welding, base metal contributes 15% dilution from each metal

while the filler metal contributes 70% to the total weld nugget composition. When welding dissimilar metals, good solid solubility is essential for sound weld properties. The trends of welding similar/ dissimilar metals present considerable challenges, still now. Welding of Ferritic and Austenitic stainless steel in general and GMAW welding of such steels in particular, can well be considered as one of the areas where more extensive research may contribute, in a significant way, to the precise control of the welding process for better and acceptable quality of weldment.

Taking all these into consideration, the present work is planned to investigate, some perspectives of GMAW of i) Austenitic stainless steel and ii) Ferritic stainless steel. Next dissimilar welding between Ferritic to Austenitic stainless steel has been studied. One major objective of the work is parametric optimization. Both single objective optimization and multi-objective optimization have been attempted. To move towards the objective just mentioned, a plan of experiments is made. Face-centered central composite design of experiments, based on response surface methodology, has been adopted. Taguchi design of experiments is also considered. Three levels of the input parameters have been employed. The selected input parameters are welding current, gas flow rate and nozzle to plate distance. After welding, visual inspection, X-ray radiography test, tensile test, micro-hardness test have been conducted. The results of these tests are discussed and interpreted. The observed data of the ultimate tensile strength, yield strength and percentage elongation under varied conditions of welding are analyzed. This is also one of the objectives of the present work. The process optimization has been done by using RSM and different optimization techniques. Optimized parametric setting has been evaluated. Microstructures of the welded samples have been examined and discussed. This also forms one part of the objective in the study. Significance of the input parameters (welding current, gas flow rate and nozzle to plate distance) on the responses like ultimate tensile strength, yield strength and percentage elongation is determined by ANOVA. Mathematical modelling is also done to identify relationship between the input variables and the responses. Finally some useful conclusions are drawn.

On summarizing the above, the present work is on gas metal arc welding of Austenitic to Austenitic, Ferritic to Ferritic and Austenitic to Ferritic stainless steels, with the objectives:

To study quality of weld under varied input parameters, in each of the three cases, through various tests, analyses of test results and microstructural studies,

To indentify optimal parametric condition, in each of the three cases.

Chapter 2

2. FUNDAMENTALS OF PROCESS OPTIMIZATION

Process Optimization is one part of the present work. Optimization techniques adopted and used in the course of the present work are discussed here to highlight the basic approach in each of these techniques.

2.1 RESPONSE SURFACE METHODOLOGY (RSM)

Response surface methodology (RSM) is a collection of mathematical and statistical techniques, generally used for empirical model building and analyzing a problem. The objective of RSM is to optimize a *response* (output variable) which is influenced by several *independent input variables*. To determine the optimum operating conditions of a system or to determine a region of the factor space in which operating requirements are satisfied, a 'design of experiment' is employed. A 'design of experiment' offers a series of tests, called runs, in which changes are made in the input variables in order to identify the reasons for changes in the output response.

RSM was introduced in the early 1950's and between the periods 1951-1975, classical RSM was developed which included the review of basic experimental designs for fitting linear response surface models. After 1976, recent modelling techniques have been added to RSM which covers Taguchi's robust parameter design and its response surface alternative approach.

The most extensive applications of RSM are in the particular situations where several input variables potentially influence some quality characteristics (response) of the process. The field of RSM consists of the experimental strategy for exploring the space of the independent process variables, empirical statistical modeling to develop a relationship between the yield and process variables, and optimizing the process variables that produce desirable values of the response. If process yield 'y' is a function of two variables x_1 and x_2, then it can be written as

$$y = f(x_1, x_2) + \varepsilon \qquad (2.1)$$

Where ε is represented as random experimental error assumed to have a zero mean. If the expected response is denoted by

$$E(y) = f(x_1, x_2) = \hat{y} \quad (2.2)$$

then the response surface can be represented by

$$\hat{y} = f(x_1, x_2) \quad (2.3)$$

The response can be represented graphically; either by 3-D surface plots or by contour plots that help visualizing the shape of the response surface. In the contour plots, lines of constant response are drawn in a plane keeping all other variables fixed. Each contour corresponds to a particular height of the response surface. The experimenter can locate the optimum with reasonable precision using a contour plot.

First order and second order models are most frequently used polynomial models in classical RSM. If the response is well modeled by a linear function of the independent variables, then the approximating function is the first order model. It is best suited when the initial estimate is far from the actual optimum. In such cases, the objective of the experimenter is to move to the general vicinity of the optimum rapidly. It is assumed that, a first order model is an adequate approximation to the true surface in a small region of the *x*'s. When the maximum increase in response is desired, the method is called steepest ascent method and if minimization of the response is desired then it is called steepest descent method. The fitted first order model is

$$y = \beta_0 + \beta_1.x_1 + \beta_2.x_2 + \ldots\ldots\ldots + \beta_k.x_k + \varepsilon \quad (2.4)$$

Where β_i' s are the regression coefficients.

The first order response surface i.e., contour of 'y' is a series of parallel lines and the direction of steepest ascent is the direction in which 'y' increases most rapidly. This direction is normal to the fitted response surface. Experiments are conducted along this path until no further increase in response is observed. Then a new first order model may be obtained, a new path of steepest descent is determined and the procedure is continued. Lack of fit of the first order model indicates if the vicinity of the optimum is reached or not.

Second order models are mostly useful when an approximation to the true response surface in a relatively small region is needed. In this case the initial estimate is close to the optimum and the

second order model is used to incorporate the curvature required to approximate the response. A second order model can be presented as

$$y = \beta_0 + \sum_{i=1}^{k} \beta_i x_i + \sum_{i=1}^{k} \beta_{ii} x_i^2 + \sum\sum_{i<j} \beta_{ij} x_i x_j + \epsilon \quad (2.5)$$

Where β_i' s are the regression coefficients and ε is represented as random experimental error

The second order models are flexible and can take on wide variety of functional forms. It is easier to estimate the parameters (β's) in the second order model. The method of least squares can be used for this purpose. In some situations, higher order (>2) polynomials are required.

2.2 TAGUCHI METHOD

Taguchi method is developed by Dr. Genichi Taguchi, a Japanese scientist. Taguchi design of experiments provides an efficient and systematic way to optimize designs for performance, quality and cost. Taguchi method is widely used in different fields of engineering to optimize the manufacturing processes / systems. It is one of the most important tools for designing high quality systems / processes at reduced cost. Taguchi method is based on orthogonal array experiments, emphasizes balanced design with equal weight age to all factors with less number of experimental runs. Therefore, cost as well as experimental time is reduced drastically with orthogonal array of Taguchi method. In order to evaluate the significance of process parameters, Taguchi method uses a statistical measure of performance called signal-to-noise (S/N) ratio that takes both the mean and the variability into account. The method explores the concept of quadratic quality loss function. The S/N ratio is the ratio of the mean (signal) to the standard deviation (noise). The ratio depends on the quality characteristics of the product/process to be optimized. The standard S/N ratios generally used are nominal-is-best (NB), lower-the-better (LB) and higher-the-better (HB).

Taguchi's S/N Ratio for (NB) Nominal-the-best

$$\eta = 10\ ln_{10} \frac{1}{n} \sum_{i=1}^{n} \frac{\mu^2}{\sigma^2} \quad (2.6)$$

Taguchi's S/N Ratio for (LB) Lower-the-better

$$\eta = -10\ ln_{10} \frac{1}{n} \sum_{i=1}^{n} y_i^2 \quad (2.7)$$

Taguchi's S/N Ratio for (HB) Higher-the-better

$$\eta = -10\ ln_{10}\frac{1}{n}\sum_{i=1}^{n}\frac{1}{y_i^2} \tag{2.8}$$

where n = experiment times

y_i= experimental value

η = S/N Ratio

μ = Standard Mean

σ = Standard Variance

2.3 GREY RELATIONAL ANALYSIS

The grey system theory proposed by Deng in 1982 has been proven to be useful for dealing with poor, incomplete, and uncertain information. The grey relational analysis based on grey system theory can be used to solve complicated inter-relationships among multiple performance characteristics effectively**.** However, the data applied in grey analysis is demanded to be preprocessed into quantitative indices to normalize raw data for analysis.

In grey relational analysis, experimental data i.e. measured features of quality characteristics of the product are first normalized ranging from zero to one. This process is known as grey relational generation. Next, based on normalized experimental data, grey relational coefficient is calculated to represent the correlation between the desired and actual experimental data. Then overall grey relational grade is determined by averaging the grey relational coefficient corresponding to selected responses. The overall performance characteristic of the multiple response process depends on the calculated grey relational grade. This approach converts a multiple- response- process optimization problem into a single response optimization situation, with the objective function in overall grey relational grade.

In grey relational generation, the normalized data corresponding to higher-the-better (HB) criterion can be expressed as:

$$x_i(k) = \frac{y_i(k) - min y_i(k)}{max y_i(k) - min y_i(k)} \tag{2.9}$$

Where $x_i(k)$ is the value after the grey relational generation, min $y_i(k)$ is the smallest value of $y_i(k)$ for the *k-th* response, and max $y_i(k)$ is the largest value of $y_i(k)$ for the *k-th* response. An ideal

sequence $x_0(k)$ is for the responses. The purpose of grey relational grade is to reveal the degrees of relation between the sequences say,[$x_0(k)$ and $x_i(k)$, i=1, 2, 3,…..].

Grey relation coefficient: After data pre-processing is carried out, a grey relational coefficient can be computed to quantify the relation between the ideal and actual normalized experiment data. The grey relational coefficient can be calculated using Eq.2.10.

$$\xi_i(k) = \frac{\Delta_{min} + \theta\Delta_{max}}{\Delta_{0i}(k) + \theta\Delta_{max}} \quad (2.10)$$

Where $\Delta_{0i} = \| x_0 - x_i(k) \|$ difference of the absolute value $x_0(k)$ and $x_i(k)$; θ is the distinguishing coefficient $0 \le \theta \le 1$; $\Delta_{min} = \forall j^{min} \in i \forall k^{min} \| x_0(k) - xj(k) \|$ = the smallest value of Δ_{0i} ; and $\Delta_{max} = \forall j^{min} \in i \forall k^{min} \| x_0(k) - xj(k) \|$ = largest value of Δ_{0i}.

Grey relational grade: Generally, the averaged value of the grey relational coefficients is taken as the grey relational grade. The grey relational grade γ_i can be computed as:

$$\gamma_i = \frac{1}{n}\sum_{k=1}^{n} \xi_i(k) \quad (2.11)$$

Where n = number of process responses. The higher value of grey relational grade corresponds to intense relational degree between the reference sequence $x_0(k)$ and the given sequence $x_i(k)$. The reference sequence $x_0(k)$ represents the best process sequence.

Grey relational ordering*:* In relational analysis, the practical meaning of the numerical values of grey relational grades between elements is not absolutely important, while the grey relational ordering between them yields more subtle information. The combination yielding the highest grey relational grade is assigned an order of 1 while the combination yielding the minimum grade is assigned the lowest order.

Combined Grey –Taguchi method is also used. Taguchi's S/N ratio concept is applied here on grey relation analysis. Optimized parametric condition is obtained from S/N ratio plots of gray relation grade.

Chapter 3

3. EXPERIMENTAL PLAN, SET-UP & PROCEDURE

Some aspects of gas metal arc welding of Austenitic stainless steel, Ferritic stainless steel and dissimilar welding between Austenitic and Ferritic stainless steels have been studied in the present work. This has been mentioned earlier in scope and objective of the present work. The effects of current, gas flow rate and nozzle to plate distance have been studied. Face-centered central composite design and Taguchi design have been adopted in order to identify optimal parametric combination for desired quality of weld. After welding, visual inspection and next, radiographic test have been carried out. Tensile tests have also been conducted. Microstructural studies have been done as well; hardness at different zones of the weldment has been measured. Confirmatory tensile tests have been carried out. The results are shown, discussed and analyzed in subsequent chapters.

3.1 EXPERIMENTAL PLAN

Three sets of experiments have been carried out based on RSM design of experiment and L9 Taguchi orthogonal design of experiment. In the first set of experiments: 316L Austenitic stainless steels have been butt welded as per RSM and Taguchi designs of experiments. In the second set of experiments welding of 409 Ferritic stainless steel has been carried out by using 316L filler wire as per RSM and Taguchi designs of experiments. And in the third set of experiments dissimilar welding between 316L Austenitic stainless steel and 409 Ferritic stainless steel has been carried out as per L9 Taguchi design of experiments. As mentioned earlier, several levels of current, gas flow rate and nozzle to plate distance have been used to do butt welding of Austenitic stainless steel (AISI 316L) of 3mm thickness. Three levels of current, gas flow rate and nozzle to plate distance have been selected based on face-centered central composite design of experiment and L9 Taguchi Orthogonal Array design of experiment. In the present work, experiments are done in a planned experimental order, named design of experiments. Face centered central composite design has been used as design of experiment. Welding current, gas flow rate and nozzle to plate distance are selected as input

parameters and 3 levels are considered for each of them. Number of center runs is selected as 6. So the total number of experiments becomes $2^3 + 2\times3 + 6 = 20$. In Table 3.1, the welding process parameters and their levels are given below. The values of the input parameters have been selected by study from the literature and trial runs. RSM Face centered central composite design matrix is shown in Table 3.2

Table 3.1 Process parameters and their levels

Process parameters	Symbols	Unit	Values	Level 1	Level 2	Level 3
Welding current	C	A	Numerical	100	112	124
			Coded	-1	0	1
Gas flow rate	F	*l/min*	Numerical	10	15	20
			Coded	-1	0	1
Nozzle to plate distance	S	mm	Numerical	9	12	15
			Coded	-1	0	1

Table 3.2 RSM Face centered central composite design matrix

Sample Nos.	Welding Current(A)	Gas flow rate(l/min)	Nozzle to plate Distance(mm)
1	112	15	12
2	100	15	12
3	124	15	12
4	100	10	9
5	100	10	15
6	100	20	15
7	100	20	9
8	112	10	12
9	112	15	12
10	124	10	9
11	112	15	12
12	112	15	15 (contd.)

13	124	20	15 (contd. from previous page)
14	124	10	15
15	112	15	12
16	112	15	12
17	112	15	12
18	112	20	12
19	112	15	9
20	124	20	9

After the experiments, welded samples are visually inspected followed by X-ray radiography test. Then from the welded samples, specimens are prepared for tensile test and Vickers micro-hardness test. The details about them have been discussed in subsequent sections.

In another set of work, experiments are done in a planned experimental order; Taguchi orthogonal array design L9 has been used as design of experiment. Welding current, gas flow rate and nozzle to plate distance are selected as input parameters and three levels are considered for each of them. Welding design matrix as per L9 Taguchi orthogonal array design is shown in Table 3.3.

Table 3.3 Welding design matrix as per L9 Taguchi orthogonal array design

Sample No.	**Current (A)**	**Gas flow rate (*l*/min)**	**Nozzle to plate distance (mm)**
1	100	10	9
2	100	15	12
3	100	20	15
4	112	10	12
5	112	15	15
6	112	20	9
7	124	10	15
8	124	15	9
9	124	20	12

Compositions of base material and the filler wire and mechanical and physical properties of parent material are given in Table 3.4

Table 3.4 Compositions of base material and filler metal *(%) and mechanical properties and physical properties of parent material*

Base Metal											
	C	Mn	Si	P	Cr	Ni	Mo	Cu	Al	S	T
316L	0.03	1.47	0.58	0.025	18.33	8.33	0.2	0.19	0.01	0.01	----
409	0.02	0.78	0.37	0.02	11.72	----	----	----	-----	0.02	0.48
Filler Metal											
316L	0.02	1.85	0.42	0.025	18.73	12.20	2.30	0.19	0.01	0.01	…

Mechanical Properties of parent material [143]

Grade	Tensile Str. (MPa) min	Yield Str. 0.2% Proof (MPa) min	Elong. (% in 50 mm) min	Hardness	
				Rockwell B (HR B) max	Brinell (HB) max
316L	485	170	40	95	217
409	450	140	25	75	131

Physical Properties of parent material [143]

Grade	Density (kg/m^3)	Elastic Modulus (GPa)	Mean Coefficient of Thermal Expansion (µm/m/°C)			Thermal Conductivity (W/m.K)		Specific Heat 0-100°C (J/kg.K)	Electrical Resistivity (nΩ.m)
			0-100°C	0-315°C	0-538°C	at 100°C	at 500°C		
409	7800	200	11.0	11.7	12.4	25.8	27.5	460	600
316L	8000	193	15.9	16.2	17.5	16.3	21.5	500	740

3.2 EXPERIMENTAL SET-UP

The photographic view of the experimental set up is shown in figure 3.1

3.2.1 EQUIPMENT AND INSTRUMENTS USED

WELDING MACHINE

Mechanized GMAW welding has been done on ESAB AUTO K - 400 MIG/MAG welding machine in M/s Das Enterprise, Howrah. The photographic view of the welding machine and the set up is shown in figure 3.1. Butt welded joints are done under varied input parameters, as mentioned above. The tensile test specimens have been tested on tensile testing machine INSTRON as per ASTM standard.

Figure 3.1 The photographic view welding set-up

Salient Features of the Welding Machine

- Digital V/A Meters
- Fully thyristorised hex phase control
- Stick out control
- Crater control
- Fresh Tip Treatment (FTT) eliminates globule formation at the wire tip during weld stop
- Quick Arc Start
- Gas pre-flow setting
- Choice of CO2 or Argon Mix
- Self hold ON function
- Servo feeder with quick changeover mechanism
- 4 roll drive option
- Suitable for solid and flux cored wires
- Separable remote control

POWER SOURCE	**AUTO K400**
Mains supply, Ph x V, Hz	3 x 415, 50
Open circuit voltage, V DC(Max)	53
Welding current range, A	60-400
Welding current at 60% duty cycle, A	400
Welding current at 100 % duty cycle, A	310
Insulation class	H
Type of cooling	Forced Air
Type of Welding Voltage/ Current Regulator	YES
Dimensions, l x w x h, mm	685 x 360 x 755
Weight, Kg	121
WIRE FEEDER	
Drive system	DC motor
Speed control	Stepless
Feed mechanism	2 Roll (optional 4 roll)
Wire feed speed, m/min	1-16
Wire diameter	0.8-1.2

Wire type	MS/Al/FC
Weight, Kg	7

MIGGYTRAC 2000

It is a small, compact, motor-operated trolley designed for the mechanization of GMAW, gas metal arc welding, in particular. The permanent magnet built-in magnet, which can be switched on/off, holds the tractor in the correct position on the work-piece.

- Travel speed, m/min 2.5
- Welding speed, m/min 0.15-1.5
- Control voltage, V, AC 36-42
- Max power consumption, W 25
- Intermittent welding range, cm 1-99
- Crater fill duration, s 0-9.9
- Weight, kg 8.5
- External dimensions, LxWxH, mm 400x340x370

X-RAY RADIOGRAPHY MACHINE

X-ray radiography tests have been carried out at SKB Metallurgical Services, Salkia, Howrah – 111062. The important specifications of the equipment used for this purpose are given below.

Source	X-ray
Equipment details	XXQ-2005
Voltage	130KV
Current	5Ma
Film	Laser NDT-7
Density	2.2-2.4
Sensitivity	<2.0 %
SOD	28''
Screen	0.15 mm (Both)
Technique	S.W.S.I

IQI	ASTM-1A
Exposure time	30s

INSTRON UNIVERSAL TESTING MACHINE

Tensile tests have been carried out on Instron universal testing machine in Jadavpur University laboratory using a hydraulic chuck. The major specifications of the machine are given below. The photographic view of the machine is given in figure 3.2.

Model No. : 5589

Maximum capacity : 600 KN

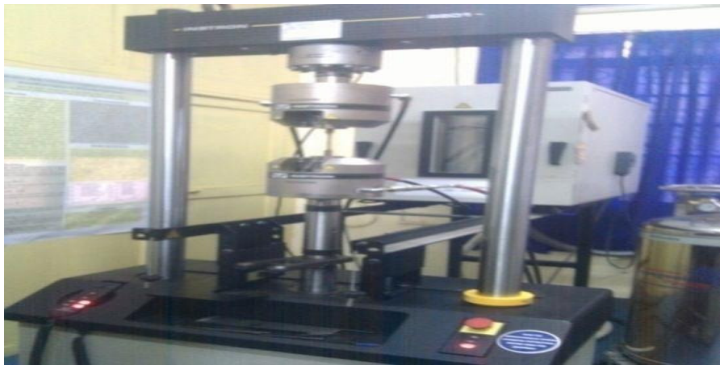

Figure 3.2 Photographic view of Instron universal testing machine

METALLURGICAL MICROSCOPE

Leica metallurgical microscope is used for study of microstructures of the welded samples. The photographic view of the microscope is given in figure 3.3.

Figure 3.3 Photographic view of the microscope

MICRO-HARDNESS TESTER

This instrument has been used to measure hardness at different regions of the weldment. This has been a LECO LM 248AT micro-hardness tester (figure 3.4). Some important specifications are:

Figure 3.4 Photographic view of the Leco LM 248AT micro-hardness tester

Model No. :LM 248AT

Software : Amh 43

Zoom : 10x – 50x

Indentation Load: 10 gf – 1 kgf

3.3 EXPERIMENTAL PROCEDURE, INSPECTION AND TESTING

Three sets of experiments have been carried out based on RSM design of experiment and L9 Taguchi orthogonal design of experiment. In first set of experiments: 316L Austenitic stainless steels, 3mm thick have been butt welded as per RSM and Taguchi designs of experiments. In second set of experiments welding of 409 Ferritic stainless steel has been carried out by using 316L filler wire as per RSM and Taguchi designs of experiments. And in the third set of experiments dissimilar welding between 316L Austenitic and 409 Ferritic stainless steel has been carried out as per L9 Taguchi designs of experiments.

Photographic view of one of the welded specimens is shown in figure 3.5.

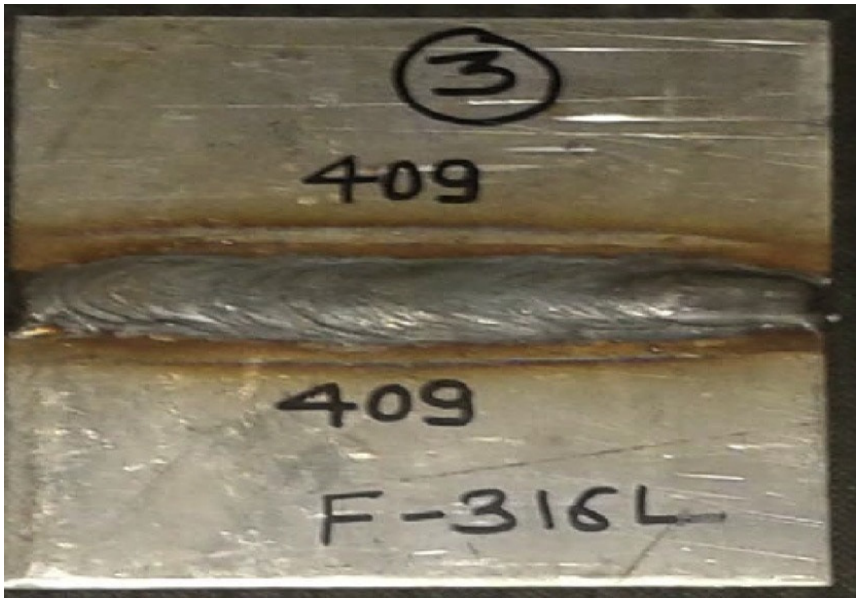

Figure 3.5 Photographic view of a welded specimen

After welding, visual inspection of all the samples has been done. X-ray radiography tests are conducted next. Now tensile test specimens are made by machining the welded samples. A schematic diagram showing the basic dimensions of the tensile test specimens is given in figure 3.6. Photographic view of a tensile test specimen is shown in figure 3.7.

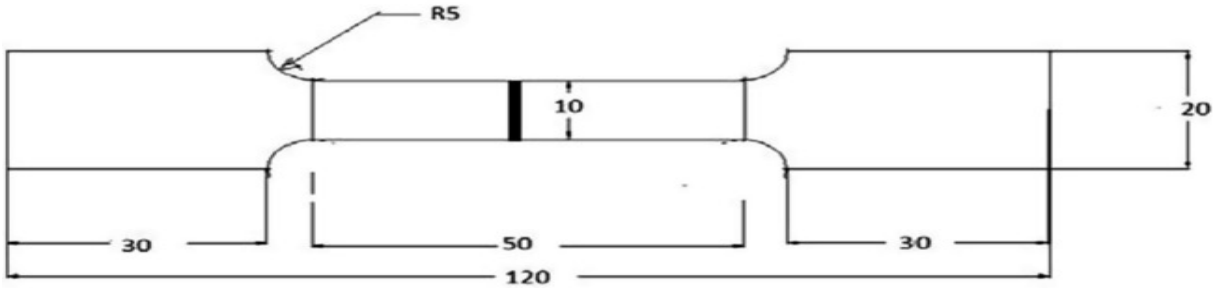

Figure 3.6 Schematic diagram of the specimen prepared for tensile test

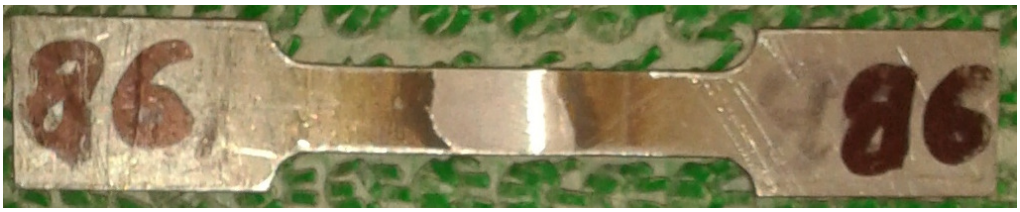

Figure 3.7 Photographic view of a specimen prepared for tensile test

During preparation of tensile test specimen, small cut-outs are made which have subsequently been ground, polished and finally etched to obtain samples for microstructural studies. The

Austenitic stainless steel samples are etched by aqua regia (3 HCL + 1 HNO_3) solution and Ferrtic stainless steel and F/A stainless steel are etched with the etchant made up of 20 ml ethylene glycol, 20 ml HNO_3 and 100ml ethanol. These samples have been studied under Leica microscope and microstructures of base metal, heat affected zone (HAZ) and weld metal are studied; photographs are taken. Hardness test has also been conducted for each of these samples. While doing this, hardness values have been measured in several points in different zones: weld metal, HAZ and base metal. Leco micro-hardness tester has been used for this purpose, as mentioned earlier.

The results of all the above mentioned experiments, tests and studies are given and discussed in the next Chapter. Process optimization has also been done, based on the observed results. This is included in Chapter 5.

Chapter 4

4. RESULTS AND DISCUSSION

The details of experimental plan, procedure and set up have been discussed in chapter 3. In the following sections the results are presented and discussed.

4.1 RESULTS OF MIG WELDING OF 316L AUSTENITIC STAINLESS STEEL (1ST SET OF EXPERIMENTS)

Three sets of experiments have been carried out based on i) RSM design of experiment and ii) L9 Taguchi orthogonal array design of experiment. In first set of experiments: 316L Austenitic stainless steels, have been butt welded as per i)RSM design of experiment and ii) L9 Taguchi orthogonal array design of experiment . In the following paragraphs, first, the results are presented and discussed as per RSM design of experiment.

4.1.1 RESULTS OF VISUAL INSPECTION AND DISCUSSION: 316L AUSTENITIC STAINLESS STEEL AS PER RSM DESIGN OF EXPERIMENT

After welding, visual inspection has been carried out to detect surface defects of weld specimens made of Austenitic stainless steels. Visual inspection is of great importance because it constitutes the principal basis of acceptance for many types of weldments. It is the most extensively used method of inspection because it is easy to apply, is quick, is relatively inexpensive, and gives very important information with regard to the welds, and general conformity of the weldment to specification requirement. Results of visual inspection are shown in Table 4.1. It is found from this table that for certain welding conditions; no defect has been observed. These are for the sample nos. S2, S3, S4, S5, S6, S7, S8, S10, S11, S12, S13, S15, and S20. Blow holes and undercut, spatter, uneven penetrations are the types of defects which are found in some other

samples. Spatter found only for sample nos. S9 and S17, is caused possibly due to damp filler rod or arc blow or bubble of gas being entrapped in the molten globule of metal, expanding with great violence and projecting small drops of metal outside the arc seam. High current might be the reason as well. Too low or two high current and/or faster travel speed might have caused blow holes. Incorrect welding technique attempting stringer or weaved beads, unclean job surface, damp filler rod are also considered as some reasons for which blow holes or porosity may form. Again, blow holes and porosity might have resulted from gas getting entrapped in solidifying metal, larger arc etc. In some samples undercuts have been found, which might have been caused by improper joint geometry or because of incorrect combination of Welding current, Gas flow rate and Nozzle to plate distance. Other possible reasons behind undercut are: faster arc travel speed during welding or larger arcs, wrong filler rod. The possible reasons of the defects found in the several samples are discussed along with discussion on the defects found in X-ray radiography test in the following section.

Table 4.1 Results of visual inspection: 316 L Austenitic stainless steel as per RSM design of experiment

Sample No.	Sample Identity	Observation
S1	C-112/F-15/S-12	Uneven penetration at the middle
S2	C-100/F-15/S-12	No defect
S3	C-124/F-15/S-12	No defect
S4	C-100/F-10/S-9	No defect
S5	C-100/F-10/S-15	No defect
S6	C-100/F-20/S-15	No defect
S7	C-100/F-20/S-9	No defect
S8	C-112/F-10/S-12	No defect
S9	C-112/F-15/S-12	Spatter, Blow hole
S10	C-124/F-10/S-9	No defect
S11	C-112/F-15/S-12	No defect
S12	C-112/F-15/S-15	No defect
S13	C-124/F-20/S-15	No Defect (contd..)

		(Contd. from previous page)
Sample No.	**Sample Identity**	**Observation**
S14	C-124/F-10/S-15	Uneven penetration
S15	C-112/F-15/S-12	No defect
S16	C-112/F-15/S-12	Non-uniform reinforcement
S17	C-112/F-15/S-12	Shallow penetration, little spatter
S18	C-112/F-20/S-12	Little spatter, weld depression
S19	C-112/F-15/S-9	Non –uniform reinforcement
S20	C-124/F-20/S-9	No defect

4.1.2 RESULTS OF X-RAY RADIOGRAPHY TEST AND DISCUSSION: 316L AUSTENITIC STAINLESS STEEL AS PER RSM DESIGN OF EXPERIMENT

After completion of the visual inspection, X-ray radiography tests of the welded samples have been carried out for all the 20 samples by XXQ-2005 X-Ray flaw detector. The results are given in Table 4.2. The photographic views of the X-ray films are shown in figures 4.1 – 4.20.

Lack of fusion at root or wall has occurred possibly due to improper setting of the current, improper cleaning, faster arc travel speed, presence of oxides, scale and other impurities which do not permit the deposited metal to fuse properly with the base metal. Too low heat input does not ensure proper melting of the weld deposit. Porosity has been found in sample nos. S9, S14 and S18 which may have resulted from gas being entrapped in the solidifying metal. Porosity can be a significant problem which is very tough to solve. The biggest causes are probably contamination of the shielding gas, followed by filler metal and base metal contamination. If the results of visual inspection and X-ray radiographic tests are compared, some consistency in the findings can be noticed. Visual and X-ray radiographic tests also, indicate that sample nos. S2, S3, S4, S5, S6, S7, S8, S10, S11, S12, S13, S15, and S20 have got no significant defect thus causing reasons for good performance of the sample under tensile testing.

Table 4.2 Results of X-ray radiography test: 316L Austenitic stainless steel as per RSM design of experiment

Sample No.	Sample Identity	Observation
S1	C-112/F-15/S-12	Lack of fusion
S2	C-100/F-15/S-12	No major defects
S3	C-124/F-15/S-12	No major defects
S4	C-100/F-10/S-9	No significant defect
S5	C-100/F-10/S-15	No significant defect
S6	C-100/F-20/S-15	No significant defect
S7	C-100/F-20/S-9	No significant defect
S8	C-112/F-10/S-12	No significant defect
S9	C-112/F-15/S-12	Lit bit of porosity
S10	C-124/F-10/S-9	No significant defect
S11	C-112/F-15/S-12	No significant defect
S12	C-112/F-15/S-15	No significant defect
S13	C-124/F-20/S-15	No significant defect
S14	C-124/F-10/S-15	Porosity, lack of fusion
S15	C-112/F-15/S-12	No significant defect
S16	C-112/F-15/S-12	Lack of penetration
S17	C-112/F-15/S-12	Lack of penetration
S18	C-112/F-20/S-12	A little bit porosity
S19	C-112/F-15/S-9	lack of fusion
S20	C-124/F-20/S-9	No Significant defect

Figure 4.1 X-ray radiographic film for Sample No. S1: 316L Austenitic stainless steel as per RSM design of experiment

Figure 4.2 X-ray radiographic film for Sample No. S2: 316L Austenitic stainless steel as per RSM design of experiment

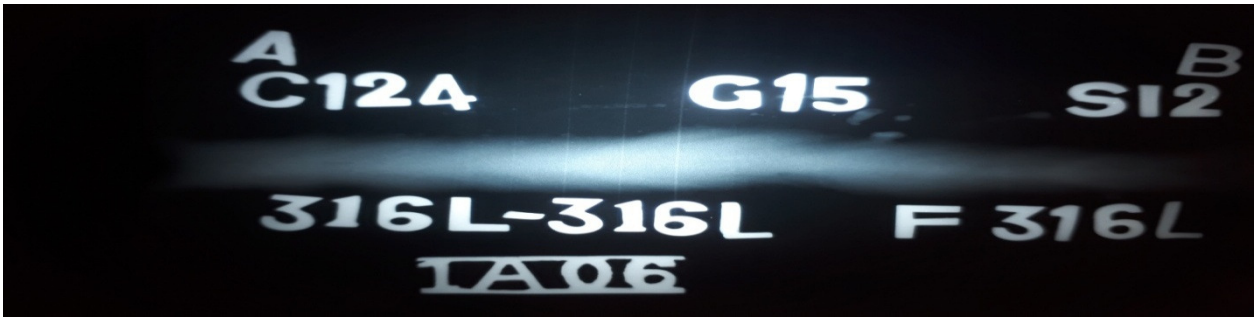

Figure 4.3 X-ray radiographic film for Sample No. S3: 316L Austenitic stainless steel as per RSM design of experiment

Figure 4.4 X-ray radiographic film for Sample No. S4: 316L Austenitic stainless steel as per RSM design of experiment

Figure 4.5 X-ray radiographic film for Sample No. S5: 316L Austenitic stainless steel as per RSM design of experiment

Figure 4.6 X-ray radiographic film for Sample No. S6: 316L Austenitic stainless steel as per RSM design of experiment

Figure 4.7 X-ray radiographic film for Sample No. S7: 316L Austenitic stainless steel as per RSM design of experiment

Figure 4.8 X-ray radiographic film for Sample No. S8: 316L Austenitic stainless steel as per RSM design of experiment

Figure 4.9 X-ray radiographic film for Sample No. S9: 316L Austenitic stainless steel as per RSM design of experiment

Figure 4.10 X-ray radiographic film for Sample No. S10: 316L Austenitic stainless steel as per RSM design of experiment

Figure 4.11 X-ray radiographic film for Sample No. S11: 316L Austenitic stainless steel as per RSM design of experiment

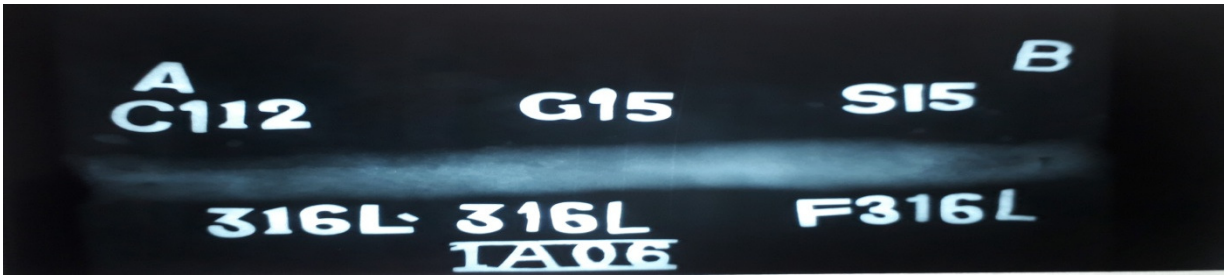

Figure 4.12 X-ray radiographic film for Sample No. S12: 316L Austenitic stainless steel as per RSM design of experiment

Figure 4.13 X-ray radiographic film for Sample No. S13: 316L Austenitic stainless steel as per RSM design of experiment

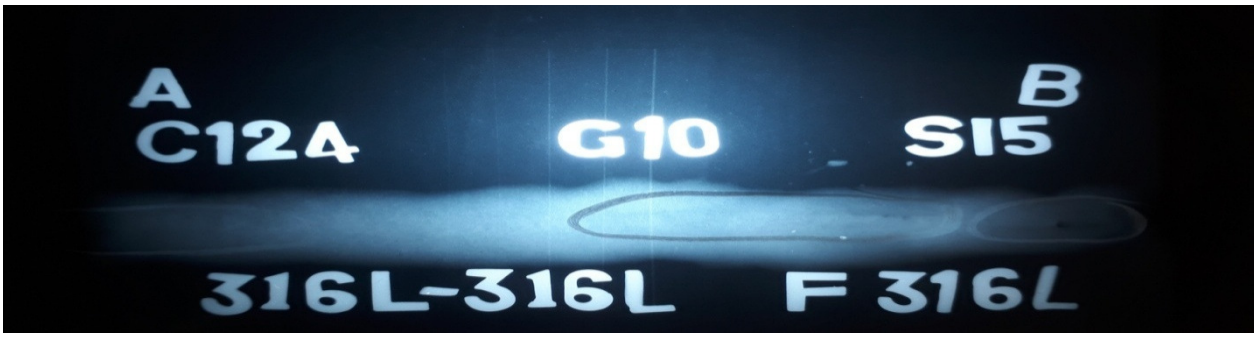

Figure 4.14 X-ray radiographic film for Sample No. S14: 316L Austenitic stainless steel as per RSM design of experiment

Figure 4.15 X-ray radiographic film for Sample No. S15: 316L Austenitic stainless steel as per RSM design of experiment

Figure 4.16 X-ray radiographic film for Sample No. S16: 316L Austenitic stainless steel as per RSM design of experiment

Figure 4.17 X-ray radiographic film for Sample No. S17: 316L Austenitic stainless steel as per RSM design of experiment

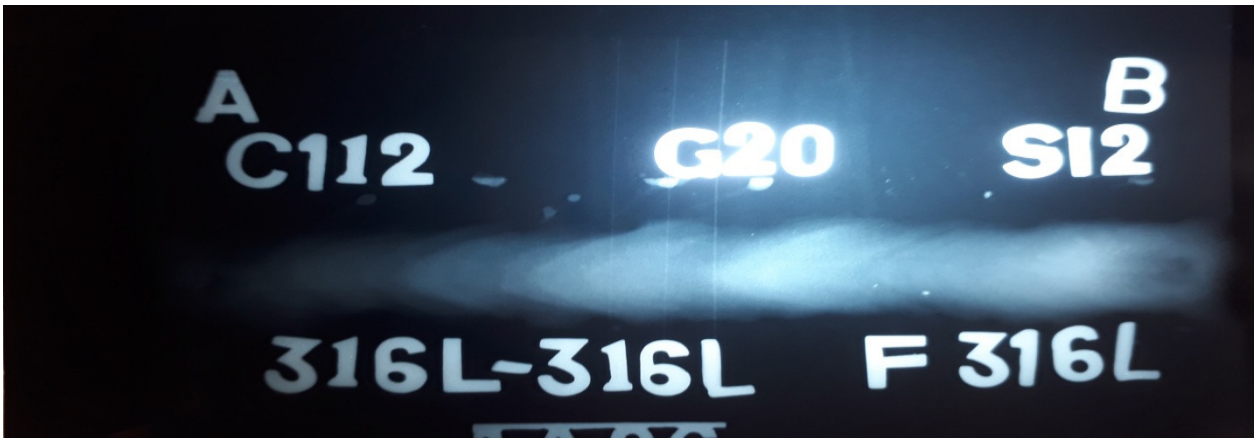

Figure 4.18 X-ray radiographic film for Sample No. S18: 316L Austenitic stainless steel as per RSM design of experiment

Figure 4.19 X-ray radiographic film for Sample No. S19: 316L Austenitic stainless steel as per RSM design of experiment

Figure 4.20 X-ray radiographic film for Sample No. S20: 316L Austenitic stainless steel as per RSM design of experiment

4.1.3 RESULTS OF TENSILE TEST AND DISCUSSION: 316L AUSTENITIC STAINLESS STEEL AS PER RSM DESIGN OF EXPERIMENT

The results of tensile test are listed in Table 4.3. The results include the ultimate tensile strength (UTS), yield strength (YS) and percentage of elongation (PE) of the welded samples. The samples being tested on Instron universal testing machine have been examined to locate the region from where failure/fracture has occurred. On examination it is noted that the sample nos. S2, S4, S5, S6, S7, S10, S11, S14, and S20 have broken/failed within the base metal; the sample nos.S1, S3, S8, S9, S12, S13, S15, S16, S17, S18, and S19 have broken approximately within the HAZ.

Table 4.3 The results of tensile test: 316L Austenitic stainless steel as per RSM design of experiment

Sample No.	Sample Identity	Yield Strength (MPa)	Ultimate Tensile Strength (MPa)	Percentage of Elongation (%)	Place Of Fracture
BASE METAL	**AISI 316L**	**301.6**	**573.8**	**65. 0**	Base
S1	C-112/F-15/S-12	302.9	554.3	32.5	HAZ
S2	C-100/F-15/S-12	302.5	520.1	30.2	BASE METAL
S3	C-124/F-15/S-12	293.6	555.9	51.3	HAZ
S4	C-100/F-10/S-9	259.7	472.3	30.7	BASE METAL
S5	C-100/F-10/S-15	253.7	502.3	38.6	BASE METAL
S6	C-100/F-20/S-15	317.9	552.0	34.6	BASE METAL
S7	C-100/F-20/S-9	242.8	498.1	44.1	BASE METAL
S8	C-112/F-10/S-12	321.1	550.1	31.2	HAZ
S9	C-112/F-15/S-12	341.8	549.1	35.4	HAZ
S10	C-124/F-10/S-9	313.5	542.9	34.1	BASE METAL
S11	C-112/F-15/S-12	303.9	538.0	34.2	BASE METAL
S12	C-112/F-15/S-15	322.7	591.2	54.5	HAZ
S13	C-124/F-20/S-15	283.4	544.3	60.7	HAZ
S14	C-124/F-10/S-15	288.8	518.2	33.0	BASE METAL
S15	C-112/F-15/S-12	305.8	550.7	36.6	HAZ
S16	C-112/F-15/S-12	280.2	551.4	35.1	HAZ
S17	C-112/F-15/S-12	300.0	546.5	34.6	HAZ (contd.)

S18	C-112/F-20/S-12	250.2	498.1	44.1	HAZ (contd. from previous page)
S19	C-112/F-15/S-9	287.9	533.3	27.9	HAZ
S20	C-124/F-20/S-9	242.4	498.0	44.0	BASE METAL

The data shown in Table 4.3 indicate that for many of the samples, performance of the butt welded joints is satisfactory. For the sample nos. S3, S6, S8, S9, S12, S13, S15 and S16 very good ultimate tensile strength is obtained, highest being 591.2MPa. Only for a few samples UTS is found to be a little bit low – that too, not very significantly low (sample nos.S4, S7, S18 and S20). The highest value of percentage elongation is observed to be 60.7% (for sample no. S13). The lowest value of percentage elongation is exhibited in the sample no. S19 (27.9 %). In so far yield strength is concerned, the results given in Table 4.3 are found to be satisfactory. Maximum yield strength (341.8MPa) is observed for sample no. S9 and minimum yield strength (242.4MPa) is found for sample no. S20.

The particular result of UTS for sample no. S12 appears to be unusual. A little bit of non uniform directional property or in-homogeneity in the material may be the probable reason for higher UTS of the joint, than UTS of base material. But it is not definite. Analysis of material property in light of failure mechanics may come out with some reason.

Stress-strain curves, corresponding to tensile test results of all the samples are shown in figures 4.21 - 4.41. Typical ductile behavior is observed in almost all the stress – strain curves.

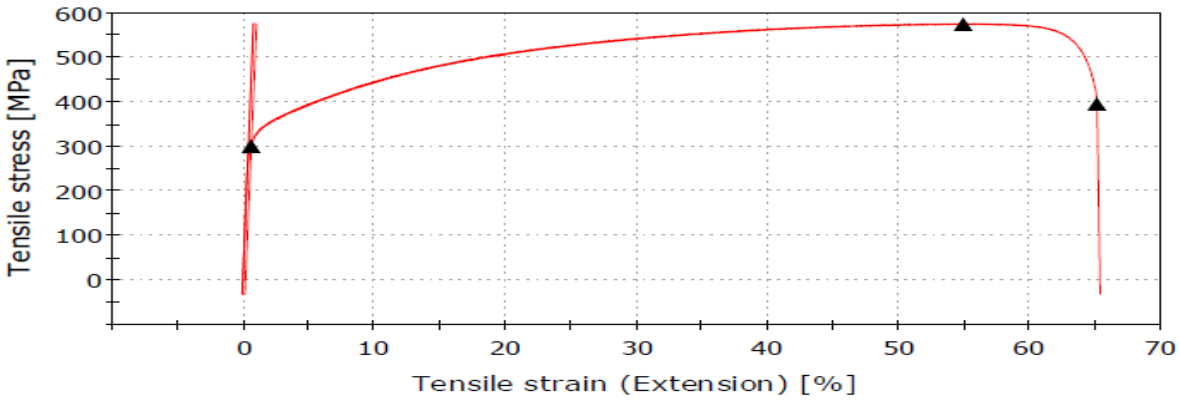

Figure 4.21 Tensile Test Diagram of BASE METAL: 316L Austenitic stainless steel

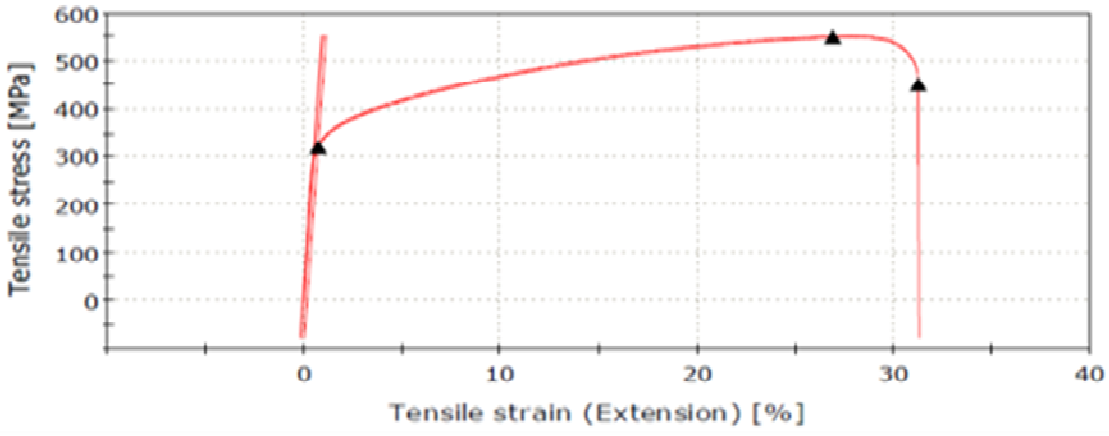

Figure 4.22 Tensile Test Diagram of Sample No. S1: 316L Austenitic stainless steel as per RSM design of experiment

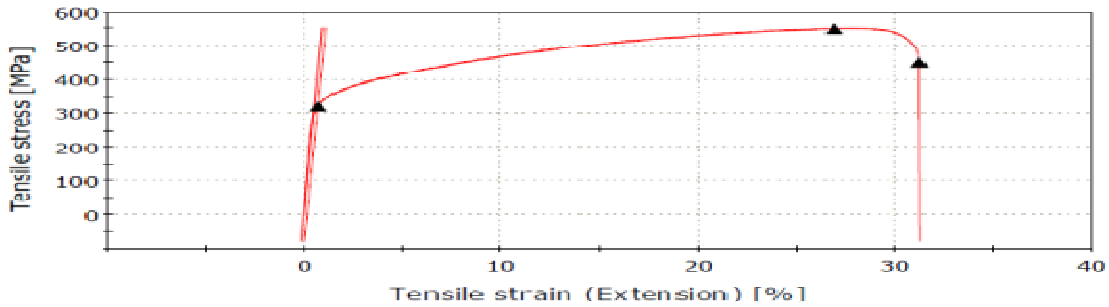

Figure 4.23 Tensile Test Diagram of Sample No. S2: 316L Austenitic stainless steel as per RSM design of experiment

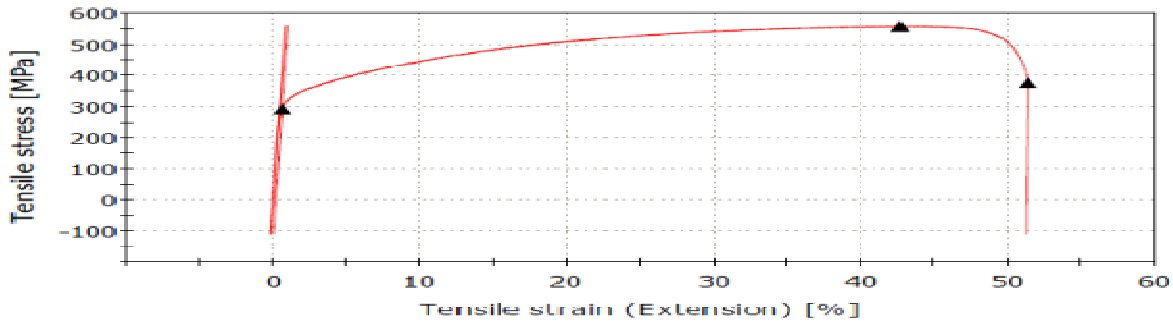

Figure 4.24 Tensile Test Diagram of Sample No. S3: 316L Austenitic stainless steel as per RSM design of experiment

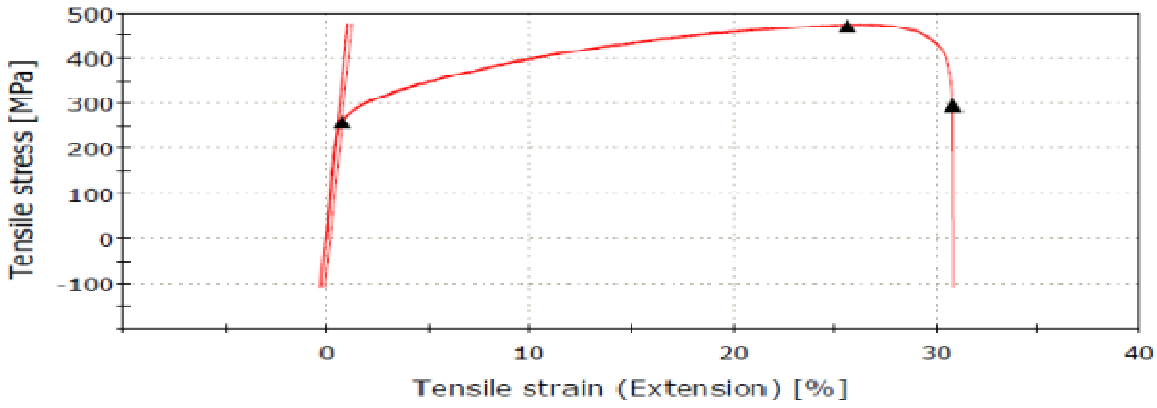

Figure 4.25 Tensile Test Diagram of Sample No. S4: 316L Austenitic stainless steel as per RSM design of experiment

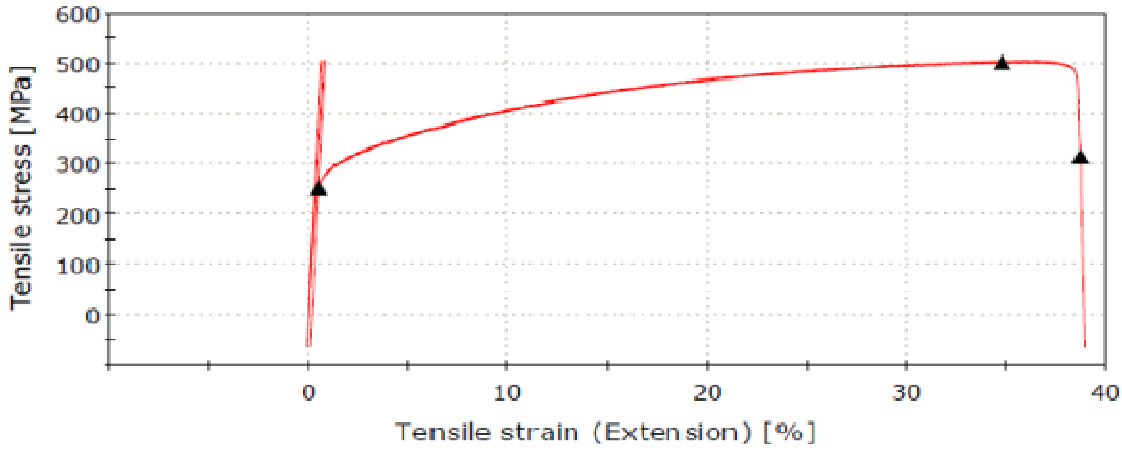

Figure 4.26 Tensile Test Diagram of Sample No. S5: 316L Austenitic stainless steel as per RSM design of experiment

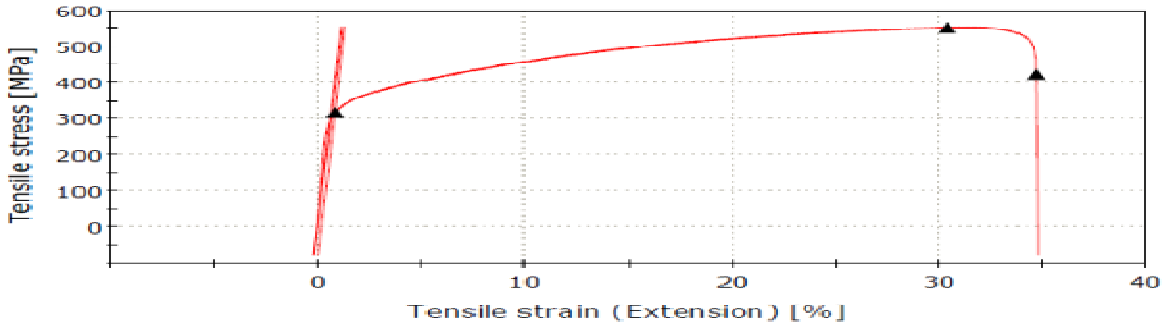

Figure 4.27 Tensile Test Diagram of Sample No. S6: 316L Austenitic stainless steel as per RSM design of experiment

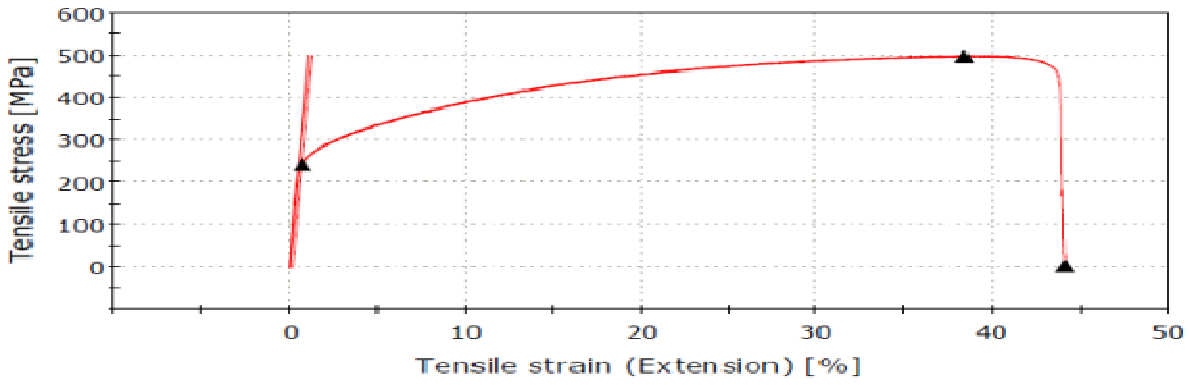

Figure 4.28 Tensile Test Diagram of Sample No. S7: 316L Austenitic stainless steel as per RSM design of experiment

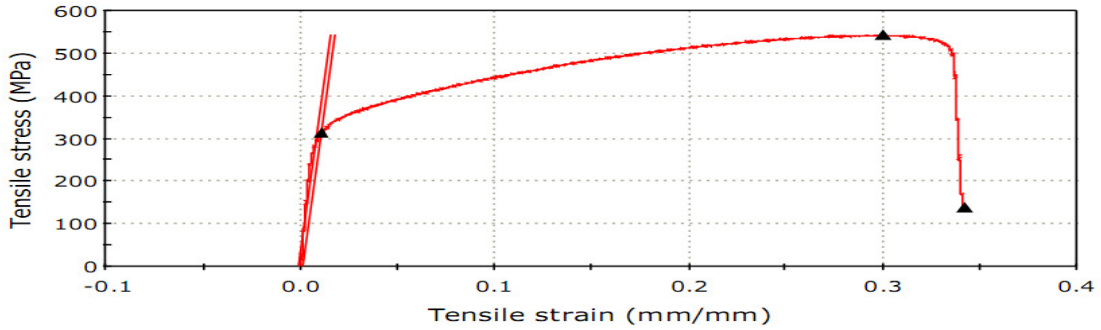

Figure 4.29 Tensile Test Diagram of Sample No. S8: 316L Austenitic stainless steel as per RSM design of experiment

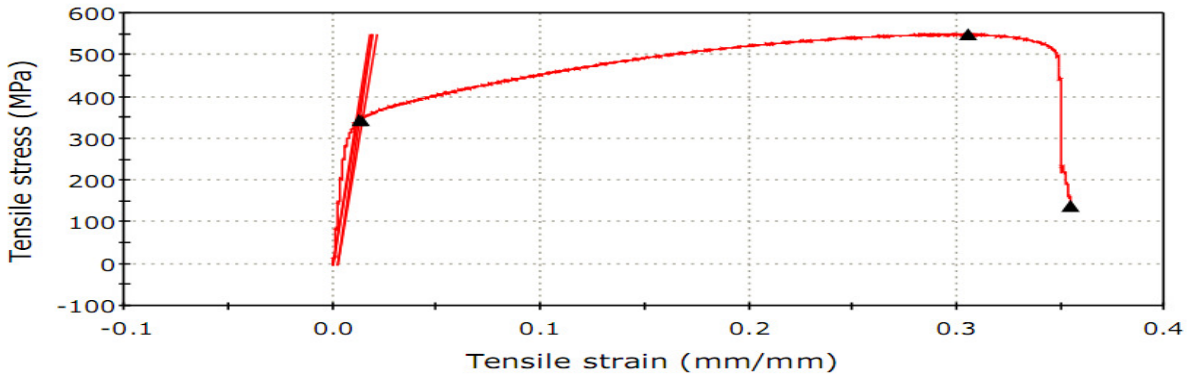

Figure 4.30 Tensile Test Diagram of Sample No. S9: 316L Austenitic stainless steel as per RSM design of experiment

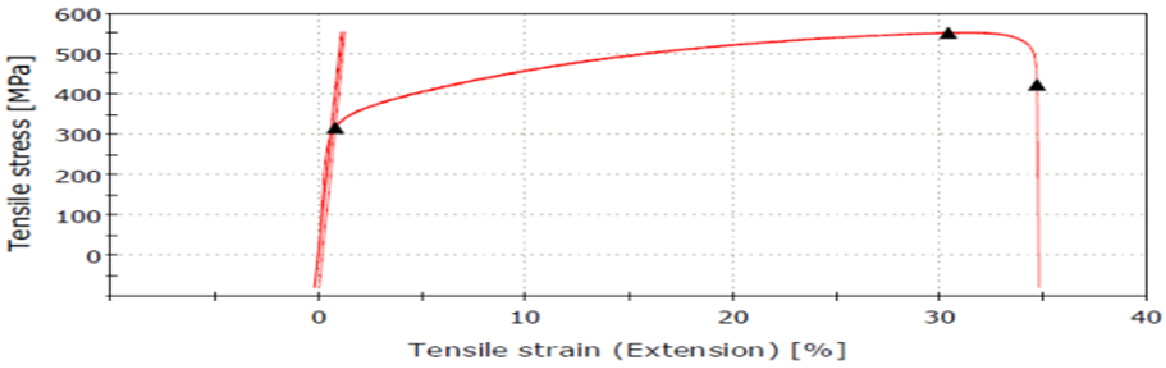

Figure 4.31 Tensile Test Diagram of Sample No. S10: 316L Austenitic Stainless Steel as per RSM design of experiment

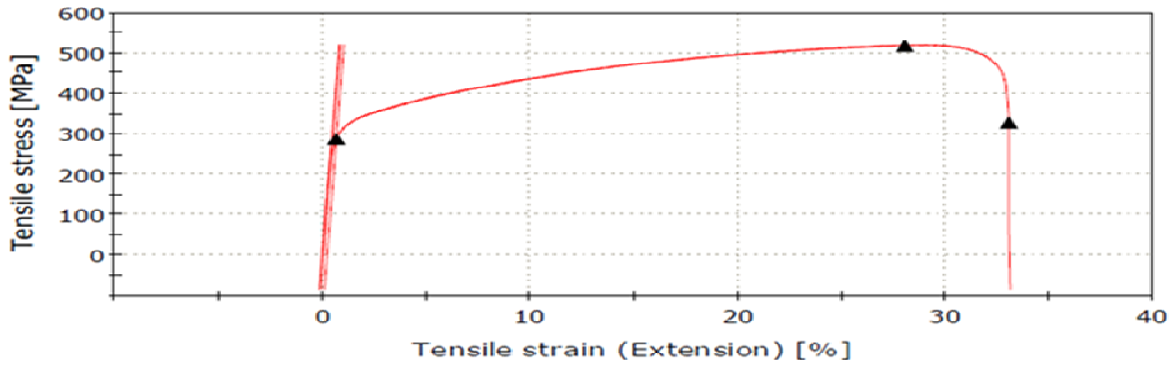

Figure 4.32 Tensile Test Diagram of Sample No. S11: 316L Austenitic stainless steel as per RSM design of experiment

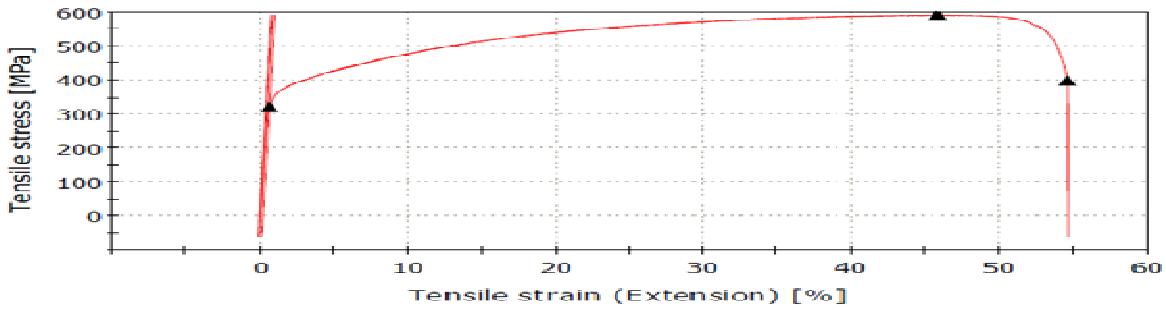

Figure 4.33 Tensile Test Diagram of Sample No. S12: 316L Austenitic stainless steel as per RSM design of experiment

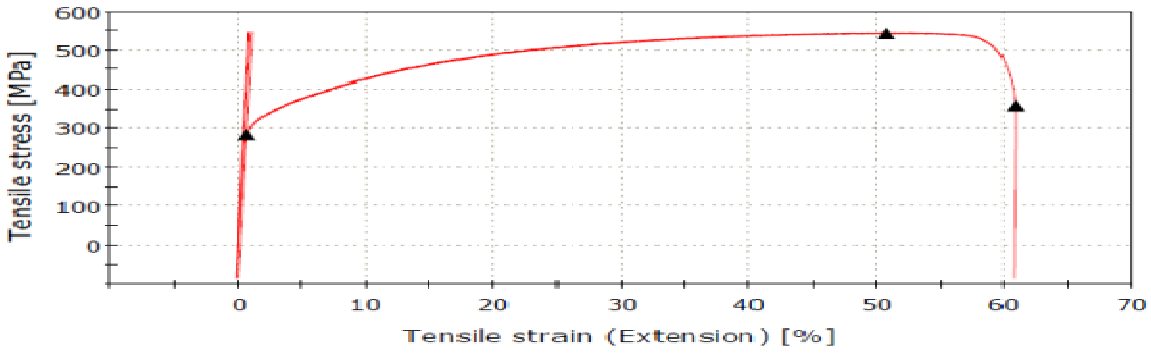

Figure 4.34 Tensile Test Diagram of Sample No. S13: 316L Austenitic stainless steel as per RSM design of experiment

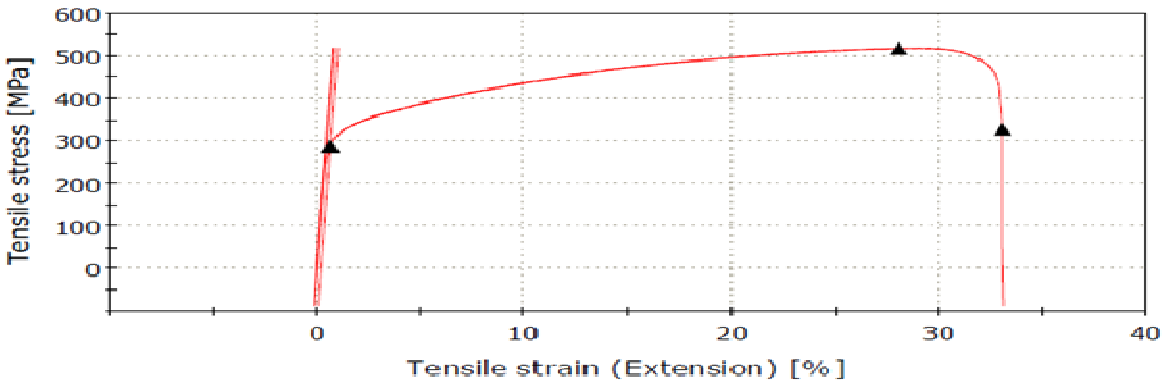

Figure 4.35 Tensile Test Diagram of Sample No. S14: 316L Austenitic stainless steel as per RSM design of experiment

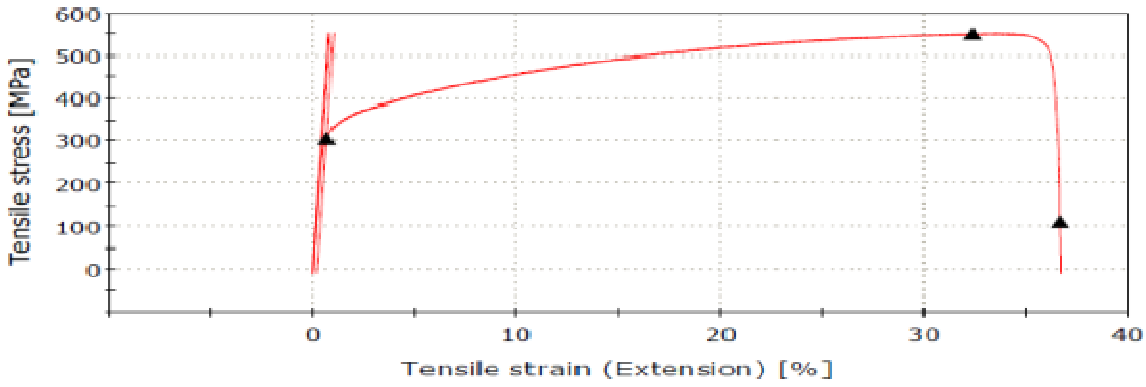

Figure 4.36 Tensile Test Diagram of Sample No. S15: 316L Austenitic stainless steel as per RSM design of experiment

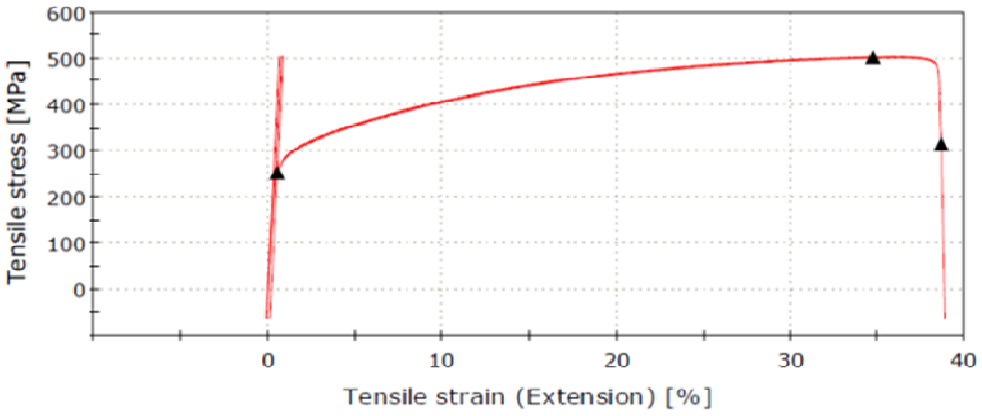

Figure 4.37 Tensile Test Diagram of Sample No. S16: 316L Austenitic stainless steel as per RSM design of experiment

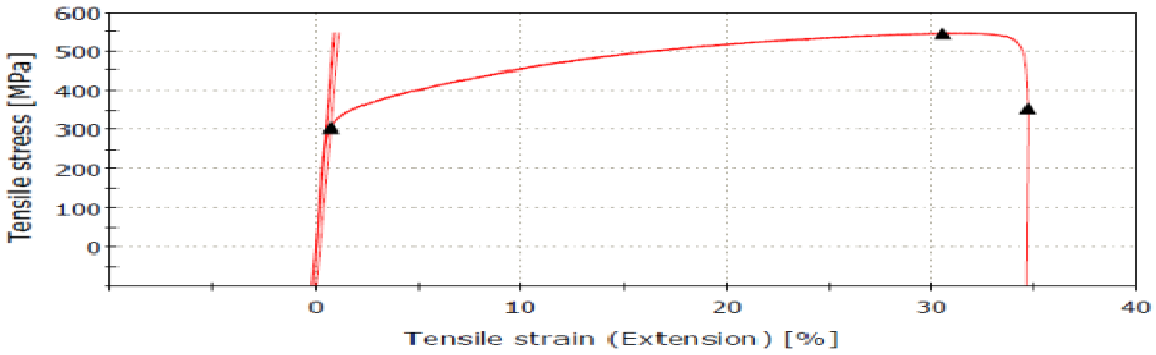

Figure 4.38 Tensile Test Diagram of Sample No. S17: 316L Austenitic stainless steel as per RSM design of experiment

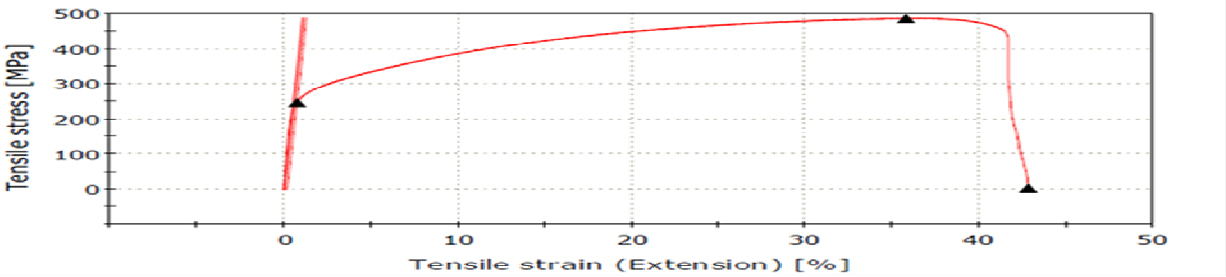

Figure 4.39 Tensile Test Diagram of Sample No. S18: 316L Austenitic stainless steel as per RSM design of experiment

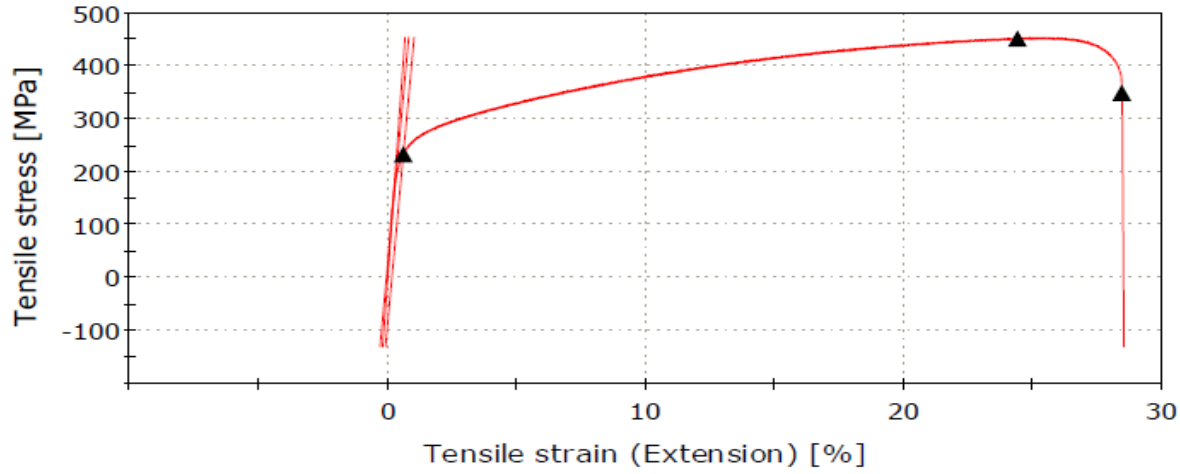

Figure 4.40 Tensile Test Diagram of Sample No. S19: 316L Austenitic stainless steel as per RSM design of experiment

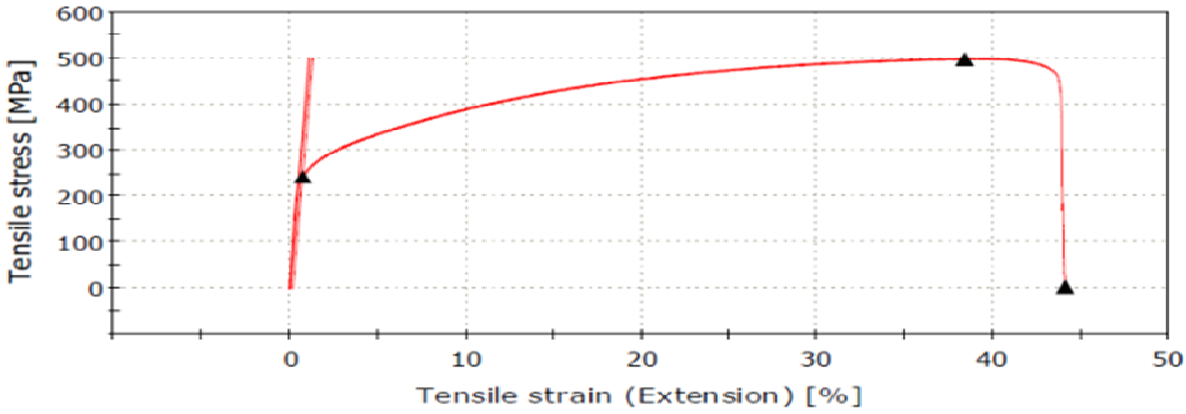

Figure 4.41 Tensile Test Diagram of Sample No. S20: 316L Austenitic stainless steel as per RSM design of experiment

4.1.4 RESULTS OF MICRO-HARDNESS TEST AND DISCUSSION: 316L AUSTENITIC STAINLESS STEEL AS PER RSM DESIGN OF EXPERIMENT

In the present study, hardness of all the welded samples has been measured by a Leco LM 248 AT micro-hardness tester. Figure 4.42 shows six different locations at which hardness is measured. Measurement is taken at 2 locations (location 1 and 6) of the base metal, at 2 locations

of HAZ (locations 2 and 5) and at 2 locations in the weld metal (locations 3 and 4). The results of the micro-hardness test are given in Table 4.4. Hardness values are in Vickers scale i.e., HV. Graphs showing change in hardness values corresponding to the change in locations: 1 - 2 – 3 – 4 – 5 - 6 of the welded samples are shown in figures 4.43 – 4.62. From these figures it is found that for most of the samples, the nature of variation in hardness values along the position 1 - 2 – 3 – 4 – 5 – 6, is similar. There is slight increase in hardness value within the region HAZ to weld, generally. However, even there are variations in HV values along 1 - 2 – 3 – 4 – 5 - 6, these variations are not very excessive. In welding, uniform mechanical properties and microstructures throughout the different regions (weld metal, HAZ and base metal) are desired, though very difficult to achieve. Hardness is one of the several characteristics, which represent quality or mechanical property of the weldment. The data in Table 4.4 (or the figures 4.43 – 4.62), suggest that, variation in the levels of the input parameters has influenced hardness of the welded samples at its different zones, though the trend of this variation is nearly same for all the samples.

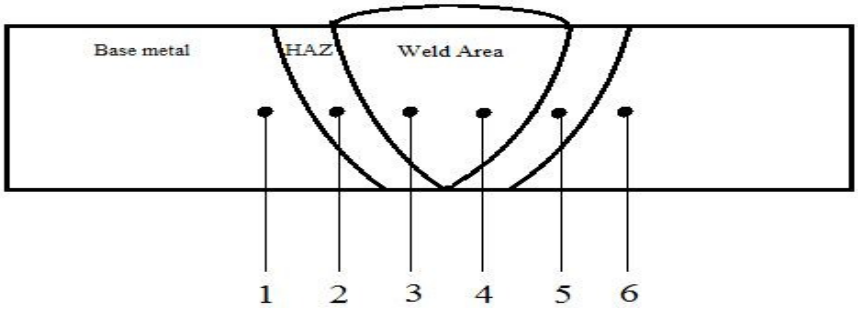

Figure 4.42 Schematic diagram showing positions of hardness measurement

Table 4.4 Results of hardness test: 316L Austenitic stainless steel as per RSM design of experiment

Sample No.	**Hardness (HV) at position**					
	1	**2**	**3**	**4**	**5**	**6**
S1	255.3	255.7	274.8	253.5	246	257.5
S2	252.7	255.6	269.9	257.3	227.2	253.1 (contd.)

S3	254.7	255.3	259.1	253	247	252.5 (contd. from previous page)
S4	255.9	226.8	246	248.3	238.4	256.7
S5	254.6	233.7	249.5	253.5	234.5	252.1
S6	254.1	231.3	267.7	233.4	229.8	253.9
S7	255.1	236.5	245.3	259.6	245.1	255.7
S8	251.8	220.5	265.7	257.6	233.8	250.2
S9	252.9	230.7	260.6	274.3	230.8	250.8
S10	255.7	220.5	260	250.5	222.5	250.6
S11	255.6	247.7	250.3	257.8	245.6	252.5
S12	255.8	220.6	265.7	265.8	237.7	253.5
S13	256.9	238.9	280.5	280.7	266.7	255.3
S14	252.8	229.7	270.7	275.8	253.6	254.8
S15	256.1	223.8	245	251.7	234.7	257.7
S16	253.6	220.8	257.6	243.8	230.5	256.7
S17	255.6	223.4	265.6	273.5	223.6	252.6
S18	254.4	230.4	267.3	271.6	220.7	253.4
S19	252.7	235.6	256.7	261.3	243.4	254.7
S20	255.5	243.5	273.6	280.4	240.2	259.7

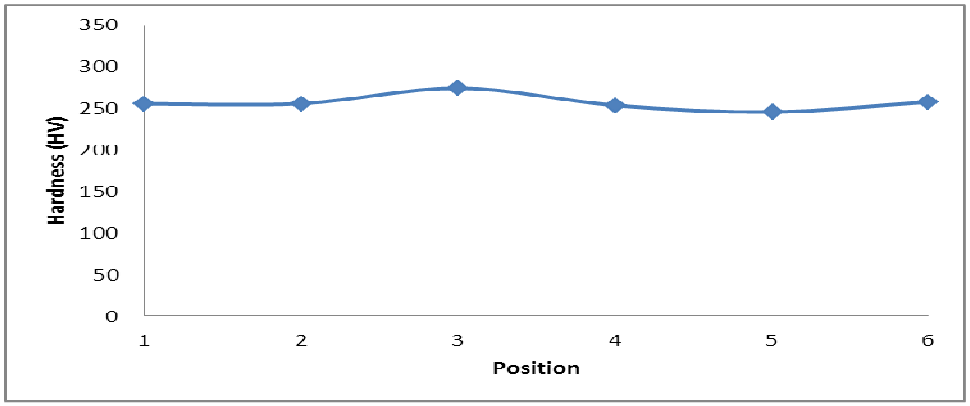

Figure 4.43 Hardness graph for Sample No. S1: 316L Austenitic stainless steel as per RSM design of experiment

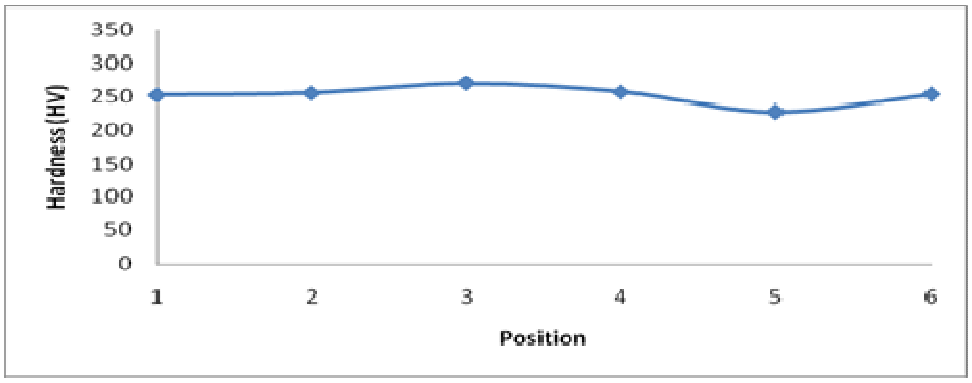

Figure 4.44 Hardness graph for Sample No. S2: 316L Austenitic stainless steel as per RSM design of experiment

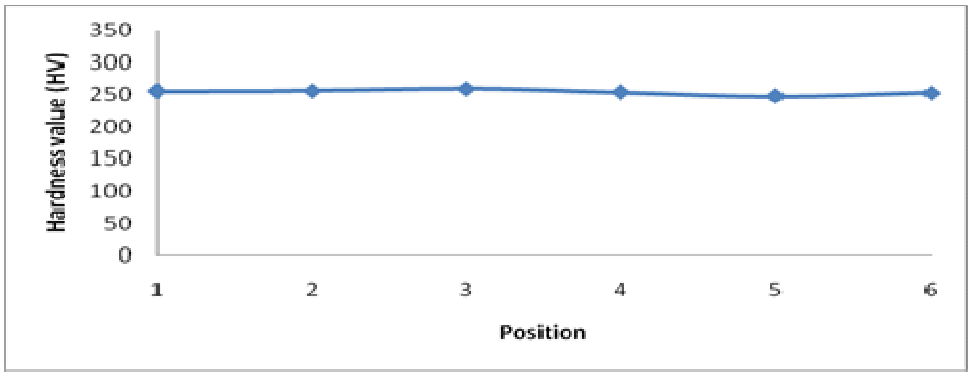

Figure 4.45 Hardness graph for Sample No. S3: 316L Austenitic stainless steel as per RSM design of experiment

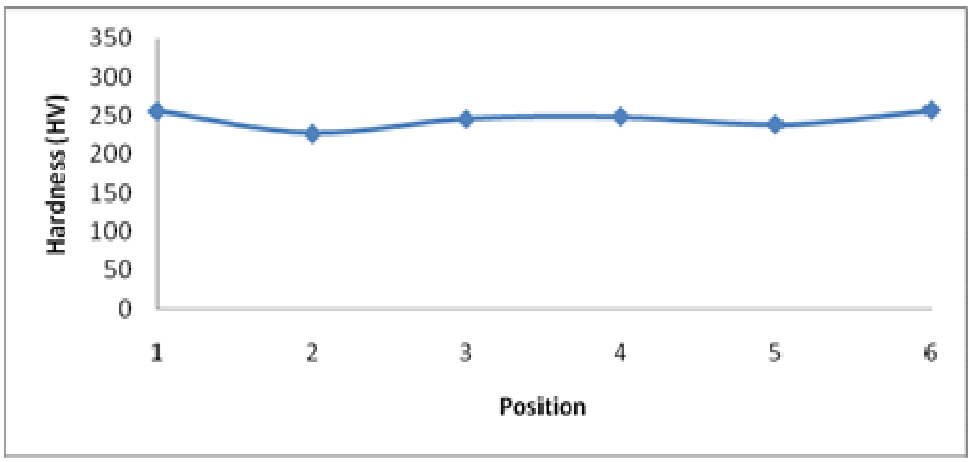

Figure 4.46 Hardness graph for Sample No. S4: 316L Austenitic stainless steel as per RSM design of experiment

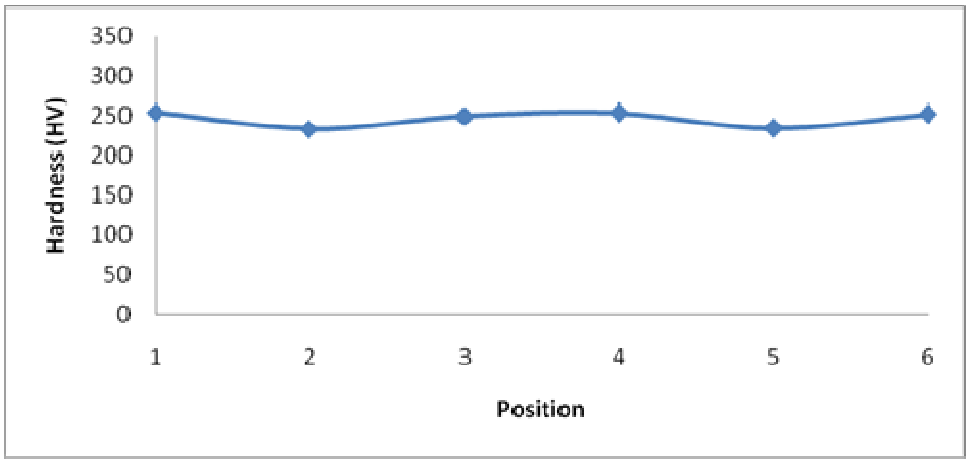

Figure 4.47 Hardness graph for Sample No. S5: 316L Austenitic stainless steel as per RSM design of experiment

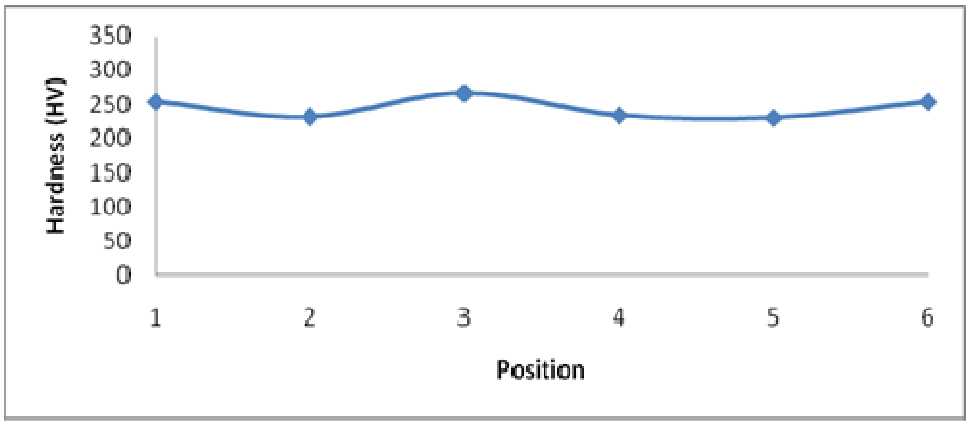

Figure 4.48 Hardness graph for Sample No. S6: 316L Austenitic stainless steel as per RSM design of experiment

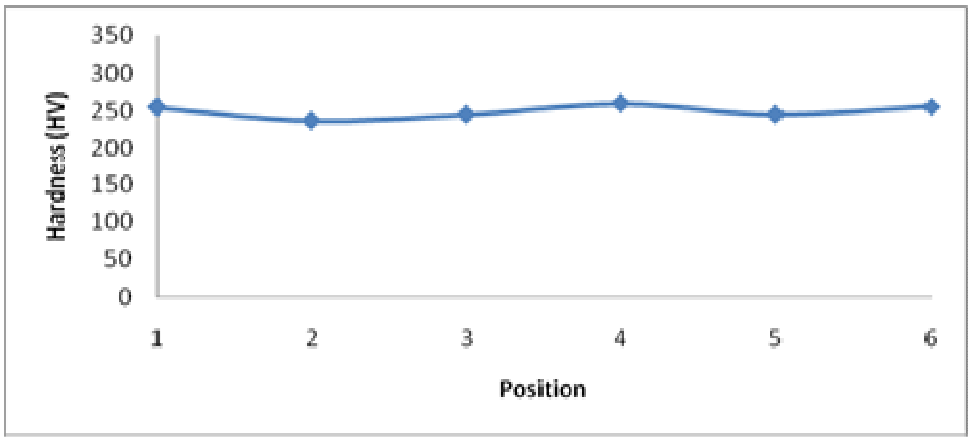

Figure 4.49 Hardness graph for Sample No. S7: 316L Austenitic stainless steel as per RSM design of experiment

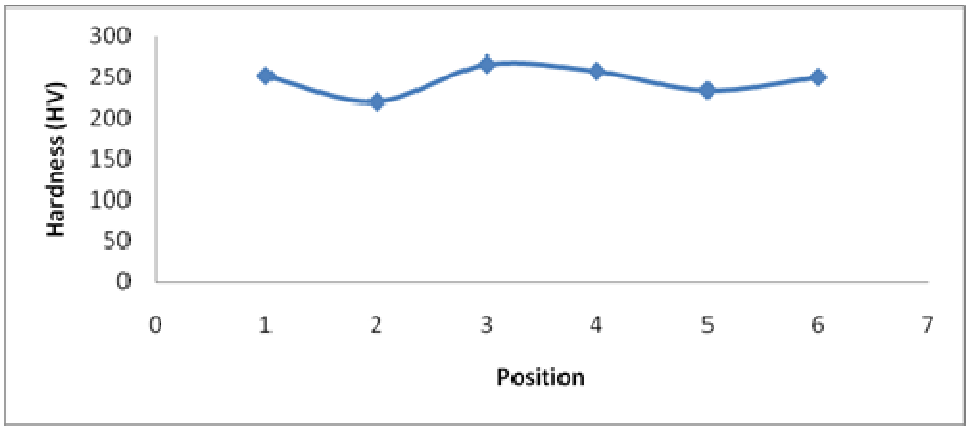

Figure 4.50 Hardness graph for Sample No. S8: 316L Austenitic stainless steel as per RSM design of experiment

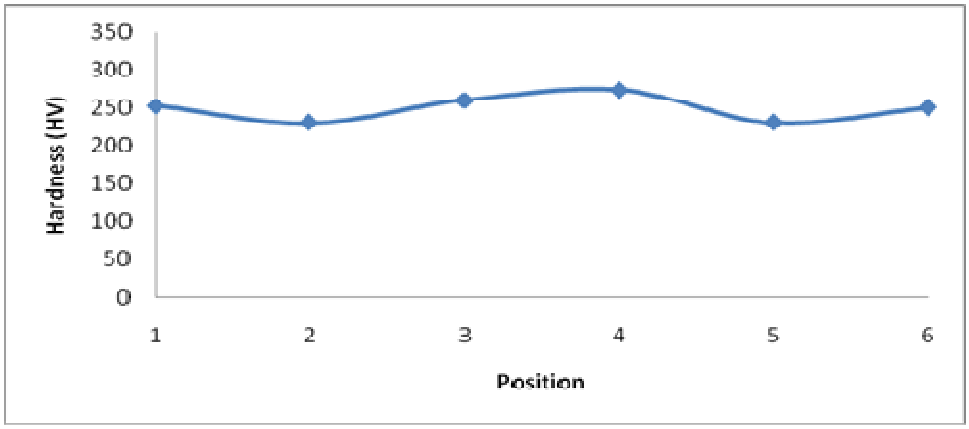

Figure 4.51 Hardness graph for Sample No. S9: 316L Austenitic stainless steel as per RSM design of experiment

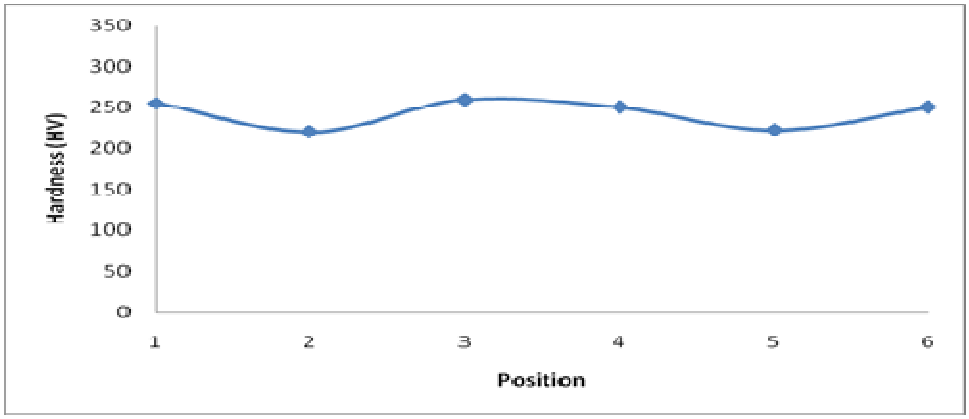

Figure 4.52 Hardness graph for Sample No. S10: 316L Austenitic stainless steel as per RSM design of experiment

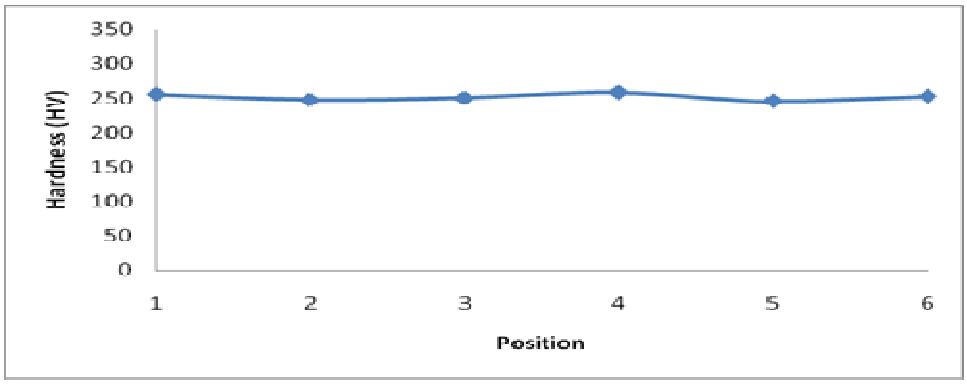

Figure 4.53 Hardness graph for Sample No. S11: 316L Austenitic stainless steel as per RSM design of experiment

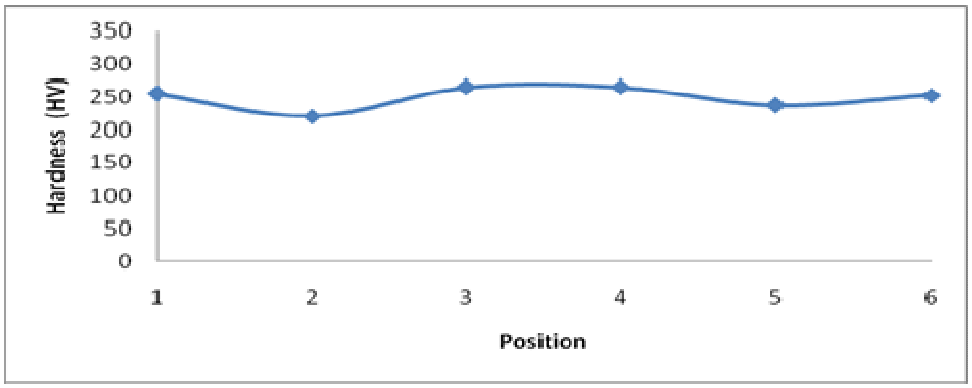

Figure 4.54 Hardness graph for Sample No. S12: 316L Austenitic stainless steel as per RSM design of experiment

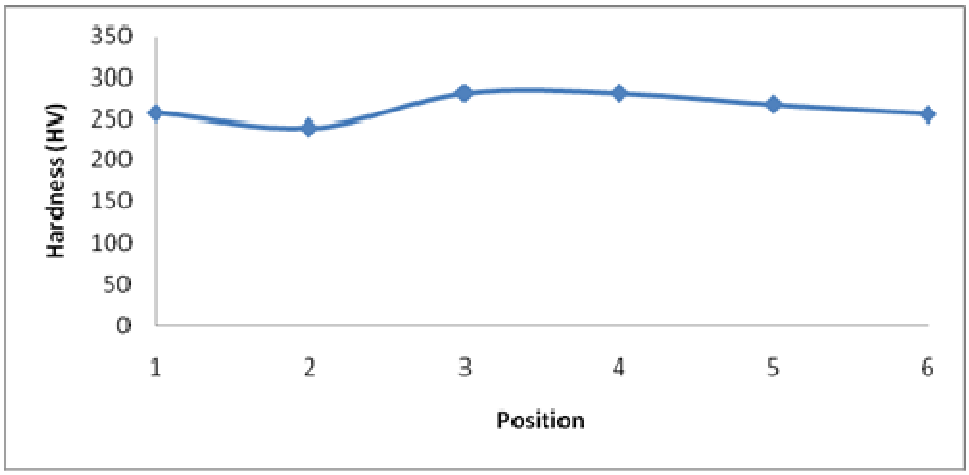

Figure 4.55 Hardness graph for Sample No. S13: 316L Austenitic stainless steel as per RSM design of experiment

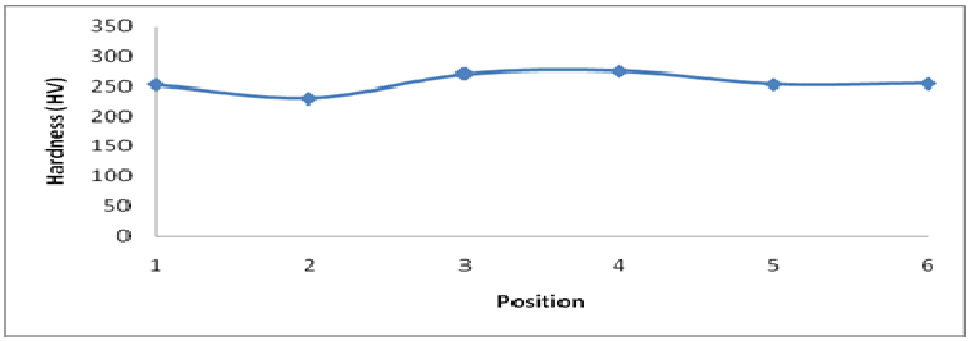

Figure 4.56 Hardness graph for Sample No. S14: 316L Austenitic stainless steel as per RSM design of experiment

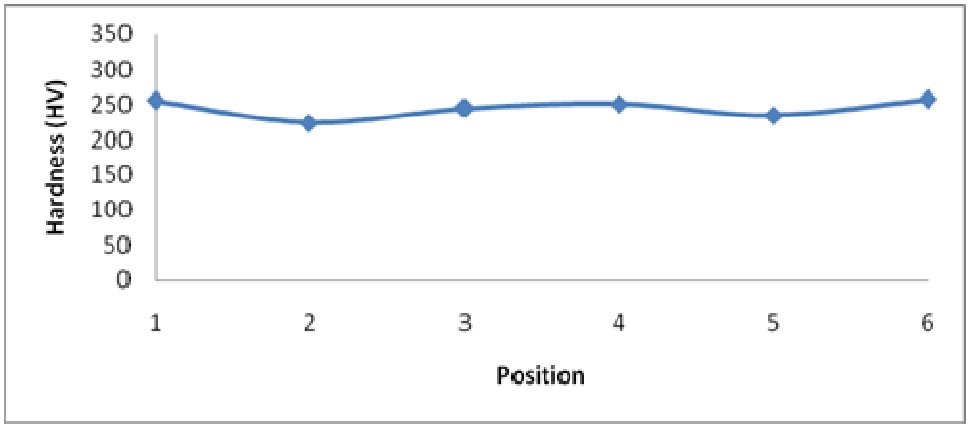

Figure 4.57 Hardness graph for Sample No. S15: 316L Austenitic stainless steel as per RSM design of experiment

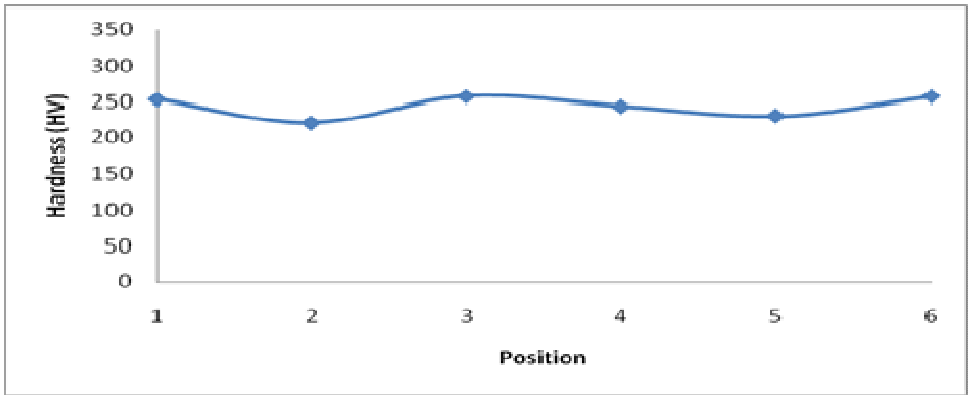

Figure 4.58 Hardness graph for Sample No. S16: 316L Austenitic stainless steel as per RSM design of experiment

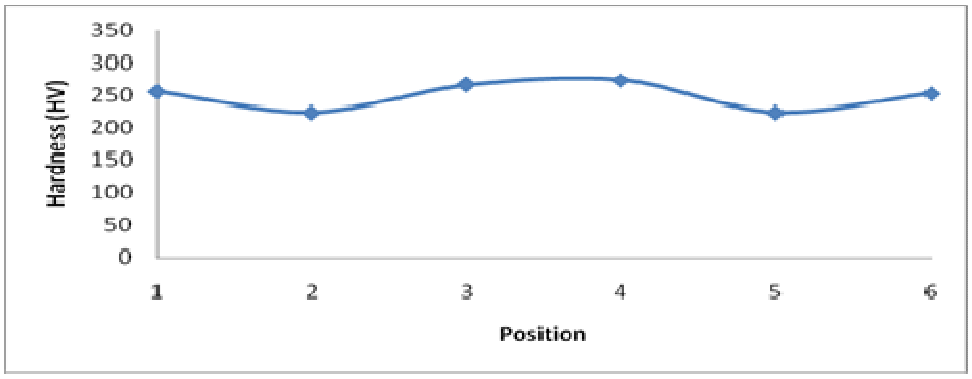

Figure 4.59 Hardness graph for Sample No. S17: 316L Austenitic stainless steel as per RSM design of experiment

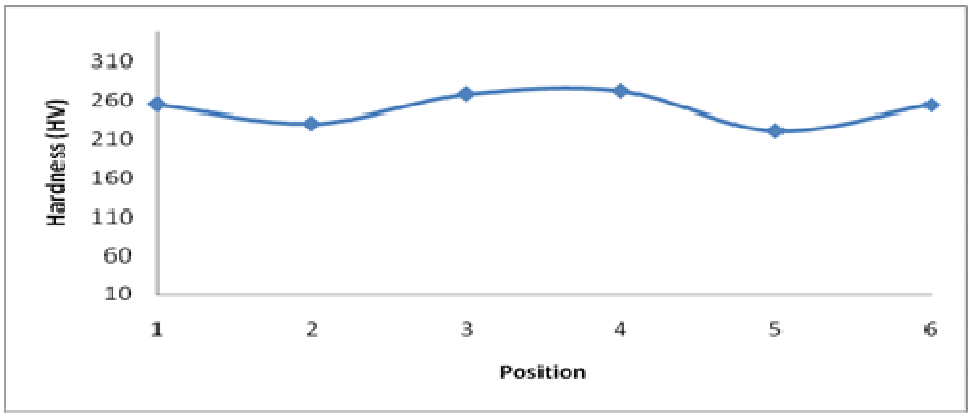

Figure 4.60 Hardness graph for Sample No. S18: 316L Austenitic stainless steel as per RSM design of experiment

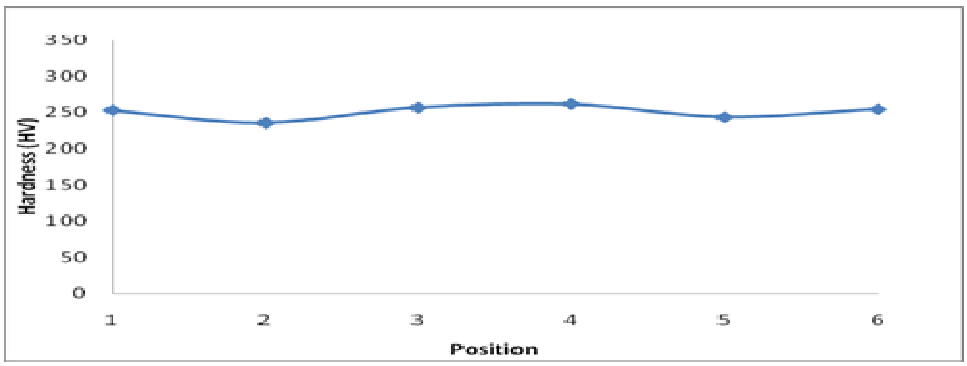

Figure 4.61 Hardness graph for Sample No. S19: 316L Austenitic stainless steel as per RSM design of experiment

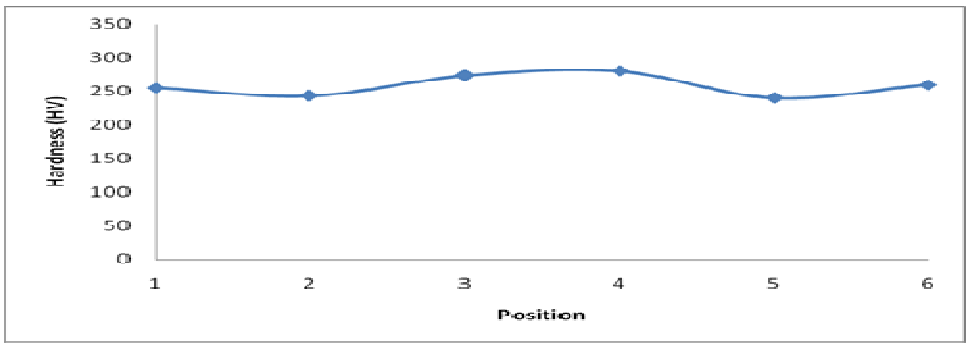

Figure 4.62 Hardness graph for Sample No. S20: 316L Austenitic stainless steel as per RSM design of experiment

Microstructures developed at different regions of the weld beads are dependent on the compositions of base and filler materials, dilution, heating and cooling cycles and many other factors. It can be noted that in the base material the difference in hardness is minimum. Regions of weld and HAZ are affected differently by various factors as mentioned above, including parametric conditions. Hardness in different zones of weldment is found to be more or less consistent with the observations in the microstructures.

4.1.5 RESULTS OF MICROSTRUCTURAL STUDY AND DISCUSSION: 316L AUSTENITIC STAINLESS STEEL AS PER RSM DESIGN OF EXPERIMENT

Study of microstructures has been made for all the welded samples and the photographs are taken in weld and HAZ regions, for each of the samples by the Leica DM LM metallurgical microscope. Base metal microstructure has also been studied. Microstructural views are shown in figures 4.63 – 4.83.

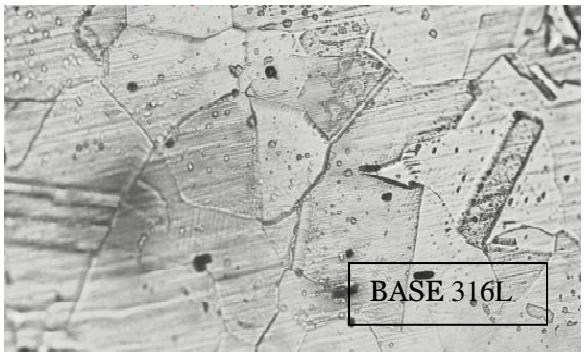

Figure 4.63 Metallographic view of Sample No. BASE METAL 316L (x500)

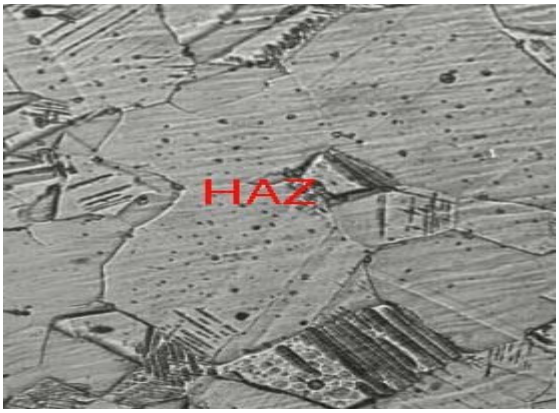

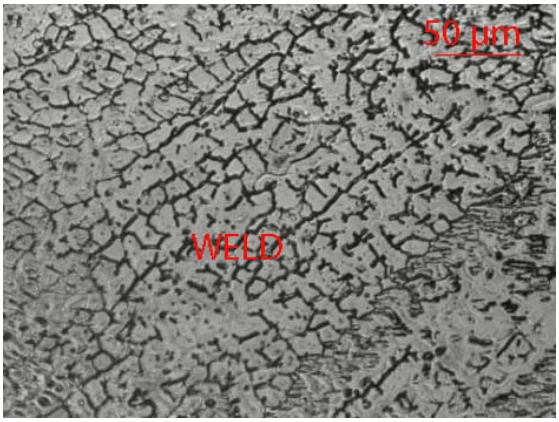

a) HAZ b) WELD

Figure 4.64 Metallographic view of Sample No. S1 (x500)

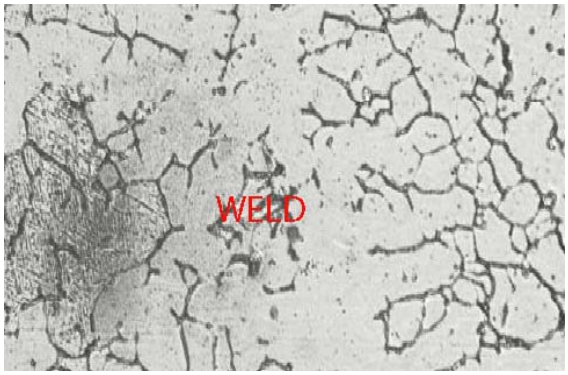

a) HAZ b) WELD

Figure 4.65 Metallographic view of Sample No. S2 (x500)

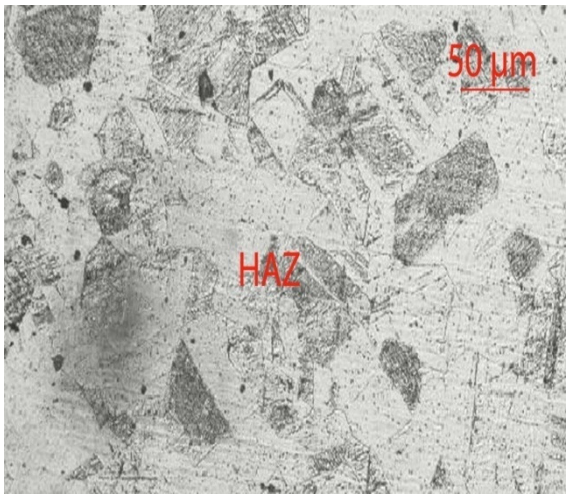

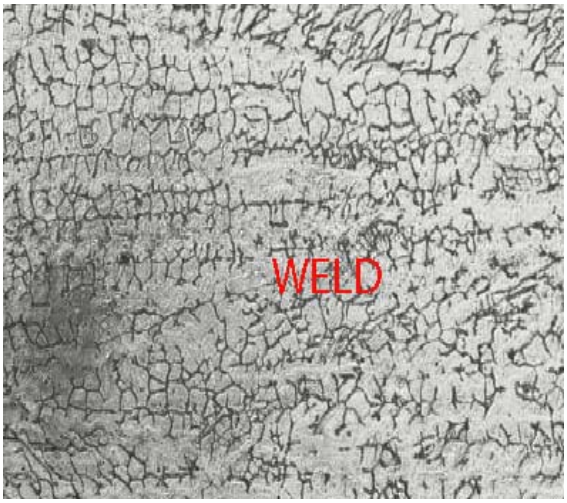

a) HAZ b) WELD

Figure 4.66 Metallographic view of Sample No. S3(x500)

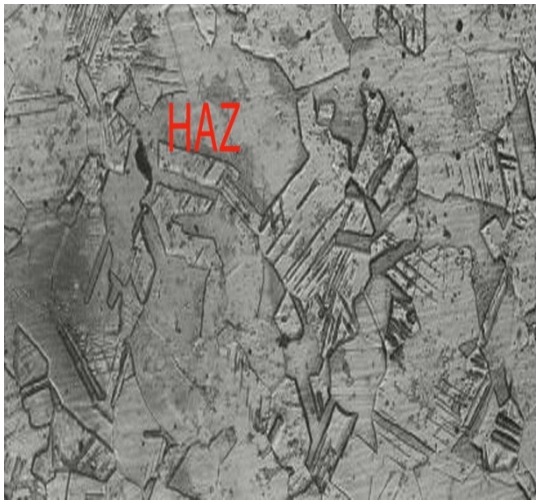

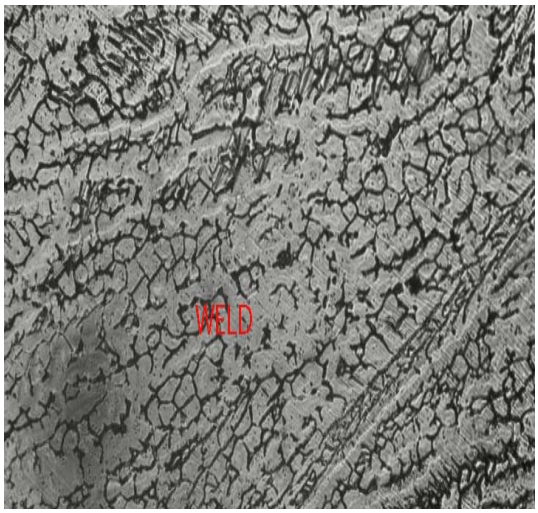

a) HAZ b) WELD

Figure 4.67 Metallographic view of Sample No. S4(x500)

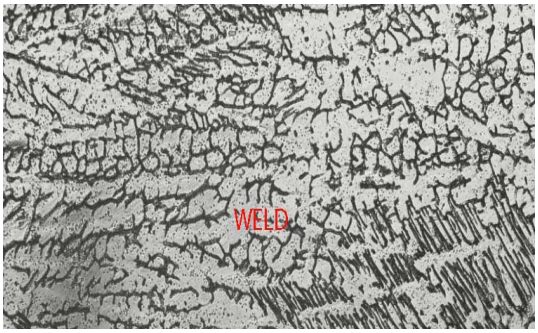

a) HAZ b) WELD

Figure 4.68 Metallographic view of Sample No. S5(x500)

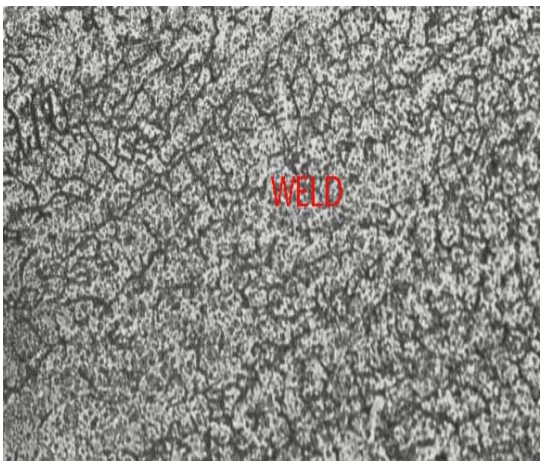

a) HAZ b) WELD

Figure 4.69 Metallographic view of Sample No. S6(x500)

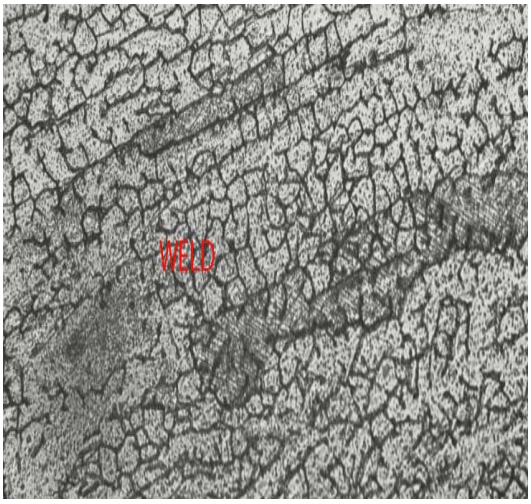

a) HAZ b) WELD

Figure 4.70 Metallographic view of Sample No. S7(x500)

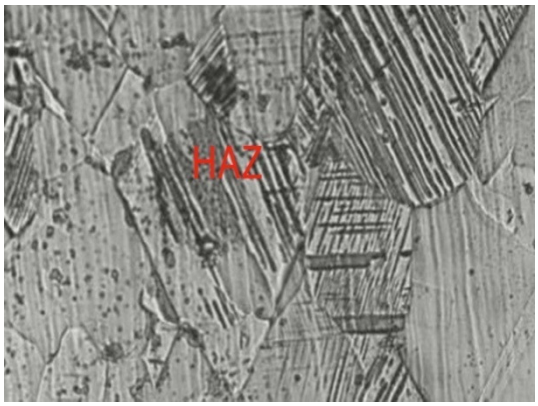

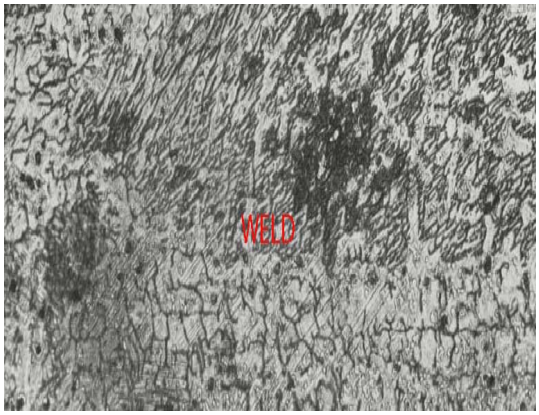

a) HAZ b) WELD

Figure 4.71 Metallographic view of Sample No. S8(x500)

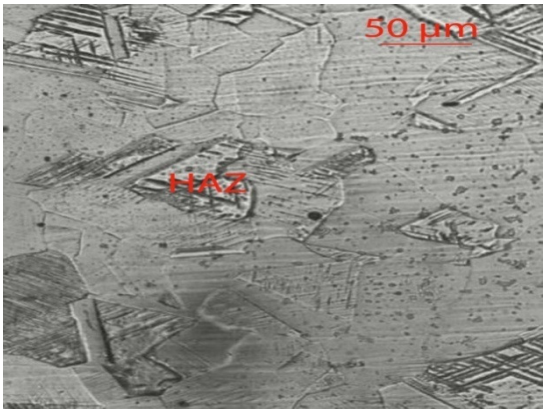

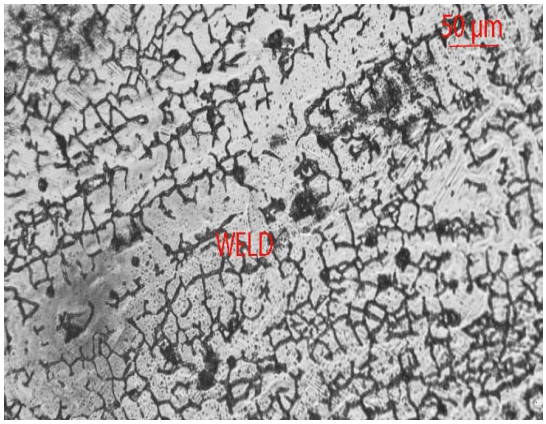

a) HAZ b) WELD

Figure 4.72 Metallographic view of Sample No. S9(x500)

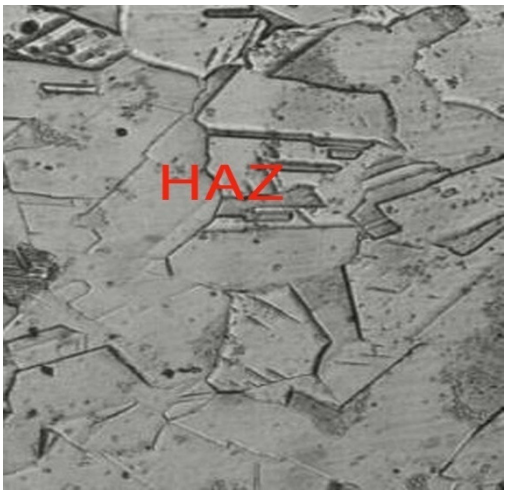

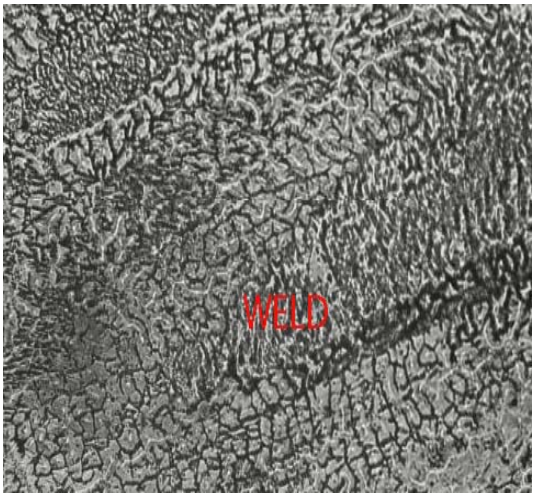

a) HAZ b) WELD

Figure 4.73 Metallographic view of Sample No. S10(x500)

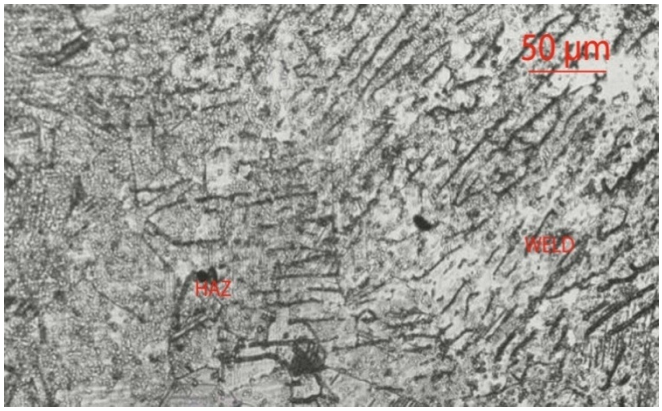

HAZ + WELD

Figure 4.74 Metallographic view of Sample No. S11(x500)

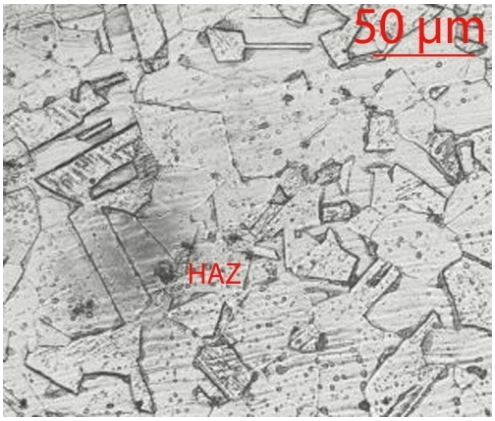

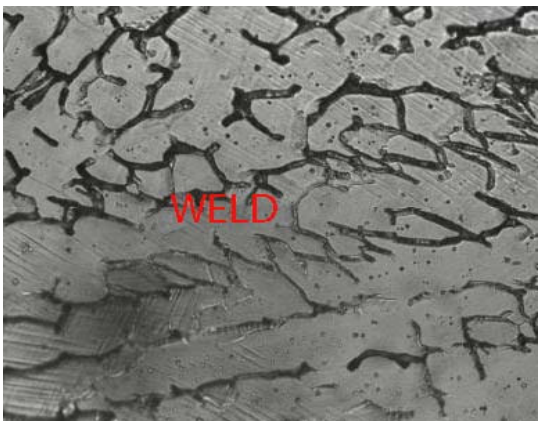

a) HAZ b) WELD

Figure 4.75 Metallographic view of Sample No. S12(x500)

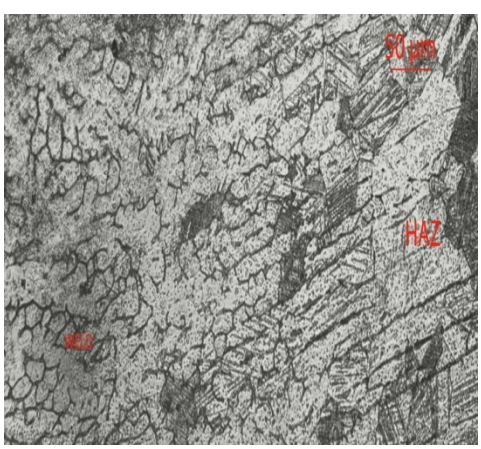

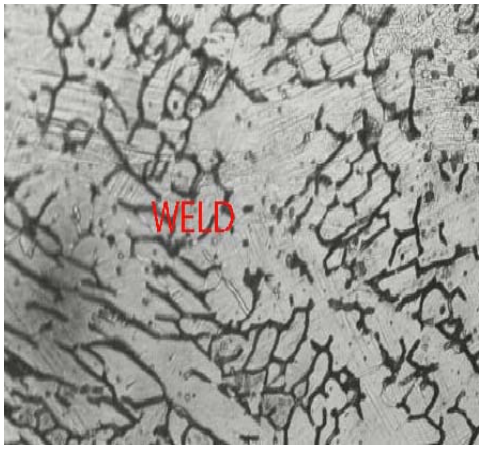

a) HAZ b) WELD

Figure 4.76 Metallographic view of Sample No. S13(x500)

HAZ +WELD

Figure 4.77 Metallographic view of Sample No. S14(x500)

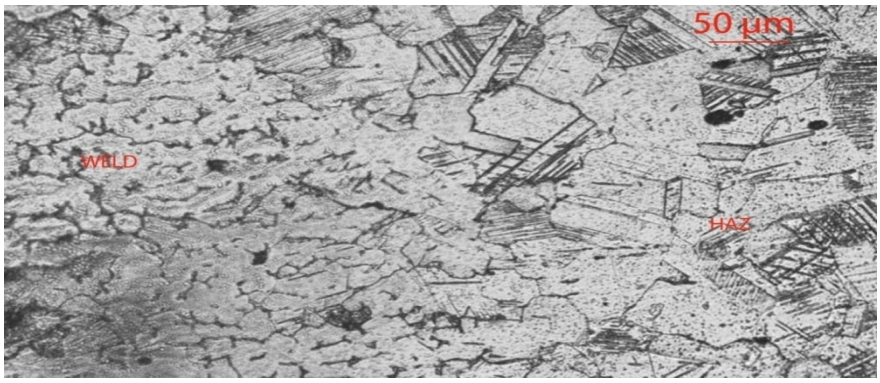

HAZ+ WELD

Figure 4.78 Metallographic view of Sample No. S15(x500)

HAZ+ WELD

Figure 4.79 Metallographic view of Sample No. S16(x500)

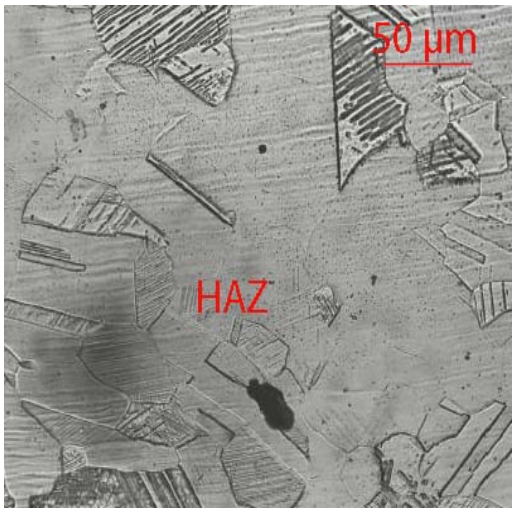

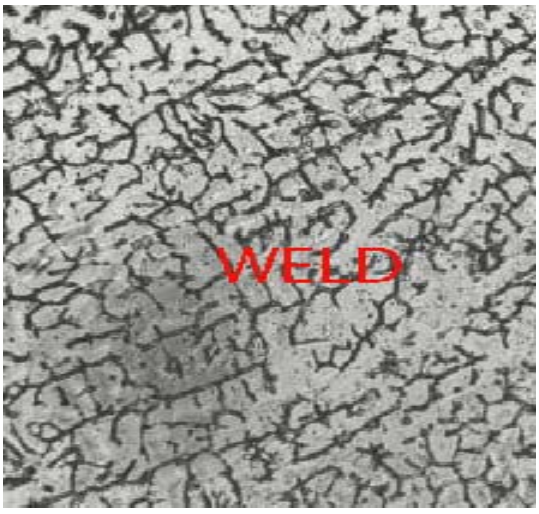

a) HAZ b) WELD

Figure 4.80 Metallographic view of Sample No. S17(x500)

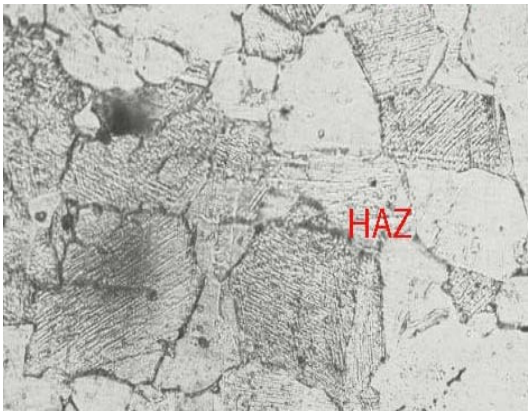

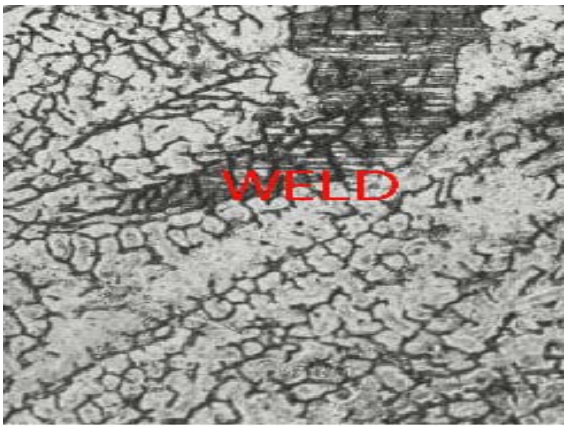

a) HAZ b) WELD

Figure 4.81 Metallographic view of Sample No. S18(x500)

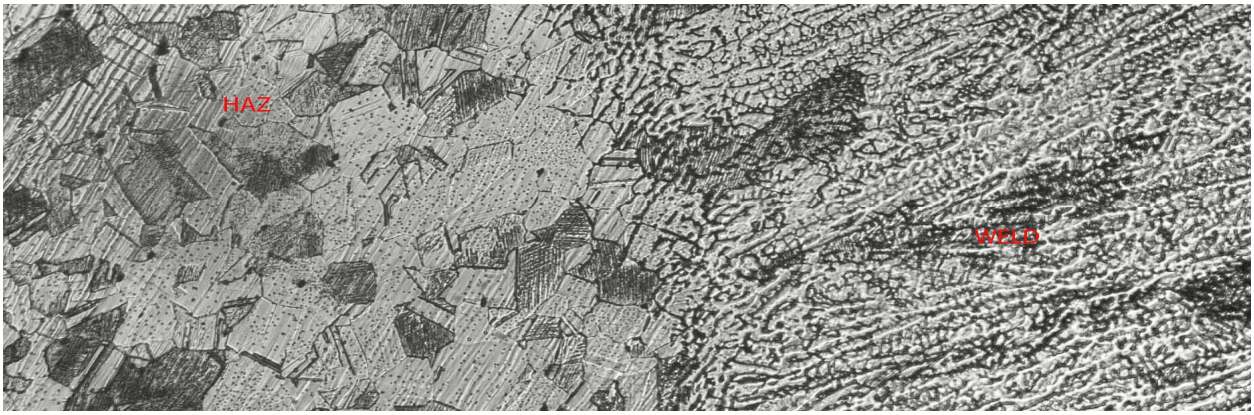

HAZ +WELD

Figure 4.82 Metallographic view of Sample No. S19(x500)

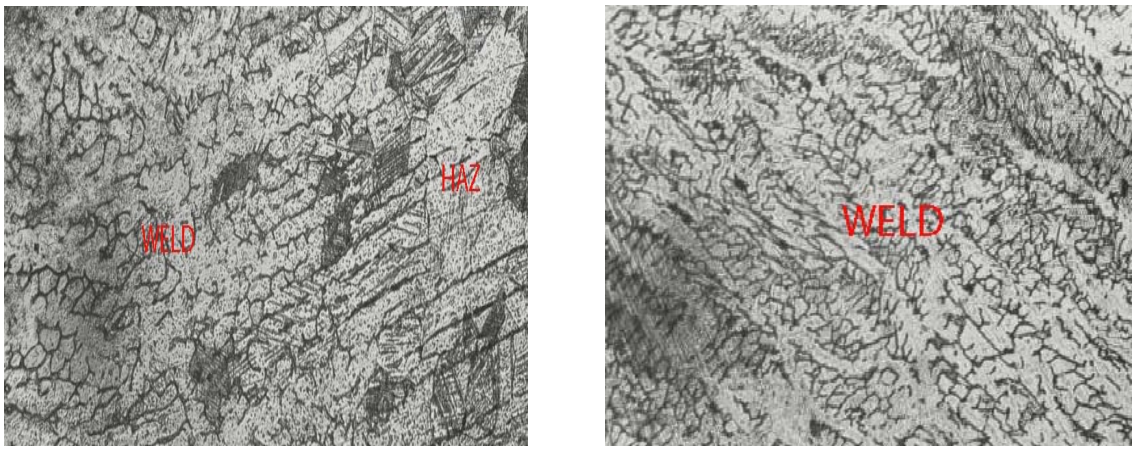

a) HAZ+WELD b) WELD

Figure 4.83 Metallographic view of Sample No. S20(x500)

In so far as the microstructure of base metal is concerned, pure austenitic grains with twin boundaries are observed in all the samples. One representative base metal microstructure is shown in figure 4.63. Not much variation is observed among the HAZ microstructures of twenty samples as found from microstructures shown in figure 4.63 – 4.83. In general, austenitic grains are found to be coarser in HAZ than in base metal. This may be attributed to lower cooling rate in the HAZ region. In figure 4.64a, HAZ region contains coarse grains of austenite as well as depletion of carbon in several places. In figure 4.65a**,** in some portions precipitation of δ ferrite is seen. Figure 4.66 shows that coarse grains of austenite; as well as depletion of carbon is found in HAZ microstructure. In figure 4.67a, grain size is elongated and the size is also longer. In figure 4.68a, in the HAZ region columnar grains of ferrite have been seen though out the structure. In some of the portions, precipitated carbide has been found. Matrix is austenitic in which some

precipitation of small carbide is also seen. In almost all the samples, traces of δ-ferrite are observed in HAZ under the microscope. Dispersed carbide phases are found in HAZ region of sample number S4 (figure 4.67a). This sample shows lowest UTS in tensile test. In figure 4.70 a, grain size is larger and precipitation of carbide is also seen. In figure 4.71a, twin boundary is also seen in HAZ microstructure. In figure 4.72a, coarse grains of austenite as well as depletion of carbon are found in HAZ microstructure. In figure 4.73a austenitic matrix is observed, on which some precipitation of carbide is seen throughout its structure.

If weld metal microstructures of all the samples are compared with either base metal or HAZ microstructures, it is found that weld metal microstructure is looking very much different from HAZ and base metal microstructures. In most of the samples columnar-dendritic grain growths are observed in the weld microstructure, as shown in figure 4.75 (example: sample no. S12). But in few samples (sample numbers S6, S8; figure 4.69 and figure 4.71) eqiaxed grain growth is observed at certain portion of the weld metal along with twin boundaries. In sample number S12, full austenitic structure with small equiaxed grain has been observed. This sample has shown highest UTS. In general, more or less uniform distribution of austenite grains of equal size is seen throughout the structure, in which precipitation of carbide is revealed. For sample no. S12, microstructure of weld metal (figure 4.75b) shows dispersed chromium carbide throughout the structure. Microstructure of HAZ (figure 4.75a) indicates that carbides are distributed throughout the structure and sizes of the grains are in finer form. HAZ microstructure consists of austenite - ferrite matrix with precipitation of carbides. For sample no. S16, weld metal microstructure indicates precipitation of chromium carbide in the grain boundary (figure 4.79). HAZ microstructure shows precipitation of super saturated carbide on the austenite ferrite matrix (figure 4.79).

In the weld-HAZ transition region, in some samples more amount of δ-ferrite is precipitated, because, dilution-less weld metal cannot reach to the base metal. So, base metal is quickly melted and solidified. As solidification time is less, δ-ferrite cannot get enough time for total transformation into complete austenitic structure.

Microstructures developed at different regions of the weld beads are dependent on the compositions of base and filler materials, dilution, heating and cooling cycles and many other factors. A little bit of variation found in the microstructures among twenty samples, may be linked with the above factors, particularly with heating and cooling cycles. Varied parametric

combinations during welding, influence heat input, heat input rate and cooling cycle. This, in turn, influences microstructures.

4.1.6 RESULTS AND DISCUSSION AS PER L9 TAGUCHI ORTHOGONAL ARRAY DESIGN OF EXPERIMENT: 316L AUSTENITIC STAINLESS STEEL (2^{ND} PART OF 1^{ST} SET OF EXPERIMENTS)

Three sets of experiments have been carried out, as mentioned in the beginning of this chapter. In first set of experiments: 316L austenitic stainless steels, have been butt welded as per i) RSM design of experiment and ii) L9 Taguchi orthogonal design of experiment . So far, the results, as per RSM design of experiments, have been presented and discussed. Now, in the following sections, the results corresponding to L9 Taguchi orthogonal design of experiment are given and discussed.

4.1.6.1 RESULTS OF VISUAL INSPECTION AND DISCUSSION: 316L AUSTENITIC STAINLESS STEEL AS PER L9 TAGUCHI ORTHOGONAL ARRAY DESIGN OF EXPERIMENT

After welding, visual inspection of the welded samples has been carried out. The observed results are summarized in Table 4.5. Results of visual inspection indicate that defects like spatter, undercut have occurred in some of the samples. Almost no defect has been found in few samples like sample nos. S1A, S3A, S4A, S6A and S8A. The possible reasons of the defects found in the several samples are discussed along with discussion on the defects found in X-ray radiography test in the following section.

Table 4.5 Results of visual inspection: 316L Austenitic stainless steel weldment as per L9 Taguchi Orthogonal Array Design of Experiment

Sample No.	Welding Current (A)	Gas flow rate (*l*/min)	Nozzle to plate distance (mm)	Result of visual inspection
S1A	100	10	9	No defects
S2A	100	15	12	Spatter
S3A	100	20	15	No defects
S4A	112	10	12	No defects
S5A	112	15	15	Spatter
S6A	112	20	9	No defects
S7A	124	10	15	Undercut
S8A	124	15	9	No defects
S9A	124	20	12	Spatter

4.1.6.2 RESULTS OF X-RAY RADIOGRAPHY TEST AND DISCUSSION: 316L AUSTENITIC STAINLESS STEEL AS PER L9 TAGUCHI ORTHOGONAL ARRAY DESIGN OF EXPERIMENT

X- Ray radiographic tests have been conducted for all the 9 samples by XXQ-2005 X-Ray flaw detector. Results of X-ray Radiographic Test are shown in Table 4.6. The copies of the X-ray films are presented through figures 4.84 – 4.92.

Table 4.6 Results of X-ray radiographic test of 316L Austenitic stainless steel: L9 Taguchi Orthogonal Array Design of Experiment

Sample No.	Welding Current (A)	Gas flow rate (*l*/min)	Nozzle to plate distance (mm)	Result of X-ray radiographic tests
S1A	100	10	9	No defects
S2A	100	15	12	Lack of fusion, porosity
S3A	100	20	15	No defects
S4A	112	10	12	No defects
S5A	112	15	15	Porosity
S6A	112	20	9	No defects
S7A	124	10	15	Porosities
S8A	124	15	9	No defects
S9A	124	20	12	Porosities

Porosity in welding is caused by the presence of gases which get entrapped during the solidification process. The most common causes of porosity are atmospheric contamination, excessively oxidized work piece surface; in addition, presence of foreign matter, inadequate shielding by gas flow or excessive shielding gas flow may result in porosity.

Most frequently the occurrence of lack of fusion due to an improper welding technology can be attributed to an improper preparation of a weld groove, an incorrect torch inclination, an improper welding position, and possible draught. A second group of causes includes insufficient energy input to the weld area. It has been confirmed that it is highly important to choose optimum welding parameters such as welding current, wire feed rate, and arc length.

The welding speed has a major influence on energy input. Welding current has the greatest effect on penetration. Incomplete penetration is usually caused by the use of too low welding current and can be eliminated by simply increasing the ampere. Other causes can be the use of too slow travel speed and an incorrect torch angle. Both will allow the metal to rise in front of the arc acting as a cushion to prevent penetration. The arc must be kept on the leading edge of the weld puddle.

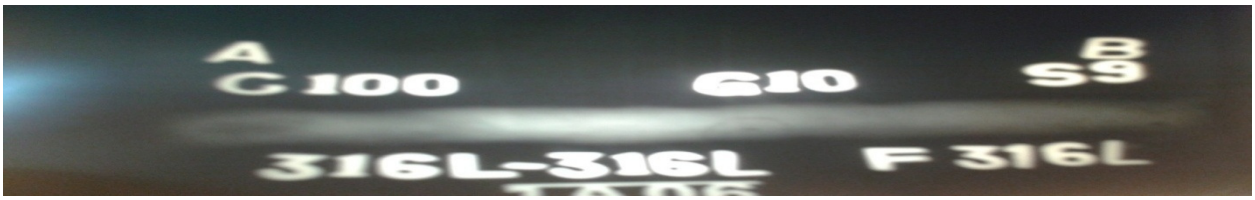

Figure 4.84 X-ray radiographic film for Sample No. S1A: 316L Austenitic stainless steel as per L9 Taguchi orthogonal array design of experiment

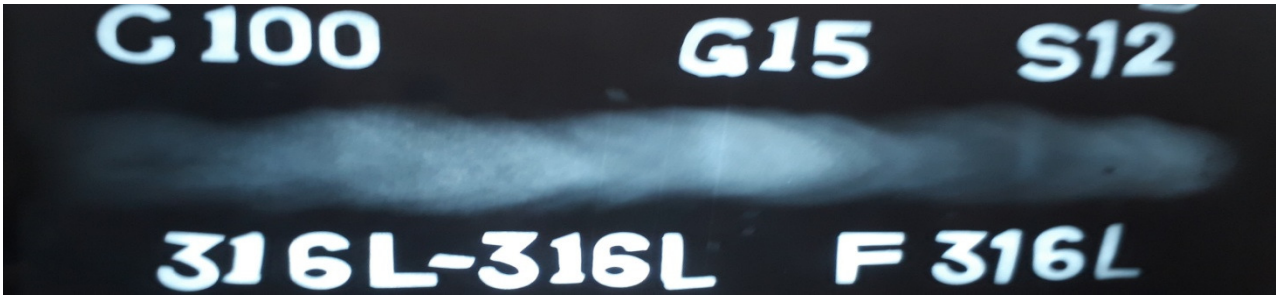

Figure 4.85 X-ray radiographic film for Sample No. S2A: 316L Austenitic stainless steel as per L9 Taguchi orthogonal array design of experiment

Figure 4.86 X-ray radiographic film for Sample No. S3A:316L Austenitic stainless steel as per L9 Taguchi orthogonal array design of experiment

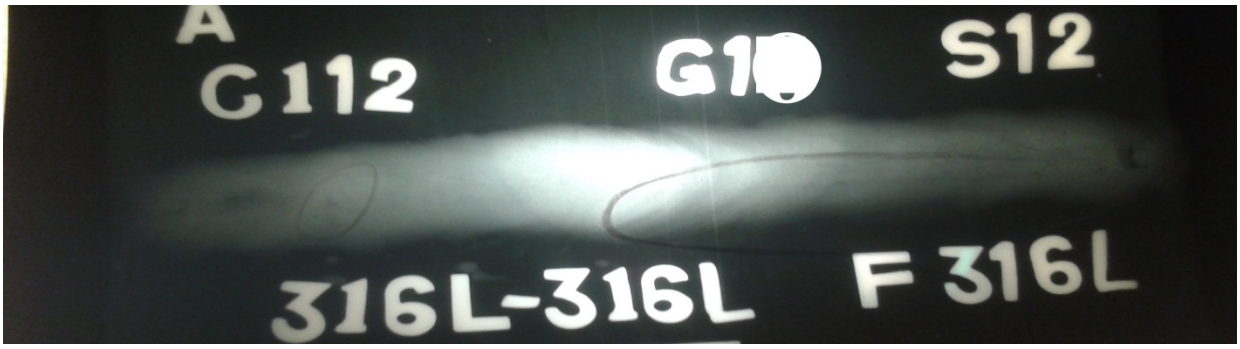

Figure 4.87 X-ray radiographic film for Sample No. S4A:316L Austenitic stainless steel as per L9 Taguchi orthogonal array design of experiment

Figure 4.88 X-ray radiographic film for Sample No. S5A:316L Austenitic stainless steel as per L9 Taguchi orthogonal array design of experiment

Figure 4.89 X-ray radiographic film for Sample No. S6A:316L Austenitic stainless steel as per L9 Taguchi orthogonal array design of experiment

Figure 4.90 X-ray radiographic film for Sample No. S7A:316L Austenitic stainless steel as per L9 Taguchi orthogonal array design of experiment

Figure 4.91 X-ray radiographic film for Sample No. S8A:316L Austenitic stainless steel as per L9 Taguchi orthogonal array design of experiment

Figure 4.92 X-ray radiographic film for Sample No. S9A: 316L Austenitic stainless steel as per L9 Taguchi orthogonal array design of experiment

4.1.6.3 RESULTS OF TENSILE TESTS OF WELDMENT AND DISCUSSION: 316 AUSTENITIC STAINLESS STEEL AS PER L9 TAGUCHI ORTHOGONAL ARRAY DESIGN OF EXPERIMENT

Results of Tensile test obtained as per L9 Taguchi Orthogonal Array Design of Experiment are shown in Table 4.7. Table 4.7 indicates that best tensile test result is obtained for the sample no. S3A. The plots of tests are given in figures 4.93- 4.101.

Table 4.7 Tensile tests result of 316L Austenitic stainless steel: L9 Taguchi Orthogonal Array Design of experiment

Sample No.	Yield strength (MPa)	Ultimate tensile strength (MPa)	Percentage of elongation (%)	Place of Fracture
BASE METAL	**301.6**	**573.8**	**65. 0**	Base
S1A	321.1	550.0	31.2	Base
S2A	317.9	552.0	34.6	Base
S3A	322.7	591.1	54.5	HAZ
S4A	288.8	518.2	33.0	Base
S5A	250.2	432.3	18.5	HAZ
S6A	264.2	481.4	33.1	HAZ
S7A	242.4	426.2	19.5	HAZ
S8A	246.7	484.9	42.8	Base
S9A	233.0	450.9	28.4	HAZ

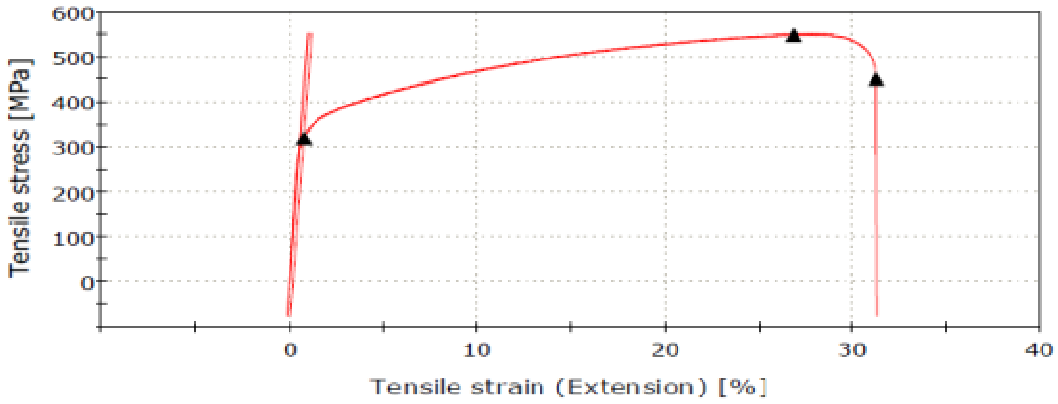

Figure 4.93 Tensile Test Diagram of Sample No. S1A: 316L Austenitic stainless steel as per L9 Taguchi orthogonal array design of experiment

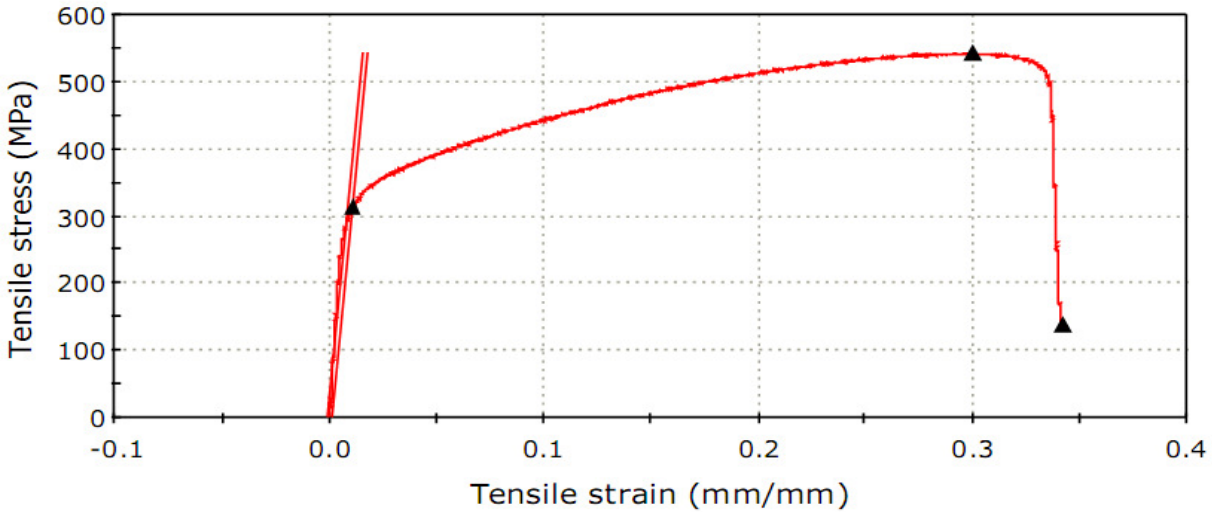

Figure 4.94 Tensile Test Diagram of Sample No. S2A: 316L Austenitic stainless steel as per L9 Taguchi orthogonal array design of experiment

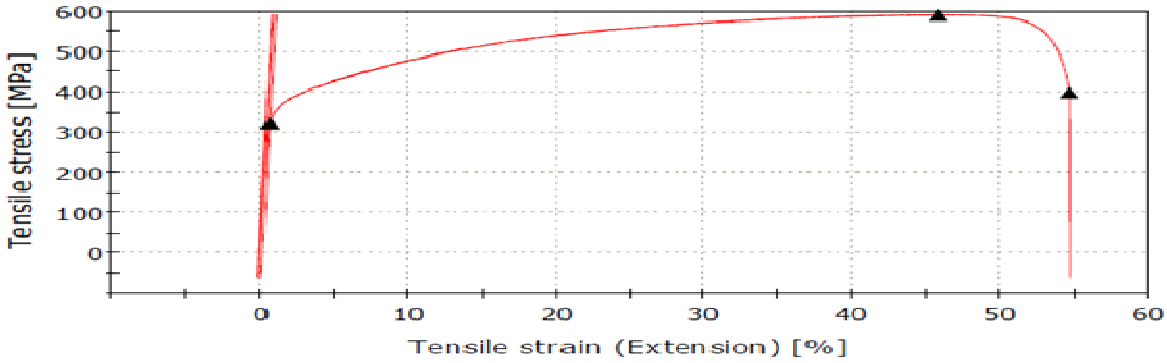

Figure 4.95 Tensile Test Diagram of Sample No. S3A: 316L Austenitic stainless steel as per L9 Taguchi orthogonal array design of experiment

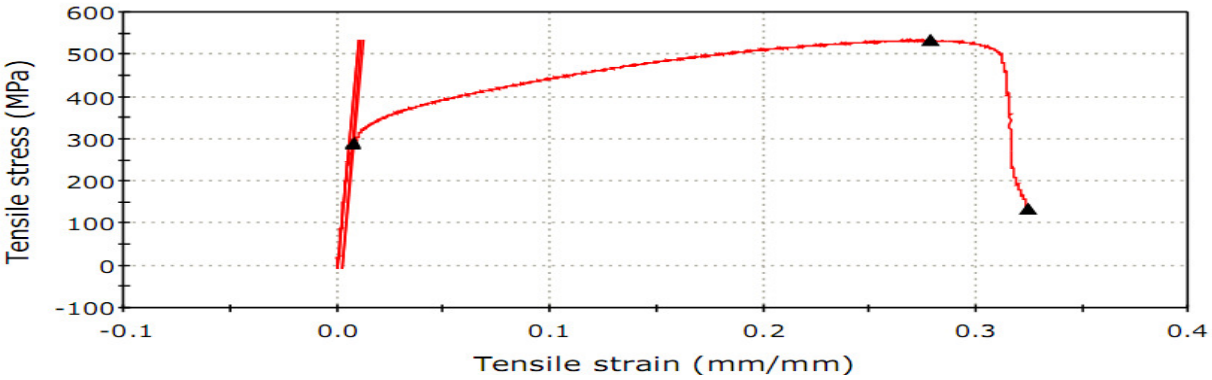

Figure 4.96 Tensile Test Diagram of Sample No. S4A: 316L Austenitic stainless steel as per L9 Taguchi orthogonal array design of experiment

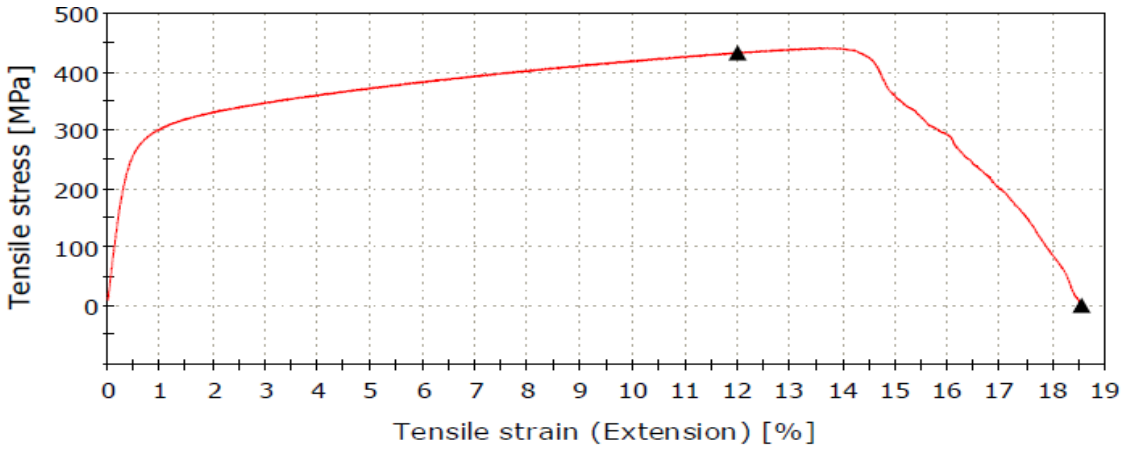

Figure 4.97 Tensile Test Diagram of Sample No. S5A: 316L Austenitic stainless steel as per L9 Taguchi orthogonal array design of experiment

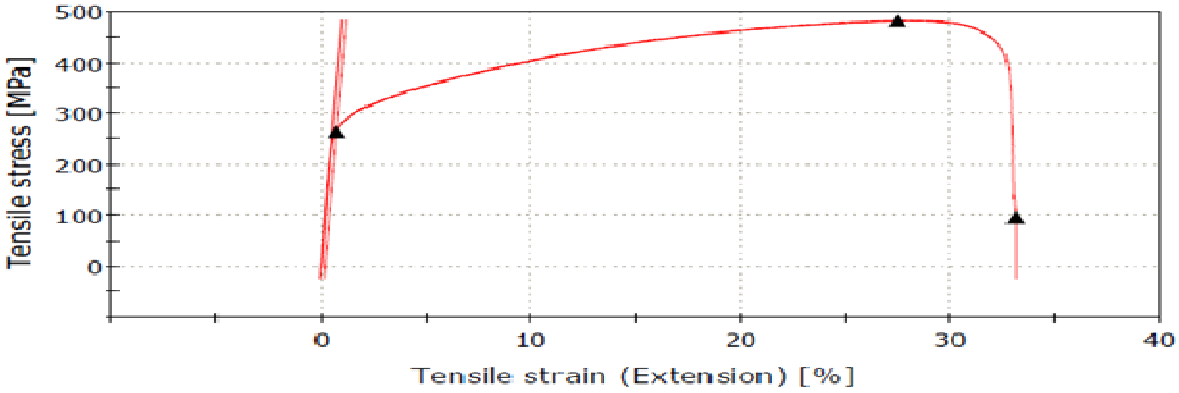

Figure 4.98 Tensile Test Diagram of Sample No. S6A:316L Austenitic stainless steel as per L9 Taguchi orthogonal array design of experiment

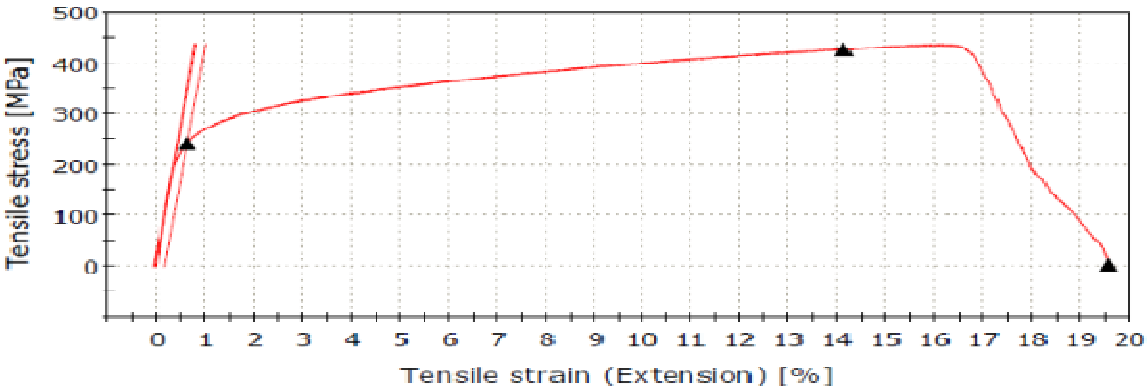

Figure 4.99 Tensile Test Diagram of Sample No. S7A: 316L Austenitic Stainless Steel as per L9 Taguchi orthogonal array design of experiment

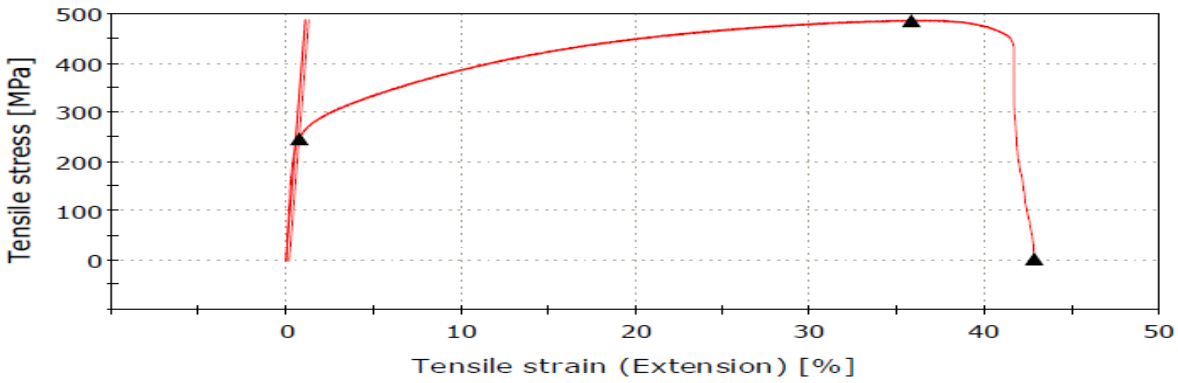

Figure 4.100 Tensile Test Diagram of Sample No. S8A: 316L Austenitic stainless steel as per L9 Taguchi orthogonal array design of experiment

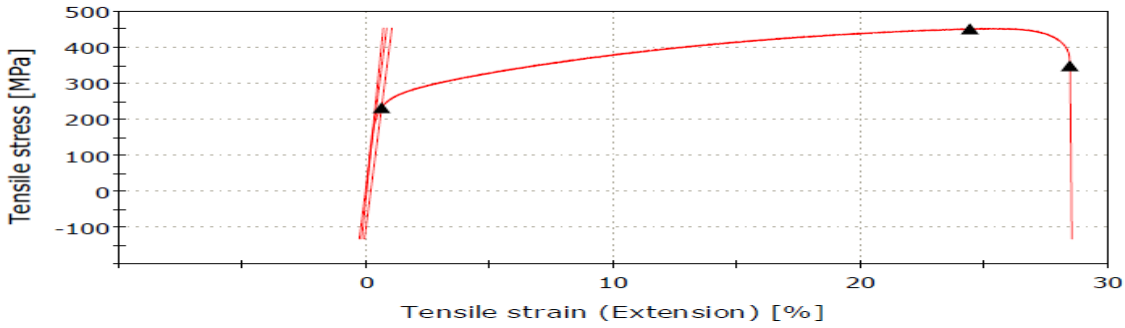

Figure 4.101 Tensile Test Diagram of Sample No. S9A: 316L Austenitic stainless steel as per L9 Taguchi orthogonal array design of experiment

Not much variation is observed in nature of the above plots. However, depending upon the conditions of welding, i.e., levels of the input parameters, there is some change in ultimate strength, yield strength, percentage elongation etc. Joints behave as ductile material. Analysis of the observed data has been made through ANOVA and process optimization in chapter 5.

4.2 RESULTS OF MIG WELDING OF 409 FERRITIC STAINLESS STEEL (2ND SET OF EXPERIMENTS)

First set of experiments discussed above are related to welding of Austenitic stainless steel. In second set of experiments welding of 409 Ferritic stainless steel has been carried out by using 316L filler wire as per i) RSM design of experiment and ii) L9 Taguchi orthogonal design of

experiment. In the following paragraphs the results are presented and discussed, first, as per RSM design of experiment.

4.2.1 RESULTS OF VISUAL INSPECTION, X-RAY RADIOGRAPHIC TESTS AND DISCUSSION: 409 FERRITIC STAINLESS STEEL AS PER RSM DESIGN OF EXPERIMENT

After welding, visual inspection and X-ray radiographic tests have been carried out to detect surface and sub-surface defects of weld specimens made of Ferritic stainless steels. Importance of these tests is outlined earlier. Results of visual inspection are shown in Table 4.8.

From the results of visually inspection (Table 4.8), it is found that for certain welding conditions no defect has been observed. These are for the samples no. S1B, S4B, S5B, S8B, S9B, S11B, S14B, S15B, S16B, S17B and S18B. Blow holes and undercut, small spatter, uneven penetrations are the types of defects which are found in some of the samples. The results of radiography test (Table 4.9) also indicate that comparative good reports are associated with the sample nos. S1B, S4B, S5B, S8B, S9B, S11B, S14B, S15B, S16B, S17B and S18B. Lack of fusion, porosity are the types of defects found in some of the samples.

Table 4.8 Results of visual inspection: 409 Ferritic stainless steel as per RSM design of experiment

Sample No.	Sample Identity	Observation
S1B	C-112/F-15/S-12	No defect
S2B	C-100/F-15/S-12	Spatter, blow hole
S3B	C-124/F-15/S-12	Spatter, blow hole
S4B	C-100/F-10/S-9	No defects
S5B	C-100/F-10/S-15	No defects
S6B	C-100/F-20/S-15	Undercut, spatter
S7B	C-100/F-20/S-9	Lack of penetration
S8B	C-112/F-10/S-12	No defect
S9B	C-112/F-15/S-12	No significant defect (contd.)

S10B	C-124/F-10/S-9	Lack of penetration (contd. from previous page)
S11B	C-112/F-15/S-12	No significant defect
S12B	C-112/F-15/S-15	Undercut, spatter
S13B	C-124/F-20/S-15	Lack of penetration
S14B	C-124/F-10/S-15	No defects
S15B	C-112/F-15/S-12	No defects
S16B	C-112/F-15/S-12	No defects
S17B	C-112/F-15/S-12	No defects
S18B	C-112/F-20/S-12	No defects
S19B	C-112/F-15/S-9	Spatter, uneven penetration
S20B	C-124/F-20/S-9	lack of penetration

If the results of visual inspection and X-ray radiographic tests are compared, some consistency in the findings is noticed in respect of defects in the samples. The results of X-ray radiography are included in Table 4.9. In X-ray radiography test, for sample nos. S1B, S4B, S5B, S8B, S9B, S11B, S14B, S15B, S16B, S17B and S18B, no significant defect is reported. In visual inspection also, no defect is observed for these samples. Again, for sample nos. S2B, S3B, S6B, S7B, S10B, S13B, S19B and S20B X-ray radiographic test indicate some significant defects like porosity and lack of fusion are noted. And in visual inspection defects like undercut, blow holes, spatter, excessive deposition and uneven penetration are reported in some of the samples. The possible causes of the defects observed in X-ray radiographic test and visual inspection are discussed as follows, though some points have already mentioned earlier.

• The combined effect of the levels of the gas flow rate, current and nozzle to plate distance has possibly enhanced / reduced the possibility of the reasons which may lead to lack of penetration, undercut, lack of fusion and uneven deposition found in several welded samples. Besides gas flow rates, current and nozzle to plate distance and other process related factors (like welding speed, skill of the welder etc.) may also cause different types of defect. Again defects may be the results of mechanical design of the joints. Defects may also be metallurgical related defects.

• Porosity and blow holes may have possibly resulted from gas getting entrapped in solidifying metal. Larger arc, faster level of travel speed, too low or too high arc currents, incorrect welding technique (stringer beads or weaved beads etc.), damp filler rod, unclean job surface are the general reasons behind porosity and blow holes.

• Undercuts found under certain conditions in the present study may have been caused by improper joint geometry for some of the samples and unfavorable combination of current, gas flow rate and nozzle to plate distance. Faster arc travel speed during welding or larger arcs may also be considered as possible reasons behind undercut.

• Lack of fusion observed in a few samples welded under some specified conditions of current, gas flow rate and nozzle to plate distance may have been resulted from any or more of the following reasons : improper current, faster arc travel speed, improper welding technique, improper distance of nozzle to plate distance, presence of oxides, scale and other impurities (on the surfaces welded), which do not permit the deposited metal to fuse properly with the base metal, incorrect joint preparation / setting, incorrect electrode / filler rod manipulation etc.

• Lack of penetration may be related to improper setting of the current, gas flow rate combination and nozzle to plate distance, wrongly held electrode, faster arc travel speed, too small root gap, excess weld metal on the back side of the joint and it is usually associated with root pass.

• Spatter, found sample no. S2B, S3B , S6B and S19B, is caused possibly due to damp filler rod or arc blow or bubble of gas being entrapped in the molten globule of metal expanding with great violence and projecting small drops of metal outside the arc seam.

• Increase in gas flow rate may lead to better protection against atmospheric contamination, yielding better quality weld. However, much increase in gas flow rate may cause turbulence causing enhanced chance of gas absorption from the surroundings and un-controlled protection of the arc and weld pool. The effect of gas flow rate exhibited in the present work can be looked upon with respect to that which is mentioned above. Current is always an important parameter in any arc welding process. Both high and low currents give rise to several advantages and disadvantages. Proper current setting provides desired fusion, penetration and energy input. Energy input, energy input rate and the related heating and cooling cycles associated in any arc-welding process finally decides the metallurgical quality of weld and heat affected zone. And another welding parameter nozzle to plate distance is also expected to influence the quality of welded specimens. Some of the above explanations are given in earlier sections also, while discussing over the results of welding of Austenitic stainless steel.

Table 4.9 Results of X-ray radiographic inspection: 409 Ferritic stainless steel as per RSM design of experiment

Sample No.	Sample Identity	Observation
S1B	C-112/F-15/S-12	No defect
S2B	C-100/F-15/S-12	Porosity
S3B	C-124/F-15/S-12	Porosity
S4B	C-100/F-10/S-9	No defects
S5B	C-100/F-10/S-15	No defects
S6B	C-100/F-20/S-15	Lack of fusion, porosity
S7B	C-100/F-20/S-9	Porosity
S8B	C-112/F-10/S-12	No defect
S9B	C-112/F-15/S-12	No significant defect
S10B	C-124/F-10/S-9	Undercut , porosity
S11B	C-112/F-15/S-12	No significant defect
S12B	C-112/F-15/S-15	Porosity
S13B	C-124/F-20/S-15	Lack of fusion
S14B	C-124/F-10/S-15	No defects
S15B	C-112/F-15/S-12	No defects
S16B	C-112/F-15/S-12	No defects
S17B	C-112/F-15/S-12	No defects
S18B	C-112/F-20/S-12	No defects
S19B	C-112/F-15/S-9	Porosity
S20B	C-124/F-20/S-9	lack of fusion

The X- ray films for 20 samples are presented in figures 4.102 – 4.121.

Figure 4.102 X-ray radiographic film for Sample No. S1B: 409Ferritic stainless steel as per RSM design of experiment

Figure 4.103 X-ray radiographic film for Sample No. S2B: 409Ferritic stainless steel as per RSM design of experiment

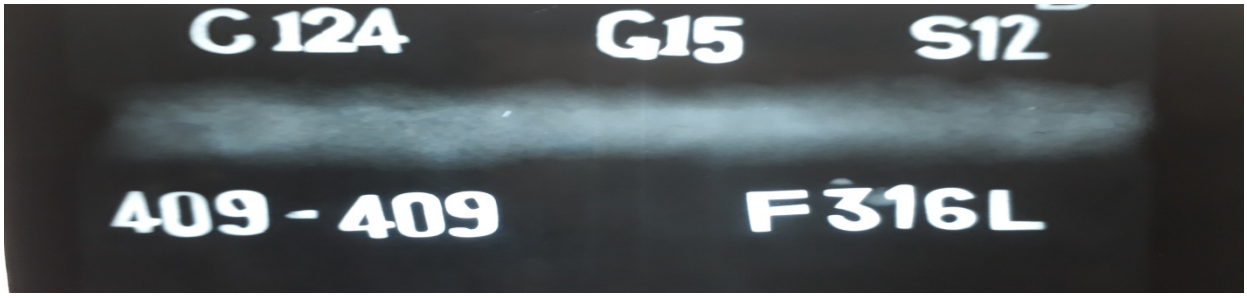

Figure 4.104 X-ray radiographic film for Sample No. S3B: 409Ferritic stainless steel as per RSM design of experiment

Figure 4.105 X-ray radiographic film for Sample No. S4B: 409 Ferritic stainless steel as per RSM design of experiment

Figure 4.106 X-ray radiographic film for Sample No. S5B: 409 Ferritic stainless steel as per RSM design of experiment

Figure 4.107 X-ray radiographic film for Sample No. S6B: 409 Ferritic stainless steel as per RSM design of experiment

Figure 4.108 X-ray radiographic film for Sample No. S7B: 409Ferritic Stainless Steel as per RSM design of experiment

Figure 4.109 X-ray radiographic film for Sample No. S8B: 409Ferritic Stainless Steel as per RSM design of experiment

Figure 4.110 X-ray radiographic film for Sample No. S9B: 409Ferritic Stainless Steel as per RSM design of experiment

Figure 4.111 X-ray radiographic film for Sample No. S10B: 409 Ferritic stainless steel as per RSM design of experiment

Figure 4.112 X-ray radiographic film for Sample No. S11B: 409 Ferritic stainless steel as per RSM design of experiment

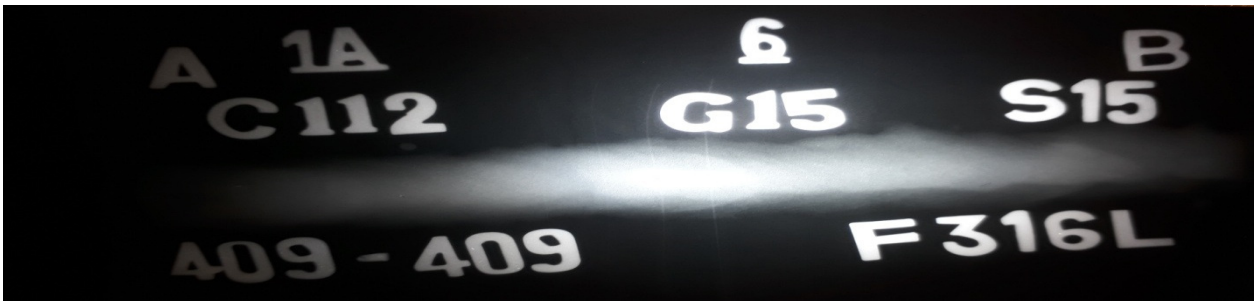

Figure 4.113 X-ray radiographic film for Sample No. S12B: 409 Ferritic stainless steel as per RSM design of experiment

Figure 4.114 X-ray radiographic film for Sample No. S13B: 409 Ferritic Stainless Steel as per RSM design of experiment

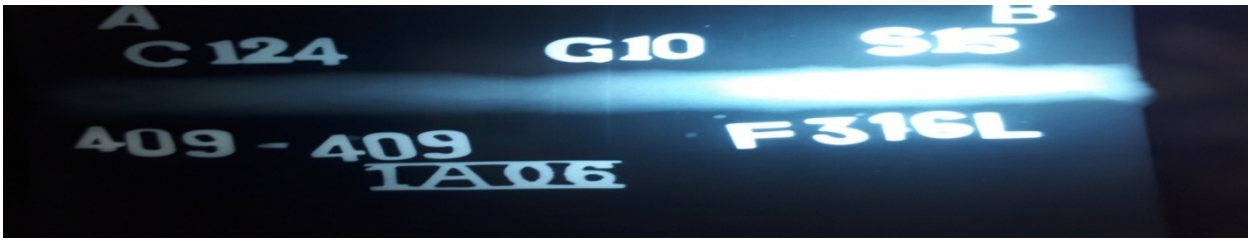

Figure 4.115 X-ray radiographic film for Sample No. S14B: 409 Ferritic stainless steel as per RSM design of experiment

Figure 4.116 X-ray radiographic film for Sample No. S15B: 409 Ferritic Stainless Steel as per RSM design of experiment

Figure 4.117 X-ray radiographic film for Sample no. S16B: 409 Ferritic stainless steel as per RSM design of experiment

Figure 4.118 X-ray radiographic film for Sample No. S17B: 409 Ferritic stainless steel as per RSM design of experiment

Figure 4.119 X-ray radiographic film for Sample No. S18B: 409 Ferritic stainless steel as per RSM design of experiment

Figure 4.120 X-ray radiographic film for Sample No. S19B: 409 Ferritic stainless steel as per RSM design of experiment

Figure 4.121 X-ray radiographic film for Sample no. S20B: 409 Ferritic stainless steel as per RSM design of experiment

4.2.2 RESULTS OF TENSILE TEST AND DISCUSSION: 409 FERRITIC STAINLESS STEEL AS PER RSM DESIGN OF EXPERIMENT

Table 4.10 indicates that for many of the welded samples test results are satisfactory. The best result is obtained for the sample no.S7B (corresponding to Welding current 100A, Gas flow rate 20 *l*.min-1 and Nozzle to plate distance 9mm) For this sample, Ultimate tensile strength = 472.6MPa and Yield strength = 349.9MPa and Percentage of elongation is 13.1. The worst result in tensile testing has been obtained for the sample no. S10B (corresponding to Welding current 124 A, Gas flow rate 10 l/min and Nozzle to plate distance 9 mm). For this sample Yield strength = 236.6MPa ,Ultimate tensile strength = 261.3MPa and Percentage of elongation is 18.5.

Table 4.10 Tensile test results: 409 Ferritic stainless steel as per RSM design of experiment

Sample No.	Sample Identity	Yield Strength (MPa)	Ultimate Tensile Strength (MPa)	Percentage of Elongation (%)
BASE METAL	AISI 409	209.9	349.3	30.9
S1B	C-112/F-15/S-12	288.0	424.0	17.0
S2B	C-100/F-15/S-12	255.1	376.5	15.0
S3B	C-124/F-15/S-12	237.0	368.2	24.5
S4B	C-100/F-10/S-9	296.5	431.6	25.5
S5B	C-100/F-10/S-15	269.9	401.7	27.0 (contd.)

S6B	C-100/F-20/S-15	256.0	377.3	18.5(contd. from previous page)
S7B	C-100/F-20/S-9	349.9	472.6	13.1
S8B	C-112/F-10/S-12	289.8	416.6	17.6
S9B	C-112/F-15/S-12	289.4	414.8	14.5
S10B	C-124/F-10/S-9	236.6	261.3	18.5
S11B	C-112/F-15/S-12	285.5	415.6	20.8
S12B	C-112/F-15/S-15	137.0	368.3	24.5
S13B	C-124/F-20/S-15	146.3	271.7	24.7
S14B	C-124/F-10/S-15	268.8	400.3	23.9
S15B	C-112/F-15/S-12	284.0	415.3	17.0
S16B	C-112/F-15/S-12	286.5	423.5	18.0
S17B	C-112/F-15/S-12	289.7	416.5	17.6
S18B	C-112/F-20/S-12	321.9	453.6	23.4
S19B	C-112/F-15/S-9	246.4	386.5	21.7
S20B	C-124/F-20/S-9	166.3	307.5	21.3

Tensile test (stress-strain) diagrams are shown in figures 4.122 - 4.142. Ductile nature is observed. Variation in the diagrams can be linked with the variation of the combinations of the input parameters apart from some other factors. This has been analyzed by statistical means in the next chapter, chapter 5.

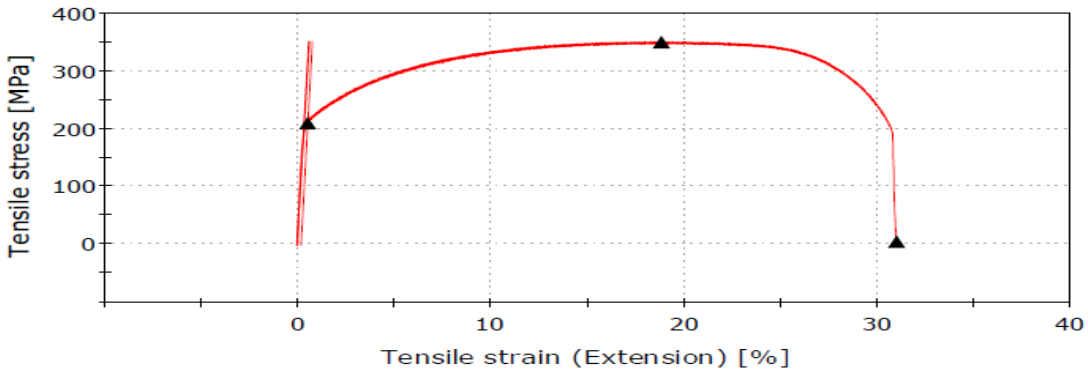

Figure 4.122 Tensile Test Diagram of Sample No. Base Metal: 409 Ferritic stainless steel as per RSM design of experiment

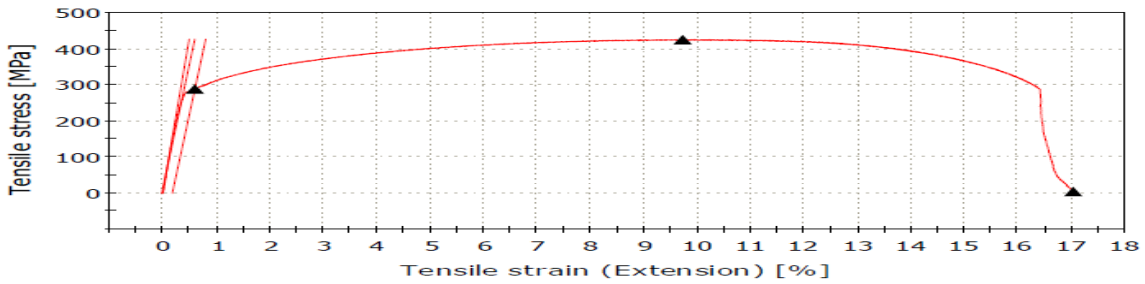

Figure 4.123 Tensile Test Diagram of Sample No. S1B: 409 Ferritic stainless steel as per RSM design of experiment

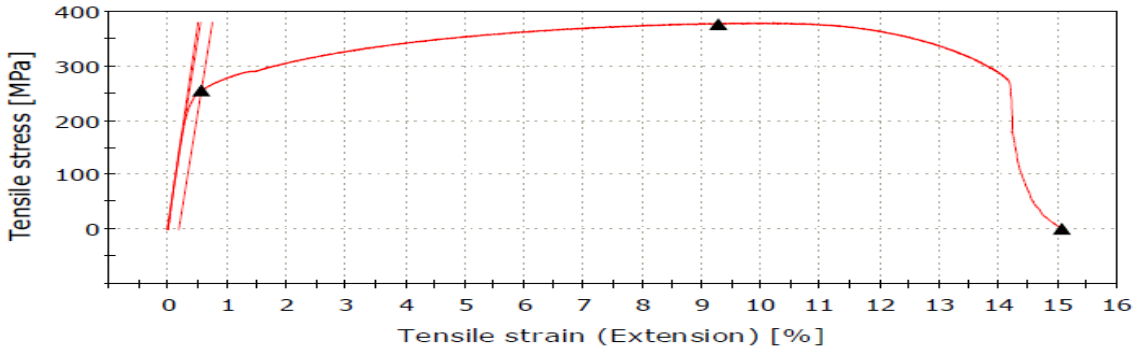

Figure 4.124 Tensile Test Diagram of Sample No. S2B: 409 Ferritic stainless steel as per RSM design of experiment

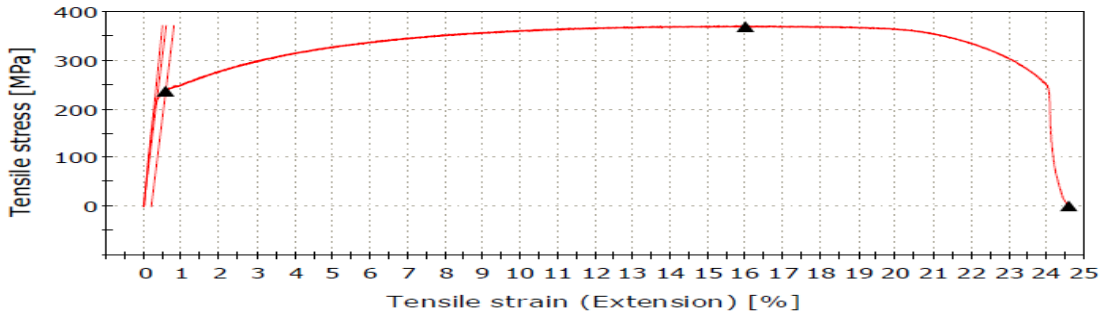

Figure 4.125 Tensile Test Diagram of Sample No. S3B: 409 Ferritic stainless steel as per RSM design of experiment

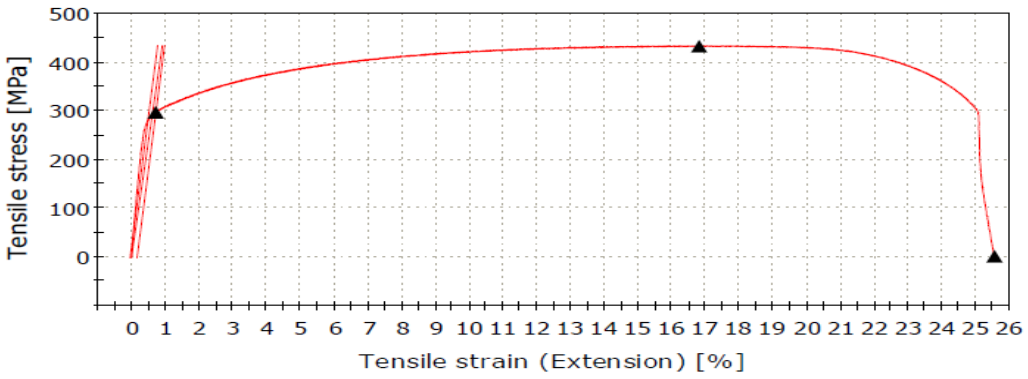

Figure 4.126 Tensile Test Diagram of Sample No. S4B:409 Ferritic stainless steel as per RSM design of experiment

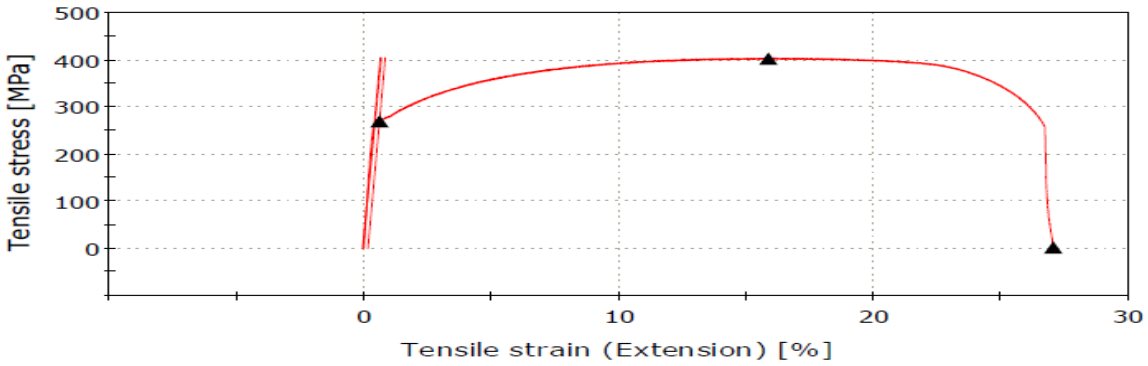

Figure 4.127 Tensile Test Diagram of Sample No. S5B: 409 Ferritic stainless steel as per RSM design of experiment

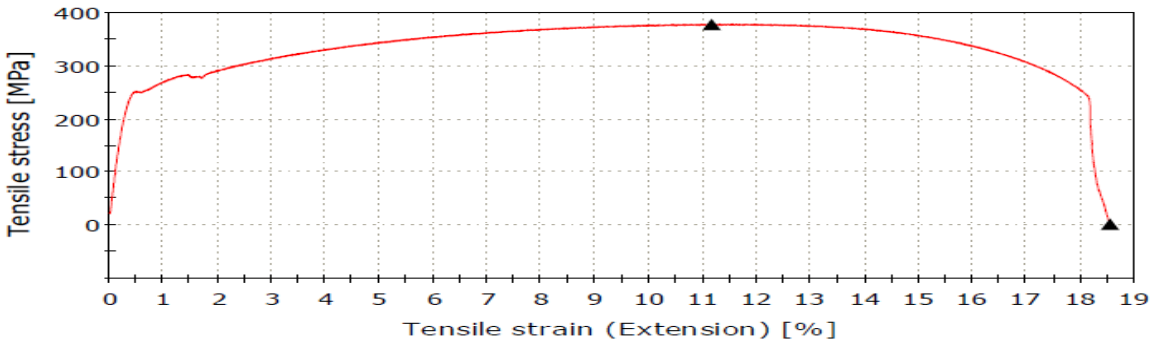

Figure 4.128 Tensile Test Diagram of Sample No. S6B: 409 Ferritic stainless steel as per RSM design of experiment

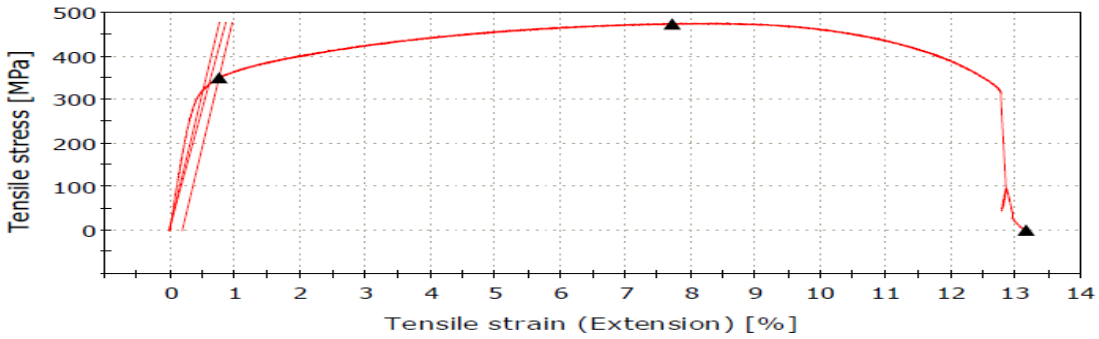

Figure 4.129 Tensile Test Diagram of Sample No. S7B: 409 Ferritic stainless steel as per RSM design of experiment

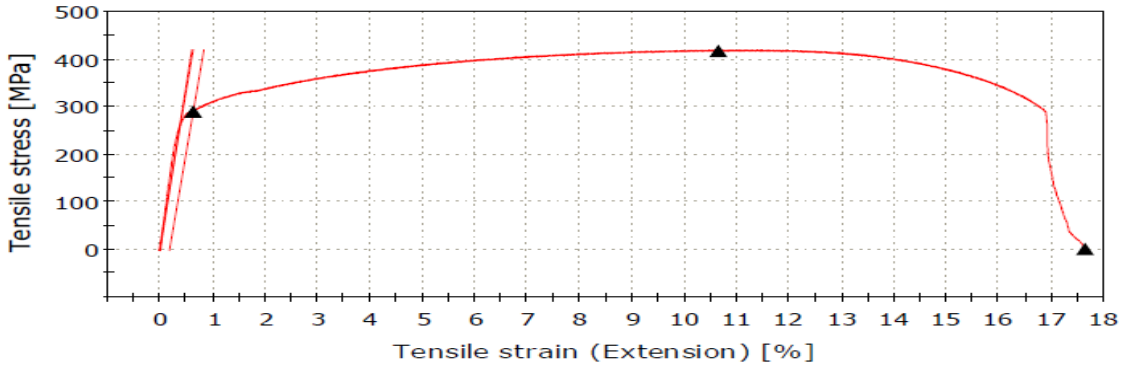

Figure 4.130 Tensile Test Diagram of Sample No. S8B: 409 Ferritic stainless steel as per RSM design of experiment

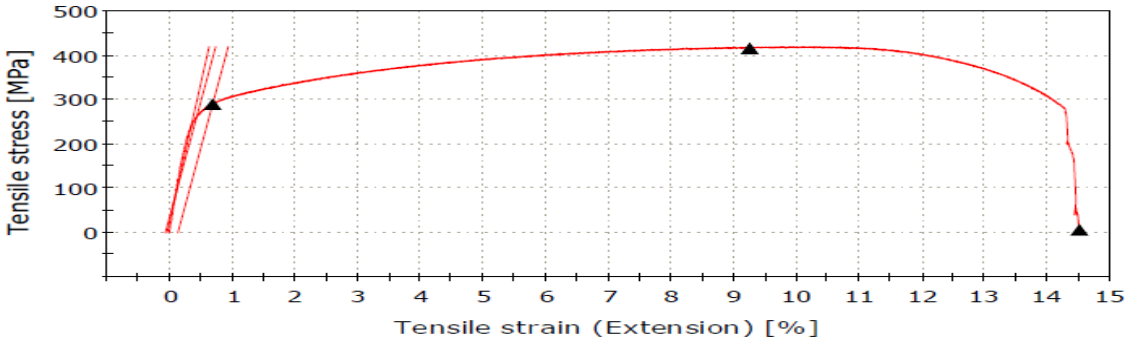

Figure 4.131 Tensile Test Diagram of Sample No. S9B: 409 Ferritic stainless steel as per RSM design of experiment

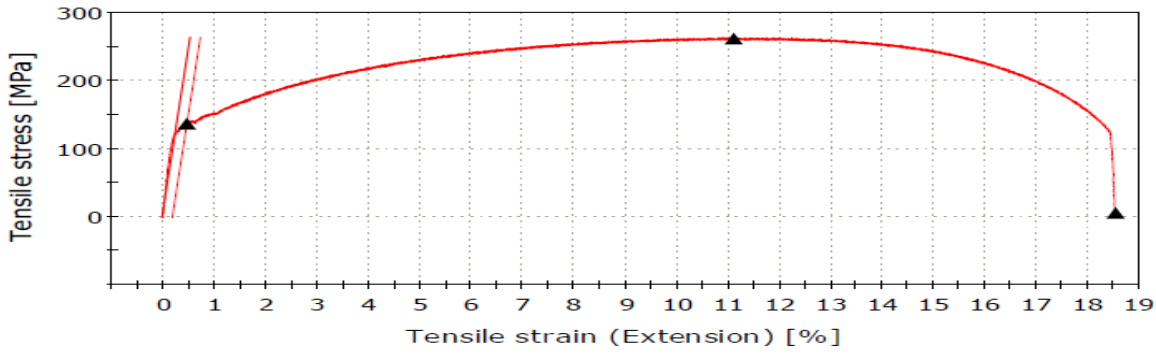

Figure 4.132 Tensile Test Diagram of Sample No. S10B: 409 Ferritic stainless steel as per RSM design of experiment

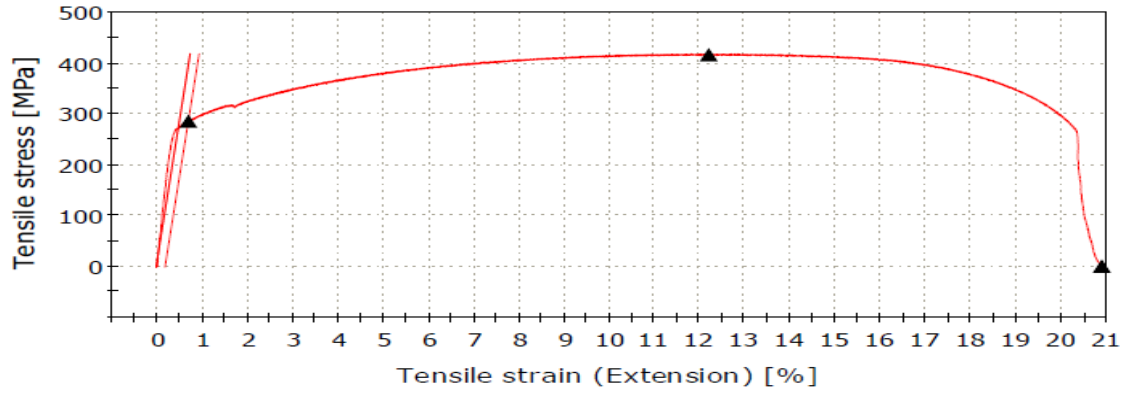

Figure 4.133 Tensile Test Diagram of Sample No. S11B: 409 Ferritic stainless steel as per RSM design of experiment

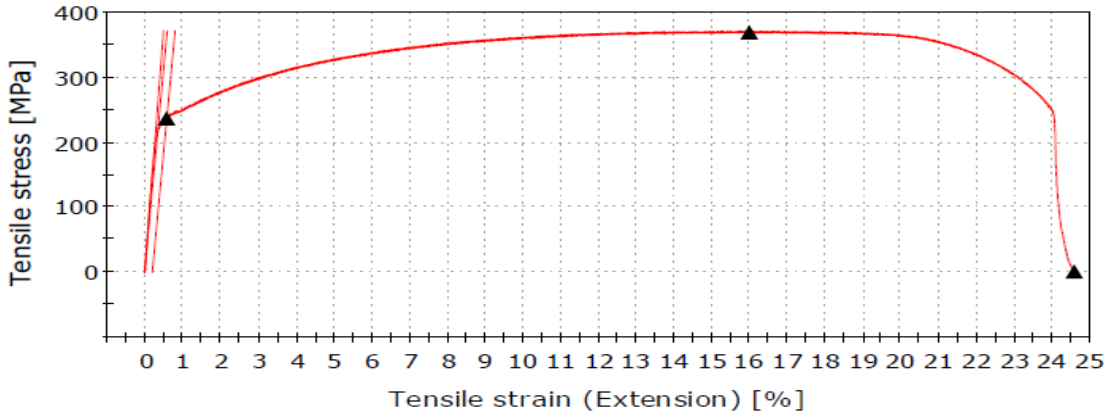

Figure 4.134 Tensile Test Diagram of Sample No. S12B: 409 Ferritic stainless steel as per RSM design of experiment

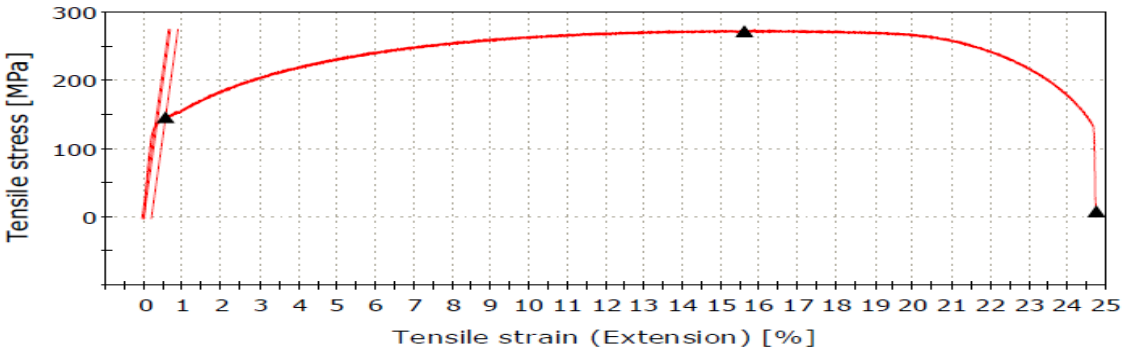

Figure 4.135 Tensile Test Diagram of Sample No. S13B: 409 Ferritic stainless steel as per RSM design of experiment

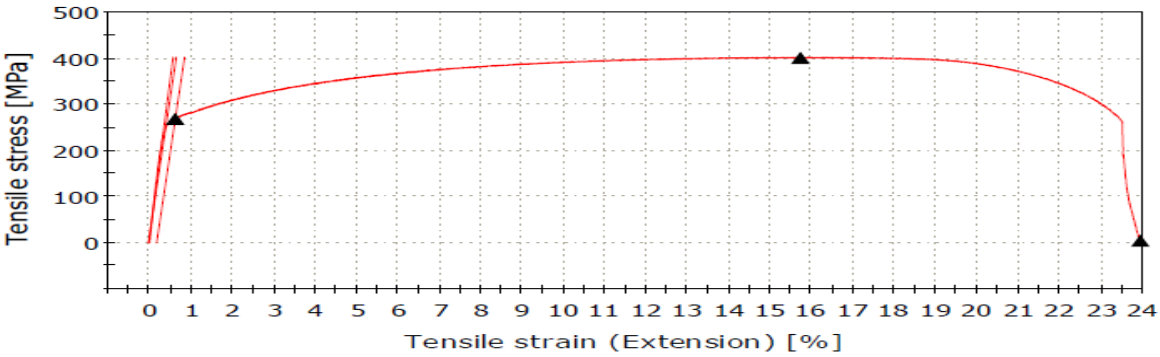

Figure 4.136 Tensile Test Diagram of Sample No. S14B: 409 Ferritic stainless steel as per RSM design of experiment

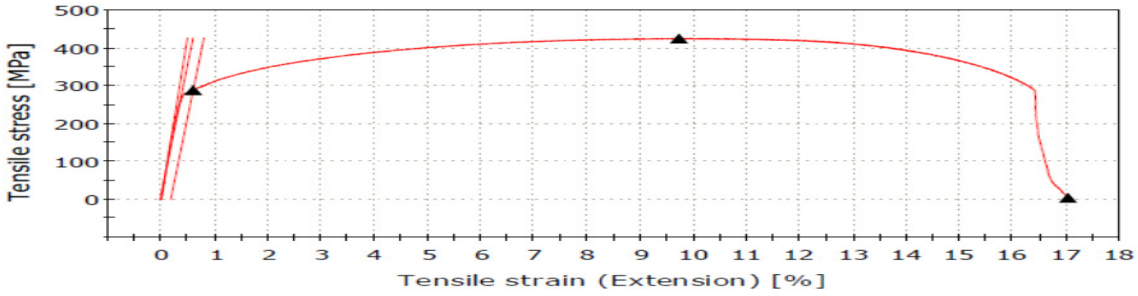

Figure 4.137 Tensile Test Diagram of Sample No. S15B: 409 Ferritic Stainless Steel as per RSM design of experiment

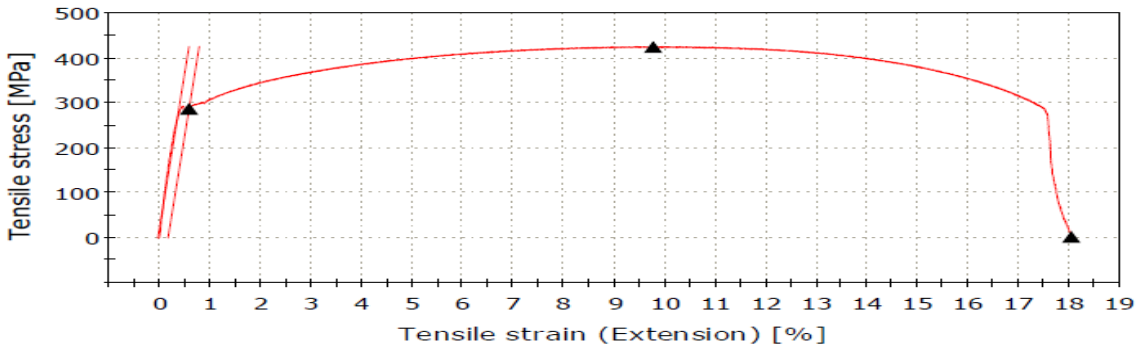

Figure 4.138 Tensile Test Diagram of Sample No. S16B: 409 Ferritic Stainless Steel as perRSM design of experiment

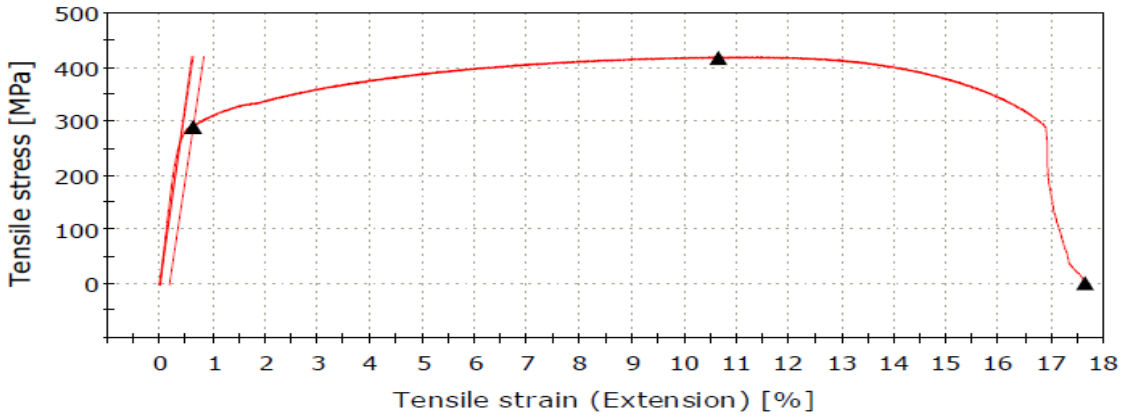

Figure 4.139 Tensile Test Diagram of Sample No. S17B: 409 Ferritic stainless steel as perRSM design of experiment

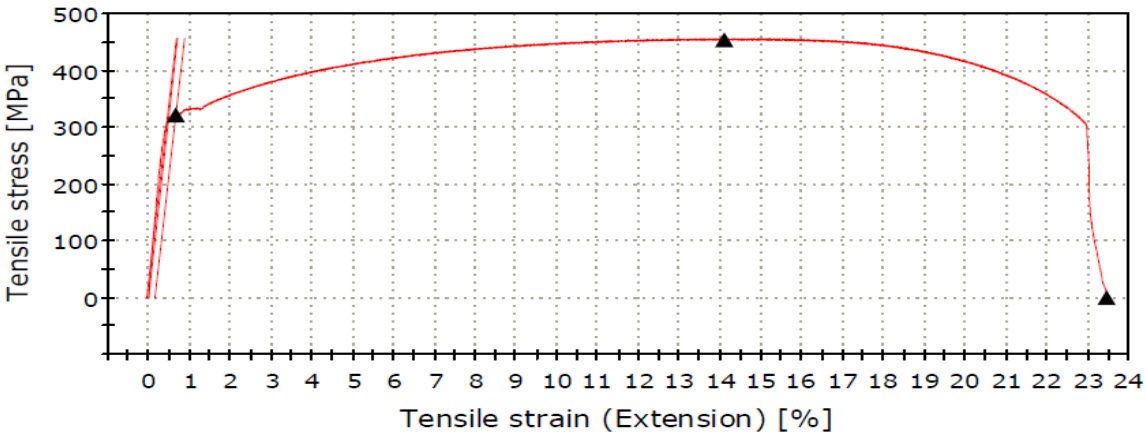

Figure 4.140 Tensile Test Diagram of Sample No. S18B: 409 Ferritic stainless steel as per RSM design of experiment

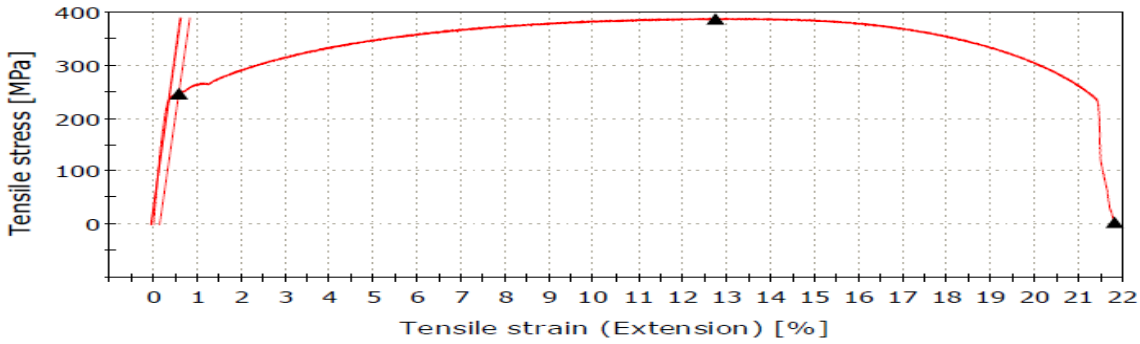

Figure 4.141 Tensile Test Diagram of Sample No. S19B:409 Ferritic stainless steel as per RSM design of experiment

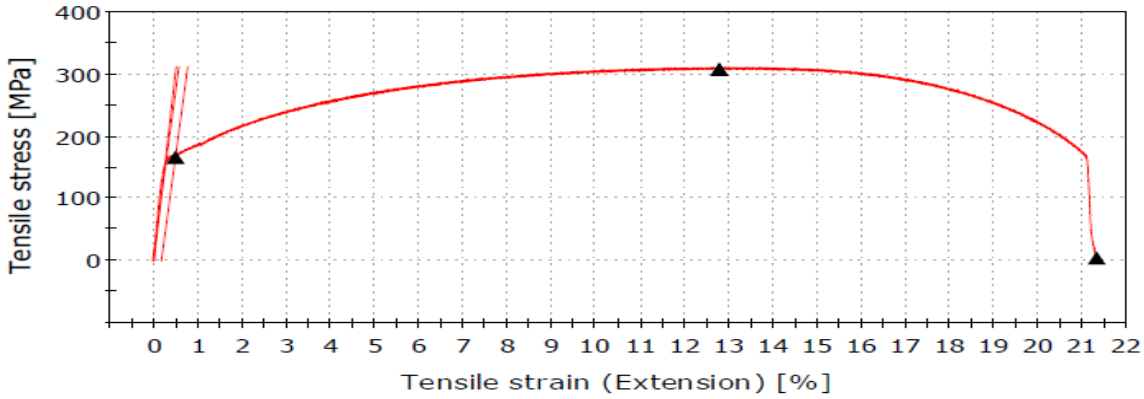

Figure 4.142 Tensile Test Diagram of Sample No. S20B: 409 Ferritic stainless steel as per RSM design of experiment

4.2.3 RESULTS OF MICRO-HARDNESS TEST AND DISCUSSION: 409 FERRITIC STAINLESS STEEL AS PER RSM DESIGN OF EXPERIMENT

In the present study, hardness of all the samples has been measured by a Leco LM 248AT micro-hardness tester. Locations at which hardness is measured are already shown in figure 4.42. Measurement is taken at 2 points of the base metal, at 2 points of HAZ and at 2 points in the weld area. The results of the micro-hardness test are given in the Table 4.11. Hardness values are in Vickers scale i.e., HV. Graphs showing change in hardness values corresponding to the change in locations: 1 - 2 – 3 – 4 – 5 - 6 of the welded samples are shown in figures 4.143 – 4.162. From these figures it is found that for most of the samples, the nature of variation in

hardness values along the position 1 - 2 – 3 – 4 – 5 – 6, is similar. Hardness is one of the several characteristics, which represent reliability and quality of the weld. The data in Table 4.11 (or the figures 4.143 – 4.162), suggest that, variation in the levels of the input parameter has influenced hardness of the welded samples at its different zones to some extent, though the trend of this variation is nearly same for all the samples.

Table 4.11 Results of hardness test: 409 Ferritic stainless steel as per RSM design of experiment

Sample No.	**Hardness (HV) at position**					
	1	**2**	**3**	**4**	**5**	**6**
S1B	220	220.8	240.2	245.8	228.3	225.8
S2B	225.3	230.6	244.4	248.2	235.8	230.1
S3B	217	225.2	255.6	257.4	235.8	220.2
S4B	220.1	230.7	250.5	260.2	234.6	225.6
S5B	220.4	252	256.4	245.6	258	225
S6B	202	233.2	245.6	224.8	234	218
S7B	232.4	245.6	257.8	260.2	255.8	258.4
S8B	210	237.7	250.3	257.8	245.4	215.6
S9B	220.5	230.4	256.8	250.5	222.5	225.6
S10B	215.2	220.3	211	214.2	225	210
S11B	223.9	238.9	250.5	255.7	240.7	230.3
S12B	235.6	234.2	245.6	248.1	238.6	238.7
S13B	232	230.4	244.4	250.6	235.8	240.2
S14B	220.2	245.1	250.2	255.4	248.2	230
S15B	240.8	220.6	255.6	257.8	237.7	243.5
S16B	213.7	220.8	257.2	243.8	225.3	230.8
S17B	230.2	245	250.8	251.7	234.6	224.3
S18B	230.2	260.2	260.8	268	254.4	227.4
S19B	235.6	234.9	238.6	240.2	239.8	240
S20B	225.8	230.8	250.3	248.1	238.6	238

Corresponding hardness vs. position graphs are drawn for all the samples and are shown in the figures 4.143 – 4.162

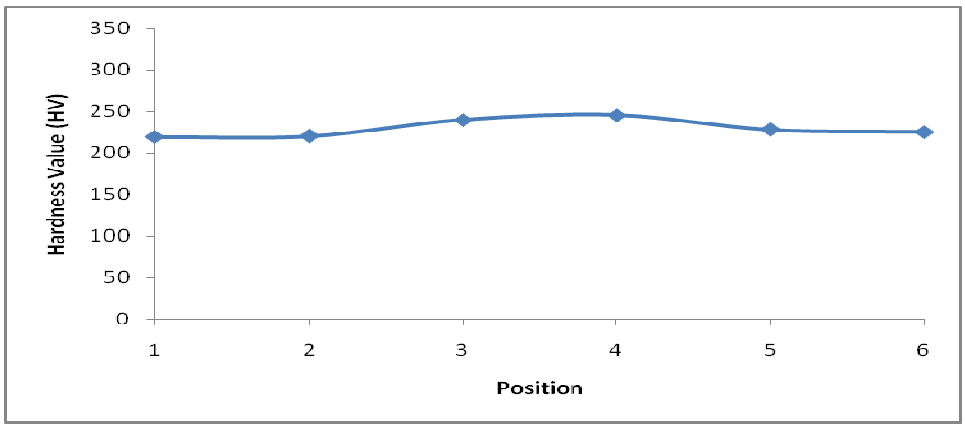

Figure 4.143 Hardness graph for Sample No. S1B: 409Ferritic stainless steel as per RSM design of experiment

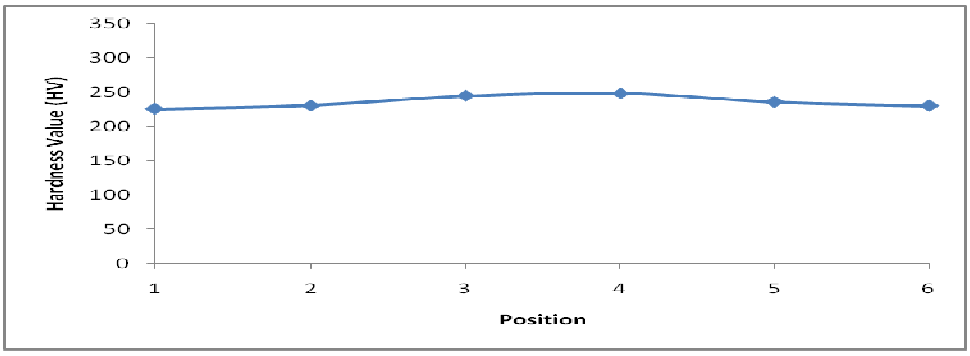

Figure 4.144 Hardness graph for Sample No. S2B: 409 Ferritic stainless steel as per RSM design of experiment

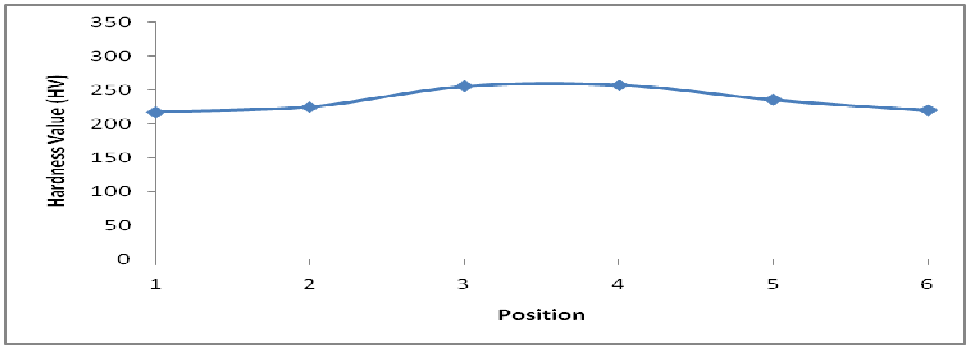

Figure 4.145 Hardness graph for Sample No. S3B: 409Ferritic stainless steel as per RSM design of experiment

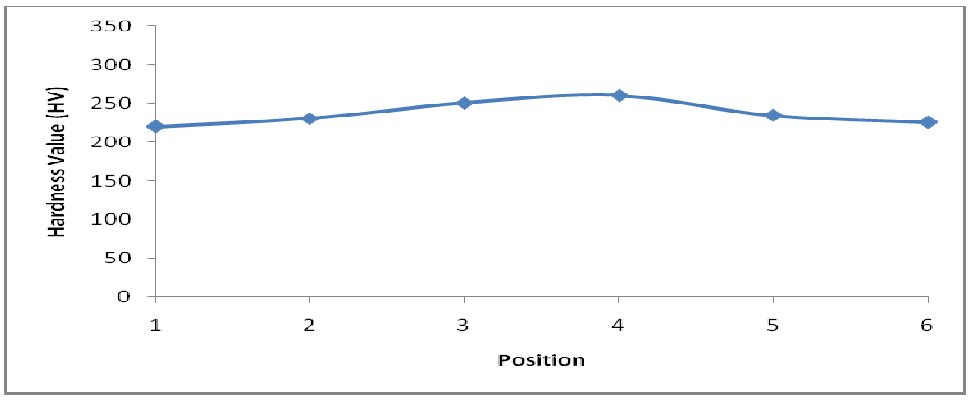

Figure 4.146 Hardness graph for Sample No. S4B: 409 Ferritic stainless steel as per RSM design of experiment

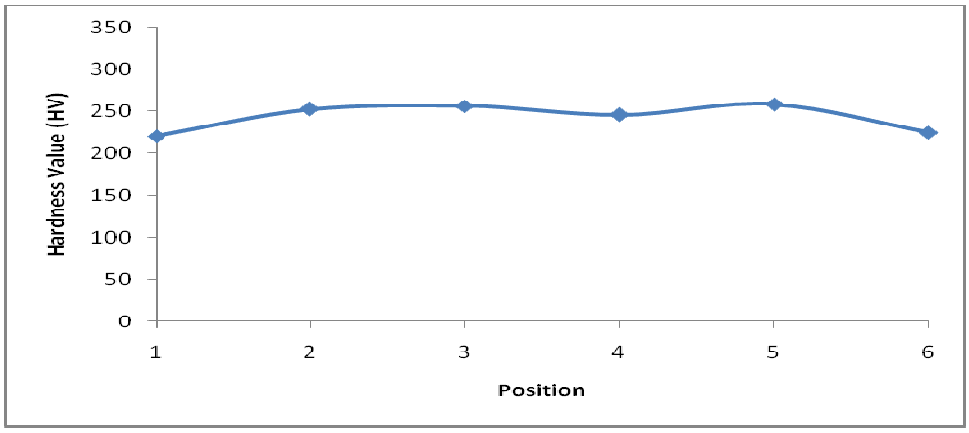

Figure 4.147 Hardness graph for Sample No. S5B: 409 Ferritic stainless steel as per RSM design of experiment

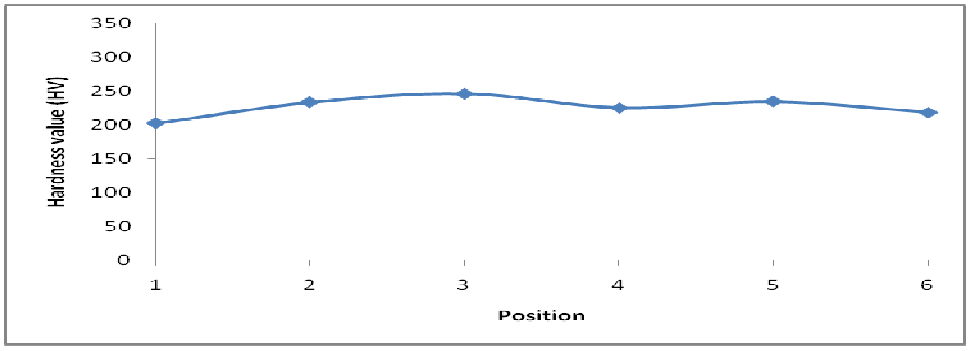

Figure 4.148 Hardness graph for Sample No. S6B: 409Ferritic stainless steel as per RSM design of experiment

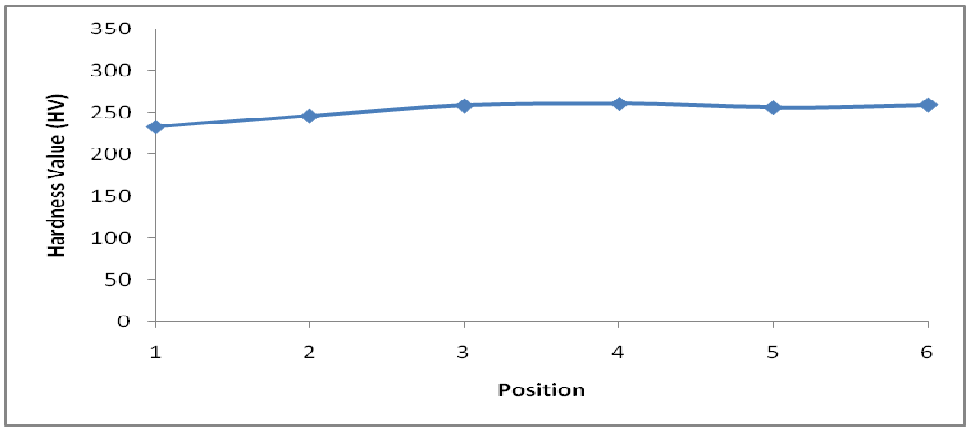

Figure 4.149 Hardness graph for Sample No. S7B: 409Ferritic stainless steel as per RSM design of experiment

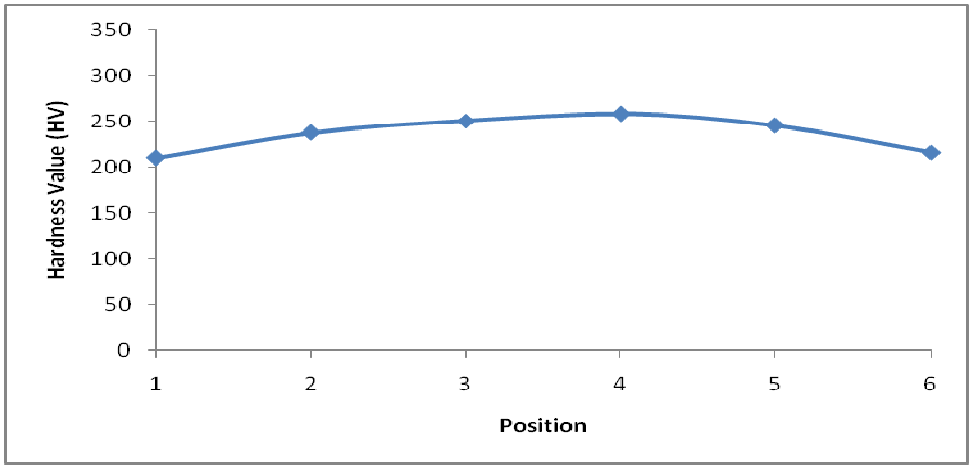

Figure 4.150 Hardness graph for Sample No. S8B: 409Ferritic stainless steel as per RSM design of experiment

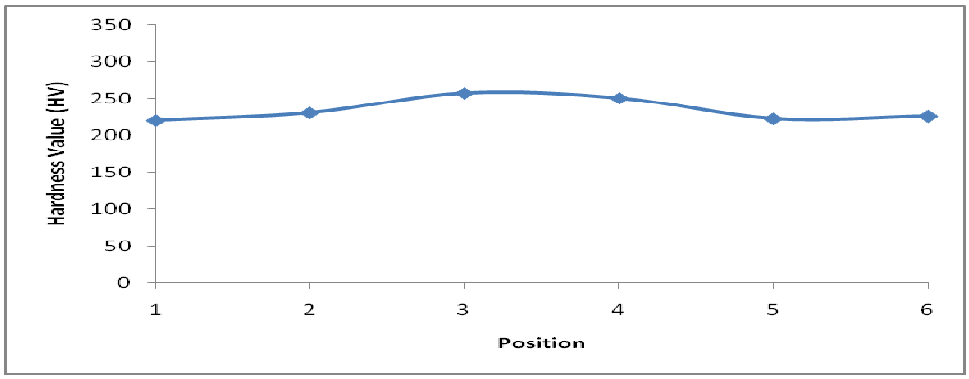

Figure 4.151 Hardness graph for Sample No. S9B: 409 Ferritic stainless steel as per RSM design of experiment

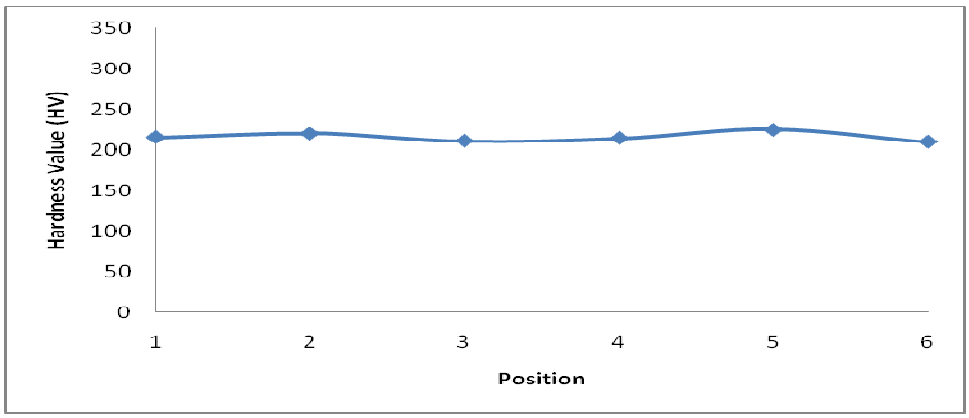

Figure 4.152 Hardness graph for Sample No. S10B: 409 Ferritic stainless steel as per RSM design of experiment

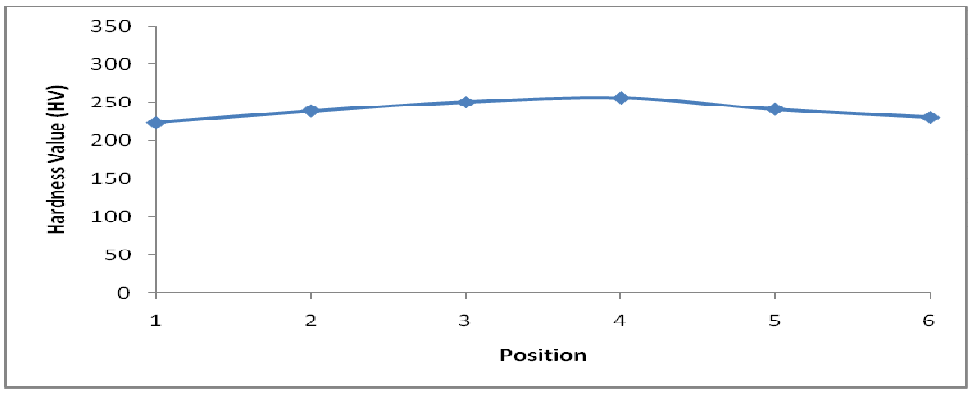

Figure 4.153 Hardness graph for Sample No. S11B: 409 Ferritic stainless steel as per RSM design of experiment

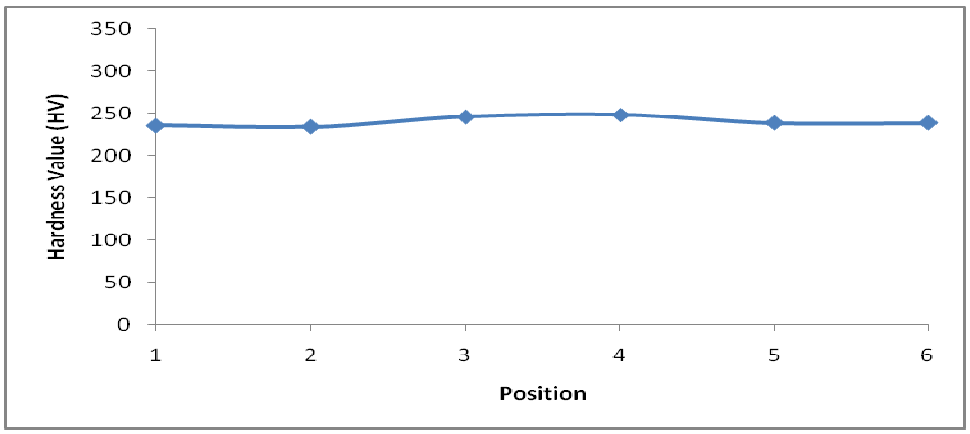

Figure 4.154 Hardness graph for Sample No. S12B: 409 Ferritic stainless steel as per RSM design of experiment

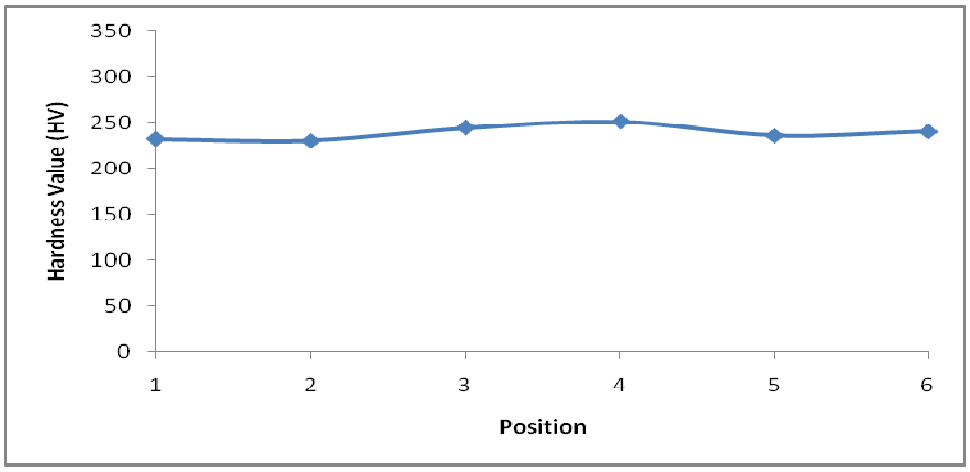

Figure 4.155 Hardness graph for Sample No. S13B: 409 Ferritic stainless steel as per RSM design of experiment

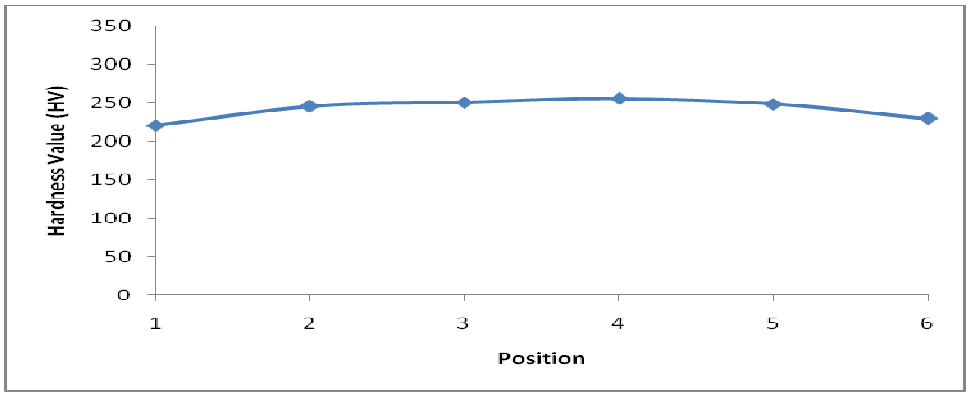

Figure 4.156 Hardness graph for Sample No. S14B: 409Ferritic stainless steel as per RSM design of experiment

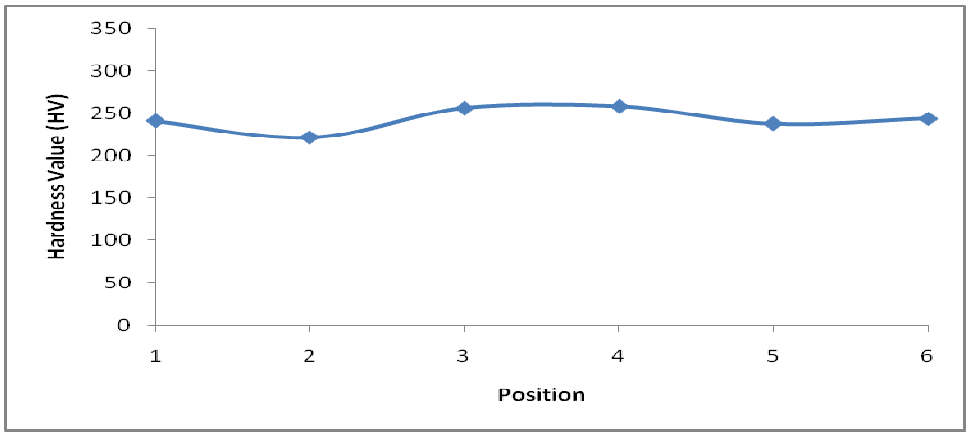

Figure 4.157 Hardness graph for Sample No. S15B: 409Ferritic stainless steel as per RSM design of experiment

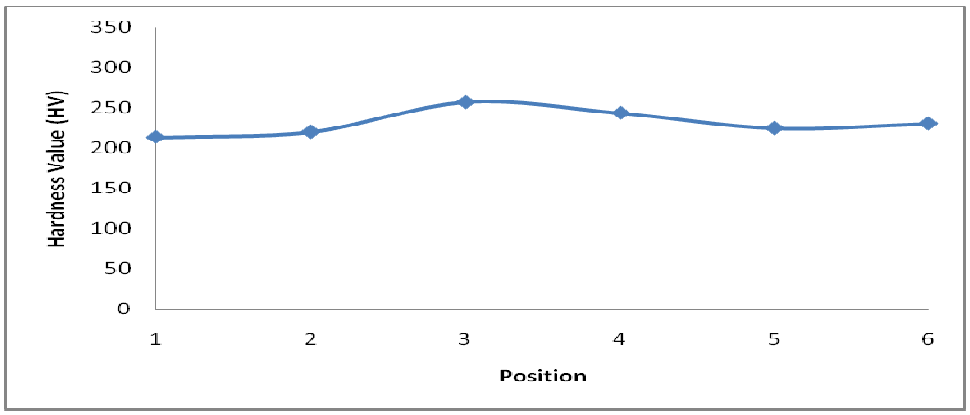

Figure 4.158 Hardness graph for Sample No. S16B: 409Ferritic stainless steel as per RSM design of experiment

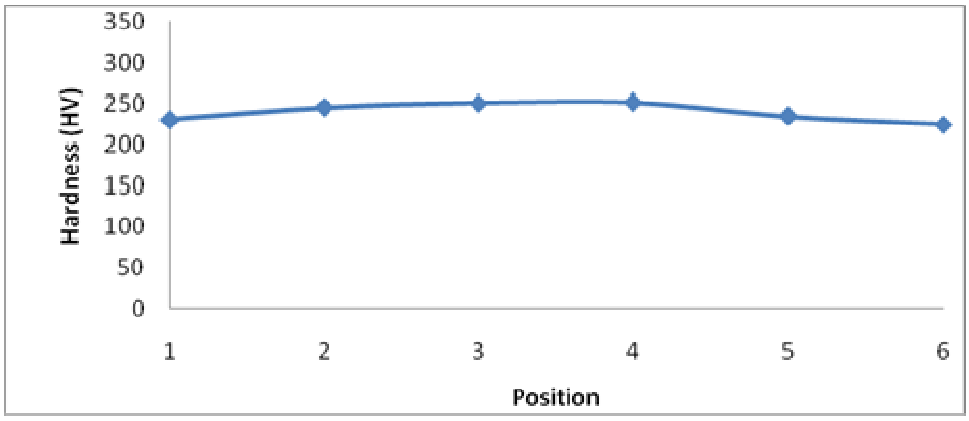

Figure 4.159 Hardness graph for Sample No. S17B: 409Ferritic stainless steel as per RSM design of experiment

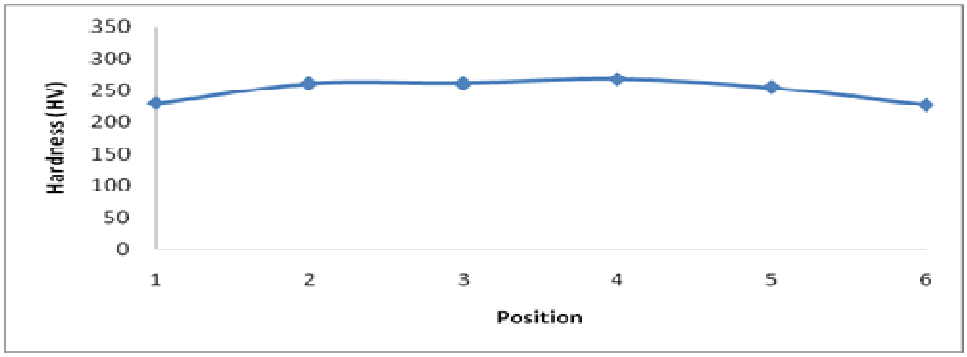

Figure 4.160 Hardness graph for Sample No. S18B: 409Ferritic stainless steel as per RSM design of experiment

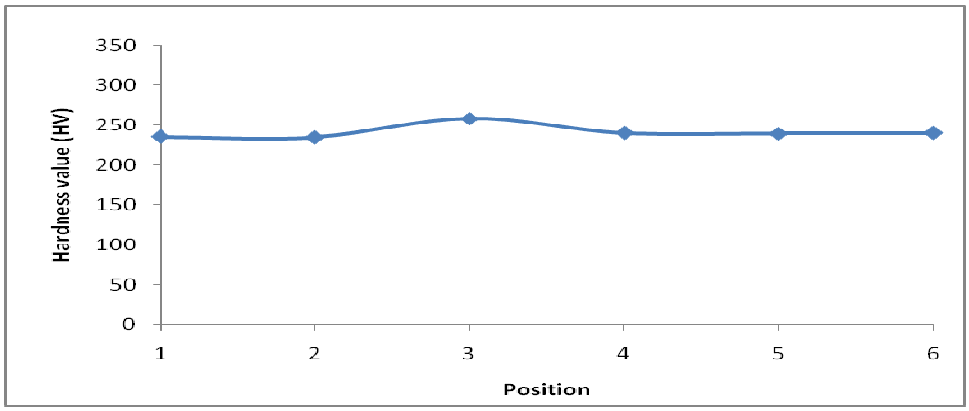

Figure 4.161 Hardness graph for Sample No. S19B:409Ferritic stainless steel as per RSM design of experiment

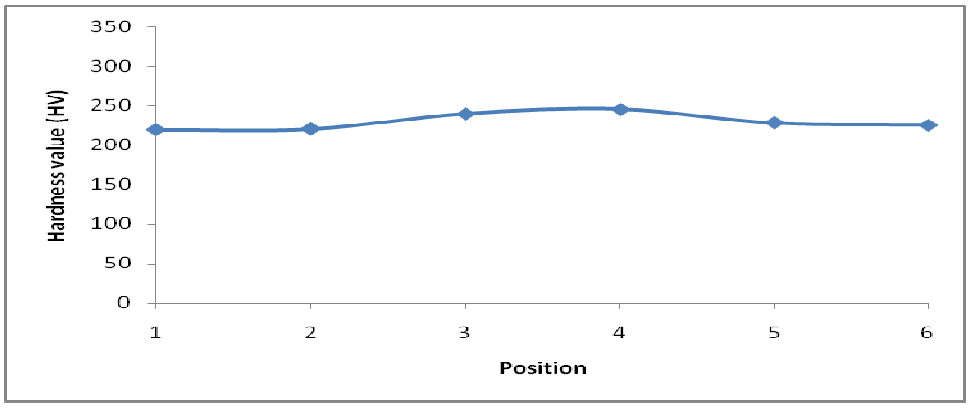

Figure 4.162 Hardness graph for Sample No. S20B: 409Ferritic stainless steel as per RSM design of experiment

4.2.4 RESULTS OF MICROSTRUCTURAL STUDY OF 409 FERRITIC STAINLESS STEEL AS PER RSM DESIGN OF EXPERIMENT

Study of microstructures has been made for all the welded samples and the photographic views are taken in weld and HAZ regions, for each of the samples by the Leica DM LM metallurgical microscope. Base metal microstructure has also been included and discussed. Microstructural views are shown in figures 4.163 – 4.183.and discussed.

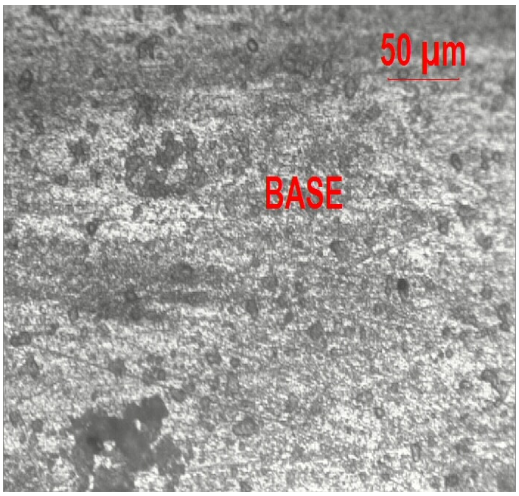

Figure 4.163 Metallographic view of Sample No. Base Metal 409 Ferritic stainless steel (x200)

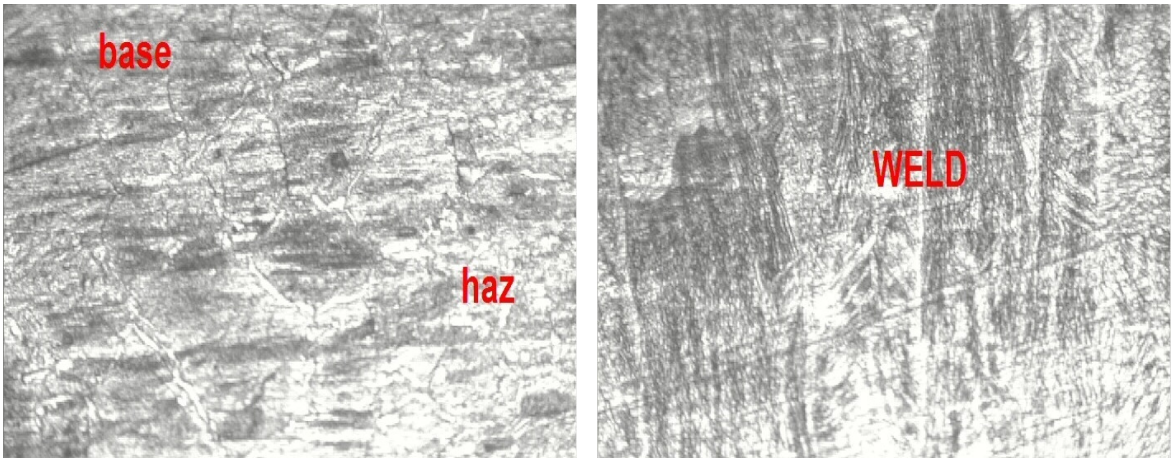

a) Base+ HAZ b) Weld

Figure 4.164 Metallographic view of Sample No. S1B (x200)

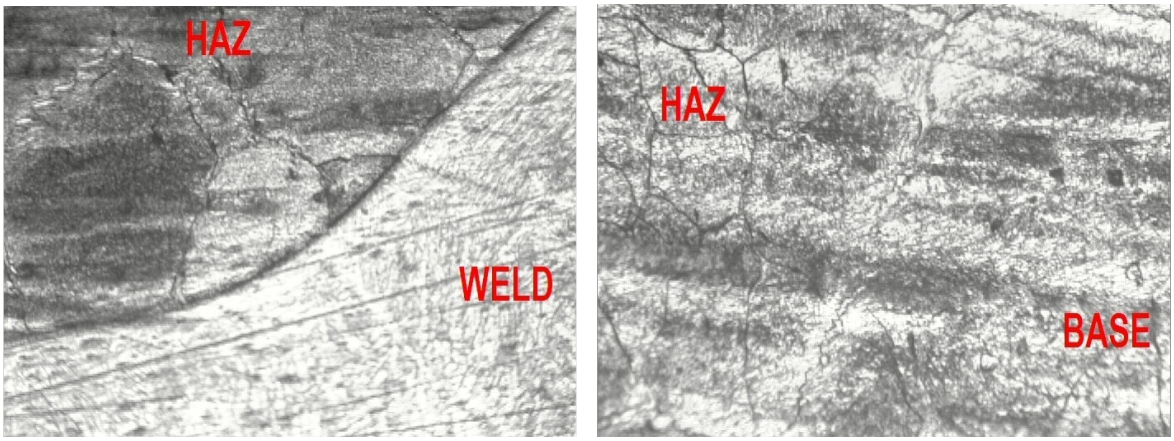

a) HAZ+Weld b) HAZ+Base

Figure 4.165 Metallographic view of Sample No. S2B (x200)

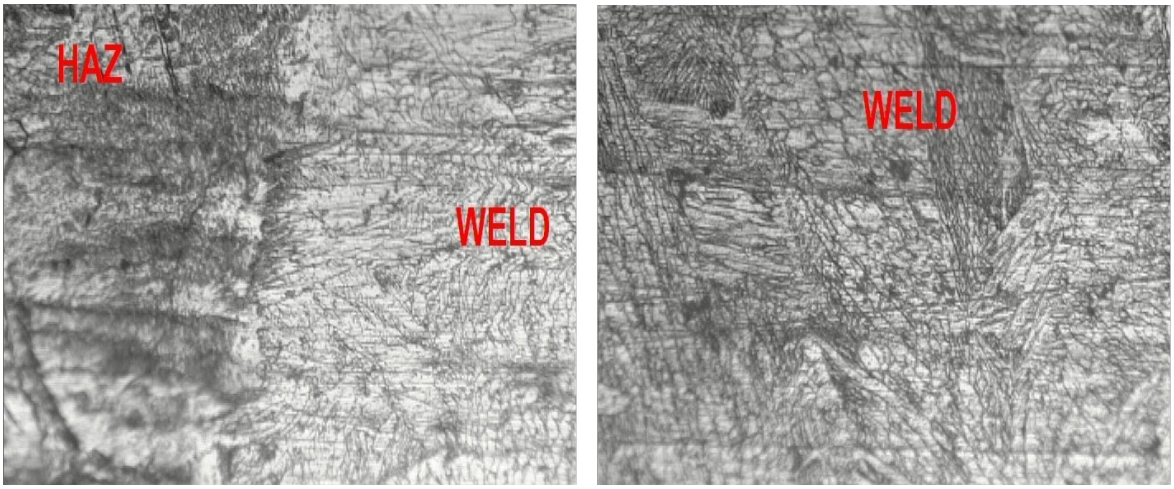

a) HAZ+Weld b) Weld

Figure 4.166 Metallographic view of Sample No. S3B (x200)

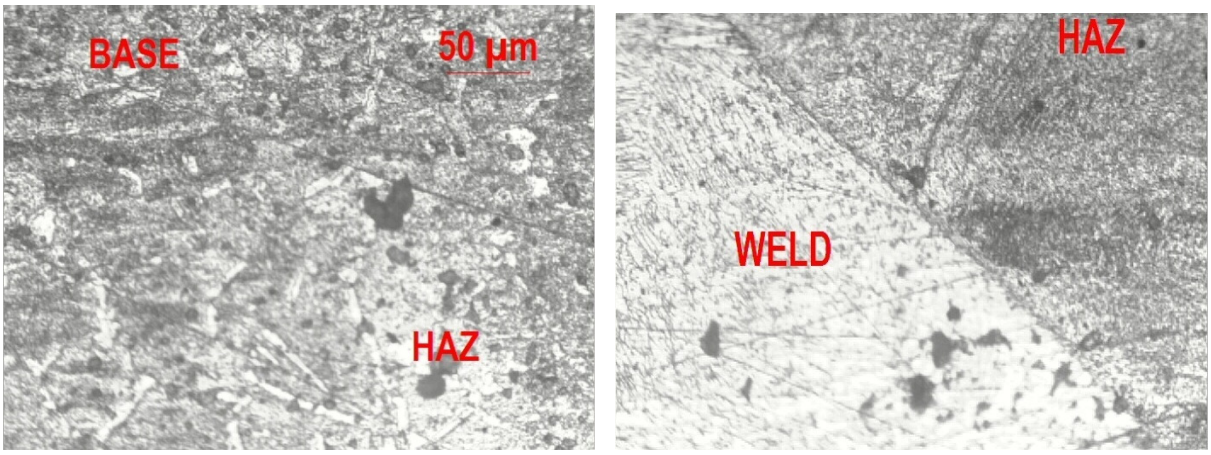

a) Base+ HAZ b) Weld

Figure 4.167 Metallographic view of Sample No. S4B (x200)

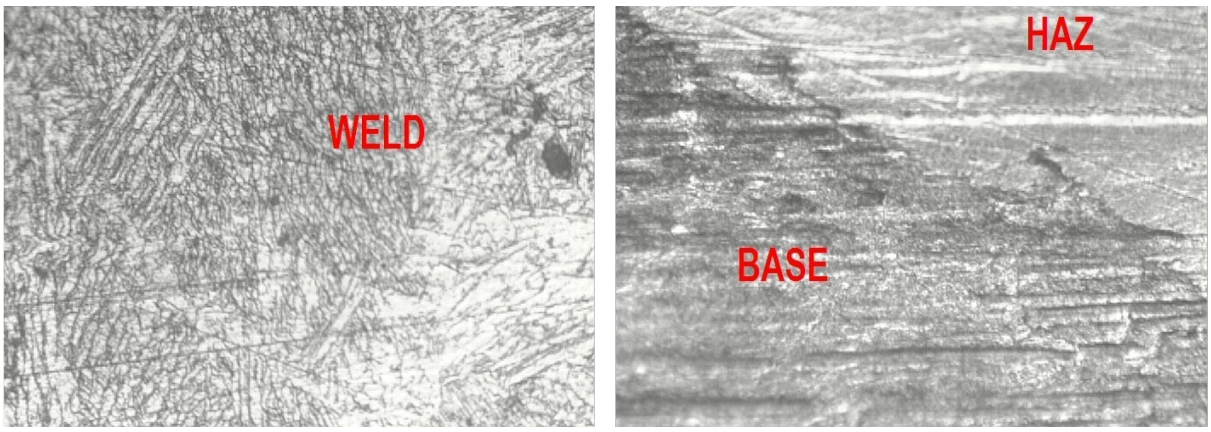

a)Weld b) Base + HAZ

Figure 4.168 Metallographic view of Sample No. S5B(x200)

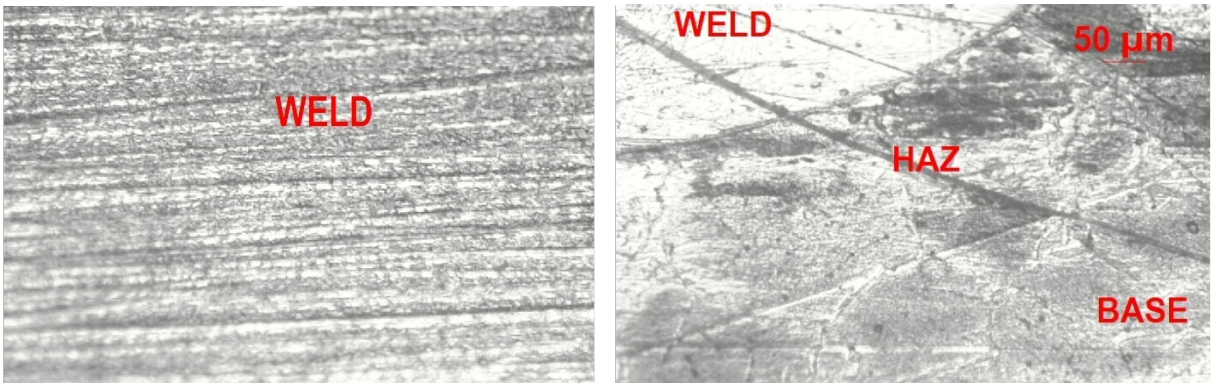

a) Weld b) Weld+HAZ+Base

Figure 4.169 Metallographic view of Sample No. S6B (x200)

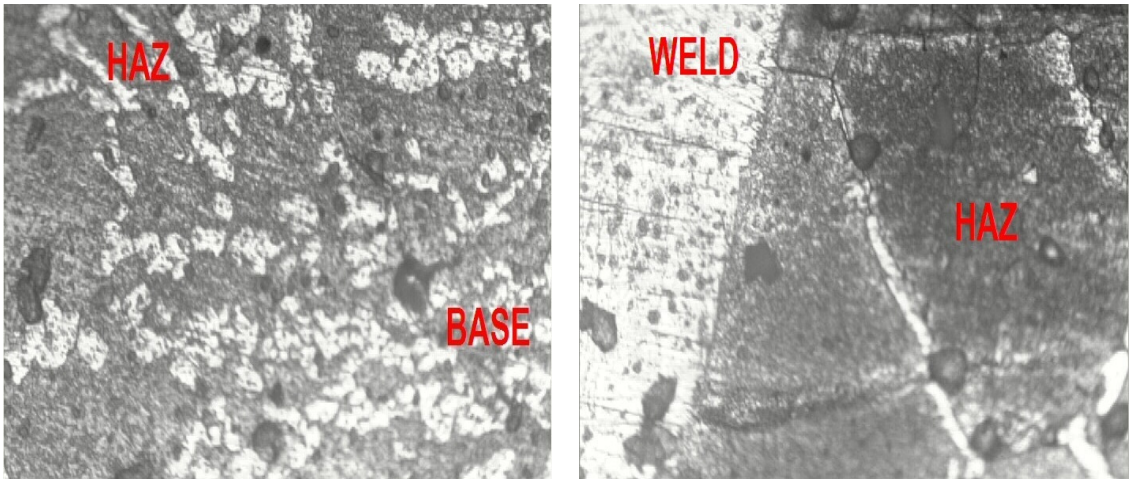

a) Base+ HAZ b) Weld+HAZ

Figure 4.170 Metallographic view of Sample No. S7B (x200)

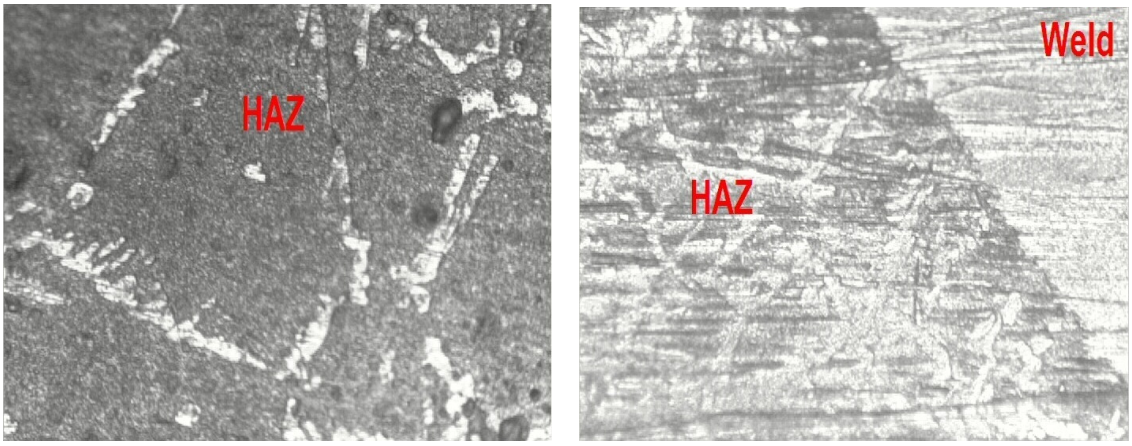

a) HAZ b) HAZ+ Weld

Figure 4.171 Metallographic view of Sample No. S8B (x200)

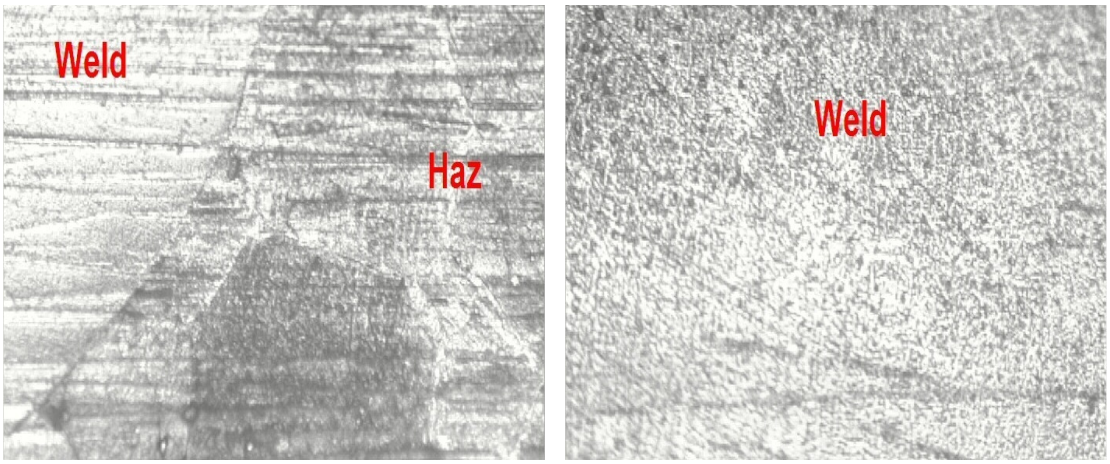

a) Weld+ HAZ b) Weld

Figure 4.172 Metallographic view of Sample No. S9B (x200)

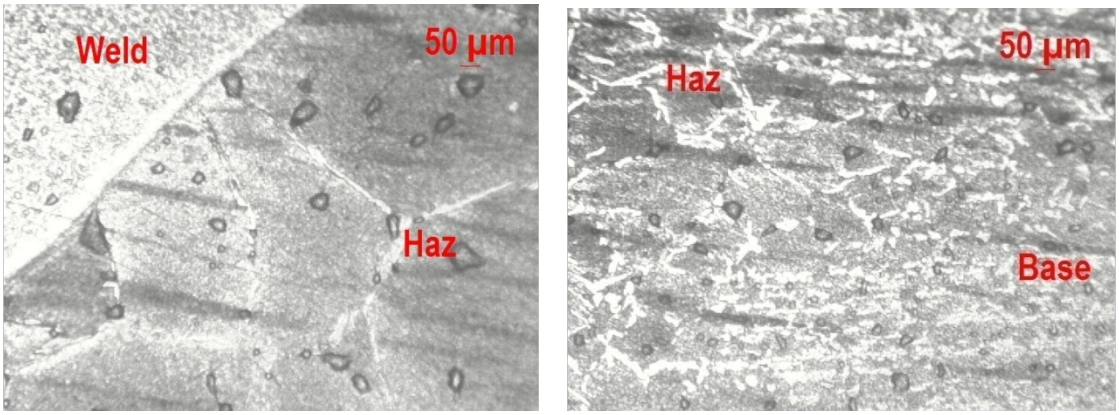

a) Weld + HAZ b) HAZ+ Base

Figure 4.173 Metallographic view of Sample No. S10B (x200)

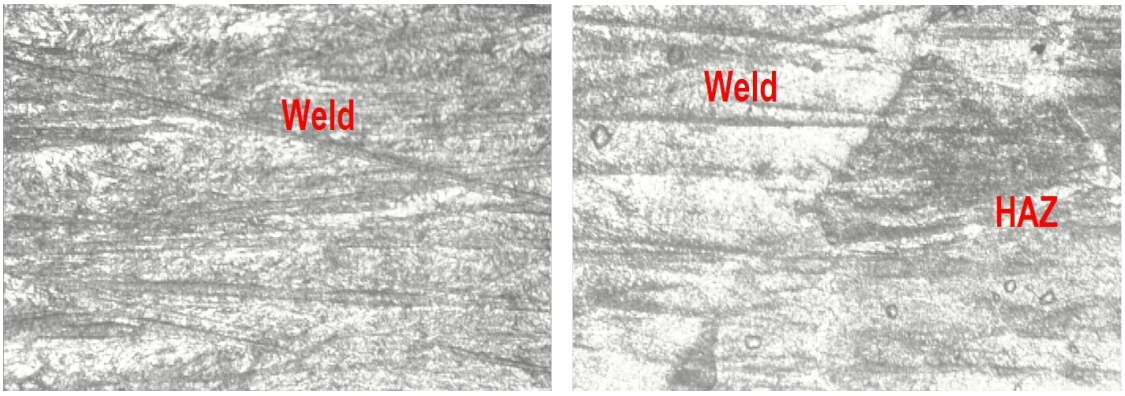

a) Weld b) Weld+HAZ

Figure 4.174 Metallographic view of Sample No. S11B (x200)

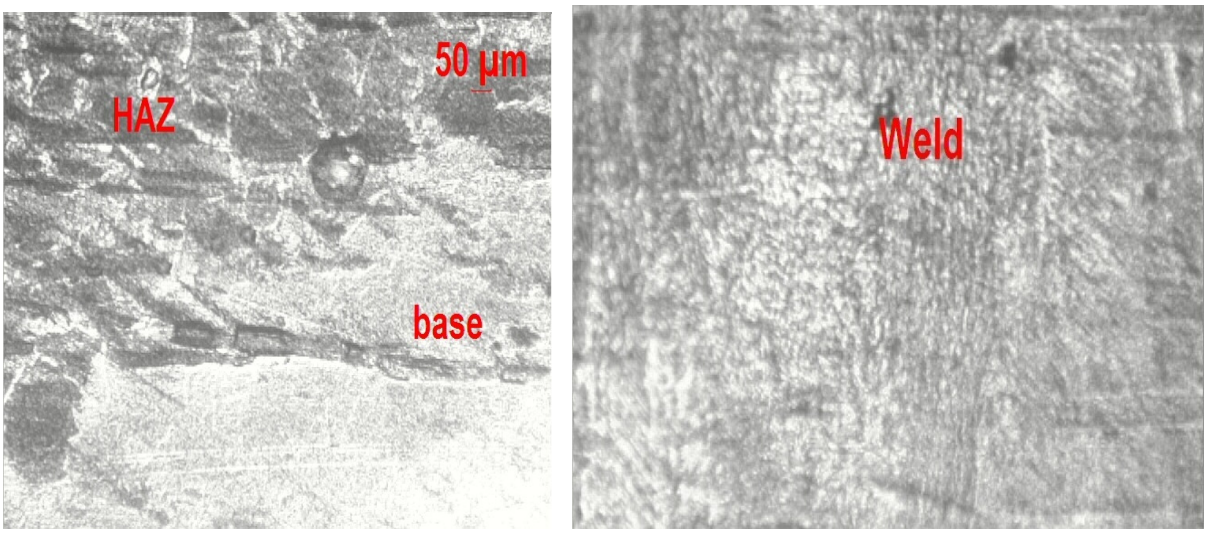

a) Base+ HAZ b) Weld

Figure 4.175 Metallographic view of Sample No. S12B (x200)

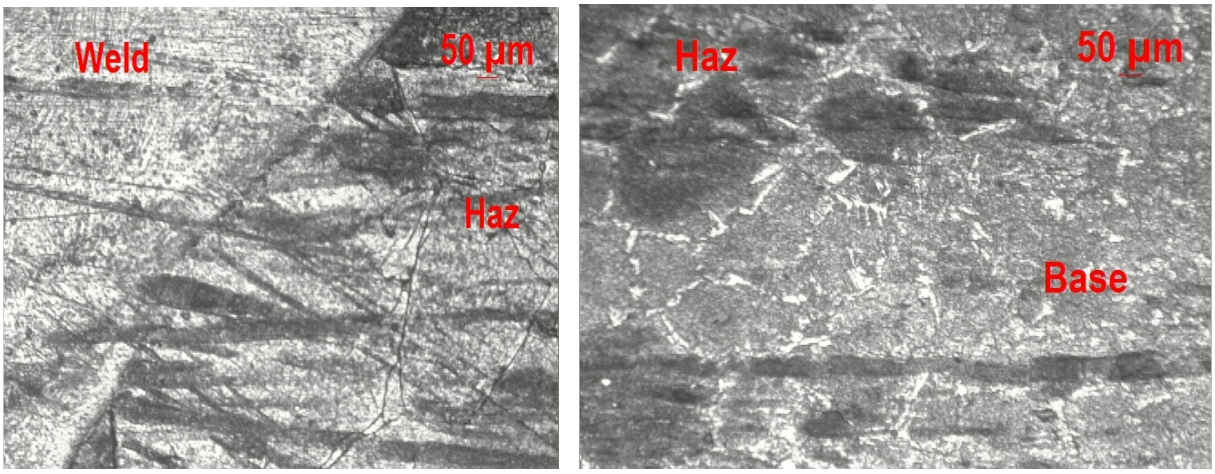

a) Weld + HAZ b) HAZ+Base

Figure 4.176 Metallographic view of Sample No. S13B (x200)

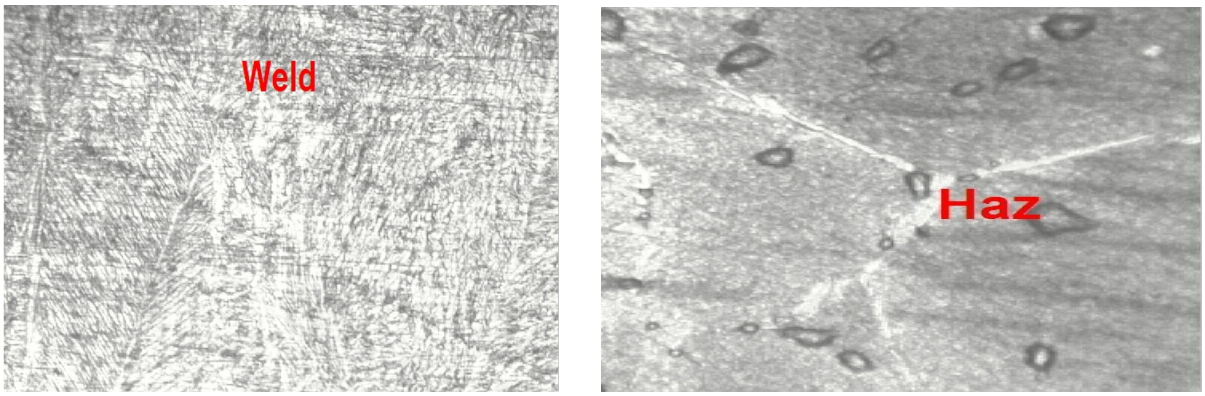

a)Weld b) HAZ

Figure 4.177 Metallographic view of Sample No. S14B (x200)

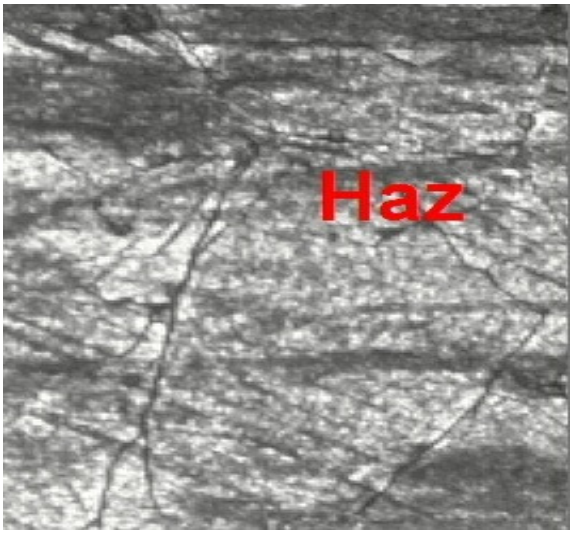

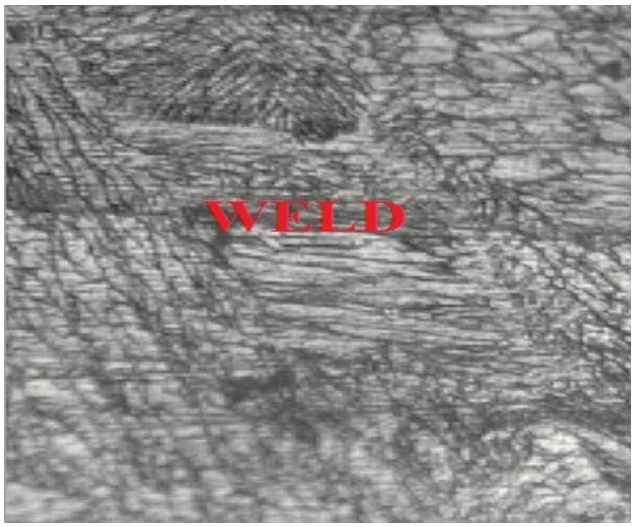

a) Haz b) Weld

Figure 4.178 Metallographic view of Sample No. S15B (x200)

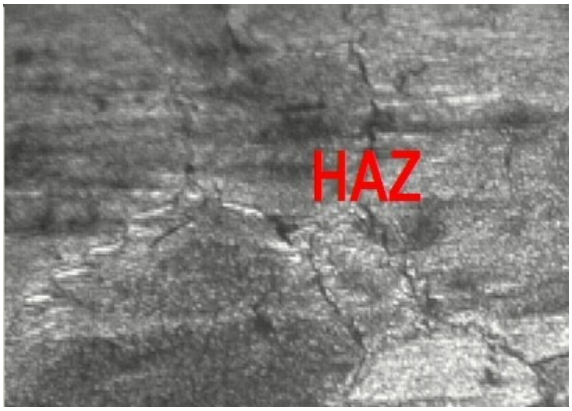

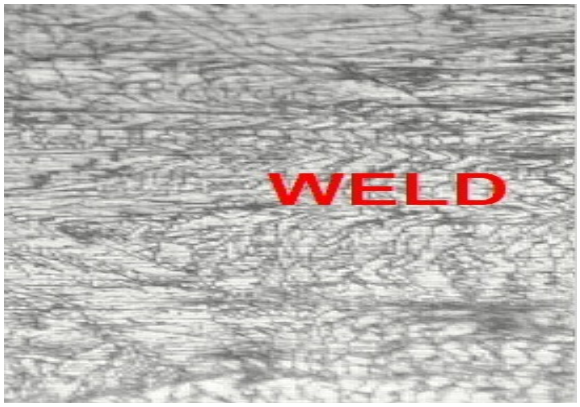

a) Haz b) Weld

Figure 4.179 Metallographic view of Sample No. S16B (x200)

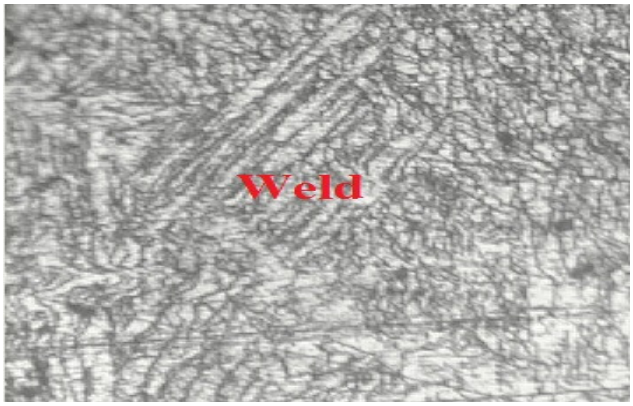

a) Haz b) Weld

Figure 4.180 Metallographic view of Sample No. S17B (x200)

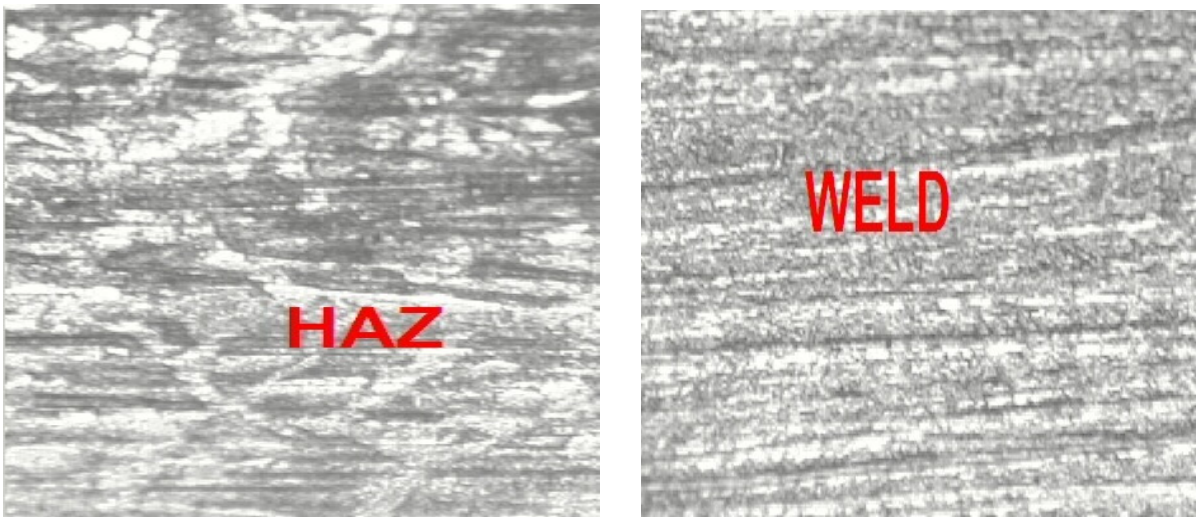

a) Haz b) Weld

Figure 4.181 Metallographic view of Sample No. S18B (x200)

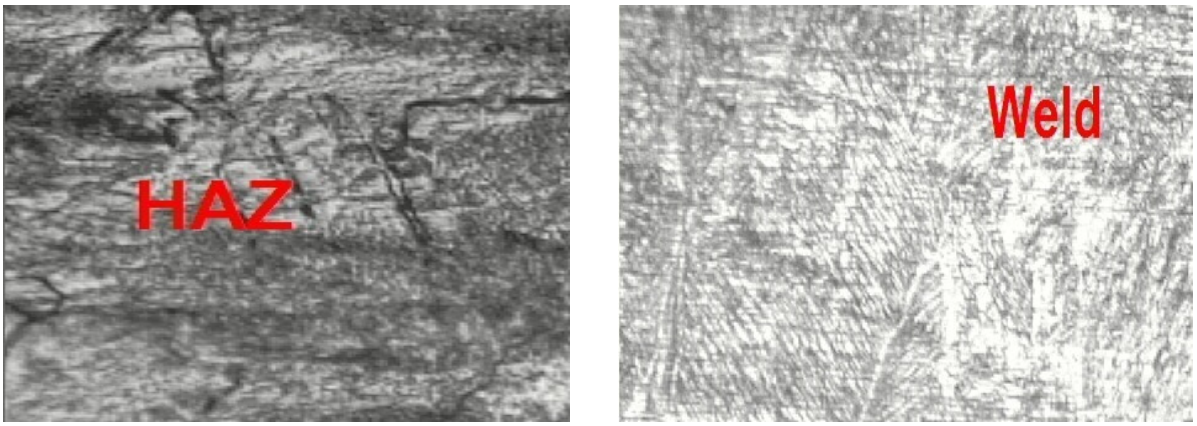

a) Haz b) Weld

Figure 4.182 Metallographic view of Sample No. S19B (x200)

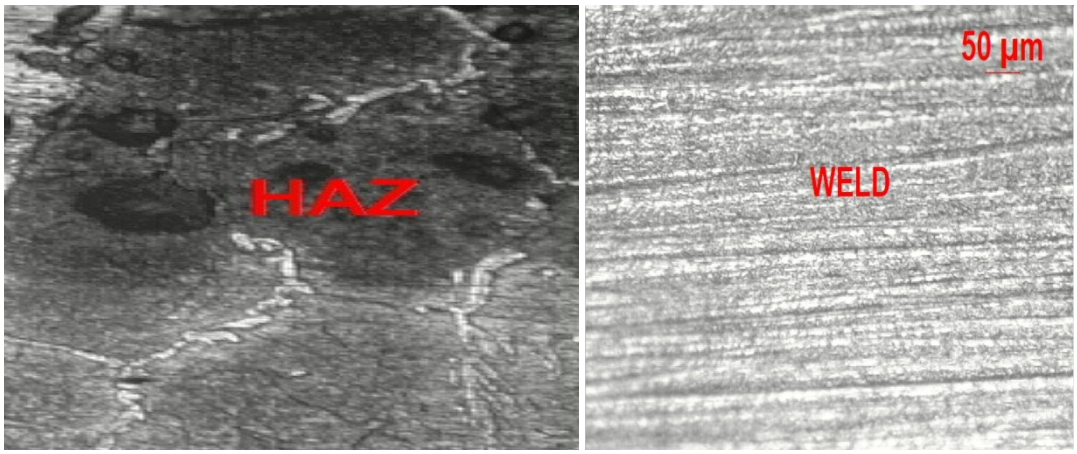

a) Haz b) Weld

Figure 4.183 Metallographic view of Sample No. S20B(x200)

In so far as the microstructure of base metal is concerned, ferrite matrix in longitudinal direction containing elongated layer of martensite is observed. One representative base metal microstructure is shown in figure 4.163. Grain size and morphologies are very different in the fusion and heat affected zones (HAZ) as compared to base metal zone of twenty samples as found from microstructures shown in figure 4.163-4.183. In general, austenitic grains are found to be coarser in HAZ than in base metal. This may be attributed to lower cooling rate in the HAZ region. Figure 4.176a (sample number S13B) shows that in the HAZ region some amount of martensite exists in heat –affected zone (HAZ), In some of the portions, precipitated carbide has been found. Dispersed carbide phases are found in HAZ region of sample number S10B (figure 4.173a). This sample shows lowest UTS in tensile test.

Comparative study of weld metal microstructures of all the samples with respect to either base metal or HAZ microstructures, reveals that weld metal microstructure is looking very much different from HAZ and base metal microstructures. In most of the samples columnar-dendritic grain growths are observed in the weld microstructure, as shown in figure 4.171 (sample no. S8B), and others. Figure 4.170 (sample no. S7B) shows the dendritic grain growth and austenite phase within fusion zone due to use of austenitic stainless steel as filler metal. This sample shows high UTS. Hardness value within weld is found to be more than the hardness value of base metal. This increment in hardness and UTS value can mainly be caused due to the formation of martensite in the fusion zone and in HAZ. The combined effects of the levels of the input parameters have made some change in the microstructures.

Microstructures developed at different regions of the weld beads are dependent on the compositions of base and filler materials, dilution, heating and cooling cycles and many other factors. A little bit of variation found in the microstructures among twenty samples, may be linked with the above factors, particularly with heating and cooling cycles. Varied parametric combinations during welding, influence heat input, heat input rate and cooling cycle. This, in turn, influences microstructures.

4.2.5 RESULTS AND DISCUSSION AS PER L9 TAGUCHI ORTHOGONAL ARRAY DESIGN OF EXPERIMENT: 409 FERRITIC STAINLESS STEEL (2^{ND} PART OF 2ND SET OF EXPERIMENTS)

The results pertaining to L9 Taguchi Orthogonal array are discussed.

4.2.5.1 RESULTS OF VISUAL INSPECTION OF WELDMENT AND DISCUSSION: 409 FERRITIC STAINLESS STEEL AS PER L9 TAGUCHI ORTHOGONAL ARRAY DESIGN OF EXPERIMENT

From the results of visually inspection (Table 4.12), it is found that for certain welding conditions no defect has been observed. These are for the samples no. S1D, S3D, S4D, S5D, S6D, S7D, S8D and S9D. Spatter is found in sample no. S2D.

Table 4.12 Results of visual inspection of 409 Ferritic stainless steel weldment: L9 Taguchi Orthogonal Array Design of Experiment

sample no.	Welding Current (A)	gas flow rate (*l*/min)	Nozzle to plate distance (mm)	Result of Visual Inspection
S1D	100	10	9	No defects
S2D	100	15	12	Spatter
S3D	100	20	15	No defects
S4D	112	10	12	No defects
S5D	112	15	15	No defects
S6D	112	20	9	No defects
S7D	124	10	15	No defects
S8D	124	15	9	No defects
S9D	124	20	12	No defects

4.2.5.2 RESULTS OF X-RAY RADIOGRAPHIC TESTS OF WELDMENT AND DISCUSSION: 409 FERRITIC STAINLESS STEEL AS PER L9 TAGUCHI ORTHOGONAL ARRAY DESIGN OF EXPERIMENT

X- Ray radiographic tests have been conducted for all the 9 samples by XXQ-2005 X-Ray flaw detector. Copies of radiographic film for the samples are shown in figures 4.184-4.192. Results of X-ray Radiographic Test are shown in Table 4.13. Porosity in welding is caused by the presence of gases which get entrapped during the solidification process. The most common causes of porosity are atmospheric contamination, excessively oxidized work piece surface, and the presence of foreign matter. This can also be caused by inadequate shielding gas flow or excessive shielding by gas flow. Most frequently the occurrence of lack of fusion due to an improper welding technology can be attributed to an improper preparation of a weld groove, an incorrect torch inclination, an improper welding position, and possible draught. A second group of causes includes insufficient energy input to the weld area. It has been confirmed that it is highly important to choose optimum welding parameters such as welding current, wire feed rate, and arc length. The welding speed has a major influence on energy input. Welding current has the greatest effect on penetration. Incomplete penetration is usually caused by the use of too low welding current and can be eliminated by simply increasing the ampere. Other causes can be the use of too slow travel speed and an incorrect torch angle. Both will allow the metal to rise in front of the arc acting as a cushion to prevent penetration. Almost same discussion has already been made earlier too.

Table 4.13 Results of X-ray radiographic test of 409 Ferritic stainless steel: L9 Taguchi Orthogonal Array Design of Experiments

Sample No.	Welding Current (A)	Gas flow rate (*l*/min)	Nozzle to plate distance (mm)	Result of X-ray radiographic tests
S1D	100	10	9	No defects
S2D	100	15	12	Lack of fusion, porosity
S3D	100	20	15	Porosity
S4D	112	10	12	No defects
S5D	112	15	15	No defects
S6D	112	20	9	Porosity
S7D	124	10	15	No defects
S8D	124	15	9	No defects
S9D	124	20	12	No defects

Figure 4.184 X-ray radiographic film for Sample No. S1D: 409 Ferritic Stainless Steel as L9 Taguchi orthogonal array design of experiment

Figure 4.185 X-ray radiographic film for Sample No. S2D: 409 Ferritic Stainless Steel as L9 Taguchi orthogonal array design of experiment

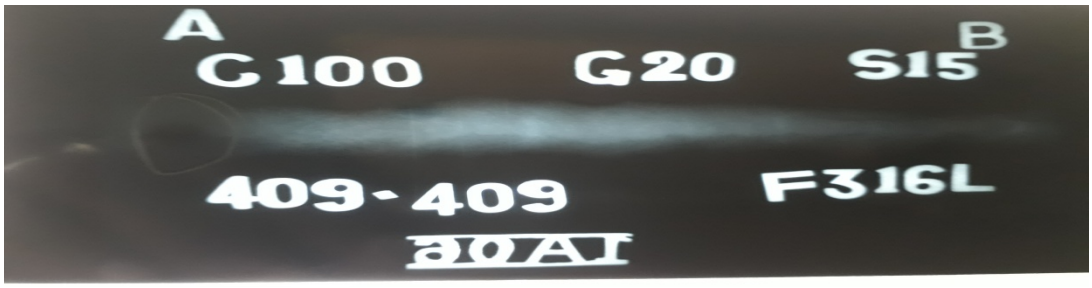

Figure 4.186 X-ray radiographic film for Sample No. S3D: 409 Ferritic Stainless Steel as L9 Taguchi orthogonal array design of experiment

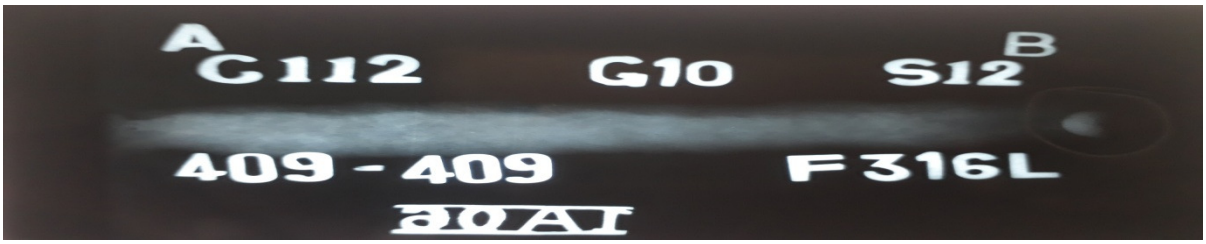

Figure 4.187 X-ray radiographic film for Sample No. S4D: 409 Ferritic Stainless Steel as L9 Taguchi orthogonal array design of experiment

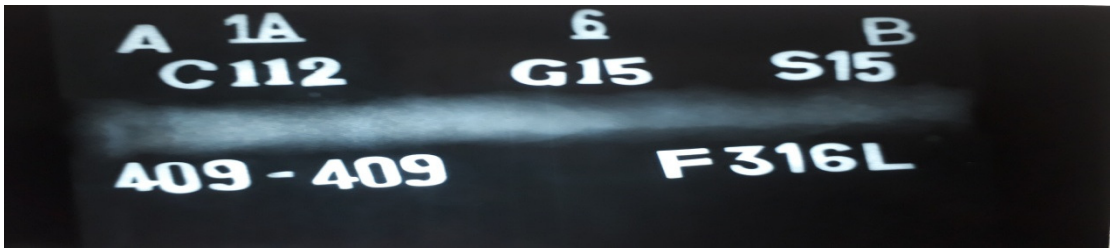

Figure 4.188 X-ray radiographic film for Sample No. S5D: 409 Ferritic Stainless Steel as L9 Taguchi orthogonal array design of experiment

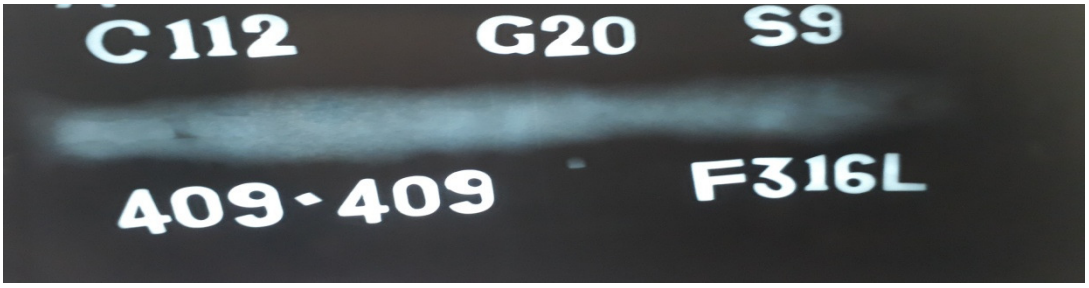

Figure 4.189 X-ray radiographic film for Sample No. S6D: 409 Ferritic Stainless Steel as L9 Taguchi orthogonal array design of experiment

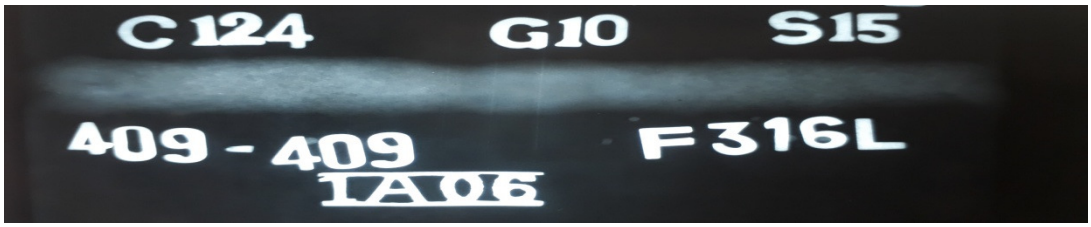

Figure 4.190 X-ray radiographic film for Sample No. S7D: 409 Ferritic Stainless Steel as L9 Taguchi orthogonal array design of experiment

Figure 4.191 X-ray radiographic film for Sample No. S8D: 409 Ferritic Stainless Steel as L9 Taguchi orthogonal array design of experiment

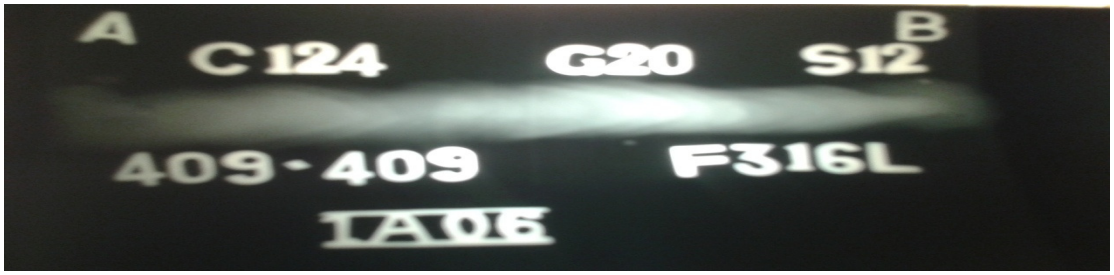

Figure 4.192 X-ray radiographic film for Sample No. S9D: 409 Ferritic Stainless Steel as L9 Taguchi orthogonal array design of experiment

4.2.5.3 RESULTS OF TENSILE TESTS OF WELDMENT AND DISCUSSION: 409 FERRITIC STAINLESS STEEL AS PER L9 TAGUCHI ORTHOGONAL ARRAY DESIGN OF EXPERIMENT

The tensile test specimens are prepared for the samples corresponding to L9 Taguchi Orthogonal Array Design of Experiment. Results of Tensile tests obtained as per L9 Taguchi Orthogonal Array Design of Experiment are shown in Table 4.14. The corresponding plots are shown in figures 4.193- 4.201. The tensile test diagrams are presented in the figures 4.193 – 4.201. Ductile behavior is observed. The discussion done earlier in this respect at section 4.2.2 is also pertinent here. So repetition is not done.

Table 4.14 Tensile test results of 409 Ferritic stainless steel: L9 Taguchi Orthogonal Array Design of experiment

Sample No.	Yield strength (Mpa)	Ultimate strength (Mpa)	Percentage of elongation (%)
S1D	296.5	431.6	25.5
S2D	255.1	376.5	15.1
S3D	256.0	377.3	18.5
S4D	289.8	416.6	17.6
S5D	237.0	368.3	24.5
S6D	288.0	424.0	17.0
S7D	296.5	431.6	25.5
S8D	286.5	423.5	18.0
S9D	321.9	453.6	23.4

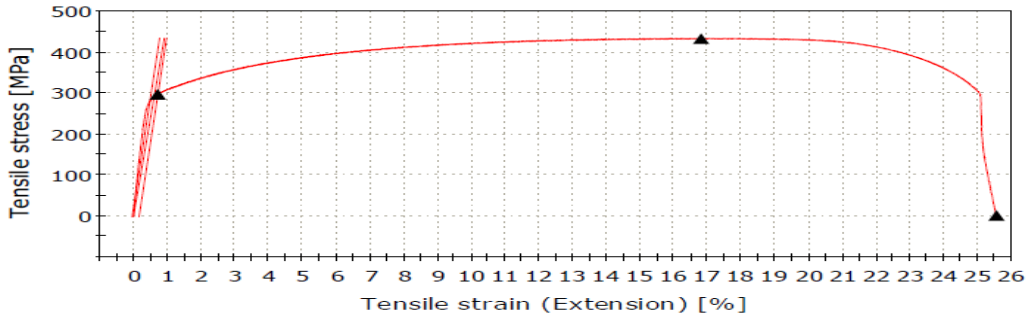

Figure 4.193 Tensile Test Diagram of Sample no. S1D: 409 Ferritic stainless steel as per L9 Taguchi orthogonal array design of experiment

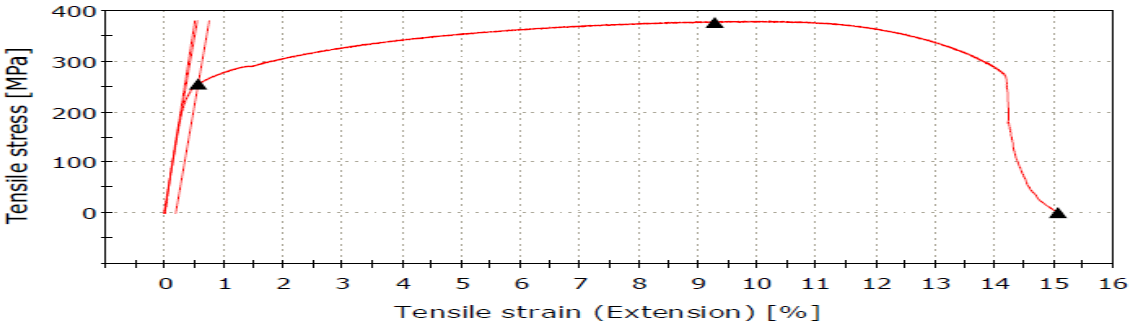

Figure 4.194 Tensile Test Diagram of Sample no. S2D: 409 Ferritic stainless steel as per L9 Taguchi orthogonal array design of experiment

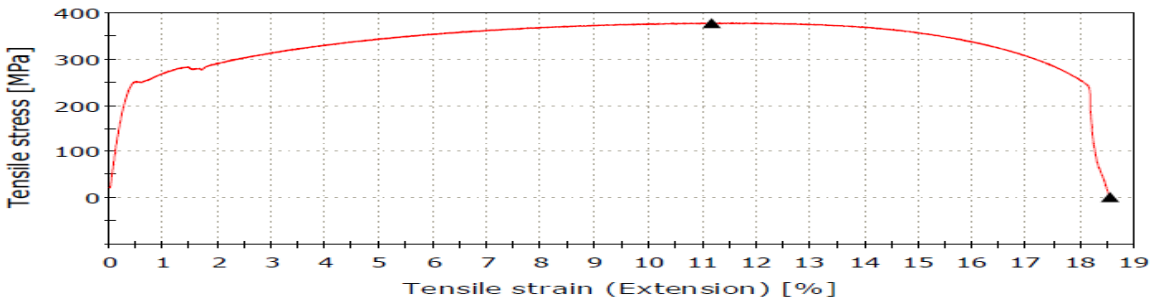

Figure 4.195 Tensile Test Diagram of Sample no. S3D: 409 Ferritic stainless teel as per L9 Taguchi orthogonal array design of experiment

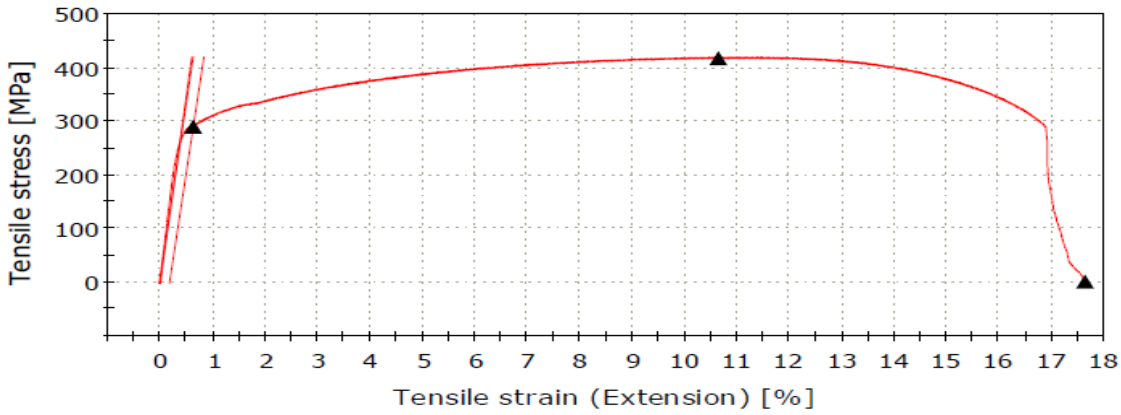

Figure 4.196 Tensile Test Diagram of Sample no. S4D: 409 Ferritic stainless steel as per L9 Taguchi orthogonal array design of experiment

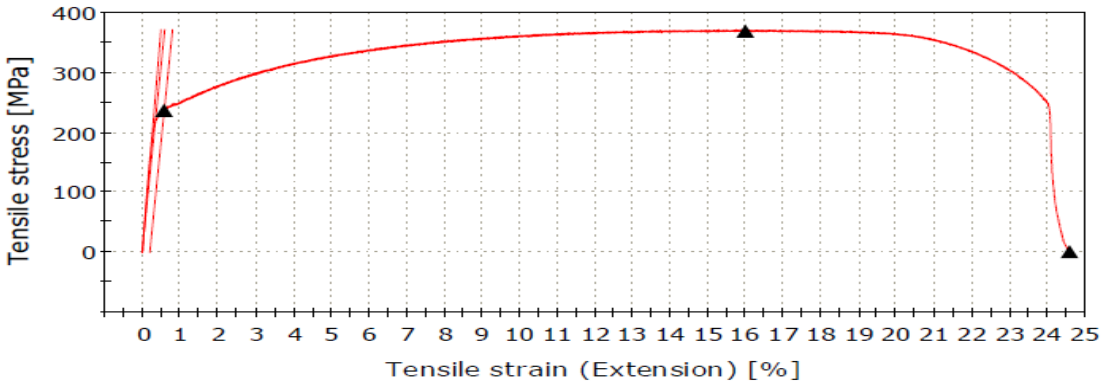

Figure 4.197 Tensile Test Diagram of Sample no. S5D: 409 Ferritic stainless steel as per L9 Taguchi orthogonal array design of experiment

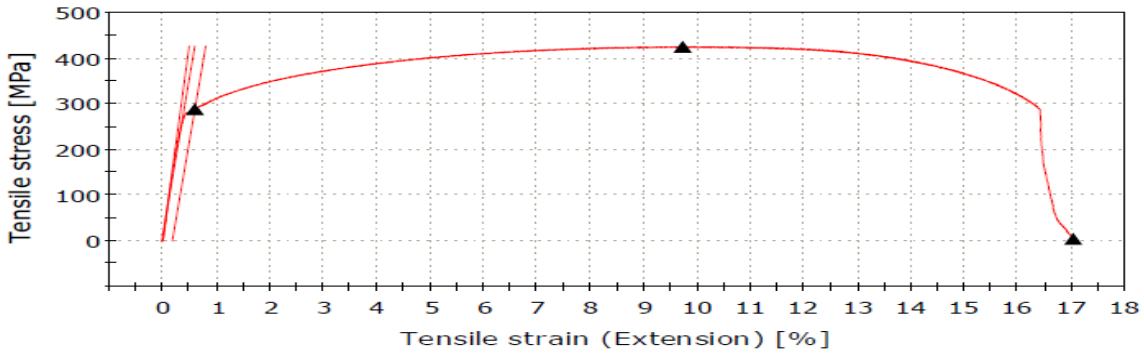

Figure 4.198 Tensile Test Diagram of Sample no. S6D:409 Ferritic stainless steel as per L9 Taguchi orthogonal array design of experiment

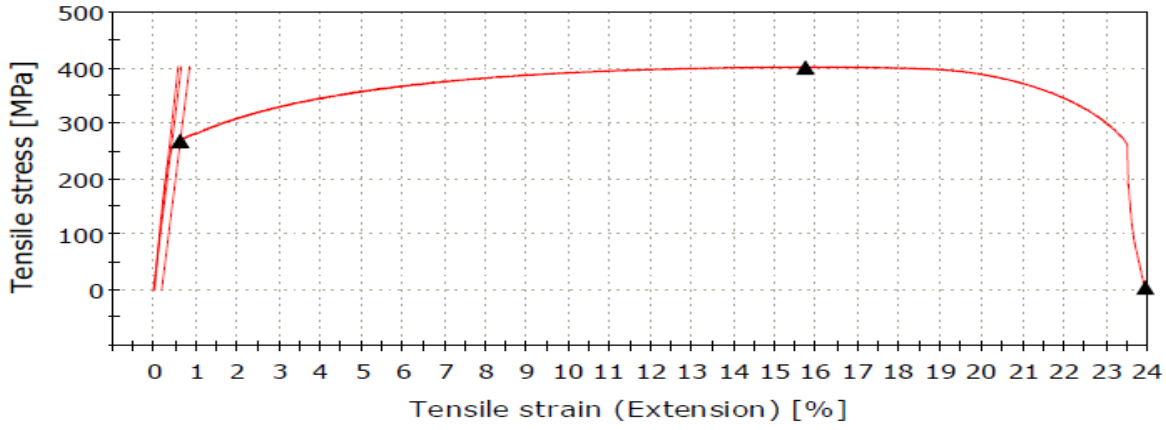

Figure 4.199 Tensile Test Diagram of Sample no. S7D: 409 Ferritic stainless steel as per L9 Taguchi orthogonal array design of experiment

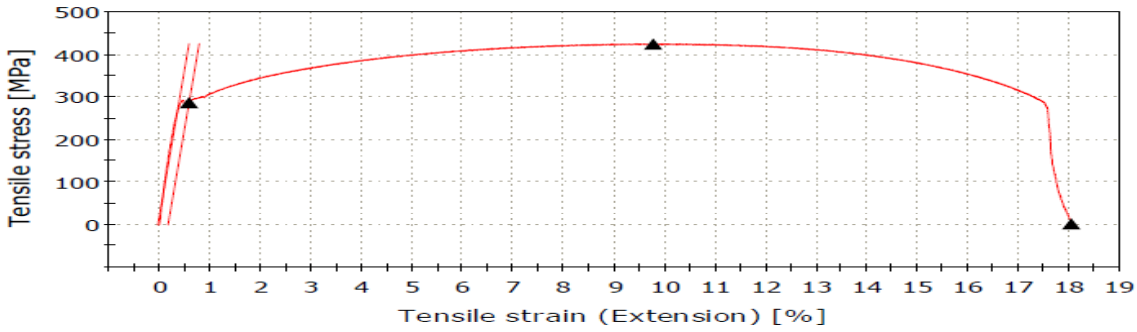

Figure 4.200 Tensile Test Diagram of Sample no. S8D: 409 Ferritic stainless steel as per L9 Taguchi orthogonal array design of experiment

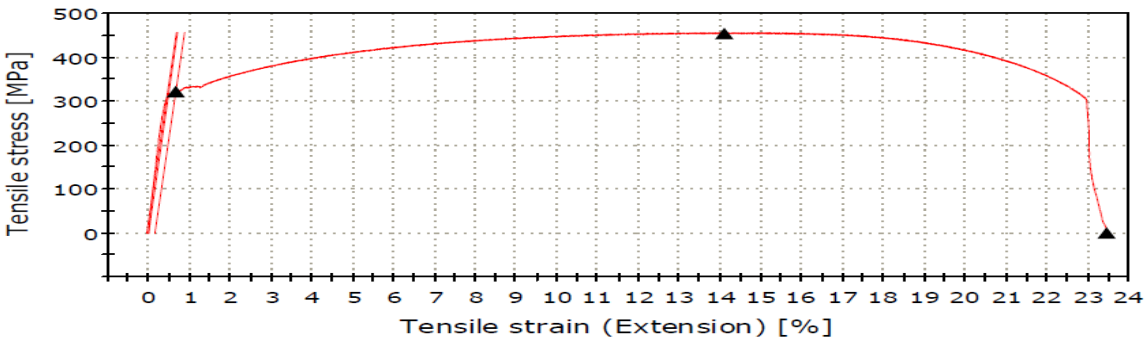

Figure 4.201 Tensile Test Diagram of Sample no. S9D: 409 Ferritic stainless steel as per L9 Taguchi orthogonal array design of experiment

4.3 RESULTS OF DISSIMILAR MIG WELDING: 316L AUSTENITIC STAINLESS STEEL TO 409 FERRITIC STAINLESS STEEL (3RD SET OF EXPERIMENTS)

In the third set of experiments dissimilar welding of 316L Austenitic to 409 Ferritic stainless steel has been carried out as per Taguchi design of experiments.

4.3.1 RESULTS OF VISUAL INSPECTION AND X-RAY RADIOGRAPHIC TEST AND DISCUSSION: 316L AUSTENITIC STAINLESS STEEL TO 409 FERRITIC STAINLESS STEEL AS PER L9 TAGUCHI ORTHOGONAL ARRAY DESIGN OF EXPERIMENT

For visual inspection, the weld surface is observed with the naked eye, in order to detect the surface defects of the weldment. X- Ray radiographic tests have also been conducted. Results of visual inspection and X-ray radiographic test are shown in Table 4.15 and Table 4.16 respectively

Table 4.15 Results of visual inspection: 316L Austenitic stainless steel to 409 Ferritic stainless steel as per L9 Taguchi orthogonal array design of experiment

Sample No.	**Welding Current (A)**	**Gas flow rate (*l*/min)**	**Nozzle to plate distance (mm)**	**Result of visual inspection**
S1C	100	10	9	No defects
S2C	100	15	12	Blow hole, Spatter
S3C	100	20	15	Excessive deposition, Spatter
S4C	112	10	12	No defects
S5C	112	15	15	Spatter
				Uneven penetration
S6C	112	20	9	No defects
S7C	124	10	15	Uneven penetration
				Undercut
S8C	124	15	9	Uneven penetration
S9C	124	20	12	No defect

The defects etc. mentioned in the Table 4.16 are visible in the copies of the X-ray films shown in figures 4.202 – 4.210. Consistency in the findings in Tables 4.15 and 4.16 can be noticed. The individual and combined effects of the levels of Gas flow rate, Welding current and Nozzle to plate distance have been reflected in the samples as defects like lack of penetration, undercut, lack of fusion, uneven deposition and weld depression. Further, the skill of the welder is a significant factor influencing weld quality. Defects may come from any irregularities in the base metal and filler wire also. Any improper welding arrangements can also lead to the significant defects. Improper selection of welding parameters like welding current, gas flow rate and nozzle to plate distance can also create welding defects. Radiographic films for Sample No. S1C, Sample No. S4C, Sample No. S6C and Sample No.S9C are almost defect free. These samples are welded with low current and low nozzle to plate distance.

Table 4.16 X-ray radiographic test results: 316L Austenitic stainless steel to 409 Ferritic stainless steel as per L9 Taguchi Orthogonal array design of experiment

Sample no.	Welding Current (A)	Gas flow rate (*l*/min)	Nozzle to plate distance (mm)	Result of X-ray radiographic tests
S1C	100	10	9	No defects
S2C	100	15	12	Porosity
S3C	100	20	15	Lack of fusion
S4C	112	10	12	No defects
S5C	112	15	15	Porosity
S6C	112	20	9	No defects
S7C	124	10	15	Porosity
S8C	124	15	9	Lack of fusion
S9C	124	20	12	No defect

Undercut is possibly caused by improper joint geometry for some of the samples. The combined effects of welding parameters may create undercut. Table 4.15 indicates that undercut has been found in sample no. S7C. Undercut occurred in sample no. S7C is mainly due to use of current higher than that is desired, high nozzle to plate distance and low gas flow rate. Lack of fusion at root or wall has occurred possibly due to improper setting of the current, improper cleaning, faster arc travel speed, presence of oxides, scale and other impurities which do not permit the deposited metal to fuse properly with the base metal. Too low heat input does not ensure proper melting of the weld deposit. With too high heat input, the weld pool becomes too large and starts to flow away in the area in front of the arc which prevents melting of the base metal. Sample No. S3C may have suffered from lack of fusion due to lower heat input and high nozzle to plate distance. Lack of penetration is a major problem affecting the strength of the weld. This may come from lower heat input; faster travel speed, improper selection of currents etc. Porosity has been found in sample nos. S2C, S5C, and S7Cwhich may have resulted from gas being entrapped in the solidifying metal. Blow holes have been observed in sample no. S2C; larger arc, faster travel rate, damp filler rod, unclean job surface etc. may be the possible reasons. Faster gas flow rate is a cause of porosity. All the samples showing porosity is found to be welded with high gas flow rate and large nozzle to plate distance. Some of these sources of the defects have, however, been pointed out in earlier sections.

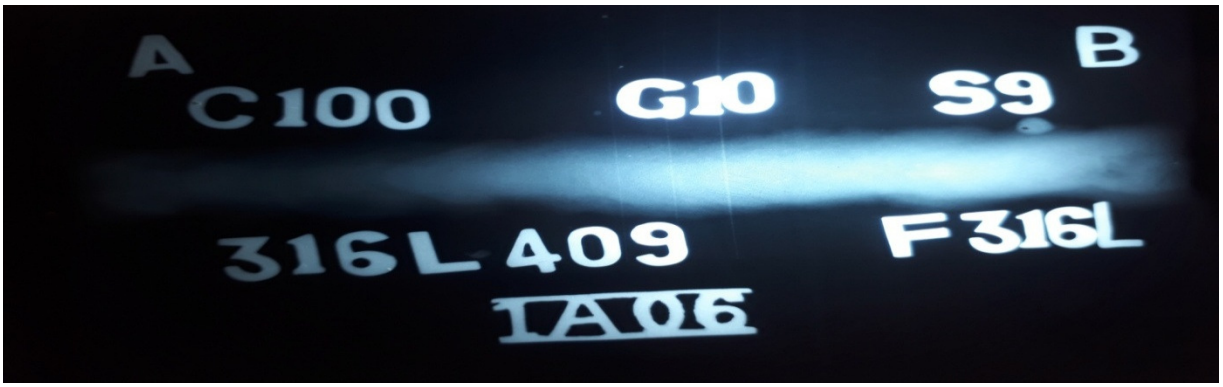

Figure 4.202 X-ray radiographic film for Sample No S1C: 316L Austenitic to 409 Ferritic stainless steel as per L9 Taguchi orthogonal array design of experiment

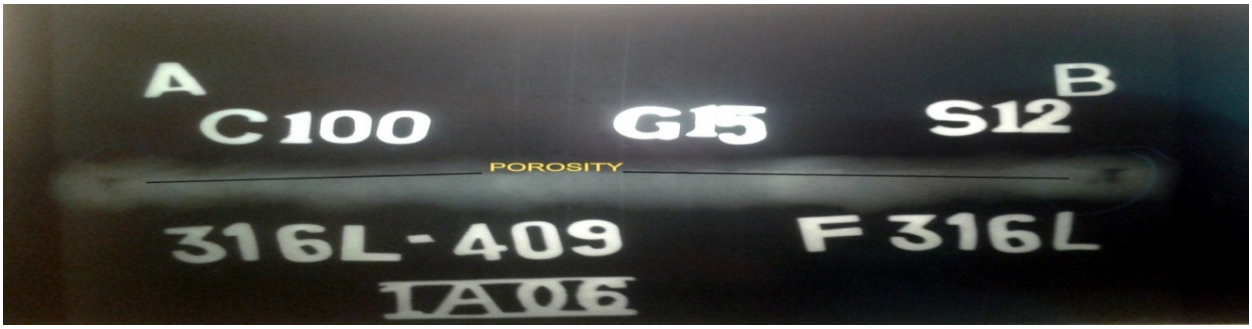

Figure 4.203 X-ray radiographic film for Sample No. S2C: 316L Austenitic to 409 Ferritic stainless steel as per L9 Taguchi orthogonal array design of experiment

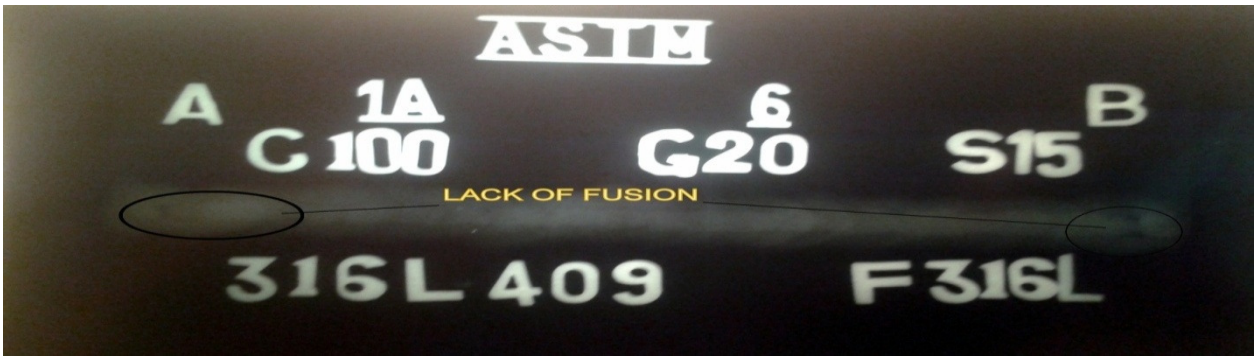

Figure 4.204 X-ray radiographic film for Sample No. S3C: 316L Austenitic to 409 Ferritic stainless steel as per L9 Taguchi orthogonal array design of experiment

Figure 4.205 X-ray radiographic film for Sample No. S4C: 316L Austenitic to 409 Ferritic stainless steel as per L9 Taguchi orthogonal array design of experiment

Figure 4.206 X-ray radiographic film for Sample No. S5C: 316L Austenitic to 409 Ferritic stainless steel as per L9 Taguchi orthogonal array design of experiment

Figure 4.207 X-ray radiographic film for Sample No. S6C: 316L Austenitic to 409 Ferritic stainless steel as per L9 Taguchi orthogonal array design of experiment

Figure 4.208 X-ray radiographic film for Sample No. S7C: 316L Austenitic to 409 Ferritic stainless steel as per L9 Taguchi orthogonal array design of experiment

Figure 4.209 X-ray radiographic film for Sample No.S8C: 316L Austenitic to 409 Ferritic stainless steel as per L9 Taguchi orthogonal array design of experiment

Figure 4.210 X-ray radiographic film for Sample No. S9C: 316L Austenitic to 409 Ferritic Stainless Steel as per L9 Taguchi orthogonal array design of experiment

4.3.2 TENSILE TEST RESULTS AND DISCUSSION: 316LAUSTENITIC TO 409 FERRITIC STAINLESS STEEL AS PER L9 TAGUCHI ORTHOGONAL ARRAY DESIGN OF EXPERIMENT

The tensile test specimens, prepared corresponding to L_9 Taguchi Orthogonal Array design of experiments, have been tested for tensile strength and the results obtained are given in Table 4.17**.** The stress-strain behavior of each sample is shown through graphical plot (figures 4.211 - 4.219) and ductile nature is observed.

Table 4.17 Tensile test results: 316L Austenitic to 409 Ferritic stainless steel as per L9 Taguchi orthogonal array design of experiment

Sample no.	Yield strength (MPa)	Ultimate strength (MPa)	Percentage of elongation (%)
S1C	283.0	412.3	18.8
S2C	247.5	369.9	21.5 (contd.)

S3C	335.9	468.7	22.1 (contd. from previous page)
S4C	257.8	385.4	19.4
S5C	257.4	389.6	18.3
S6C	294.1	429.1	18.5
S7C	286.5	414.2	15.9
S8C	233.4	366.7	17.5
S9C	304.0	430.6	20.5

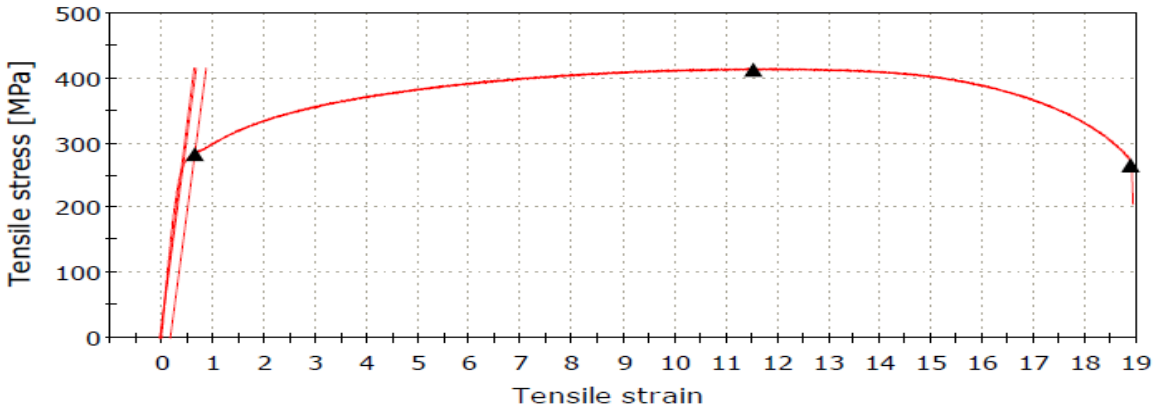

Figure 4.211 Tensile Test Diagram of Sample No. S1C: 316L Austenitic to 409 Ferritic stainless steel as per L9 Taguchi orthogonal array design of experiment

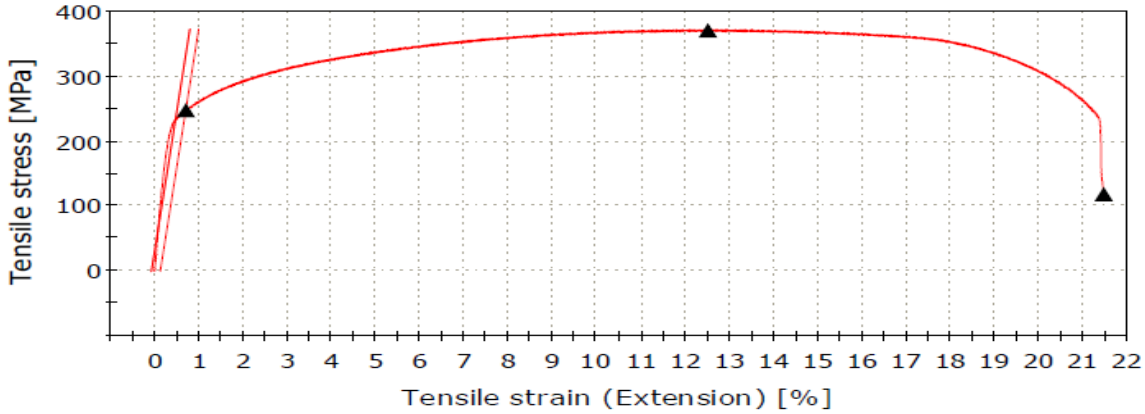

Figure 4.212 Tensile Test Diagram of Sample No. S2C: 316L Austenitic to 409 Ferritic stainless steel as per L9 Taguchi orthogonal array design of experiment

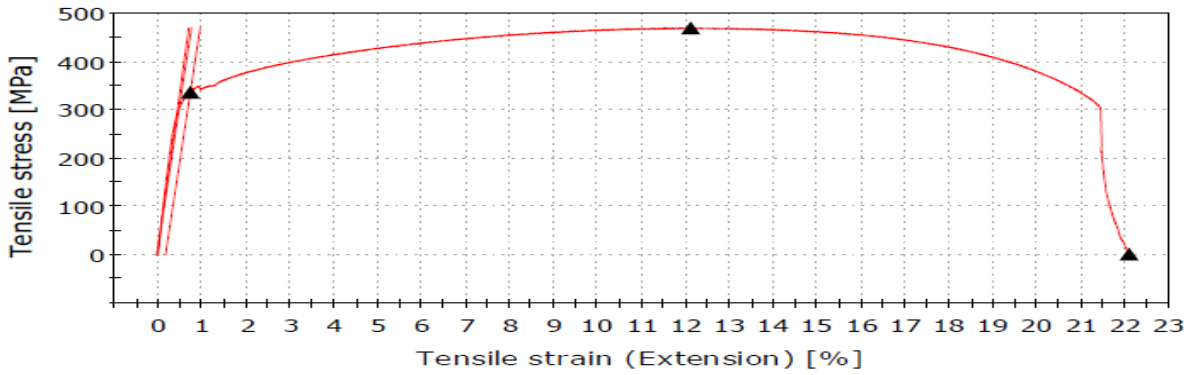

Figure 4.213 Tensile Test Diagram of Sample No. S3C: 316L Austenitic to 409 Ferritic Stainless Steel as per L9 Taguchi orthogonal array design of experiment

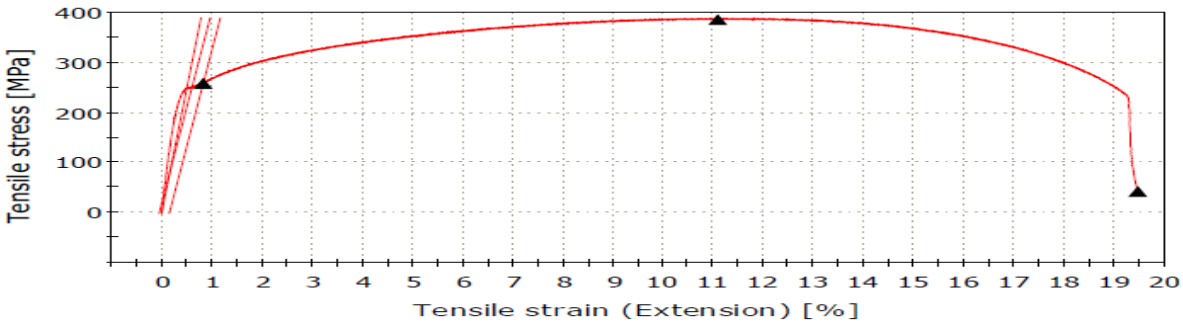

Figure 4.214 Tensile Test Diagram of Sample No. S4C: 316L Austenitic to 409 Ferritic stainless steel as per L9 Taguchi orthogonal array design of experiment

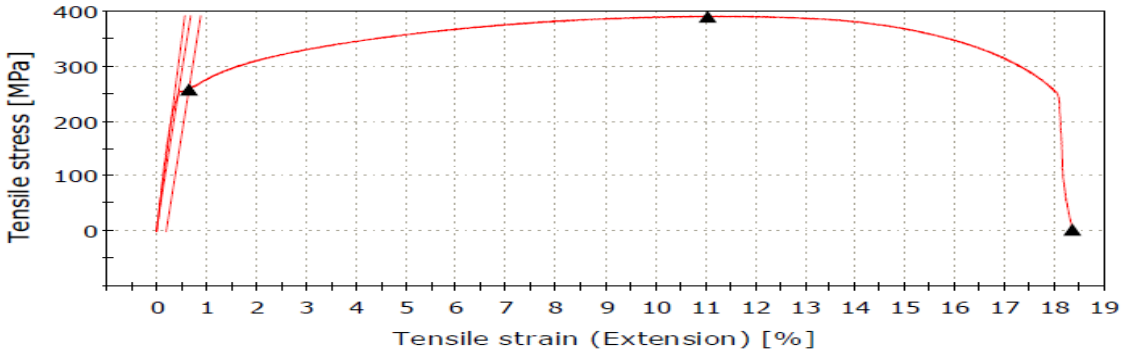

Figure 4.215 Tensile Test Diagram of Sample No. S5C: 316L Austenitic to 409 Ferritic stainless steel as per L9 Taguchi orthogonal array design of experiment

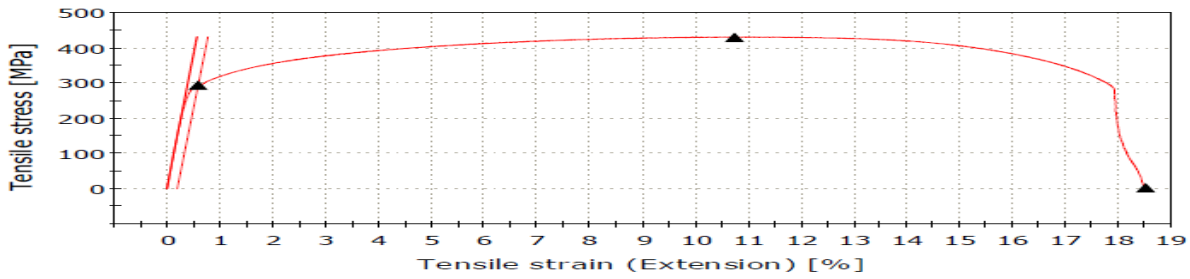

Figure 4.216 Tensile Test Diagram of Sample No. S6C:316L Austenitic to 409 Ferritic stainless steel as per L9 Taguchi orthogonal array design of experiment

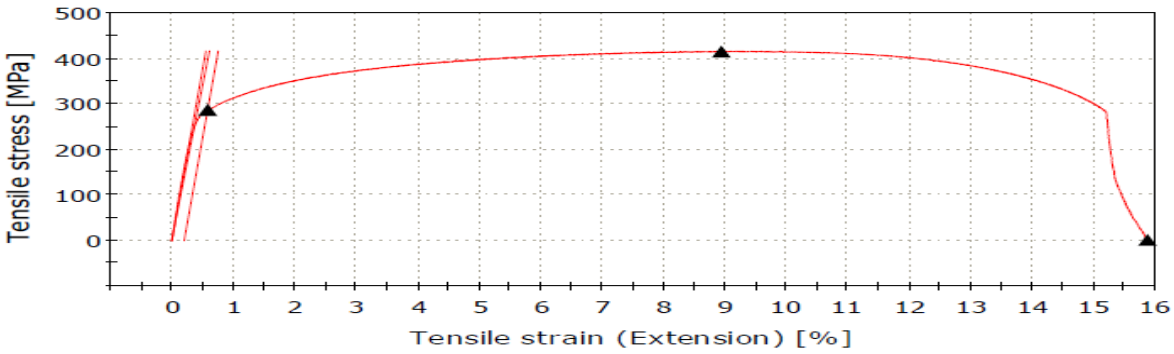

Figure 4.217 Tensile Test Diagram of Sample No. S7C: 316L Austenitic to 409 Ferritic stainless steel as per L9 Taguchi orthogonal array design of experiment

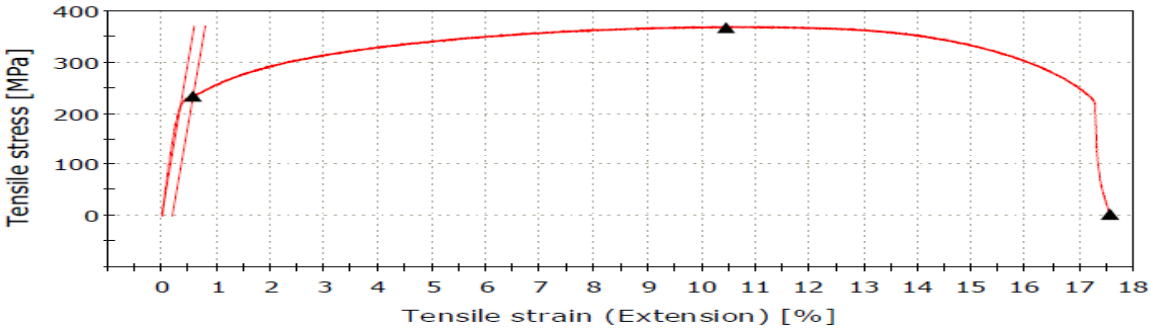

Figure 4.218 Tensile Test Diagram of Sample No. S8C: 316L Austenitic to 409 Ferritic stainless steel as per L9 Taguchi orthogonal array design of experiment

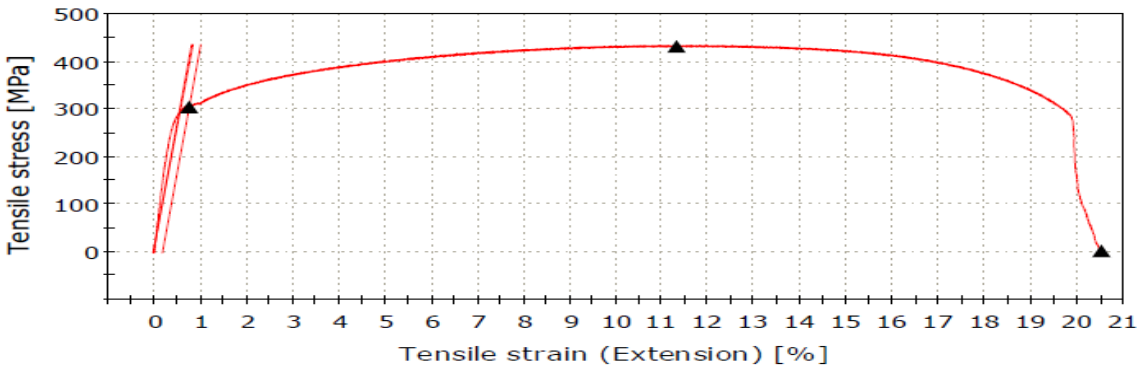

Figure 4.219 Tensile Test Diagram of Sample No. S9C: 316L Austenitic to 409 Ferritic stainless steel as per L9 Taguchi orthogonal array design of experiment

From Table 4.17 it is found that under some parametric conditions of Welding current, Gas flow rate and Nozzle to plate distance, ultimate tensile strength values are remarkably good. For sample no. S3C, ultimate tensile strength is maximum and for the sample no. S8C, ultimate tensile strength is minimum. The maximum (sample no. S3C) and minimum (sample no. S8C) values of UTS are 468.7MPa and 366.7MPa respectively. The highest value of percentage elongation is observed to be 22.1% (for sample no. S3C). The lowest value of percentage elongation is exhibited in the sample no. S7C (15.9 %). In so far yield strength is concerned, the results given in Table 4.17 are found to be satisfactory. Maximum yield strength (335.9MPa) is observed for sample no. S3C and minimum yield strength (233.4MPa) is found for sample no. S8C. In tensile tests, UTS values are found satisfactory in the sense that these values are in between the UTS of Ferritic stainless steel and the UTS of Austenitic stainless steel.

4.3.3 RESULTS OF MICRO-HARDNESS TEST AND DISCUSSION: 316L AUSTENITIC STAINLESS STEEL TO 409 FERRITIC STAINLESS STEEL AS PER L9 TAGUCHI ORTHOGONAL ARRAY DESIGN OF EXPERIMENT

Like in other cases, for dissimilar welding also, hardness of all the samples has been measured by Leco LM 248AT micro-hardness tester. Six different locations of measurement have already

been shown in figure 4.42. Measurement is taken at 2 points of the base metal, at 2 points of HAZ and at 2 points in the weld area. The results of the micro-hardness test are given in the Table 4.18. Hardness in HAZ is of lower value than in weld in most of the cases. Changes in the hardness value corresponding to the change in locations of the welded samples are shown by using graphs in figures 4.220-4.228. From these figures it is found that for most of the samples, the nature of variation in hardness values along the position 1-2-3-4-5-6 is almost similar.

Table 4.18 The results of the micro-hardness test: 316L Austenitic to 409 Ferritic stainless steel as per L9 Taguchi orthogonal array design of experiment

Sample Nos.	**Hardness (HV) at position**					
	1 (Austenitic steel base zone)	**2 (HAZ zone near Austenitic steel)**	**3 (Weld zone)**	**4 (Weld zone)**	**5 (HAZ Zone near Ferritic steel)**	**6 (Ferritic steel base zone)**
S1C	235.9	226.8	246	248.3	238.4	256.7
S2C	253.7	245.6	259.9	257.3	227.2	243.1
S3C	269.1	231.3	267.7	233.4	229.8	259.9
S4C	249.8	220.5	265.7	257.6	233.8	250.2
S5C	240.8	220.6	265.7	265.8	237.7	253.5
S6C	250	230.5	275.7	244.5	225	247.8
S7C	260.8	229.7	270.7	275.8	253.6	262.8
S8C	236.5	221.6	264.6	247.8	235.5	254.4
S9C	235.8	236.6	245	257.4	230.8	243.2

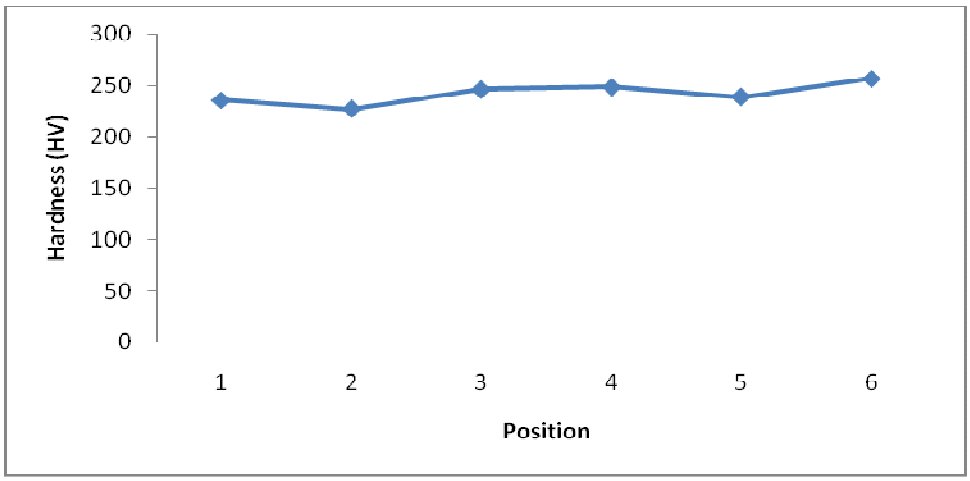

Figure 4.220 Hardness graph for Sample No. S1C: 316L Austenitic stainless steel to 409 Ferritic stainless steel

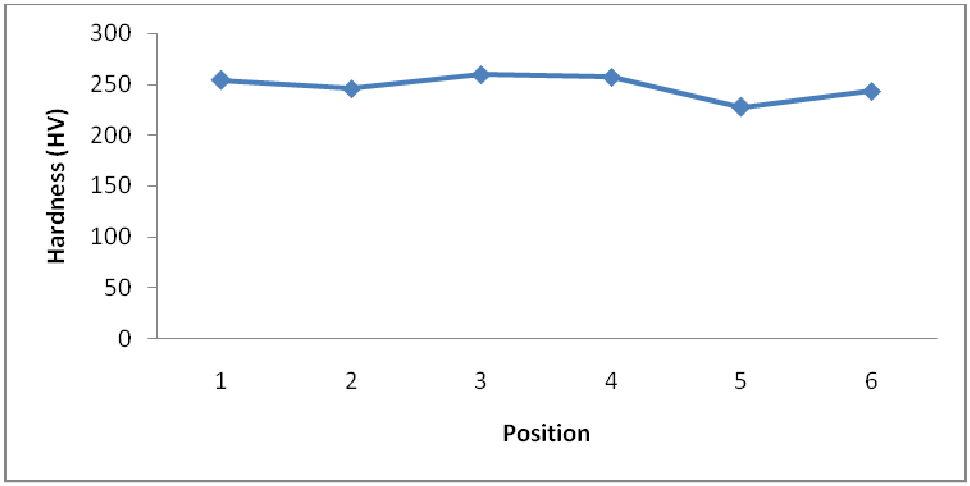

Figure 4.221 Hardness graph for Sample No. S2C: 316L Austenitic stainless steel to 409 Ferritic stainless steel

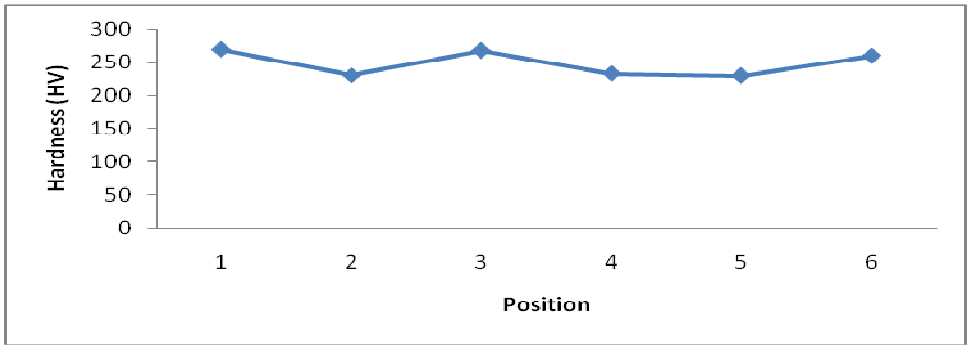

Figure 4.222 Hardness graph for Sample No. S3C: 316L Austenitic stainless steel to 409 Ferritic stainless steel

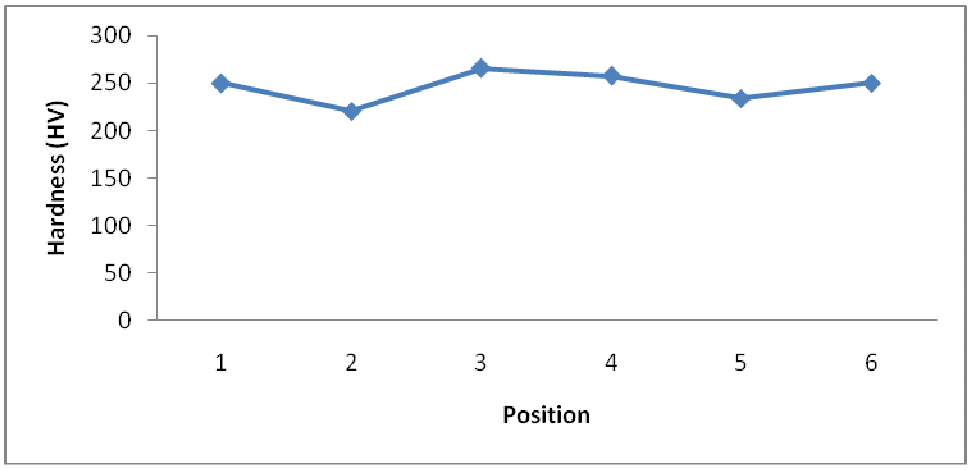

Figure 4.223 Hardness graph for Sample No. S4C: 316L Austenitic stainless steel to 409 Ferritic stainless steel

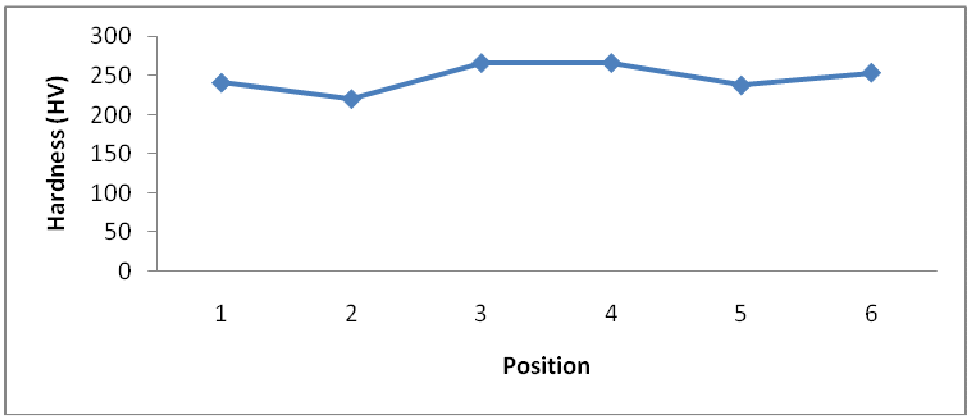

Figure 4.224 Hardness graph for Sample No. S5C: 316L Austenitic stainless steel to 409 Ferritic stainless steel

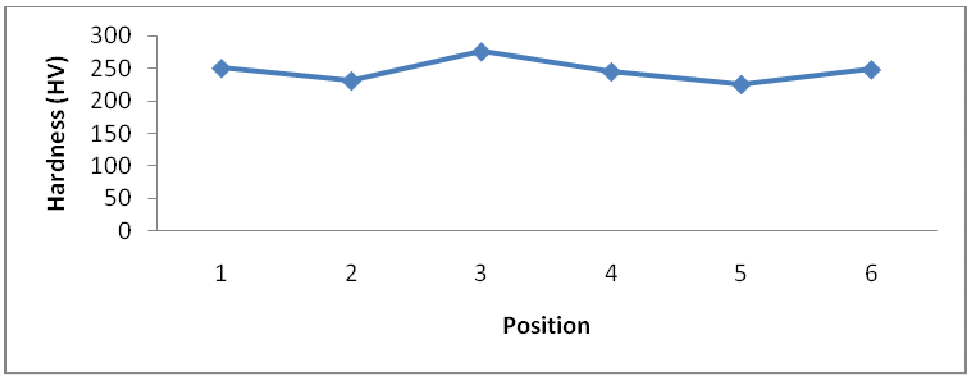

Figure 4.225 Hardness graph for Sample No. S6C: 316L Austenitic stainless steel to 409 Ferritic stainless steel

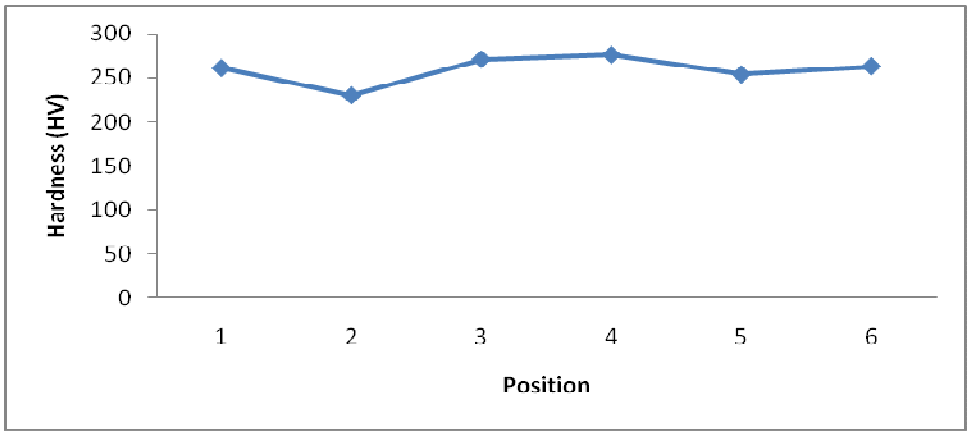

Figure 4.226 Hardness graph for Sample No. S7C: 316L Austenitic stainless steel to 409 Ferritic stainless steel

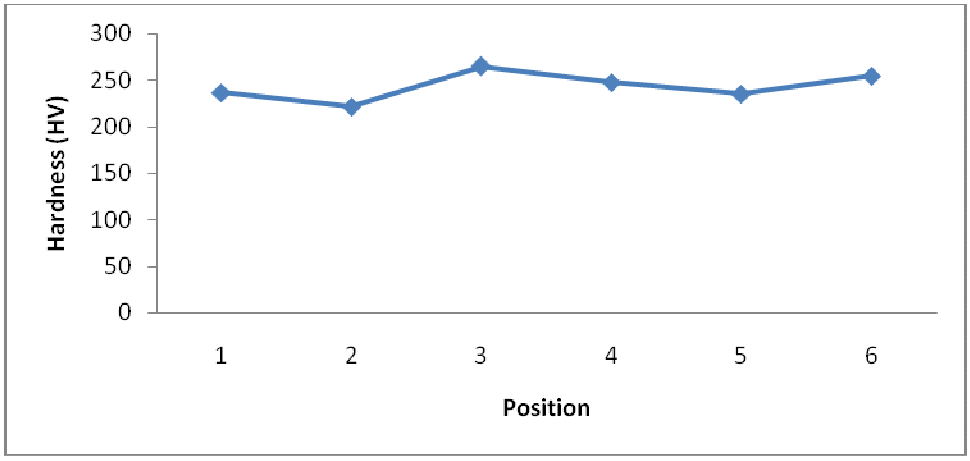

Figure 4.227 Hardness graph for Sample No. S8C: 316L Austenitic stainless steel to 409 Ferritic stainless steel

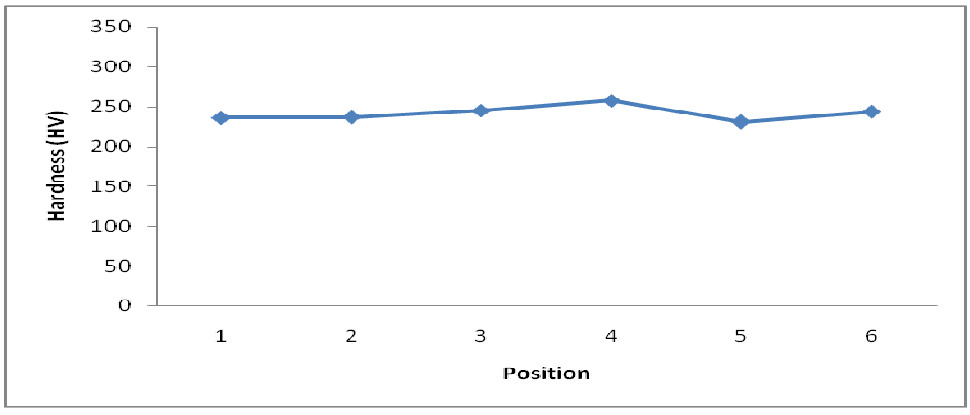

Figure 4.228 Hardness graph for Sample No. S9C: 316L Austenitic stainless steel to 409 Ferritic stainless steel

4.3.4 RESULTS OF MICROSTRUCTURAL STUDY AND DISCUSSION: 316L AUSTENITIC STAINLESS STEEL TO 409 FERRITIC STAINLESS STEEL AS PER L9 TAGUCHI ORTHOGONAL ARRAY DESIGN OF EXPERIMENT

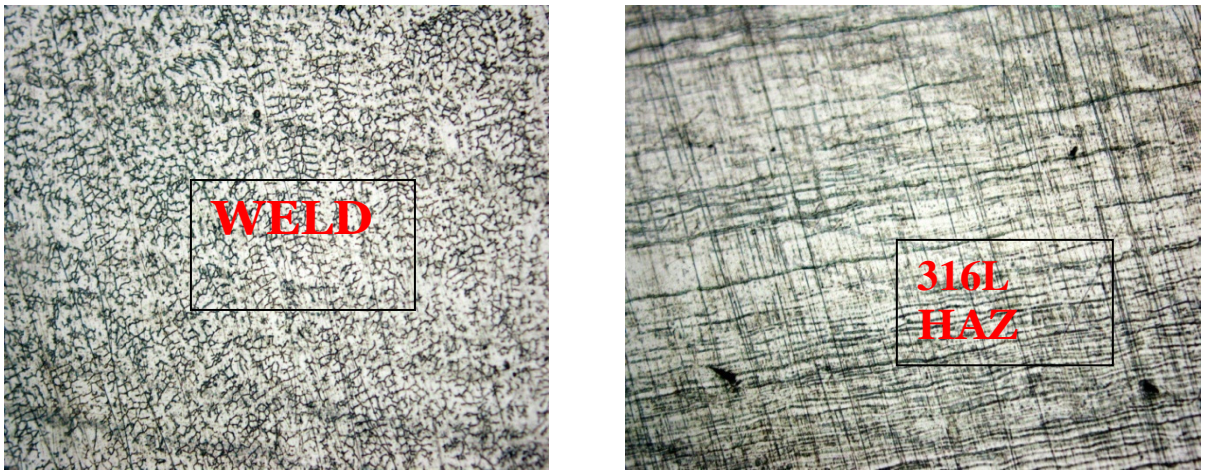

Figure 4.229 Metallographic view of Sample No. S1C: 316L Austenitic stainless steel to 409 Ferritic stainless steel (x500)

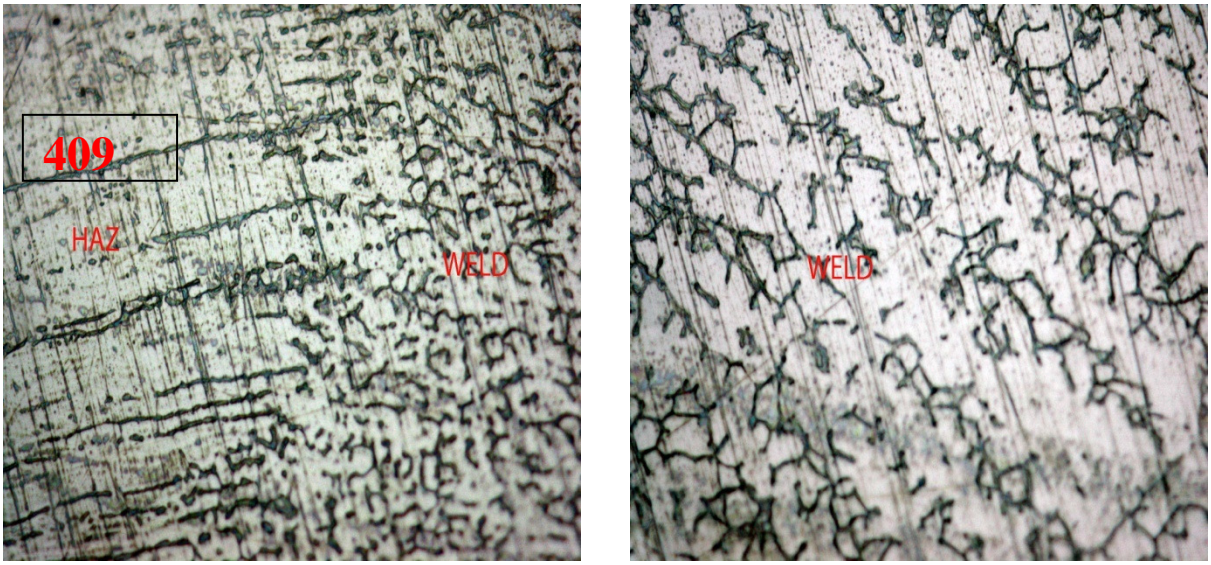

Figure 4.230 Metallographic view of Sample No. S2C: 316L Austenitic stainless steel to 409 Ferritic stainless steel (x500)

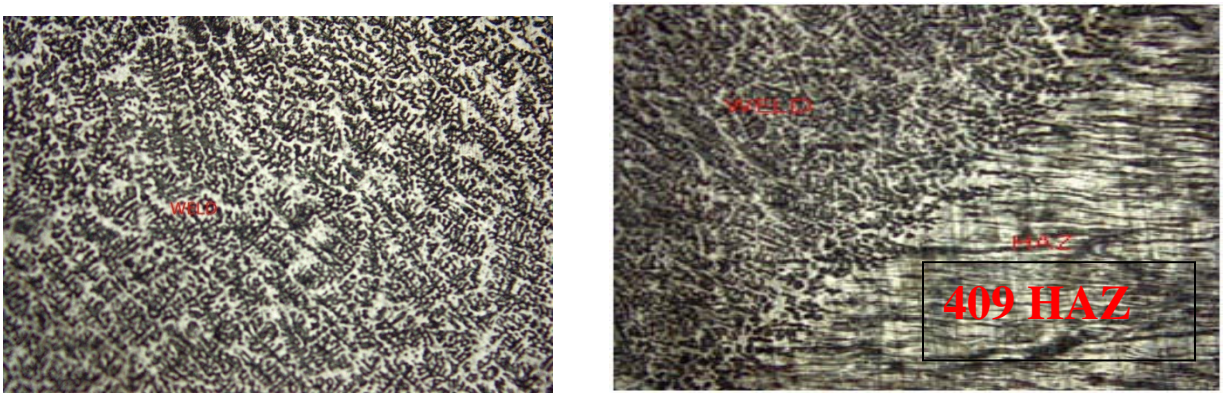

Figure 4.231 Metallographic view of Sample No. S3C: 316L Austenitic stainless steel to 409 Ferritic stainless steel (x500)

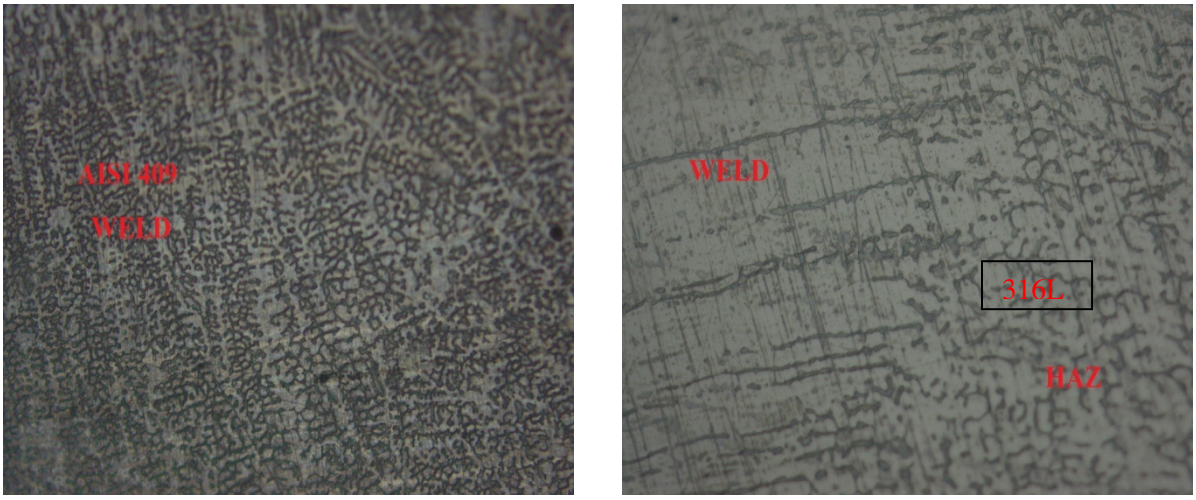

Figure 4.232 Metallographic view of Sample No. S4C: 316L Austenitic stainless steel to 409 Ferritic stainless steel (x500)

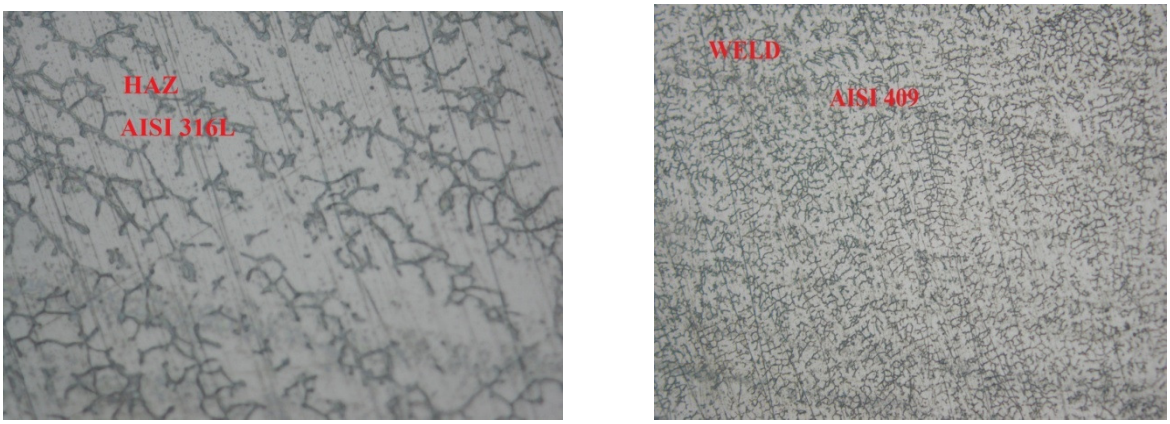

Figure 4.233 Metallographic view of Sample No. S5C: 316L Austenitic stainless steel to 409 Ferritic stainless steel (x500)

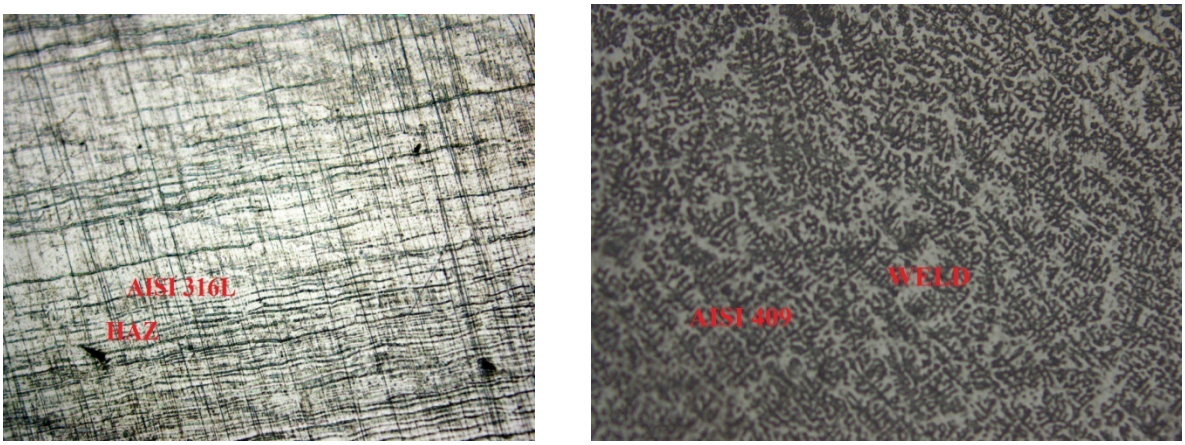

Figure 4.234 Metallographic view of Sample No. S6C: 316L Austenitic stainless steel to 409 Ferritic stainless steel (x500)

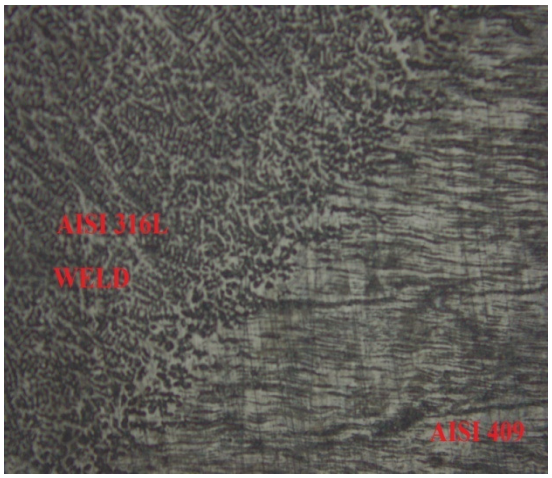

Figure 4.235 Metallographic view of Sample No. S7C: 316L Austenitic stainless steel to 409 Ferritic stainless steel (x500)

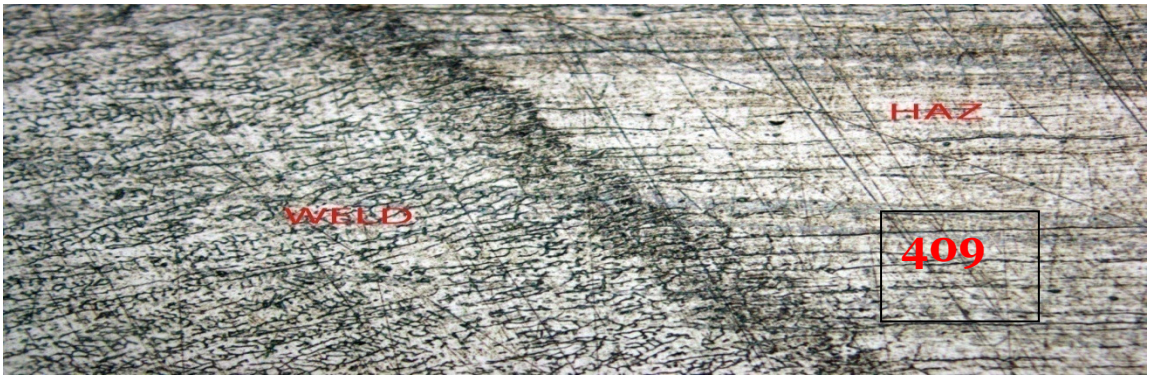

Figure 4.236 Metallographic view of Sample No. S8C: 316L Austenitic stainless steel to 409 Ferritic stainless steel (x500)

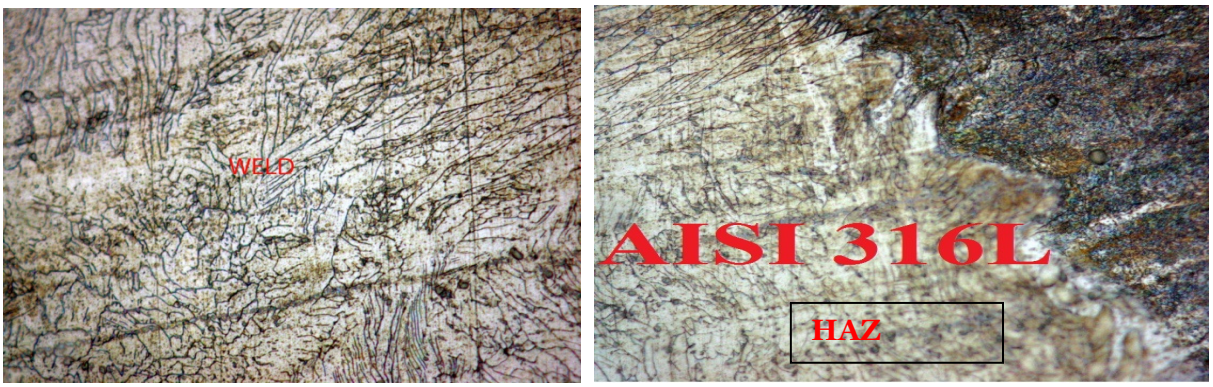

Figure 4.237 Metallographic view of Sample No. S9C: 316L Austenitic stainless steel to 409 Ferritic stainless steel

In the present work, dissimilar welding of 316L Austenitic stainless steel to 409 Ferritic stainless steel has been carried out by gas metal arc welding with 316L Austenitic filler wire. So, there are three types of material, 409 Ferritic stainless steel, 316l Austenitic filler wire and 316L Austenitic stainless steel. So a complex type of weld microstructure is expected. Study of microstructures has been done for all the welded samples made and the photographs are taken in weld and HAZ regions, for each of the samples by the Leica DM LM metallurgical microscope. Microstructural views are shown in figures 4.229 – 4.237**.**

Figure 4.229 (sample no. S1C) and figure 4.234 (sample no. S6C), show that, in weld microstructure, precipitation of ferrite and austenite in the globular form exists and sizes are very small which indicates high hardness. In Figure 4.230 (Sample no. S2C) columnar grain growth is seen in ferrite zone. In addition, the fusion boundary next to the austenitic parent metal 316L, has a partially melted zone with equiaxial austenitic grains and δ ferrite dendrites in the austenitic grain boundaries. Figure 4.231 (sample no. S3C) gives evidence of ferrites in austenitic matrix and reveals austenite with ferritic stringers in the microstructure. Microstructure given in figure 4.233 (sample no. S5C) consists of austenite and δ ferrite. Ferrite shape is lacy and vermicular, in figure 4.235 (sample no. S7C) and in figure 4.237 (sample no. S9C), dendritic structure of ferrite is observed along with layers of austenite. In the weld metal, ferritic solidification involves an epitaxial growth from parent material at the fusion boundary. The austenite starts to precipitate at the ferrite grain boundaries and at the weld metal surface due to higher free energy at these locations. In figure 4.236 (sample no. S8C) coarse grain HAZ is observed. Primary austenitic grains are clearly seen. Pro-eutectoid and Widmansttaten ferrite on

grain boundaries can be seen too. In figure 4.236, (sample no. S8C) on the left hand portion grains are elongated towards HAZ and on the HAZ most of the phase is austenite. Some portions are pro-eutectoid ferrite. The microstructure of the weld zone is depended on the composition of the filler metal as well. Austenitic stainless steel weld metal provides a microstructure in the weld zone consisting on an austenitic matrix (white) with skeletal or vermicular ferrite - dark etching; this microstructure is obtained when weld cooling rates are moderate and/or when Creq/Nieq is low but still within the ferrite-austenite (FA) range. The FA solidification mode starts with primary ferrite solidification followed by the formation of austenite along the ferrite cell and the dendrite boundaries. As the weld metal cools the ferrite becomes increasingly unstable and the austenite begins to consume the ferrite by a diffusion-controlled reaction. The skeletal morphology is a consequence of the advance of the austenite consuming the ferrite. As the process proceeds, the ferrite is enriched in ferrite promoting elements and depleted in austenite promoting elements, which makes it stable at lower temperatures where diffusion is limited.

The fusion boundary next to the ferritic 409 parent metal shows a columnar solidification growing from the ferrite parent grains. A coarse grain zone followed by a refined grain zone is observed in the HAZ-409. The coarse grain zone is formed because grain growth is diffusion controlled, driven by surface energy and requires no nucleation; the energy is given by the welding process. The refined grains zone is due to a recrystallization process where new grains are formed by the movement and annihilation of dislocations in the grains previously deformed in the parent metal.

Microstructure also depends upon the heating cycle and cooling cycle. The temperature of welding has a considerable effect on microstructure. If large heat is applied then the flow ability of material increases and it affects the HAZ. If low heat is available then different type of HAZ is found. Generally, if the cooling rate is high finer grains are produced but when cooling rate is low then coarse grain structure is produced.

In general weld microstructures found here contain fine grains with much less variation with change in input parameters. Hardness in weld zone as discussed earlier is found to be more or less consistent with the observations in microstructures.

Chapter 5

5. ANALYSIS OF THE EXPERIMENTAL RESULTS

Response surface methodology (RSM) is used in the present study for developing mathematical model. It is also used for response prediction and optimization. Grey – based Taguchi method has also been employed in certain parts. Ultimate tensile strength, yield strength and percentage elongation are the response parameters. Analysis of variance (ANOVA) has been applied to check adequacy of the model. Confirmatory tests have been conducted and validated with optimized parametric settings, proposed by RSM/Grey-Taguchi method. Response surface plots and contour plots have also been made. As explained earlier, in the engineering experiments, general aim is to determine the conditions that can lead to optimum results. Both single and multiple objective optimizations are carried out. Mathematical modeling of the process parameters is also very much necessary. Some fundamentals of RSM linear regression modeling has been discussed in section 2.1. It has already been mentioned that, RSM expresses a mathematical model in a functional relationship between the independent variables and the response.

The analyses have been done separately for three sets of experimental results: MIG welding of i) Austenitic stainless steel ii) Ferritic stainless steel and iii) Austenitic to Ferritic stainless steel.

5.1 ANALYSIS: RESULTS OF MIG WELDING OF 316L AUSTENITIC STAINLESS STEEL (1ST SET OF EXPERIMENTS)

In the following paragraphs, the results of MIG welding of 316L Austenitic stainless steel as per RSM design of experiment and L9 Taguchi orthogonal array design of experiment are analyzed by RSM and Grey-Taguchi methodology.

5.1.1 RESPONSE SURFACE ANALYSIS OF TENSILE TEST FOR ULTIMATE TENSILE STRENGTH (UTS): 316L AUSTENITIC STAINLESS STEEL

In this section, response surface analysis of ultimate tensile strength (UTS) has been done using MINITAB 16 software. At first a mathematical model is developed with the help of data obtained from Table 4.3. The adequacy of the developed model has been tested using ANOVA. Surface plots and contour plots for UTS have also been presented.

A) MATHEMATICAL MODELLING

Ultimate tensile strength (UTS) has been expressed in terms of the process variables welding current (C), gas flow rate (F) and nozzle to plate distance (S) as

$$UTS = \beta_0 + \beta_1(C) + \beta_2(F) + \beta_3(S) + \beta_{11}(C*C) + \beta_{22}(F*F) + \beta_{33}(S*S) + \beta_{12}(C*F) + \beta_{13}(C*S) + \beta_{23}(F*S) \quad (5.1)$$

Where β_0 is the constant coefficient, β_1, β_2 and β_3 are the coefficients of Welding current, Gas flow rate and Nozzle to plate distance respectively.

The final mathematical model to estimate UTS is given as

$$Y_{UTS} = 550.031 + 11.450(C) + 0.470(F) + 16.340(S) - 14.577(C*C) - 28.477(F*F) + 9.673(S*S) - 11.788(C*F) - 7.787(C*S) + 11.862(F*S) \quad (5.2)$$

Where Y_{UTS} is in MPa, C is in A, F is in *l/min* and S is in mm.

B) ANOVA OF THE MODEL

The adequacy of the developed model is tested using the analysis of variance (ANOVA) and the results of the second order response surface model, fitting in the form of variance are given in Table 5.1

Table 5.1 ANOVA table for UTS: 316L Austenitic stainless steel

Source	DF	Seq SS	Adj SS	Adj MS	F	P
Regression	9	12282.7	12282.7	1364.75	4.96	**0.010**
Linear	3	3983.2	3983.2	1327.73	4.83	0.025
Welding current	1	1311.0	1311.0	1311.02	4.77	**0.054**
Gas flow rate	1	2.2	2.2	2.21	0.01	0.930
Nozzle to plate distance	1	2670.0	2670.0	2669.96	9.70	**0.011**
Square	3	5577.1	5577.1	1859.02	6.76	0.009
Welding current*Welding current	1	3343.7	584.4	584.37	2.12	0.176
Gas flow rate*Gas flow rate	1	1976.1	2230.1	2230.13	8.11	**0.017**
Nozzle to plate distance*Nozzle to plate distance	1	257.3	257.3	257.29	0.94	0.356
Interaction	3	2722.5	2722.5	907.49	3.30	0.066
Welding current*Gas flow rate	1	1111.6	1111.6	1111.56	4.04	**0.072**
Welding current*Nozzle to plate distance	1	485.2	485.2	485.16	1.76	0.214
Gas flow rate*Nozzle to plate distance	1	1125.8	1125.8	1125.75	4.09	**0.071**
Residual Error	10	2751.3	2751.3	275.13		
Lack-of-Fit	5	2589.9	2589.9	517.99	16.05	0.004
Pure Error	5	161.3	161.3	32.27		
Total	19	15034.0				

S = 16.5869 PRESS = 24429.0
R-Sq = 81.70% R-Sq(pred) = 0.00% R-Sq(adj) = 65.23%

From Table 5.1, it is seen that P-value of the regression equation is P = 0.010 which is very close to P = 0.05 (95% confidence level). It supports the validity of the proposed regression model. **F** in Table 5.1 is different from the symbol F used as a nomenclature of Gas flow rate.

It is observed that, Nozzle to plate distance (S) is the most significant factor, at 95% confidence limit, affecting the response UTS as it has the lowest P value (P = 0.011, which is less than 0.05), followed by Welding current (C) (P = 0.054) and Gas flow rate (F) (P = 0.930). Among the others, inner interaction terns, Gas flow rate* Gas flow rate (F*F) (P=0.017), Gas flow rate * Nozzle to plate distance (F*S) (P=0.071) and Welding current * Gas flow rate (C*F) (P = 0.072)

have higher significance. The determination factor (R^2) indicates the goodness of fit of the model. The value of R^2 of this model is 81.70% which is greater than 80 %. This implies that at least 81% of the variability in data for the response is explained by the model. This indicates that the proposed model is adequate.

C) SURFACE PLOTS AND CONTOUR PLOTS FOR UTS

The relationship between UTS and the welding parameters has been illustrated graphically by surface plots and contour plots. Surface plots are three dimensional plots, where a response is plotted against any two variables when the other variable is held constant. Contour plot provides one of the most revealing ways of illustrating and interpreting the response surface design. The contour plots are two-dimensional graphs that show contours of constant response, with the axis system being a specific pair of the process variables, while the other variable is held constant. The plots are particularly necessary when the stationary point is a saddle point or is remote from the design region. But it should be kept in mind that the contour plots are only estimator, they are not generated by deterministic equations. Every point on a contour has a standard error. The surface plots are shown in figures 5.1 –5.3 and contour plots are shown in figures 5.4– 5.6. Response surface plots show the combined effect of any two factors (i.e. input parameters) on the selected responses (UTS, YS and PE), while the third parameter is held constant. (In the present work, three factors have been considered). These plots are also useful for identifying the interaction effects of the parameters on the response(s). If the response surface exhibits appreciable bend, curvature or undulation, then interaction effect is considered to be significant.

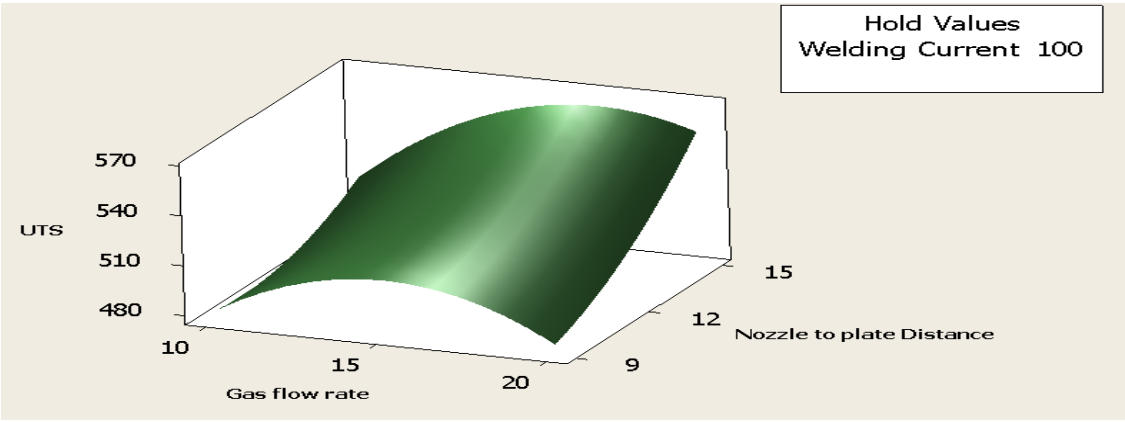

(5.1a)Welding current (C) constant at lowest level

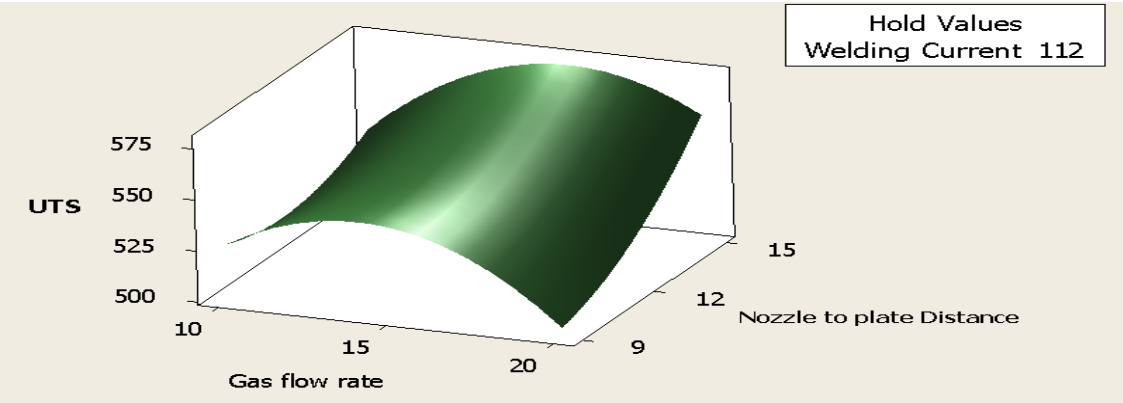

(5.1b)Welding current (C) constant at middle level

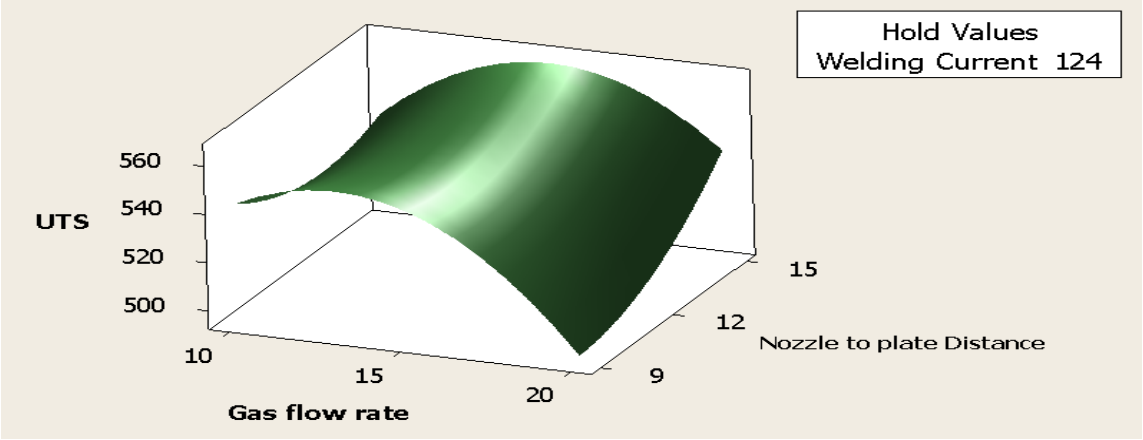

(5.1c)Welding current (C) constant at highest level

Figure 5.1 Response surface plots showing combined effects of Gas flow rate (F) and Nozzle to plate distance(S) on UTS when Welding current (C) is kept constant: 316L Austenitic stainless steel

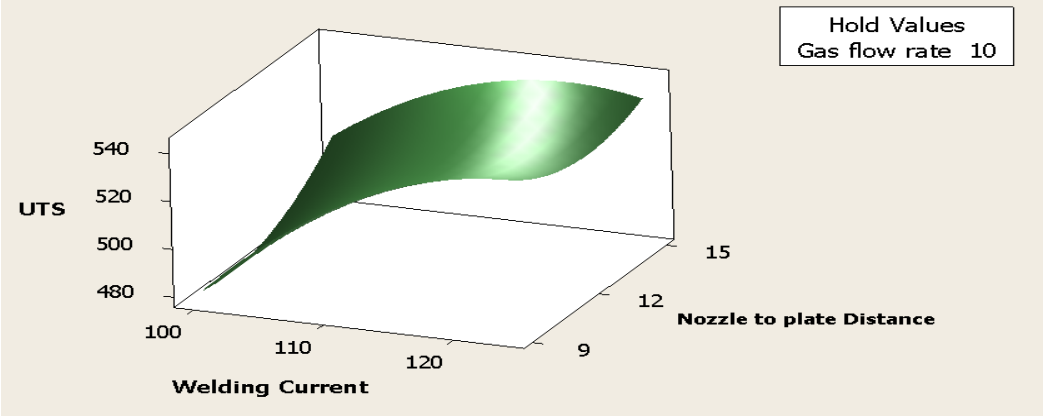

(5.2a) Gas flow rate (F) constant at lowest level

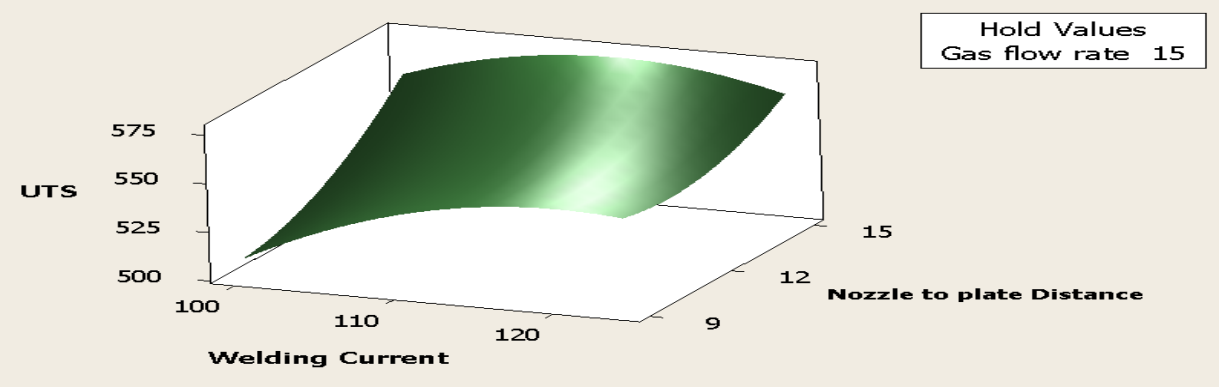

(5.2b)Gas flow rate (F) constant at middle level

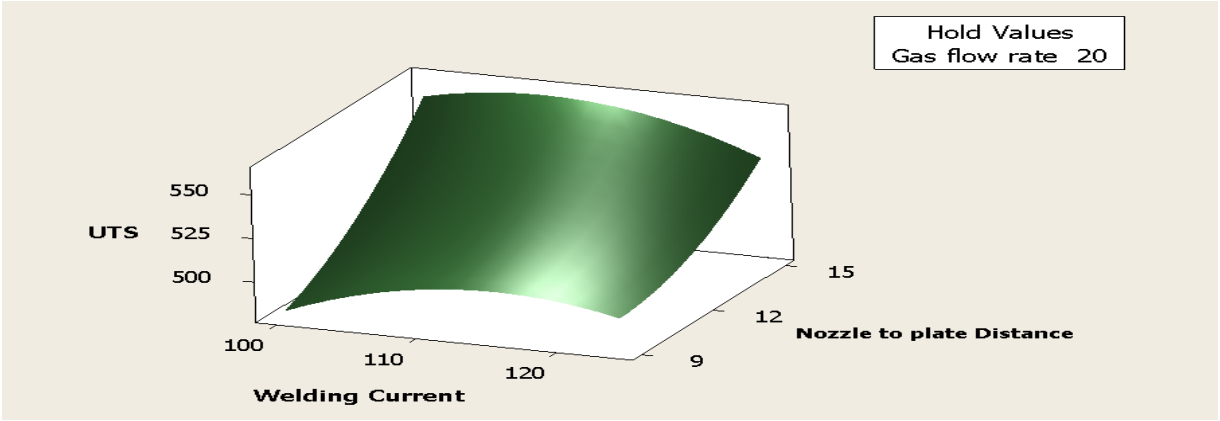

(5.2c) Gas flow rate (F) constant at highest level

Figure 5.2 Response surface plots showing combined effects of Welding current (C) and Nozzle to Plate distance (S) on UTS when Gas flow rate (F) is kept constant: 316L Austenitic stainless steel

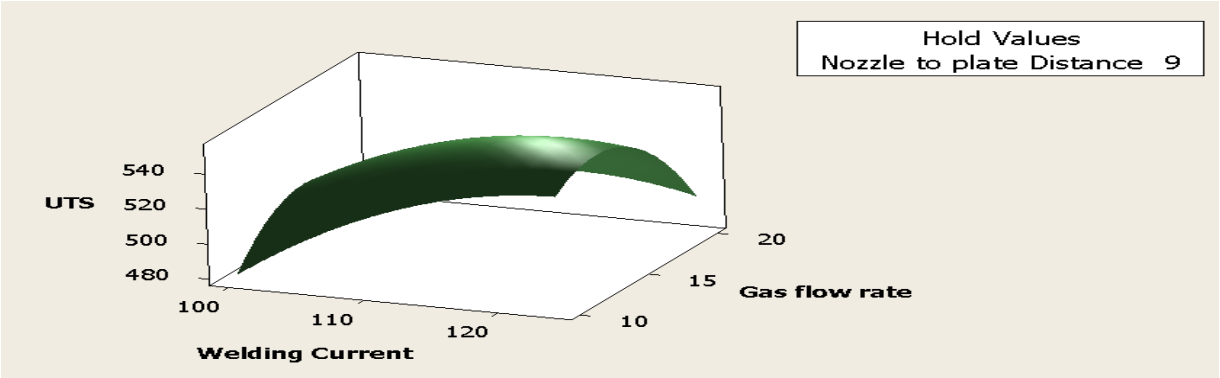

(5.3a)Nozzle to plate distance (S) constant at lowest level

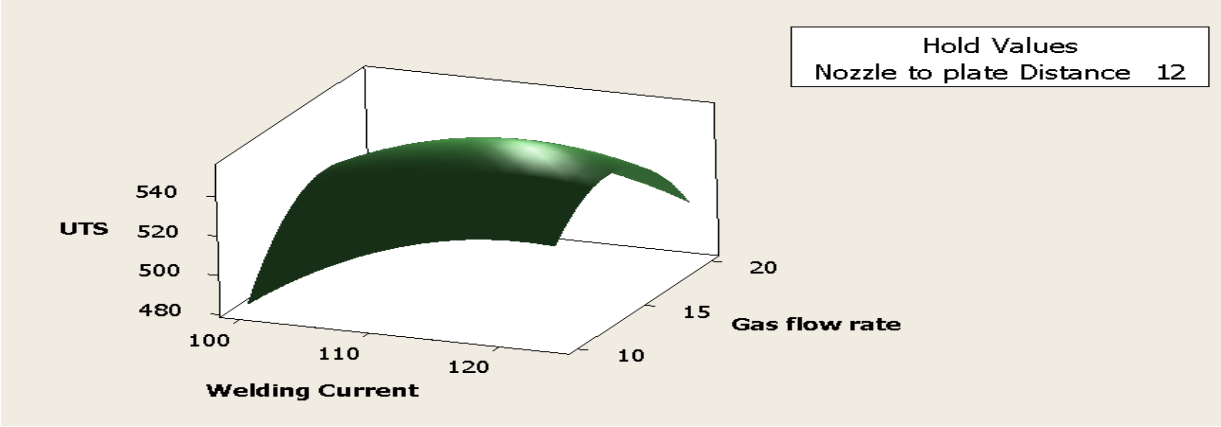

(5.3b)Nozzle to plate distance (S) constant at middle level

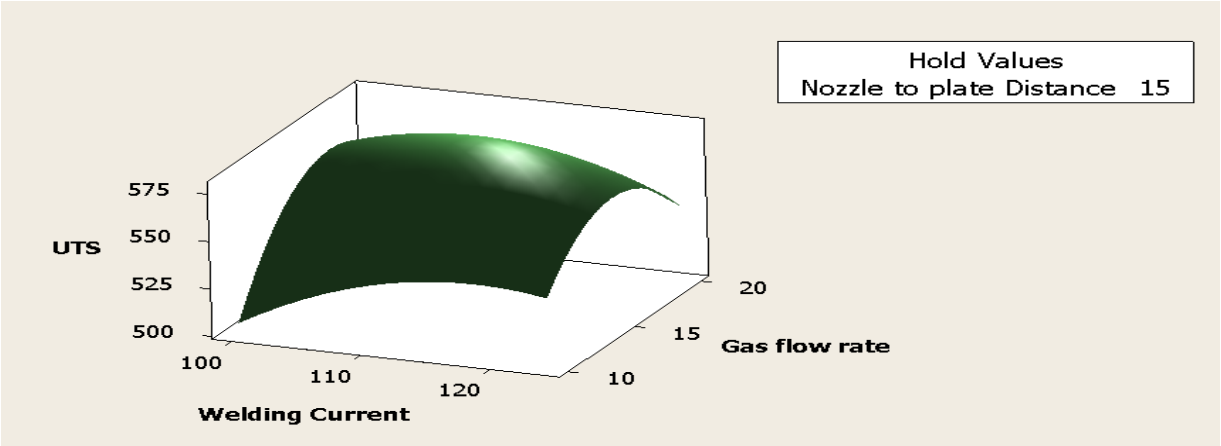

(5.3c) Nozzle to plate distance (S) constant at highest level

Figure 5.3 Response surface plots showing combined effects of Welding current (C) and Gas flow rate (F) on UTS when Nozzle to plate distance (S) is kept constant: 316L Austenitic stainless steel

Response surface plots show the combined effect of any two factors (i.e. input parameters) on the selected responses, while the third parameter is held constant. These plots are also useful for identifying the interaction effects of the parameters on the response(s). If the response surface exhibits appreciable bend, curvature or undulation, then interaction effect is considered to be significant. Response surface with no or very little bend/curvature or undulation leads to the fact that interaction effect is less or insignificant. For examples, interaction effects revealed in figures 5.2 (a-c) are comparatively less significant than those revealed in the figures 5.1 (a-c) and 5.3 (a-c). This means interaction among the factors Welding current (C) and Nozzle to plate distance

(S) causes lesser influence on the response UTS (figures 5.2 a-c) as compared to the interactions among the factors Gas flow rate (F) and Nozzle to plate distance(S) (figures 5.1 a-c), Welding current (C)and Gas flow rate (F) (figures 5.3 a-c).

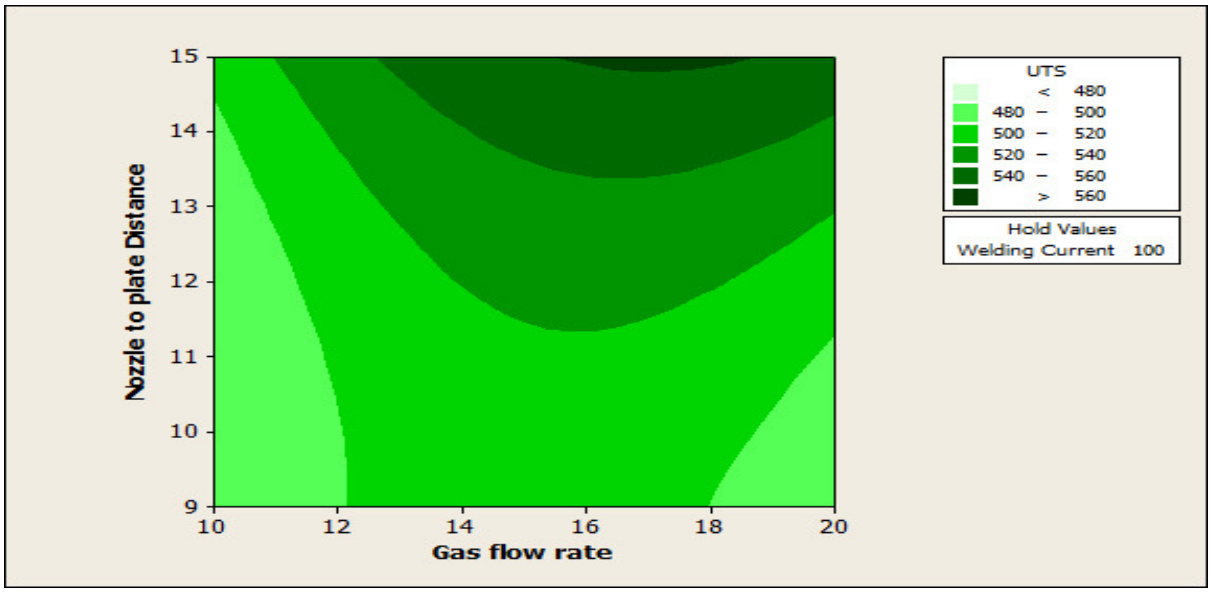

(5.4a) Welding current (C) at lowest level

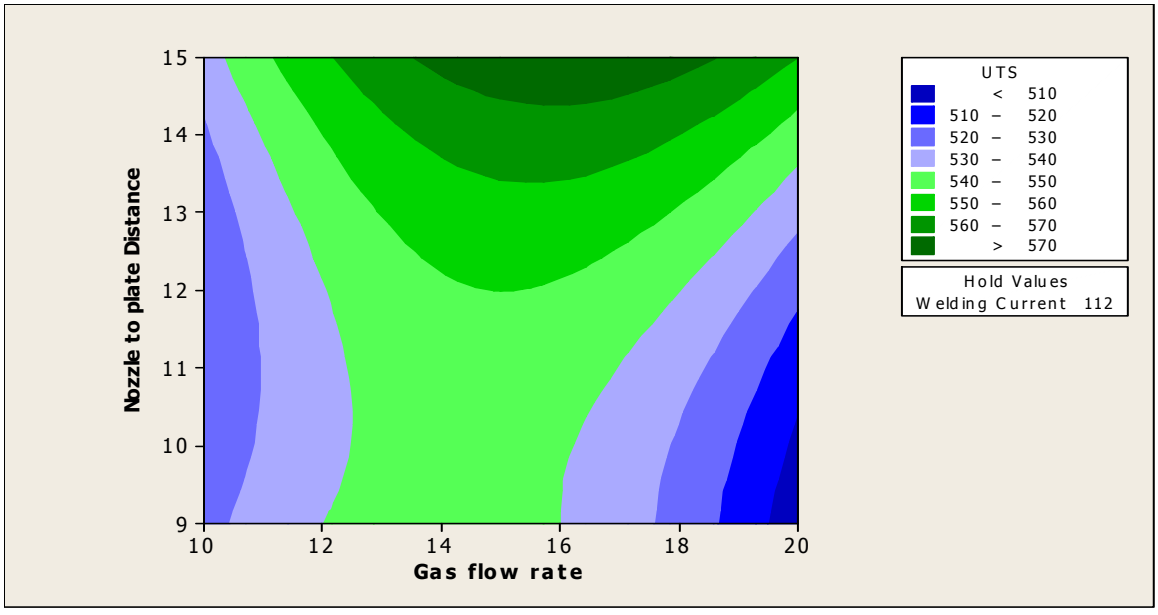

(5.4b)Welding current (C) at middle level

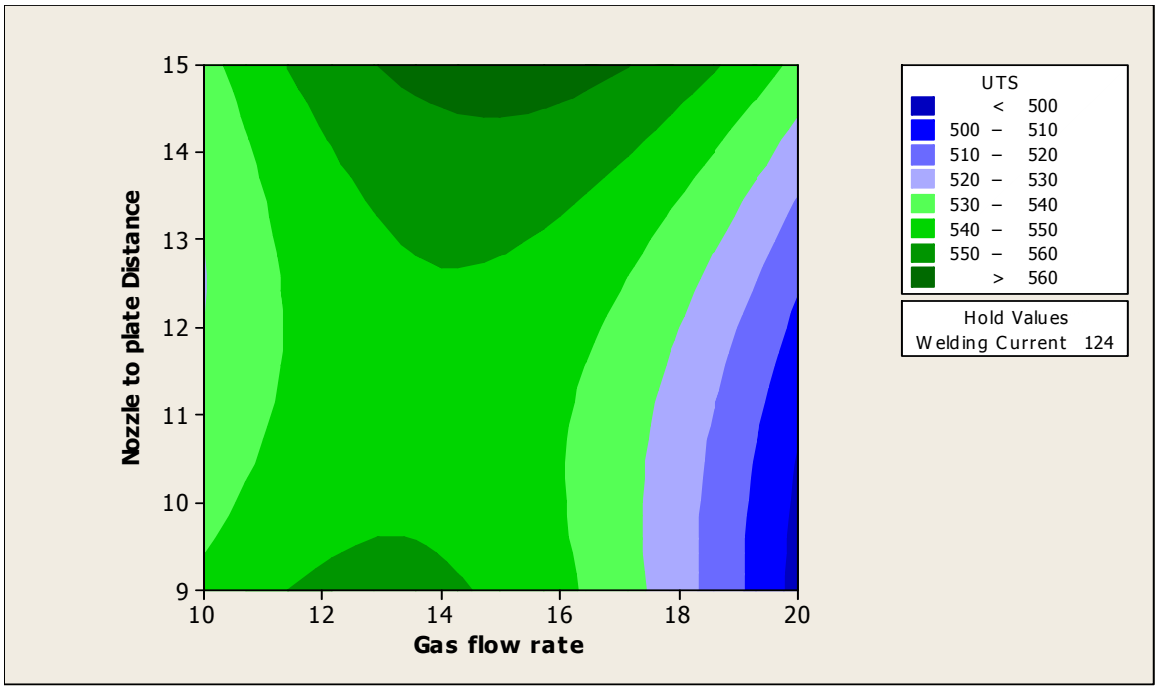

(5.4c) Welding current (C) at highest level

Figure 5.4 Contour plots showing combined effects of Gas flow rate (F) and Nozzle to plate distance(S) on UTS when Welding current (C) is kept constant: 316L Austenitic stainless steel

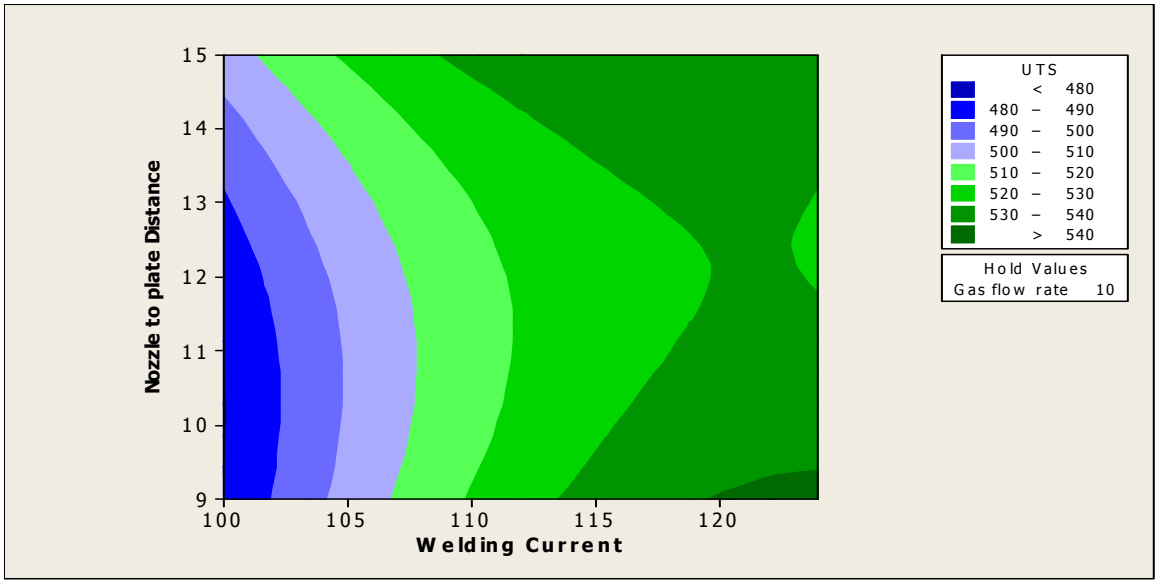

(5.5a) Gas flow rate (F) constant at lowest level

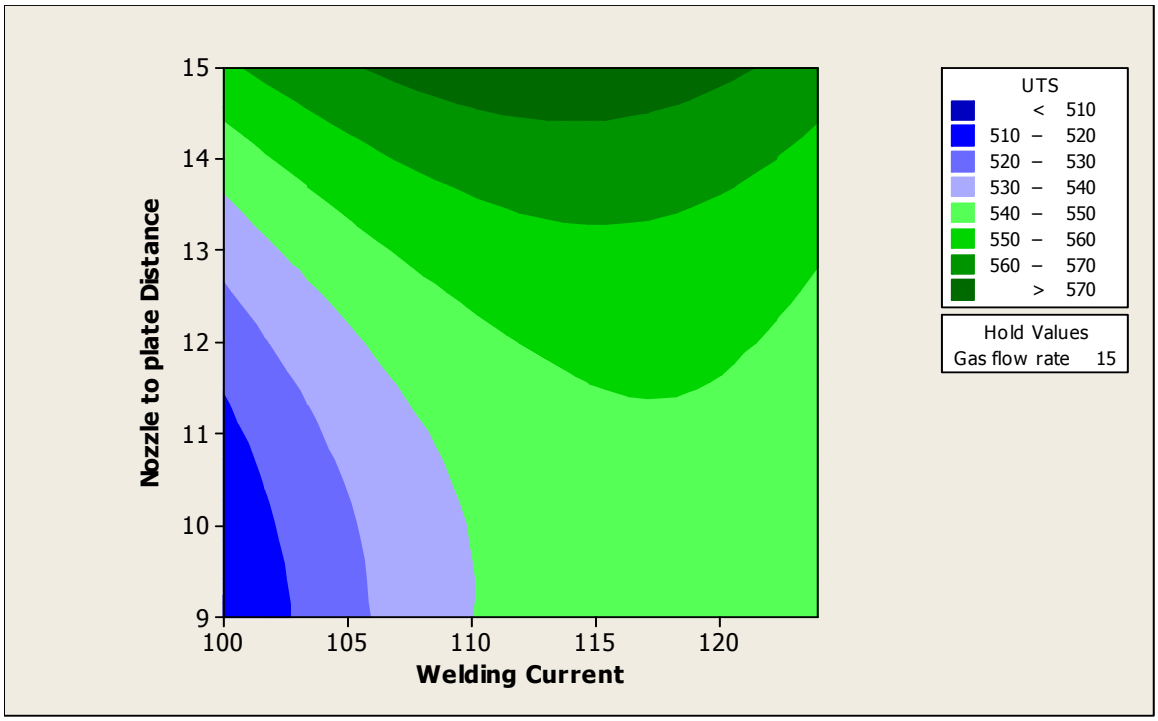

(5.5b) Gas flow rate (F) constant at middle level

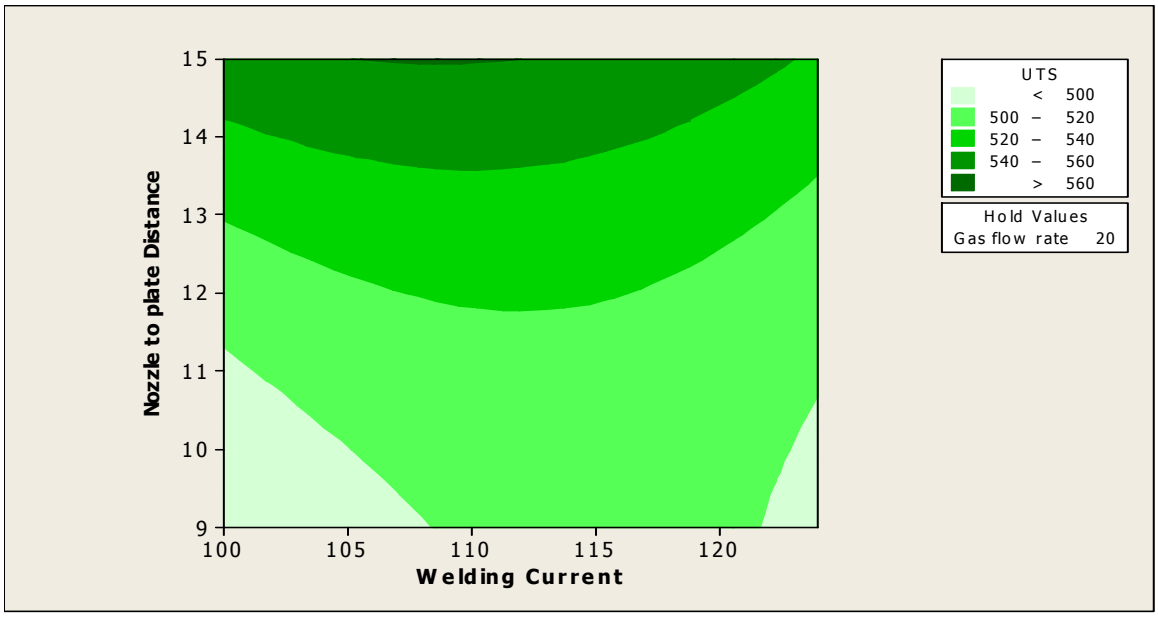

(5.5c) Gas flow rate (F) constant at highest level

Figure 5.5 Contour plots showing combined effects of Welding current (C) and Nozzle to plate distance(S) on UTS when Gas flow rate (F) is kept constant: 316L Austenitic stainless Steel

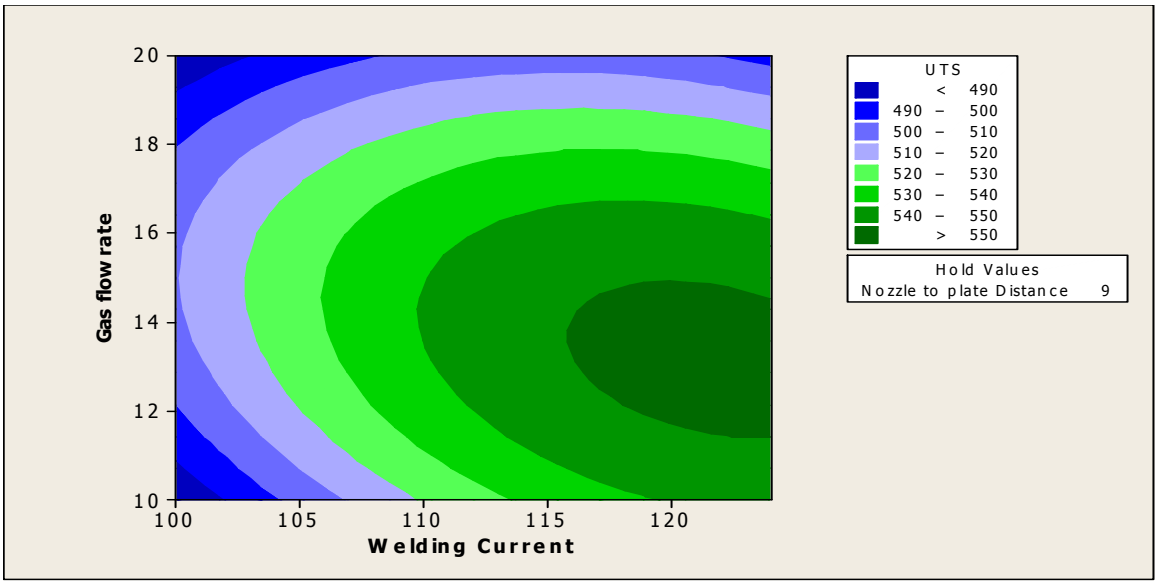

(5.6a) Nozzle to plate distance (S) constant at lowest level

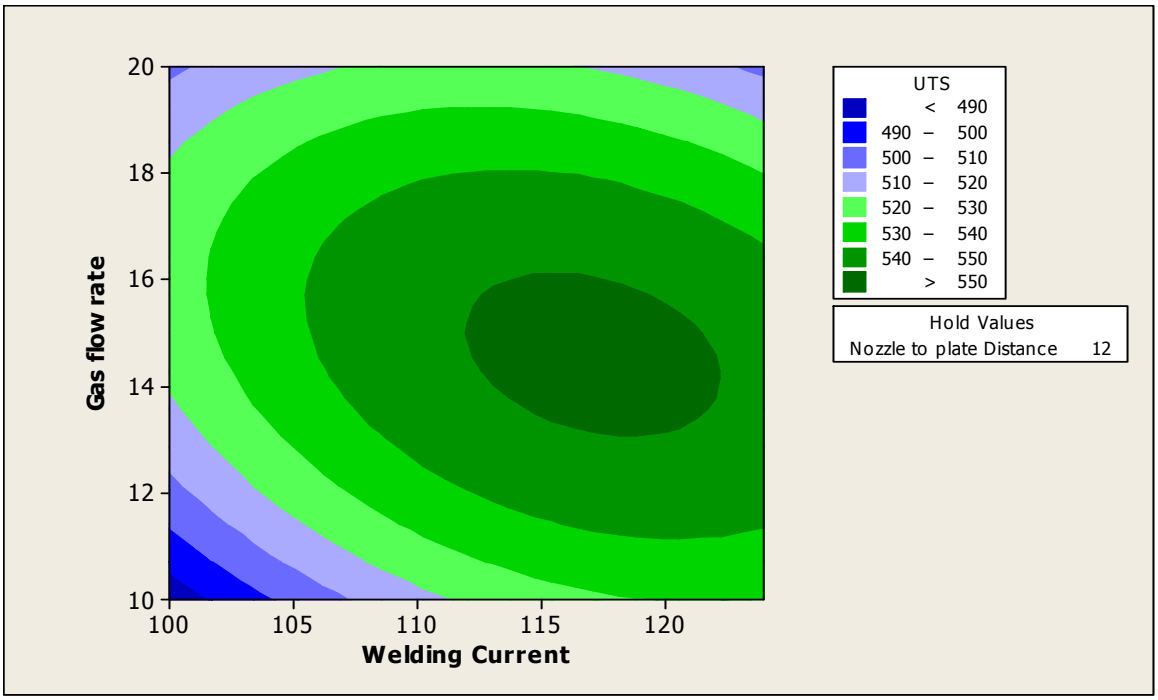

(5.6b) Nozzle to plate distance (S) at middle level

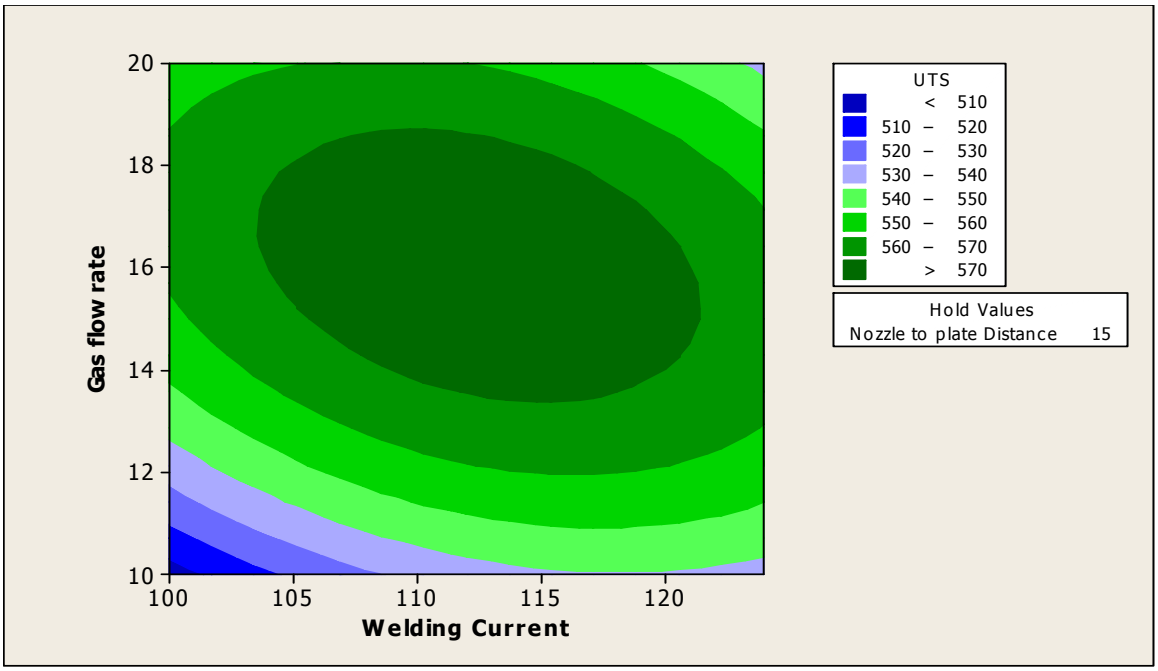

(5.6c) Nozzle to plate distance (S) at highest level

Figure 5.6 Contour plots showing combined effects of Welding current (C) and Gas flow rate (F) on UTS when Nozzle to plate distance (S) is kept constant: 316L Austenitic stainless steel

Contour plots (shown in figures 5.4 – 5.6) are helpful for estimating the combined effects of any two parameters on the response. Each line in the plots is a constant - response line. These plots can be utilized almost in the same manner as discussed in the context of response surface plots. The contour lines, with little or no curvature indicate lesser or no interaction effect; whereas bent or circular contours suggest interaction effect to be significant on the response. For example, interaction among the factors Welding current (C) and Gas flow rate (F) is found to be significant in so far as the effect of this interaction on UTS is concerned (figures 5.6 a-c). Interaction effect of Welding current (C) and Nozzle to plate distance (S) on UTS is not so much significant, as revealed in figure 5.5a, while Gas flow rate is kept constant at 10 *l/min*.

5.1.2 RESPONSE SURFACE ANALYSIS FOR YIELD STRENGTH (YS): 316L AUSTENITIC STAINLESS STEEL

In this section, response surface analysis for Yield strength (YS) of welded Austenitic stainless steel has been done. In the beginning, a mathematical model is developed through regression analysis using the data contained in Table 4.3 in chapter 4. The adequacy of the model has been checked using ANOVA. Surface plots and contour plots for yield strength have also been drawn.

A) MATHEMATICAL MODELLING

Yield Strength (YS) has been expressed in terms of the process parameters i.e., Welding current (C), Gas flow rate (F) and Nozzle to Plate distance (S) using the following form.

$$YS = \beta_0 + \beta_1(C) + \beta_2(F) + \beta_3(S) + \beta_{11}(C*C) + \beta_{22}(F*F) + \beta_{33}(S*S) + \beta_{12}(C*F) + \beta_{13}(C*S) + \beta_{23}(F*S) \quad (5.3)$$

The form of equation is already mentioned in eq. (5.1), chapter 5.

The equation of the model to estimate Yield strength is obtained as:

$$Y_{YS} = 306.085 + 4.510(C) - 10.010(F) + 12.020(S) - 8.514(C*C) - 20.914(F*F) - 1.264(S*S) - 15.475(C*F) - 6.60(C*S) + 18.350(F*S) \quad (5.4)$$

Where Y_{YS} is in MPa, C is in A, F is in *l*/min and S is in mm

B) ANOVA OF THE MODEL

ANOVA technique is applied and the results of the second order response surface model fitting in the form of variance are listed in Table 5.2.

Table 5.2 ANOVA table for YS: 316L Austenitic stainless steel

Source	DF	Seq SS	Adj SS
Regression	9	11457.0	11457.0
Linear	3	2650.2	2650.2
Welding current	1	203.4	203.4
Gas flow rate	1	1002.0	1002.0
Nozzle to plate distance	1	1444.8	1444.8
Square	3	3848.7	3848.7
Welding current*Welding current	1	2380.6	199.3
Gas flow rate*Gas flow rate	1	1463.8	1202.8
Nozzle to plate distance*Nozzle to plate distance	1	4.4	4.4
Interaction	3	4958.1	4958.1
Welding current*Gas flow rate	1	1915.8	1915.8
Welding current*Nozzle to plate distance	1	348.5	348.5
Gas flow rate*Nozzle to plate distance	1	2693.8	2693.8
Residual Error	10	3919.8	3919.8
Lack-of-Fit	5	1922.8	1922.8
Pure Error	5	1997.0	1997.0
Total	19	15376.8	

Source	Adj MS	F	P
Regression	1273.00	3.25	**0.040**
Linear	883.40	2.25	0.145
Welding current	203.40	0.52	**0.488**
Gas flow rate	1002.00	2.56	**0.141**
Nozzle to plate distance	1444.80	3.69	**0.084**
Square	1282.90	3.27	0.067
Welding current*Welding current	199.33	0.51	**0.492**
Gas flow rate*Gas flow rate	1202.80	3.07	**0.110**
Nozzle to plate distance*Nozzle to plate distance	4.39	0.01	0.918
Interaction	1652.69	4.22	0.036
Welding current*Gas flow rate	1915.81	4.89	**0.051**
Welding current*Nozzle to plate distance	348.48	0.89	0.368
Gas flow rate*Nozzle to plate distance	2693.78	6.87	**0.026**
Residual Error	391.98		
Lack-of-Fit	384.56	0.96	0.516
Pure Error	399.40		
Total			

S = 19.7985 PRESS = 17949.2
R-Sq = 74.51% R-Sq(pred) = 0.00% R-Sq(adj) = 51.57%

From Table 5.2, it is seen that P-value of the regression equation is P = 0.040 which is lower than the P value (P = 0.05) corresponding to 95% confidence level. It highly supports the validity of the proposed regression model. From the statistical analysis it is obtained that Nozzle to Plate distance (S) is the most significant factor affecting the response: yield strength, having the lowest corresponding P factor (P = 0.084) followed by Gas flow rate (P = 0.141) and Welding current (P = 0.488). However none of these factors is found to be significant at 95% confidence limit. Among the inner interaction terms, C- C and F-F have higher significance with P value 0.492 and 0.110 respectively. Cross interaction terms, i.e., C-F and F-S show high significance, with P value 0.051, 0.026 respectively.

The determination factor (R^2) indicates goodness of fit of the model. The value R^2 of this model is 74.51% which is very close to 80%. This implies that at least 74.5% of the variability in data for the response can be explained by this model. This indicates that the model is moderately adequate.

C) SURFACE PLOTS AND CONTOUR PLOTS FOR YIELD STRENGTH

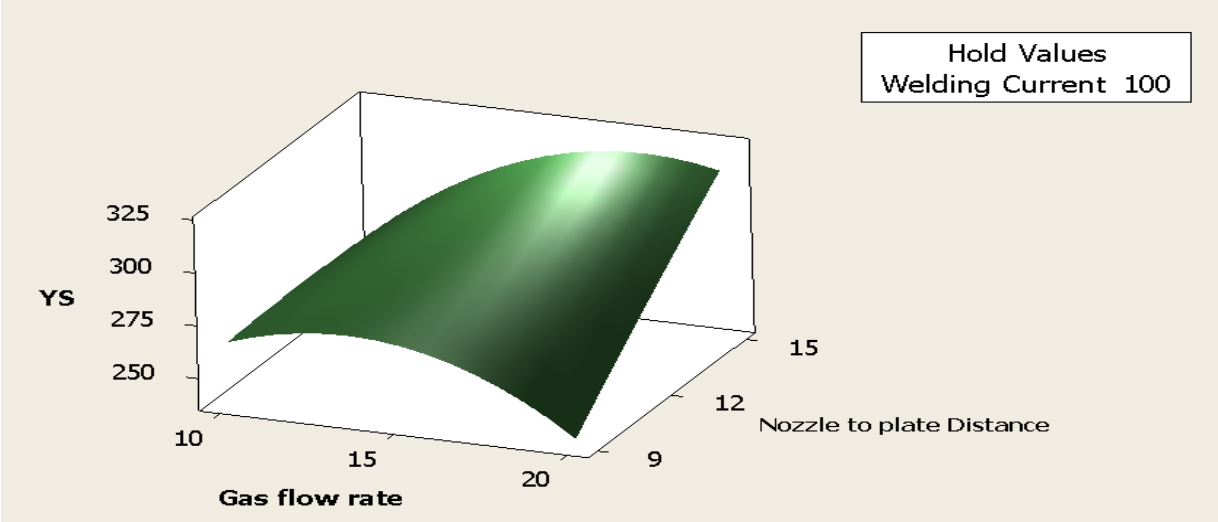

(5.7a) Welding current (C) constant at lowest level

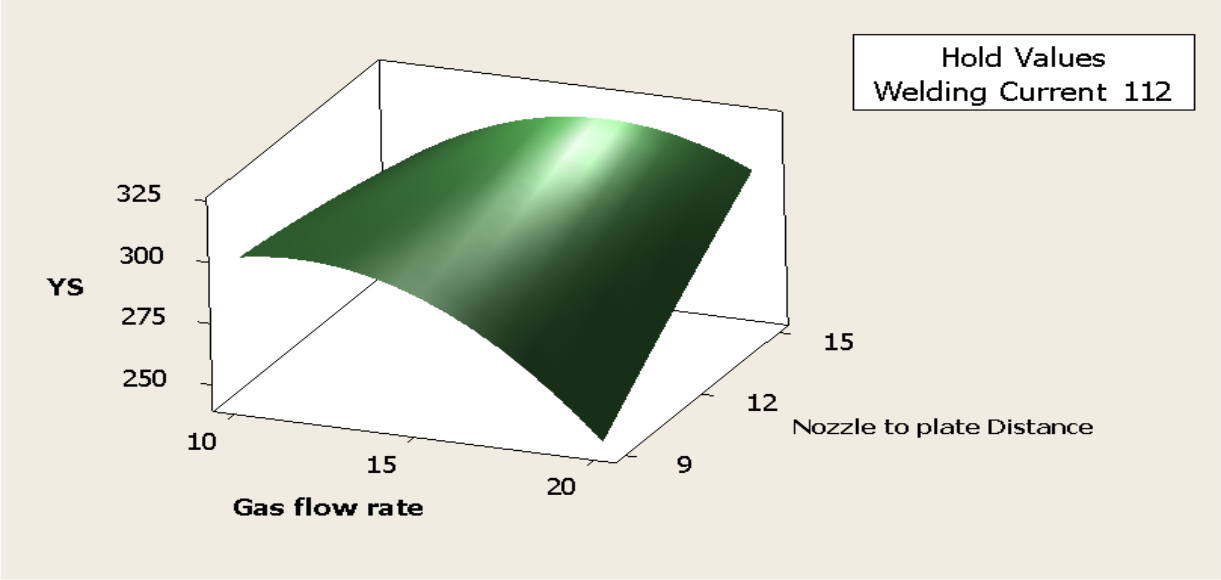

(5.7b) Welding current (C) at middle level

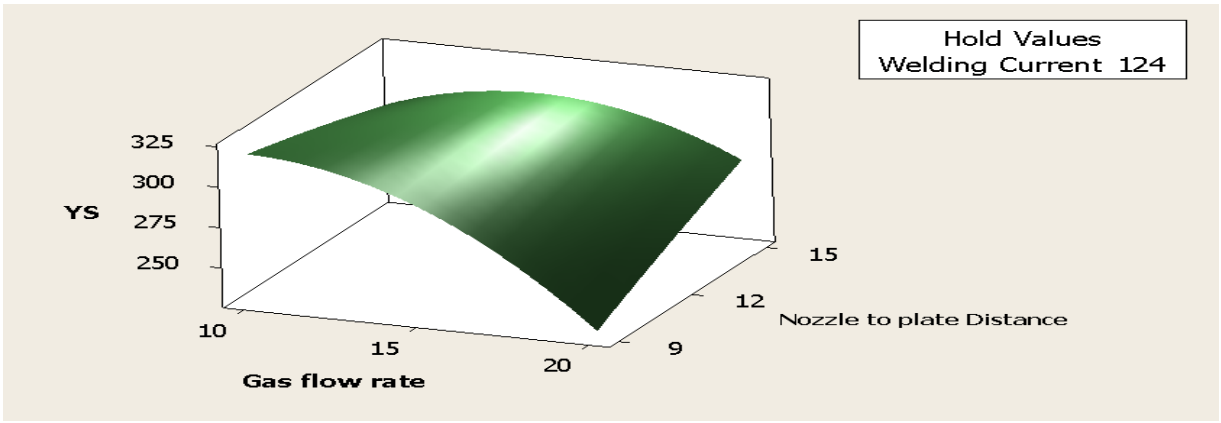

(5.7c) Welding current (C) constant at highest level

Figure 5.7 Response surface plots showing combined effects of Gas flow rate (F) and Nozzle to plate distance (S) on YS when Welding current (C) is kept constant: 316L Austenitic Stainless Steel

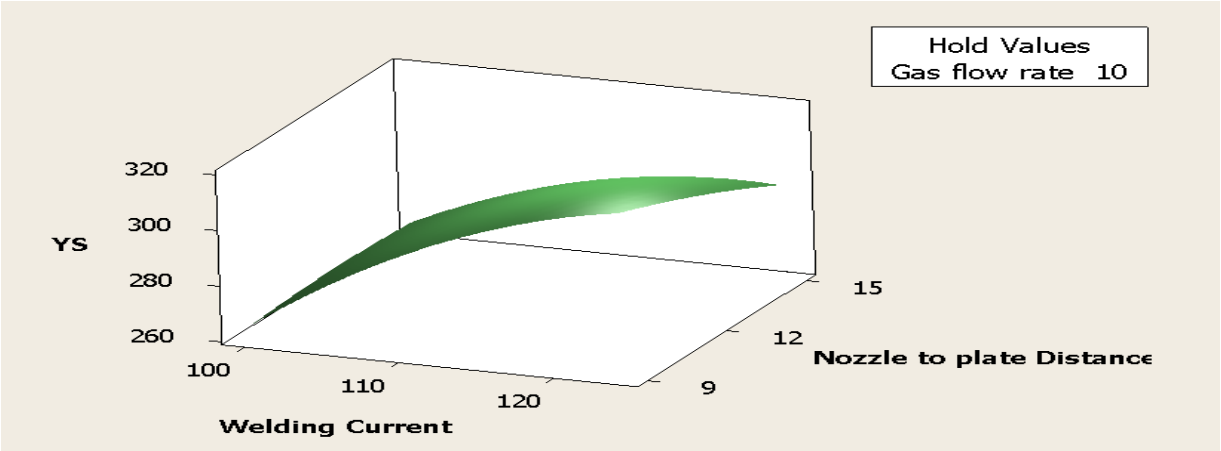

(5.8a) Gas flow rate (F) constant at lowest level

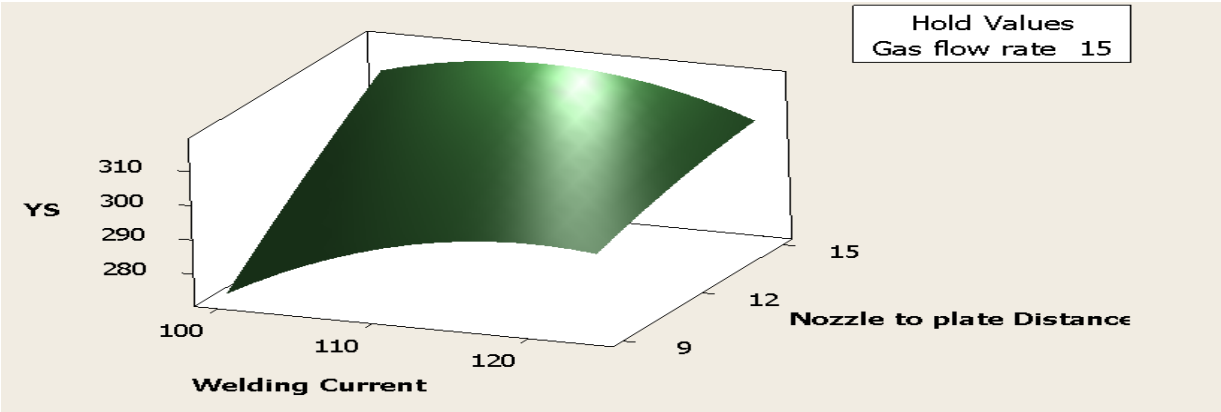

(5.8b) Gas flow rate (F) constant at middle level

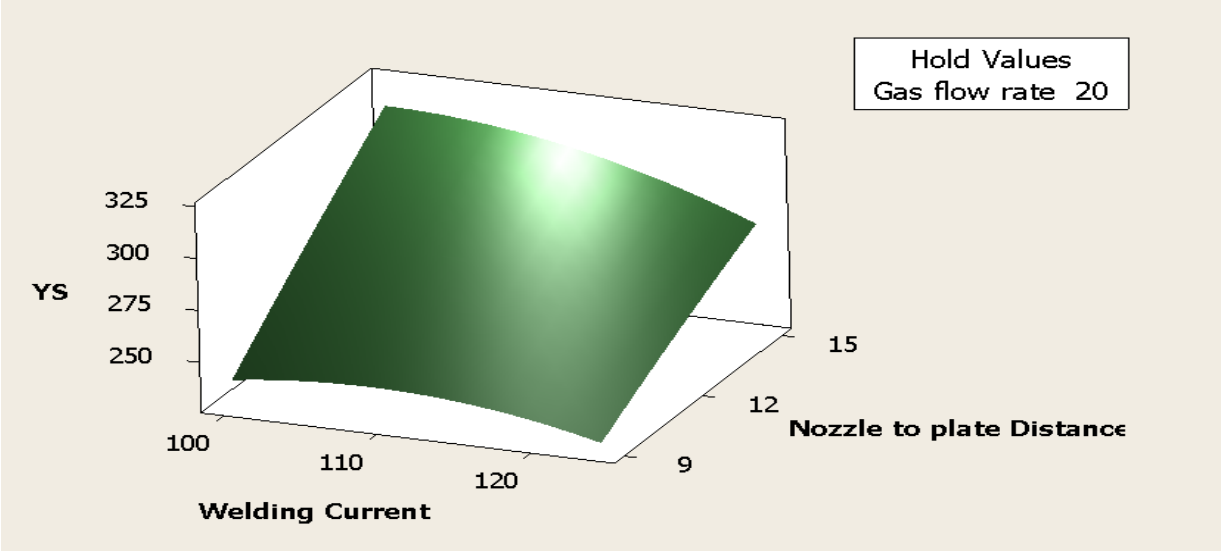

(5.8c) Gas flow rate (F) constant at highest level

Figure 5.8 Response surface plots showing combined effects of Welding Current (C) and Nozzle to Plate distance (S) on YS when Gas flow rate (F) is kept constant: 316L Austenitic stainless steel

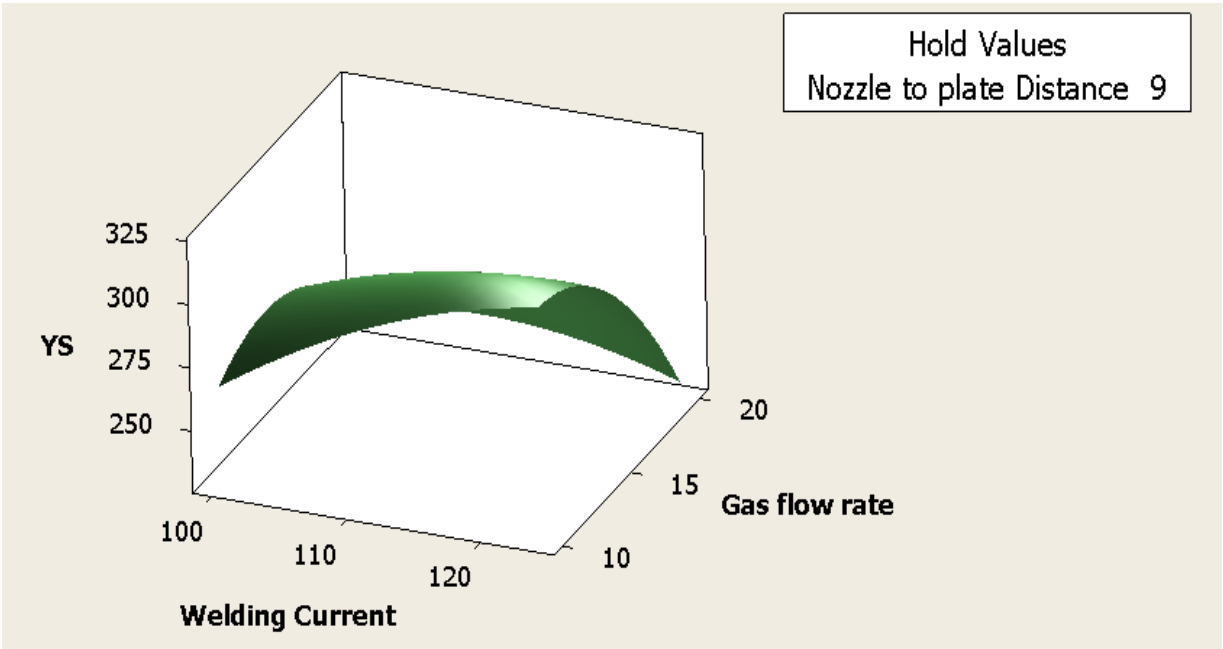

(5.9a) Nozzle to plate distance (S) constant at lowest level

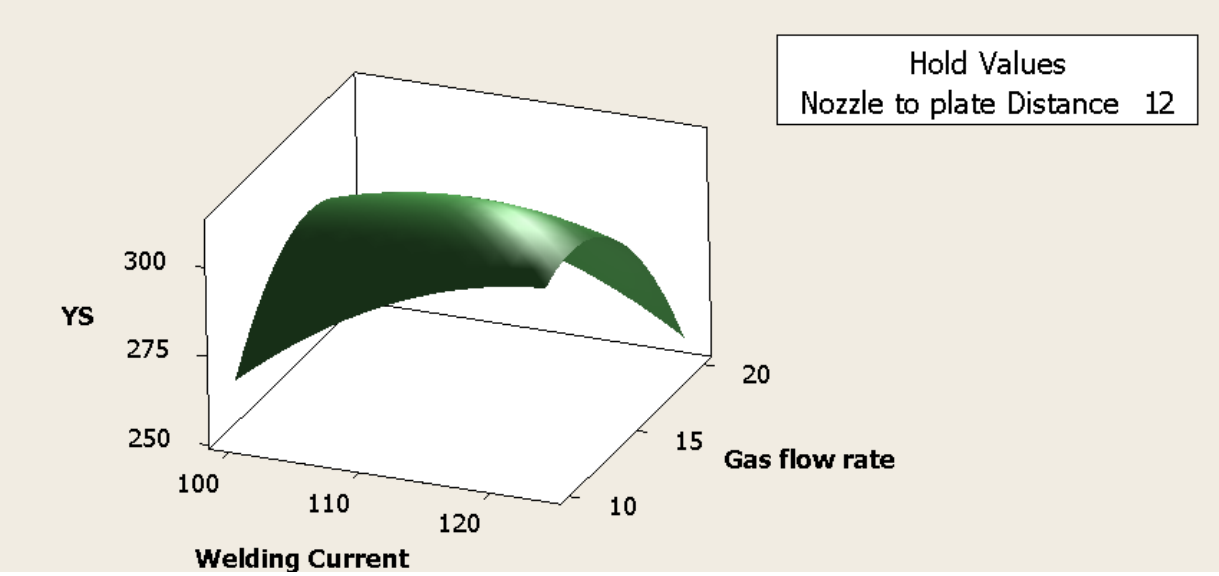

(5.9b) Nozzle to plate distance (S) constant at middle level

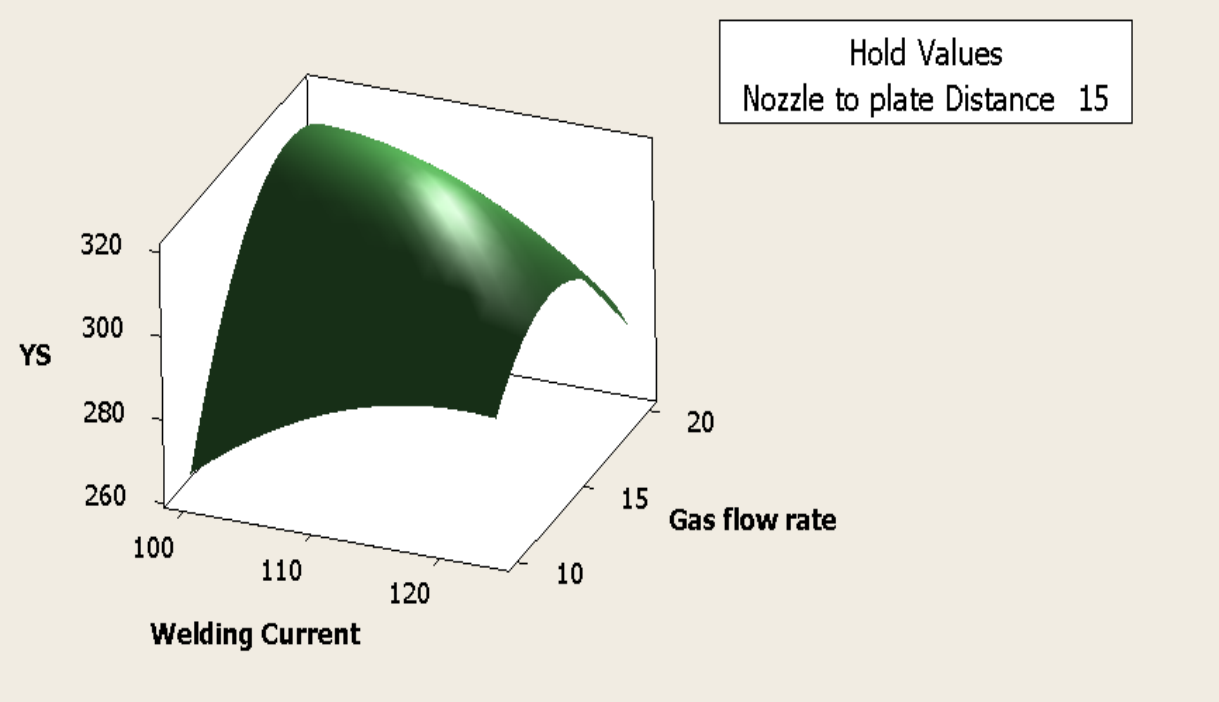

(5.9c) Nozzle to plate distance (S) constant at highest level

Figure 5.9 Response surface plots showing combined effects of welding current (C) and gas flow rate (F) on UTS when Nozzle to plate distance (S) is kept constant: 316L Austenitic stainless steel

Surface plots are shown in figures 5.7-5.9. Interaction effects revealed in figures 5.8 (a-c) are comparatively less significant than those revealed in the figures 5.7 (a-c) and 5.9 (a-c). This means interaction among the factors Welding current (C) and Nozzle to plate distance (S) causes lesser influence on the response YS (figures 5.8 a-c) as compared to the interactions among the factors Gas flow rate (F) and Nozzle to plate distance(S) (figures 5.7 a-c), Welding current (C) and Gas flow rate (F) figures 5.9 (a-c).

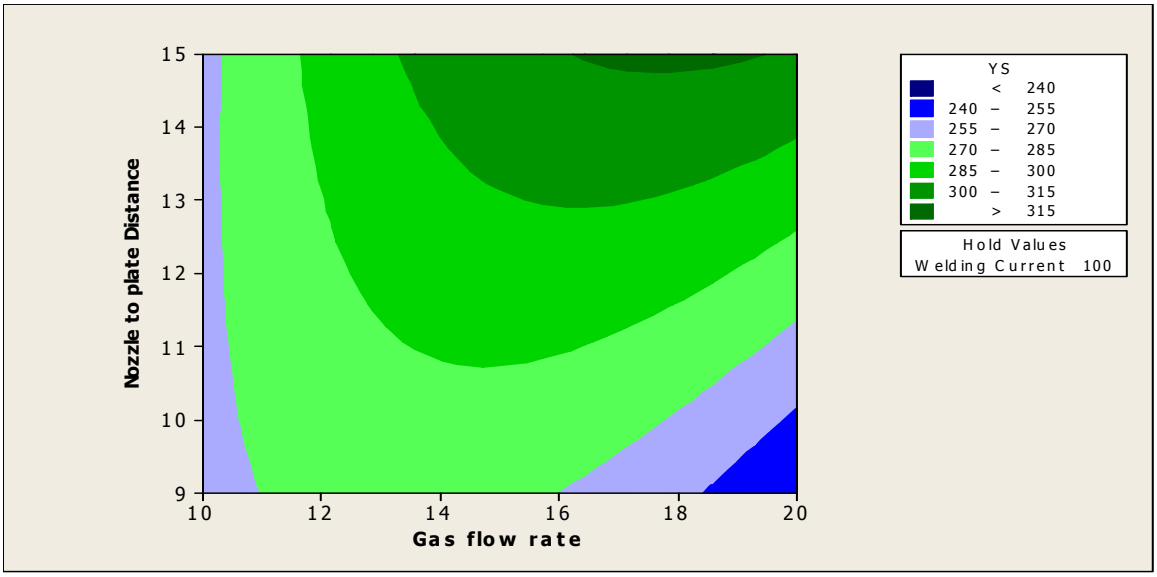

5.10(a) Welding current (C) constant at lowest level

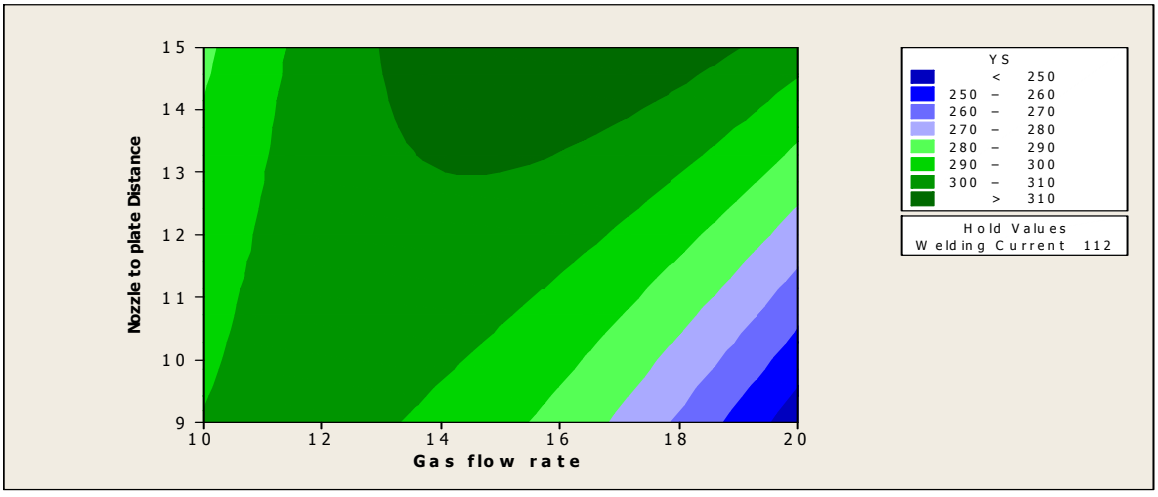

(5.10b) Welding current (C) constant at middle level

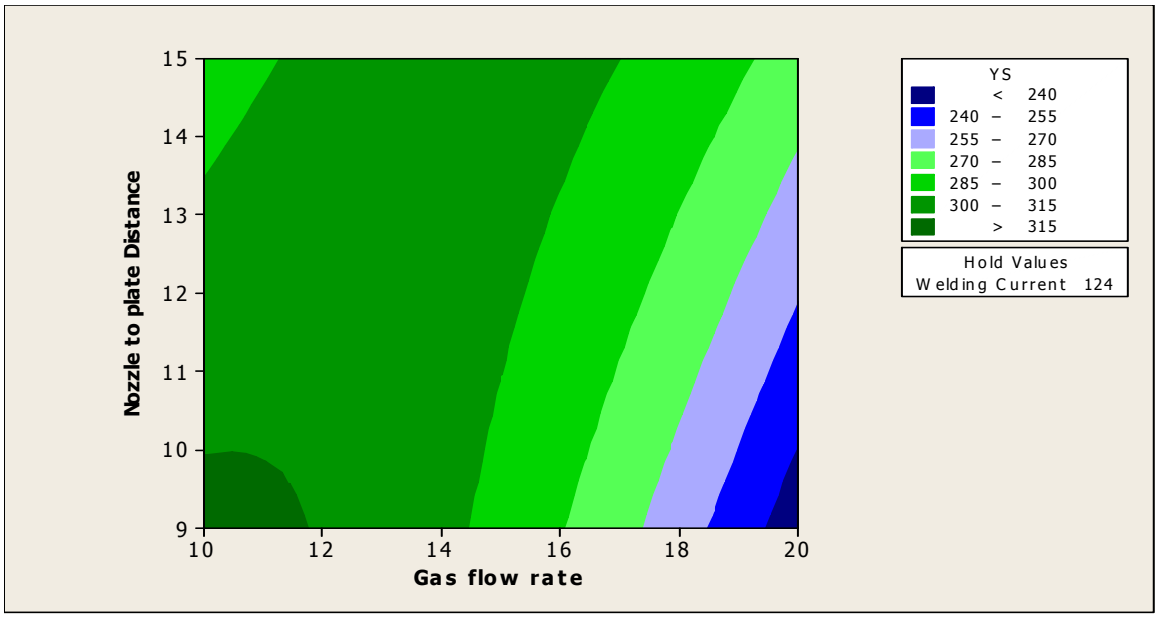

(5.10c) Welding current (C) constant at highest level

Figure 5.10 Contour plots showing combined effects of Gas flow rate (F) and Nozzle to plate distance (S) on YS when Welding current (C) is kept constant: 316L Austenitic stainless steel

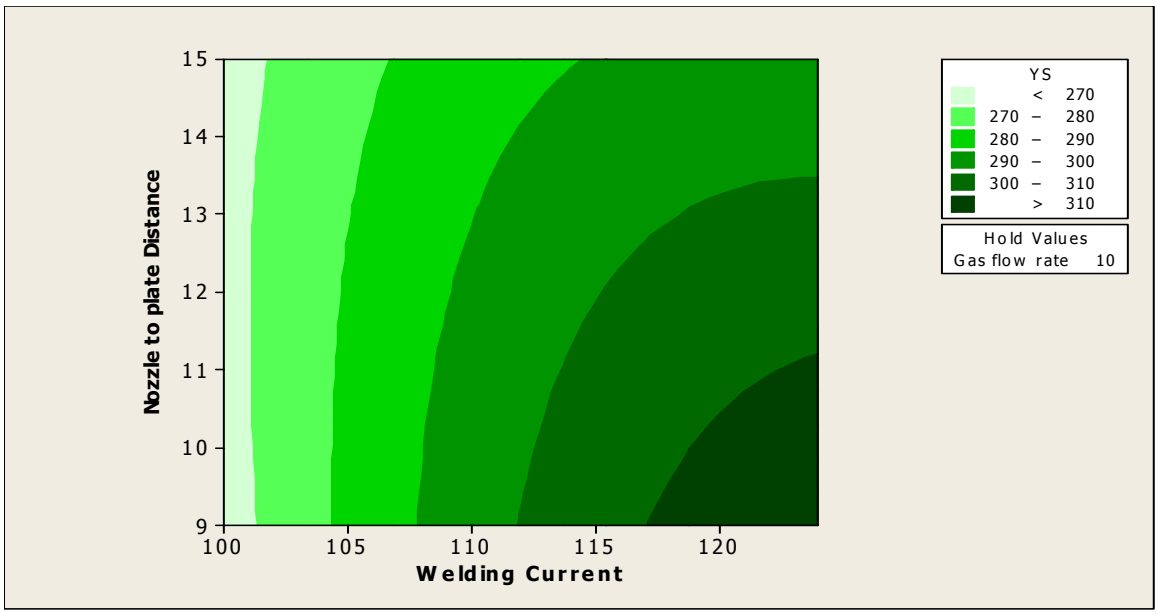

(5.11a) Gas flow rate (F) constant at lowest level

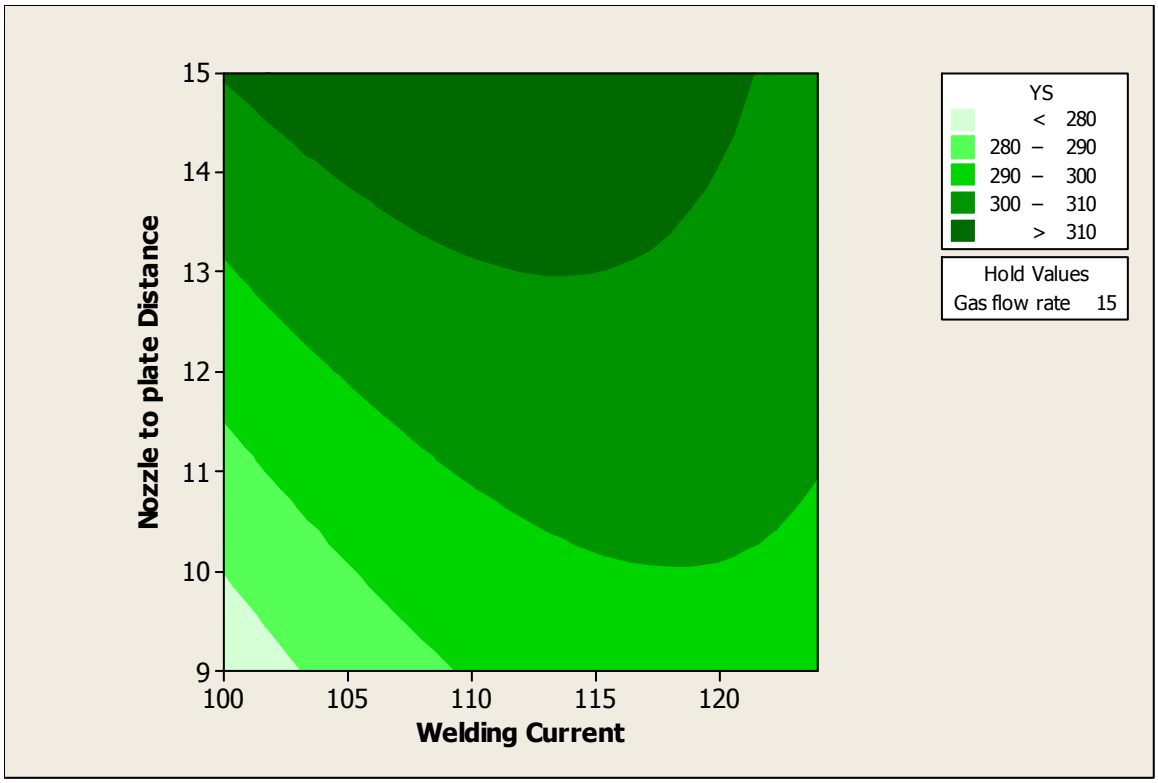

(5.11b) Gas flow rate (F) constant at middle level

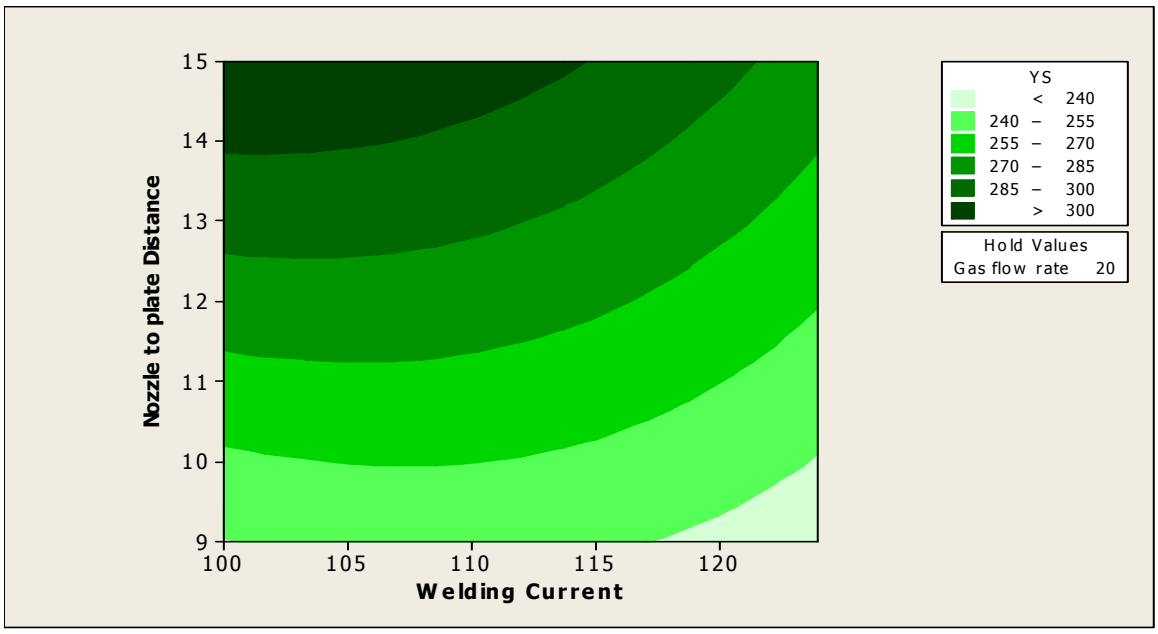

(5.11c) Gas flow rate (F) constant at highest level

Figure 5.11 Contour plots showing combined effects of Welding current (C) and Nozzle to plate distance (S) on YS when Gas flow rate (F) is kept constant: 316L Austenitic stainless steel

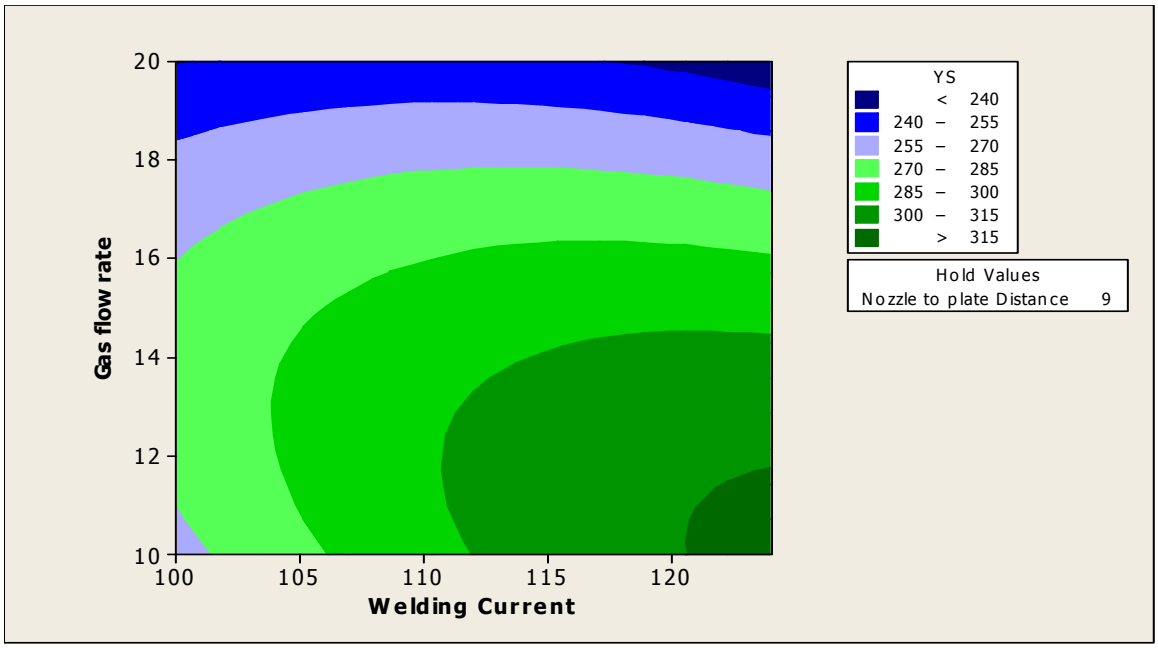

(5.12a) Nozzle to plate distance (S) constant at lowest level

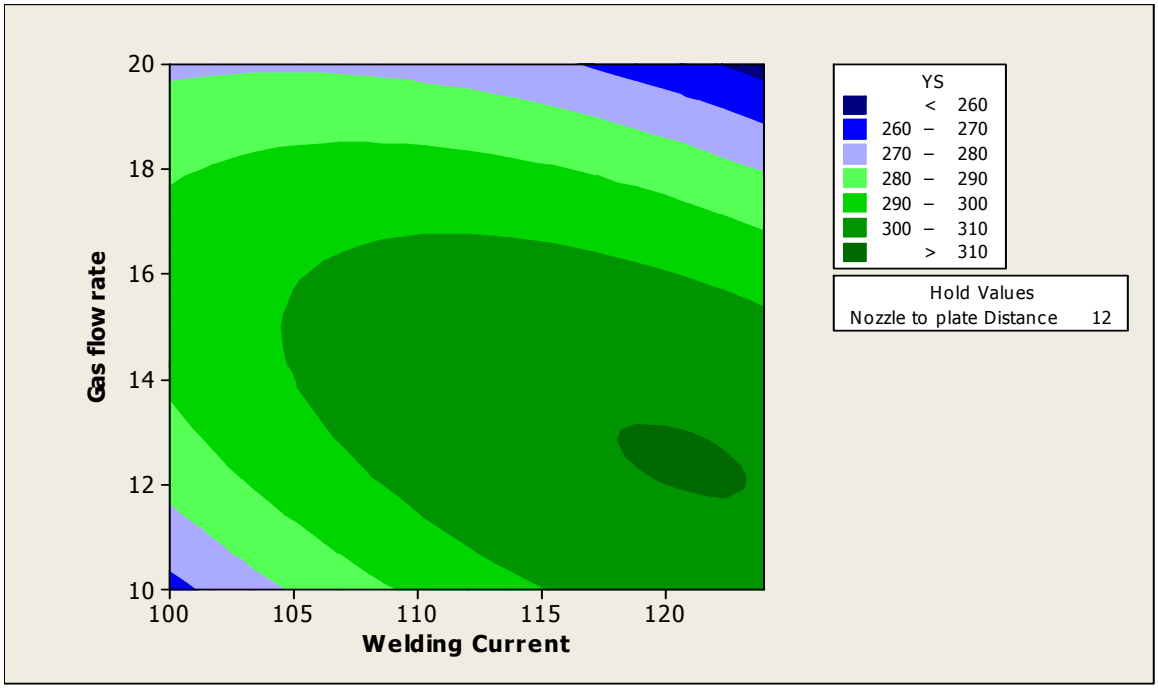

(5.12b) Nozzle to plate distance (S) constant at middle level

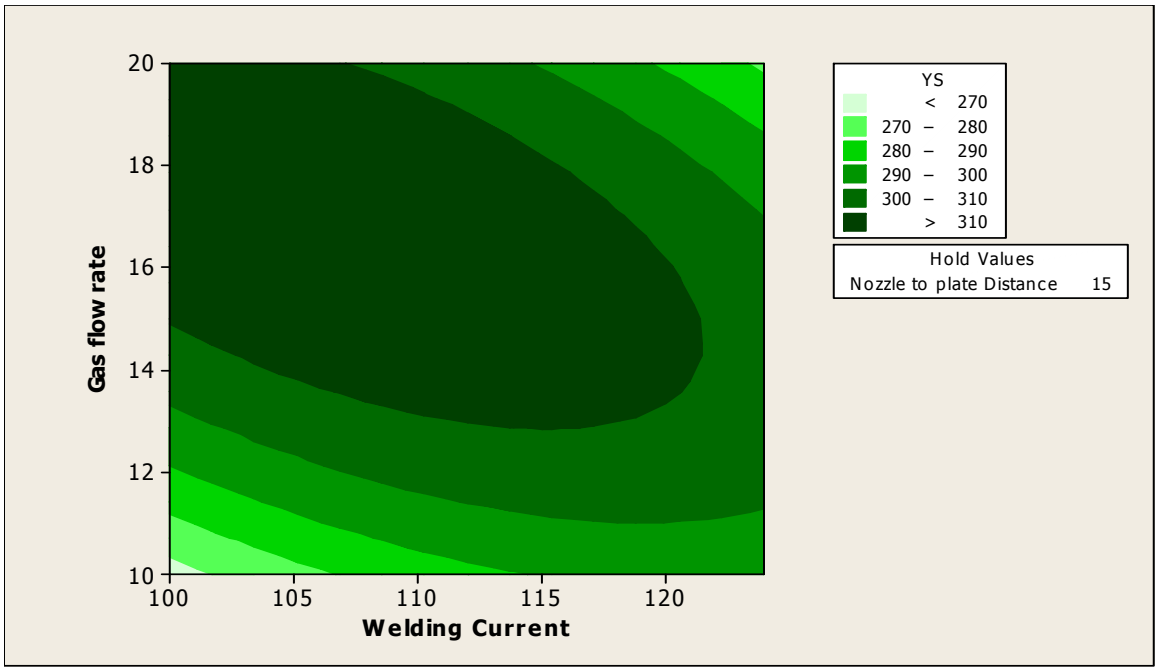

(5.12c) Nozzle to plate distance (S) constant at highest level

Figure 5.12 Contour plots showing combined effects of Welding current (C) and Gas flow rate (F) on YS when Nozzle to plate distance (S) is kept constant: 316L Austenitic stainless steel

Contour plots (shown in figures 5.10 – 5.12) can be interpreted and used in the same manner as discussed earlier. For example, interaction among the factors Welding current (C) and Gas flow rate (F) is found to be significant in so far as the effect of this interaction on YS is concerned (figures 5.12 a-c). Interaction effect of Gas flow rate (F) and Nozzle to plate distance (S) on YS is not so much significant, as revealed in figure 5.10c, while welding current is kept constant at 124A.

5.1.3 RESPONSE SURFACE ANALYSIS FOR PERCENTAGE ELONGATION (PE): 316L AUSTENITIC STAINLESS STEEL

Response surface generation and analysis of Percentage Elongation (PE) have been done using MINITAB 16 software. A model is developed to estimate PE. The adequacy of the developed model has been tested using ANOVA. Surface plots and contour plots for PE have also been presented.

A) MATHEMATICAL MODELLING

Percentage Elongation (PE) is expressed in terms of the process variables Welding current (C), Gas flow rate (F) and Nozzle to plate distance (S) as

$$PE = \beta_0 + \beta_1(C) + \beta_2(F) + \beta_3(S) + \beta_{11}(C*C) + \beta_{22}(F*F) + \beta_{33}(S*S) + \beta_{12}(C*F) + \beta_{13}(C*S) + \beta_{23}(F*S) \quad (5.5)$$

The equation derived is:

$$Y_{PE} = 36.2109 + 4.49(C) + 5.99(F) + 4.0600(S) + 2.3227(C*C) - 0.7773(F*F) + 2.7727(S*S) + 3.5250(C*F) + 2.150(C*S) + 0.050(F*S) \quad (5.6)$$

Here numerical values of C, F and S are to be used with same units as used earlier.

B) ANOVA OF THE MODEL

Analysis of variance (ANOVA) is carried out and the results are given in Table 5.3.

Table 5.3 ANOVA table for PE: 316L Austenitic stainless steel

Source	DF	Seq SS	Adj SS	Adj MS	F	P
Regression	9	944.96	944.958	104.995	2.04	**0.141**
Linear	3	725.24	725.238	241.746	4.69	0.027
Welding current	1	201.60	201.601	201.601	3.91	**0.076**
Gas flow rate	1	358.80	358.801	358.801	6.97	**0.025**
Nozzle to plate distance	1	164.84	164.836	164.836	3.20	**0.104**
Square	3	83.31	83.315	27.772	0.54	0.666
Welding current*Welding current	1	61.95	14.836	14.836	0.29	0.603
Gas flow rate*Gas flow rate	1	0.22	1.661	1.661	0.03	0.861
Nozzle to plate distance*Nozzle to plate distance	1	21.14	21.142	21.142	0.41	0.536
Interaction	3	136.40	136.405	45.468	0.88	0.483
Welding current*Gas flow rate	1	99.40	99.405	99.405	1.93	**0.195**
Welding current*Nozzle to plate distance	1	36.98	36.980			
Gas flow rate*Nozzle to plate distance	1	0.02	0.020			
Residual Error	10	515.04	515.044			
Lack-of-Fit	5	505.69	505.691			
Pure Error	5	9.35	9.353			
Total	19	1460.00				

(contd.)

Welding current*Nozzle to plate distance	36.980	0.72	0.417
Gas flow rate*Nozzle to plate distance	0.020	0.00	0.985
Residual Error	51.504		
Lack-of-Fit	101.138	54.07	0.000
Pure Error	1.871		
Total			

S = 7.17666 PRESS = 6194.56
R-Sq = 64.72% R-Sq(pred) = 0.00% R-Sq(adj) = 32.97%

From Table 5.3, it is seen that P-value of the regression equation is P = 0.141 which is very close to P = 0.1 (90% confidence level). It supports the validity of the proposed regression model. **F** in Table 5.3 is different from the symbol F used as a nomenclature of Gas flow rate. From ANOVA it is observed that, Gas flow rate (F) is the most significant factor affecting the response PE as it has the lowest P value (P = 0.025), followed by Welding current(C) (P = 0.076) and Nozzle to plate distance (S) (P = 0.104). At 95% confidence level Gas flow rate is the only significant factor as its P value is less than 0.05. Among the others, inner interaction terns, Welding current * Gas flow rate (C*F) (P = 0.195) have higher significance. The determination factor (R^2) indicates the goodness of fit of the model. The value of R^2 of this model is 64.72% which is greater than 64 %. This implies that at least 64% of the variability in data for the response is explained by the model. This indicates that the proposed model is roughly adequate, though not precisely.

C) SURFACE PLOTS AND CONTOUR PLOTS FOR PE

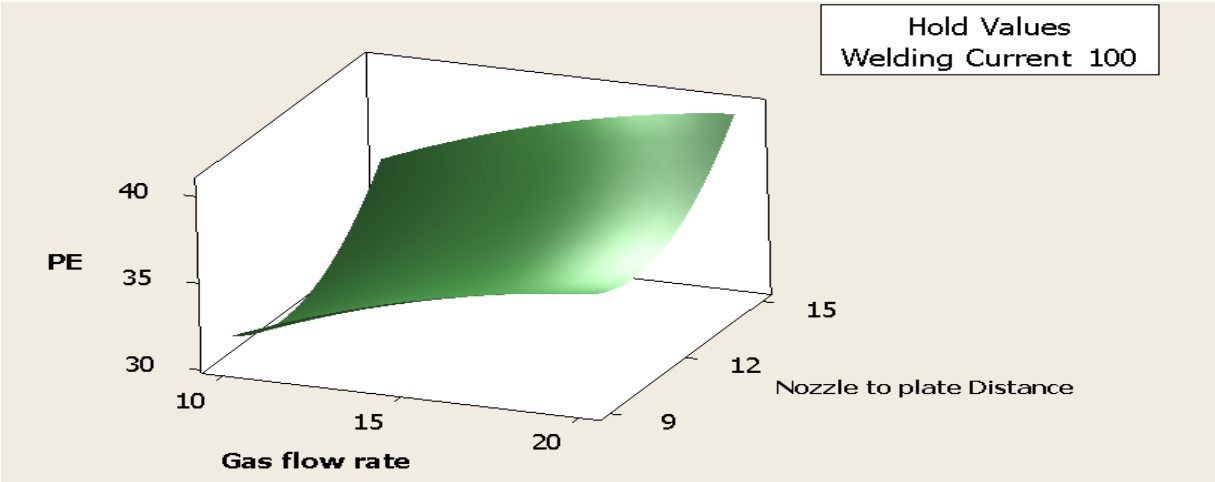

(5.13a) Welding Current (C) constant at lowest level

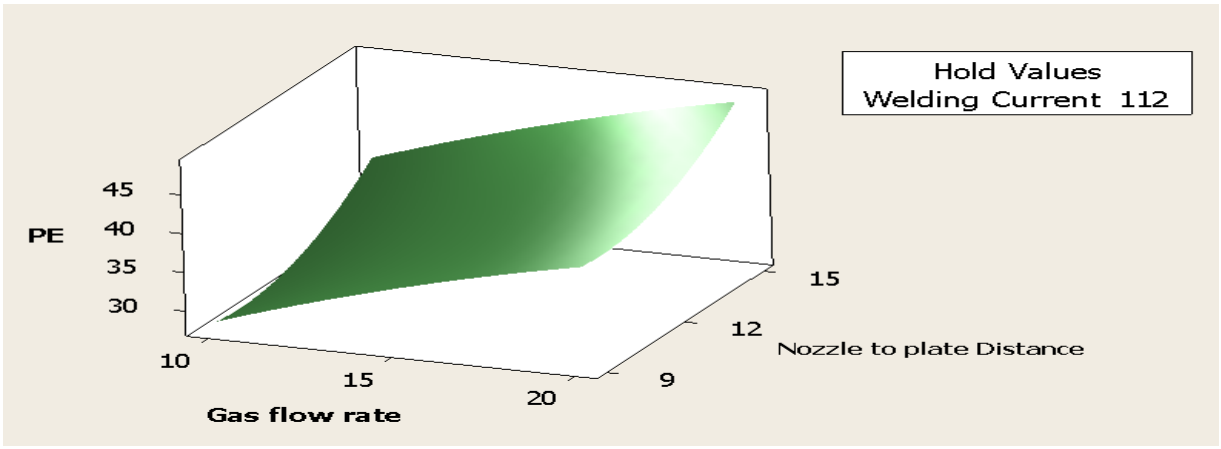

(5.13b) Welding current (C) constant at middle level

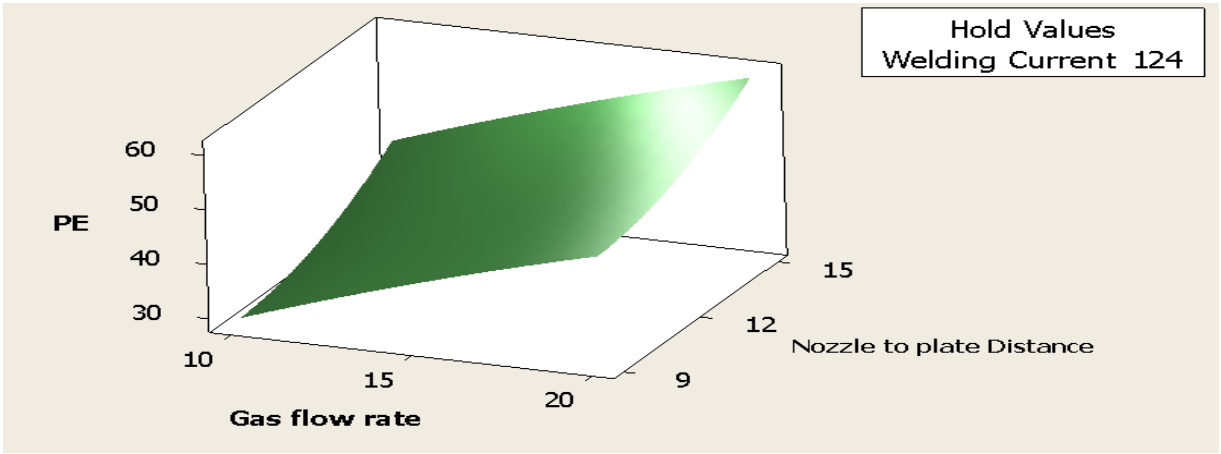

(5.13c) Welding current (c) constant at highest level

Figure 5.13 Response surface plots showing combined effects of Gas flow rate (F) and Nozzle to plate distance(S) on PE when Welding current (C) is kept constant: 316L Austenitic Stainless steel

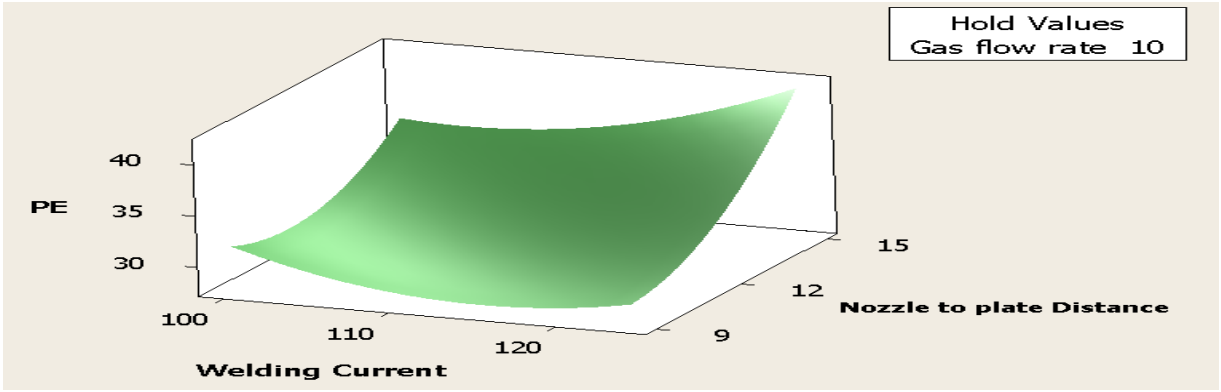

(5.14a) Gas flow rate (F) constant at lowest level

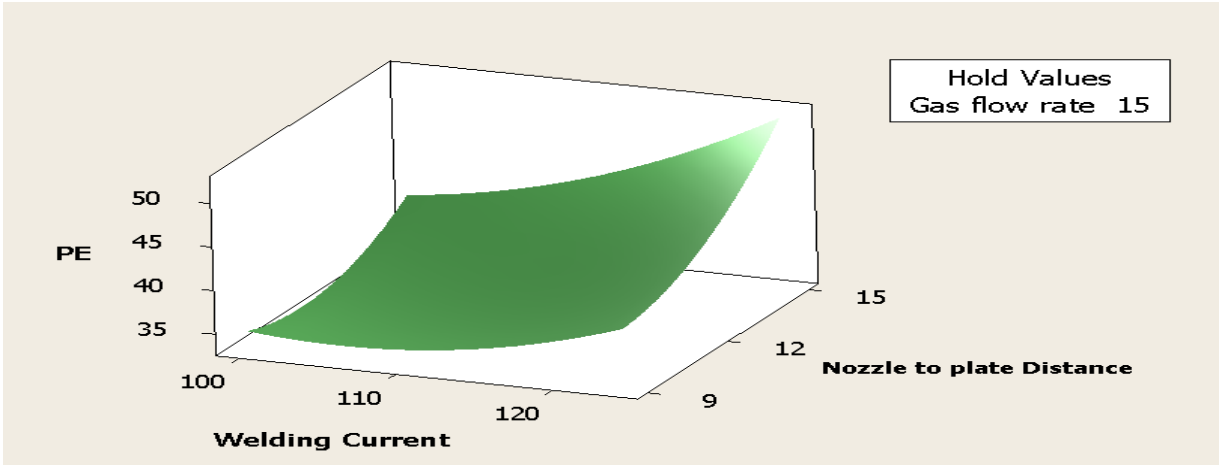

(5.14b) Gas flow rate (F) constant at middle level

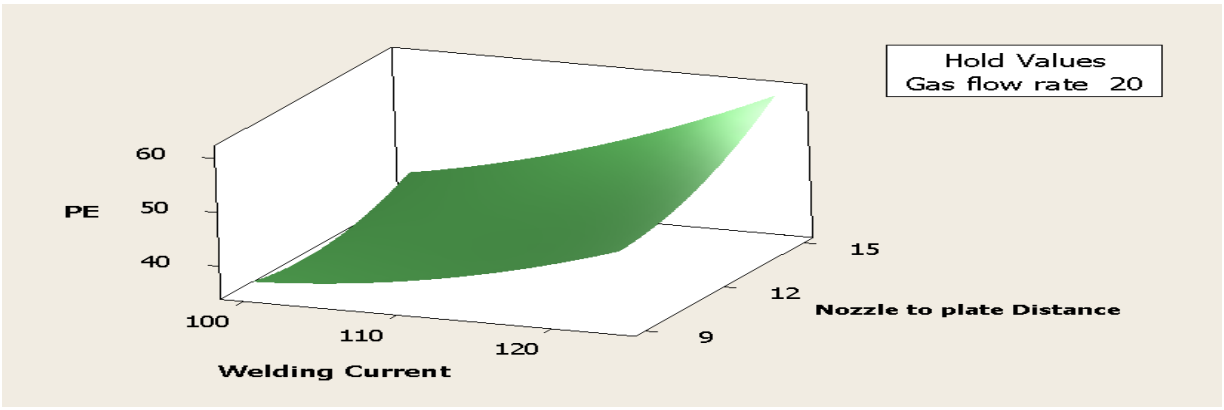

(5.14c) Gas flow rate (F) constant at highest level

Figure 5.14 Response surface plots showing combined effects of Welding current (C) and Nozzle to plate distance (S) on PE when Gas flow rate (F) is kept constant: 316L Austenitic stainless steel

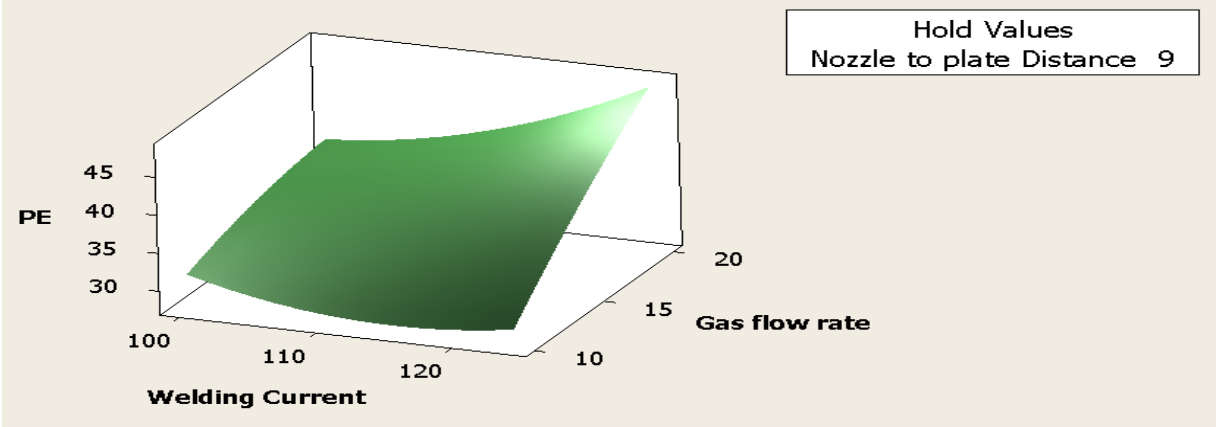

(5.15a) Nozzle to plate distance (S) constant at its lowest level

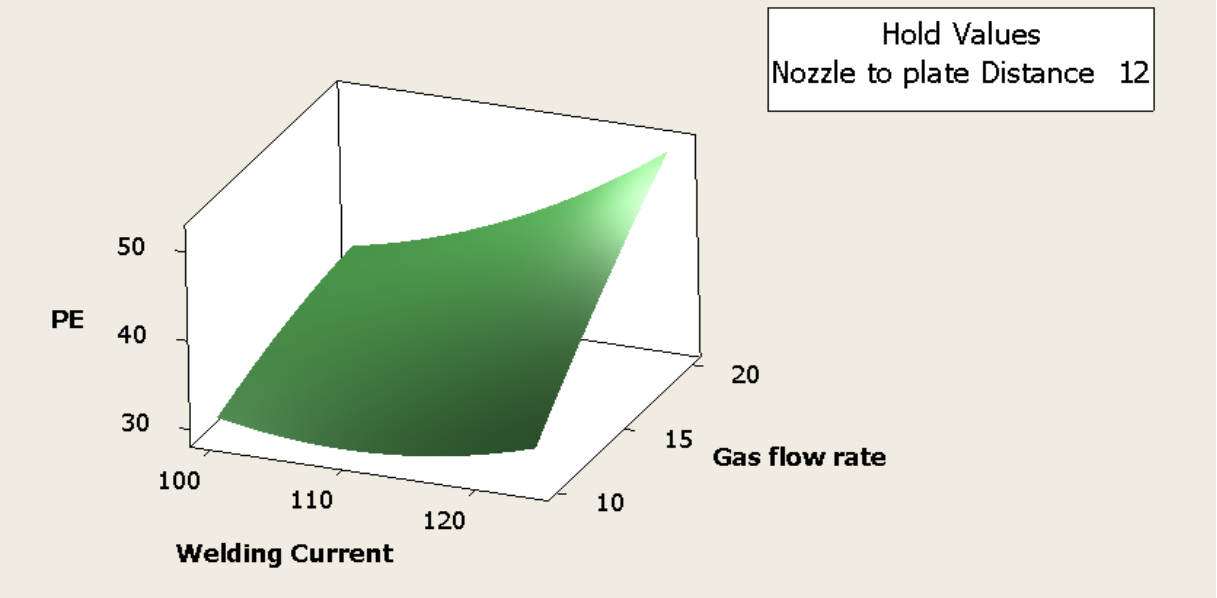

(5.15b) Nozzle to plate distance (S) constant at middle level

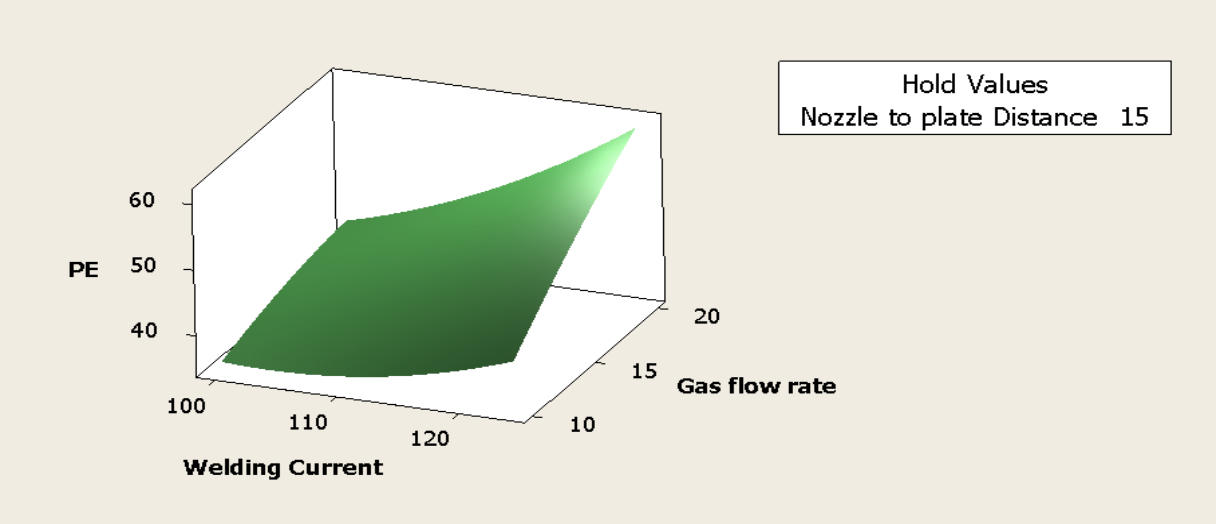

(5.15c) Nozzle to plate distance (S) constant at highest level

Figure 5.15 Response surface plots showing combined effects of Welding current (C) and Gas flow rate (F) on PE when Nozzle to plate distance(S) is kept constant: 316L Austenitic stainless steel

Surface plots are shown in figures 5.13-5.15. Interaction effects revealed in figures 5.13 (a-c) are comparatively less significant than those revealed in the figures 5.14 (a-c) and 5.15 (a-c). This

means interaction among the factors Gas flow rate (F) and Nozzle to plate distance (S) causes lesser influence on the response PE (figures 5.13 a-c) as compared to the interactions among the factors Welding current (C) and Nozzle to plate distance(S) (figures 5.14 a-c), Welding current (C) and Gas flow rate (F) figures 5.15 (a-c).

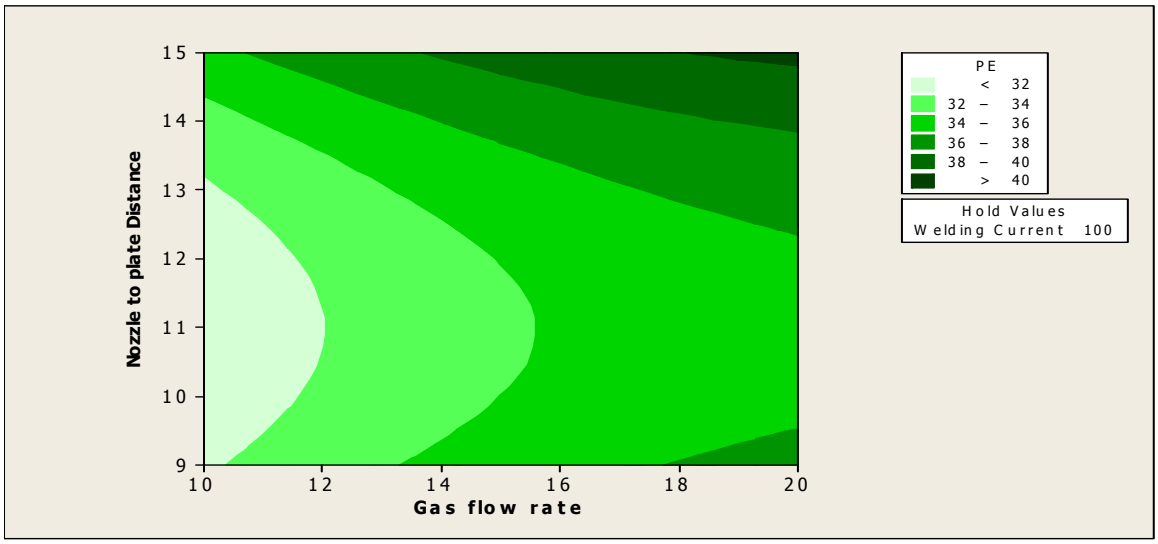

(5.16a) Welding current (C) constant at lowest level

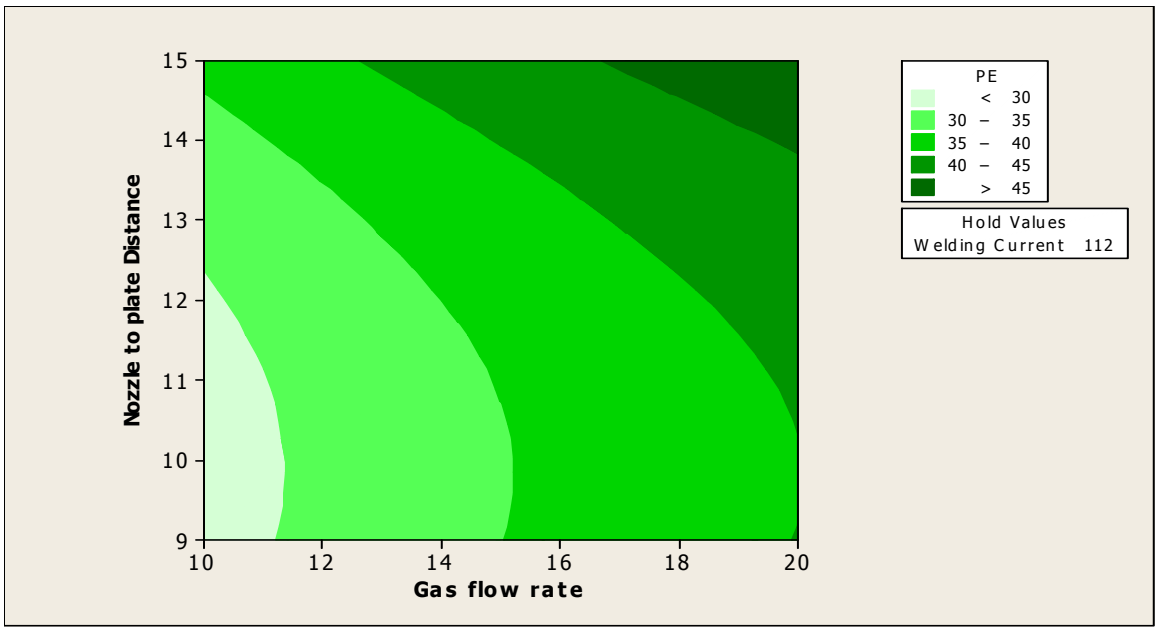

(5.16b) Welding current (C) constant at middle level

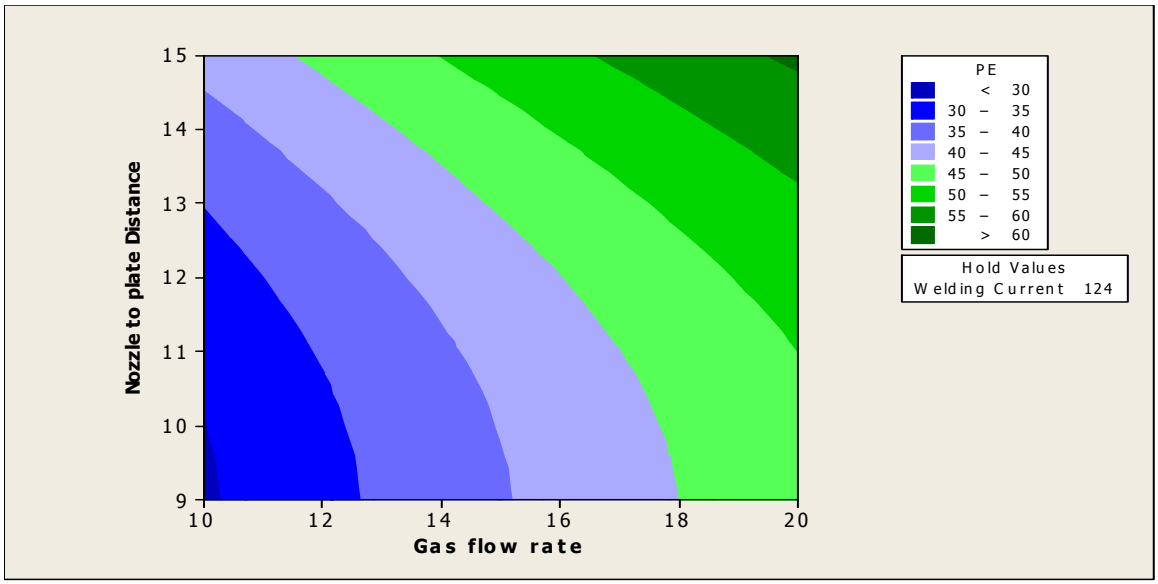

(5.16c) Welding current (C) constant at highest level

Figure 5.16 Contour plots showing combined effects of Nozzle to plate distance (S) and Gas flow rate(F) on PE when Welding current (C) is kept constant: 316L Austenitic stainless steel

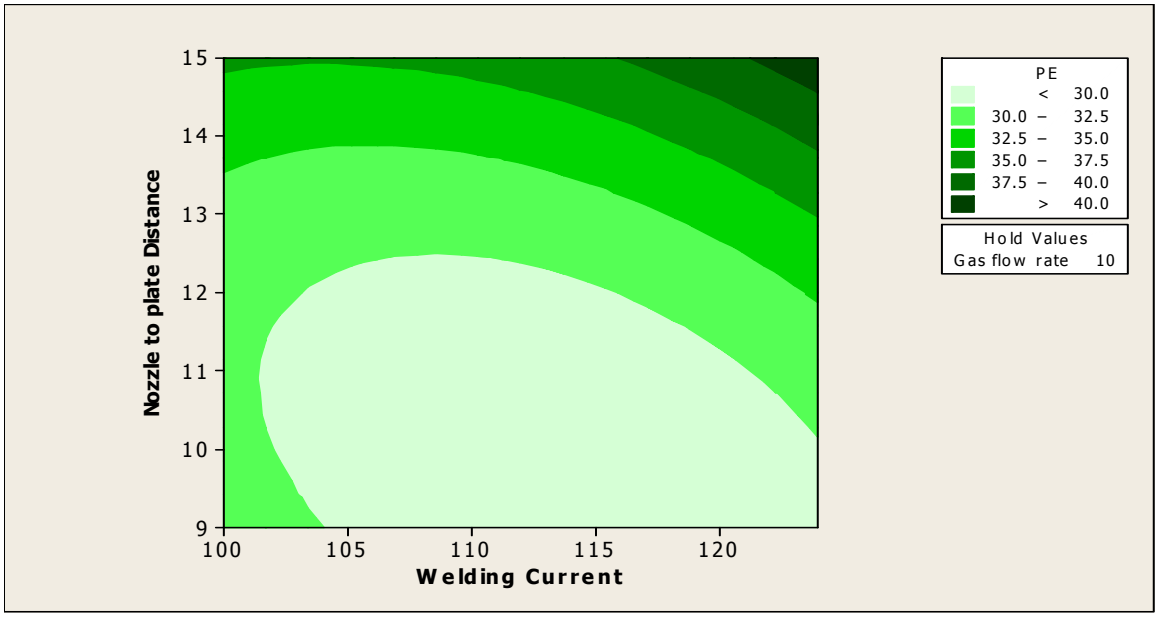

(5.17a) Gas flow rate (F) constant at lowest level

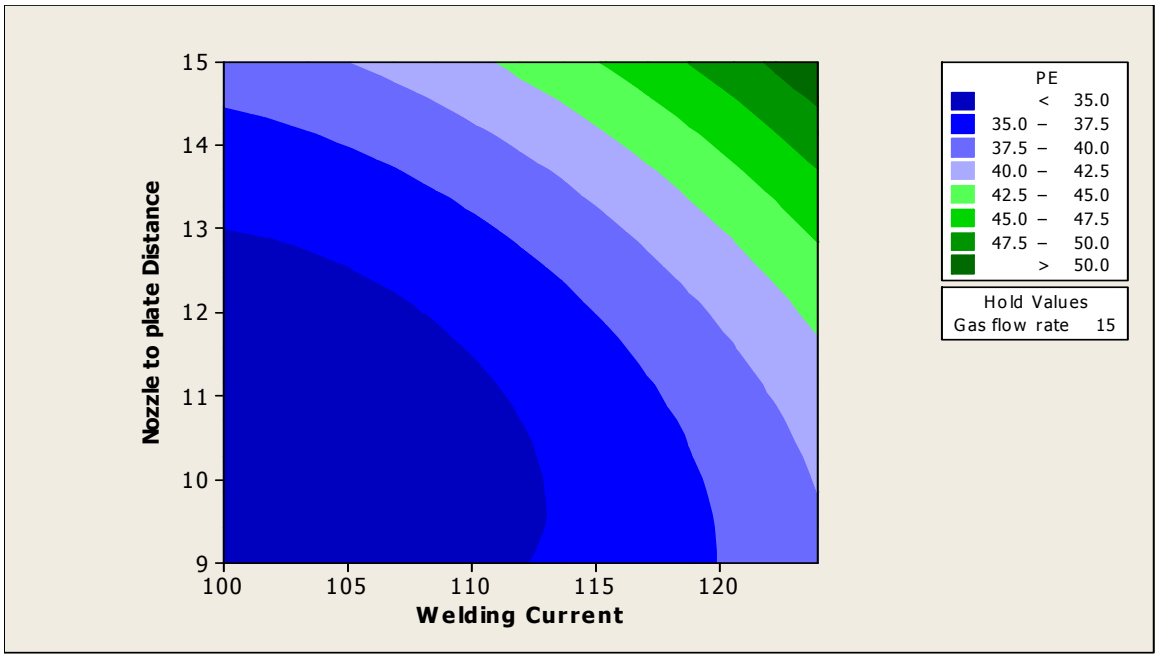

(5.17b) Gas flow rate (F) constant at middle level

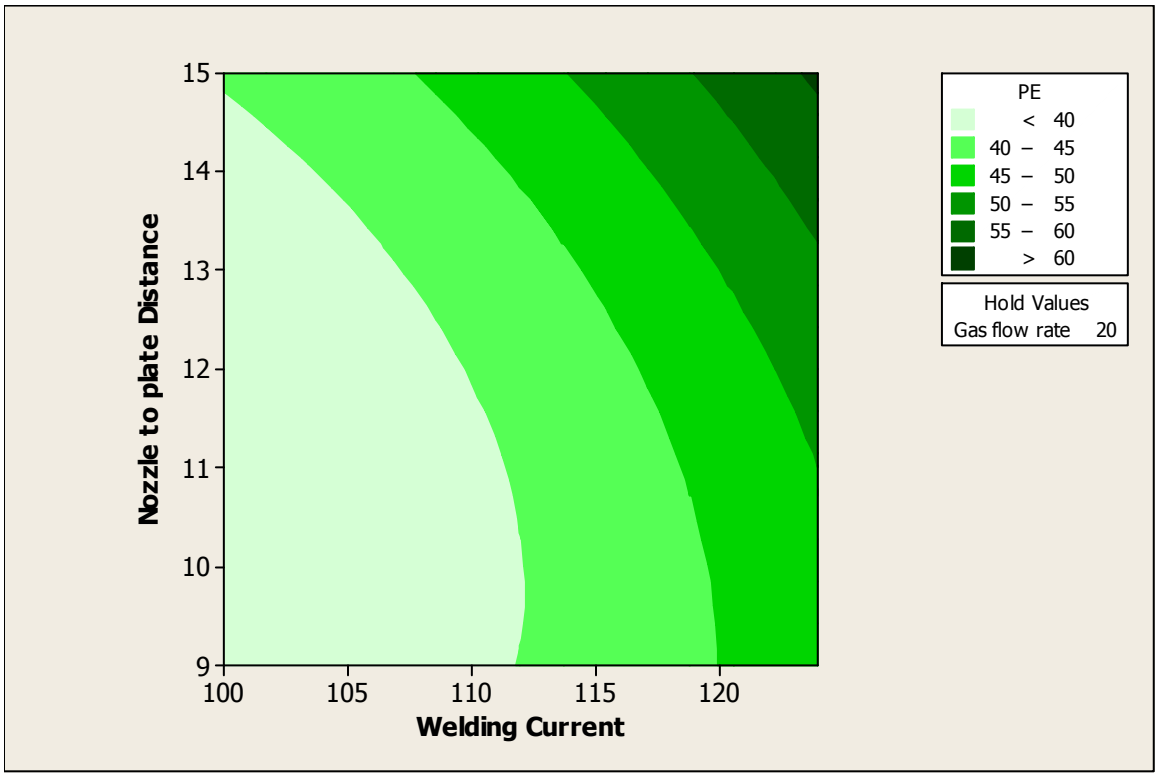

(5.17c) Gas flow rate (F) constant at highest level

Figure 5.17 Contour plots showing combined effects of Welding current (C) and Nozzle to plate distance (S) on PE when Gas flow rate (F) is kept constant: 316L Austenitic stainless steel

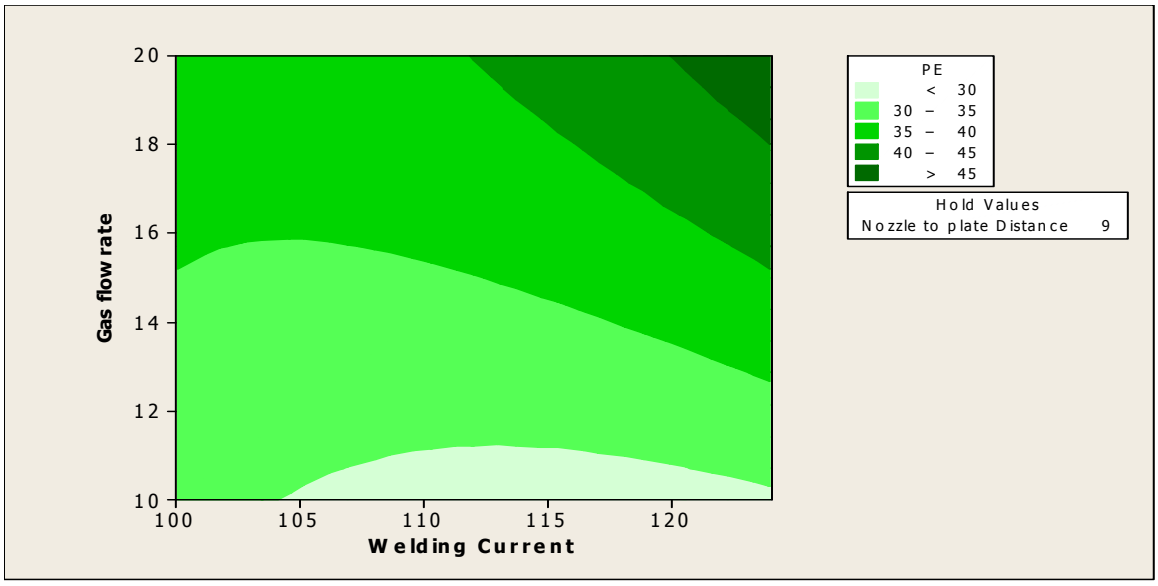

(5.18a) Nozzle to Plate Distance (S) constant at lowest level

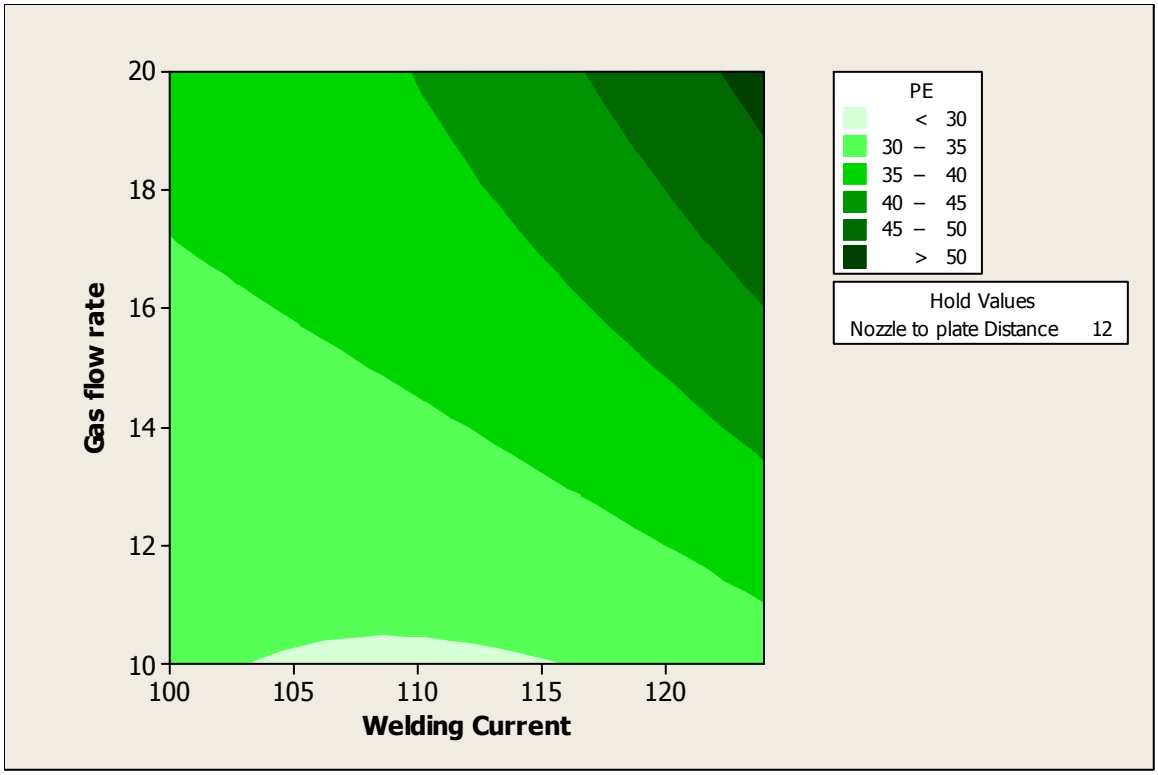

(5.18b) Nozzle to Plate Distance (S) constant at middle level

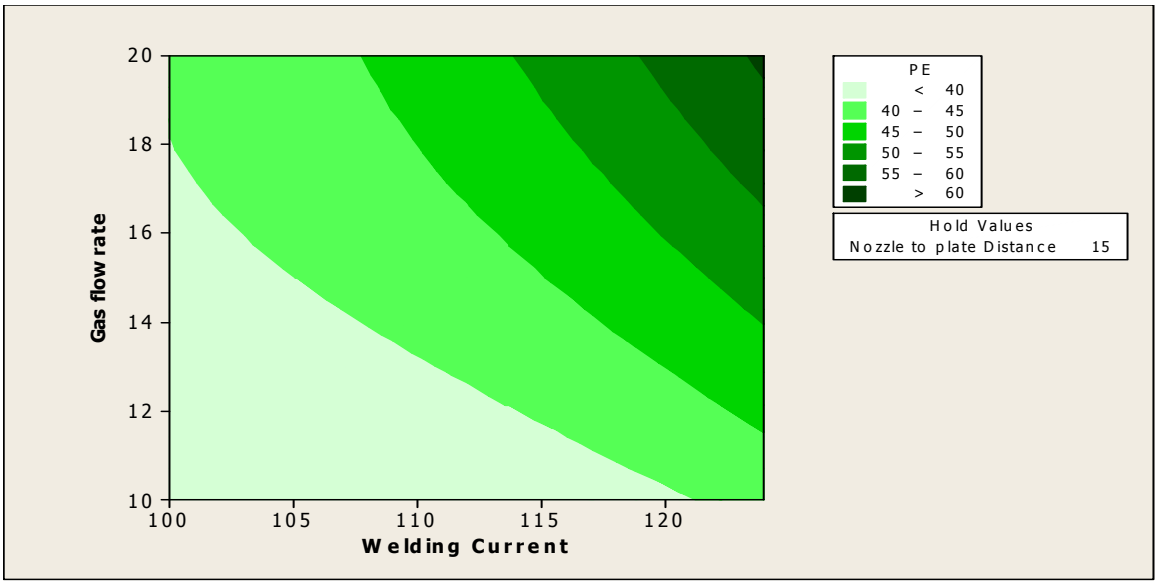

(5.18c) Nozzle to Plate Distance (S) constant at highest level

Figure 5.18 Contour plots showing combined effects of Welding current (C) and Gas flow rate(F) on PE when Nozzle to plate distance (S) is kept constant: 316L Austenitic stainless steel

Contour plots (shown in figures 5.16 – 5.18) give indication of the interaction effects. Each constant response line in these plots can be used to select several combinations of any two input parameters to achieve the desired value of the particular response. In the present case, interaction among the factors Welding current (C) and Nozzle to plate distance (S) is found to be significant in so far as the effect of this interaction on PE is concerned (figures 5.17 a-c). Interaction effect of Gas flow rate (F) and Welding current on PE is not so much significant, as revealed in figure 5.18c, while Nozzle to plate distance is kept constant at 15mm. This is based on what has been explained in some earlier sections.

5.1.4 PROCESS OPTIMIZATION: MIG WELDING OF 316L AUSTENTIC STAINLESS STEEL

For process optimization, multiple objective optimizations have been carried out in all the three separate sets of study: MIG welding of i) 316L Austenitic stainless steel ii) 409 Ferritic stainless steel and iii) 316L Austenitic to 409 Ferritic stainless steel. The following sections deal for the

first set. Single objective optimization has been carried by RSM philosophy. Multi-objective optimization has been done by two techniques: RSM and Grey based Taguchi Method.

5.1.4.1 SINGLE-OBJECTIVE OPTIMIZATION BY RSM: 316L AUSTENITIC STAINLESS STEEL

One of the main objectives of the study is to optimize the responses by identifying the best parametric condition. Here RSM is used for single-objective optimization of ultimate tensile strength, yield strength and percentage elongation separately. UTS and YS are the major design criterion of a welded sample which gives the idea about the maximum load it can withstand. Percentage elongation gives the idea of the ductility of the joint. The purpose of the optimization is to maximize both.

A) SINGLE-OBJECTIVE OPTIMIZATION OF UTS BY RSM

The optimized parametric condition for UTS by RSM is shown in the figure 5.19. This is obtained by using the observed results given in Table 4.3 of chapter 4 and using the MINITAB 16 software for solving single objective optimization problem using RSM. The optimized UTS are 577.4135 MPa with desirability 0.88412. The optimized parametric combination is Welding current C = 112.36 A, Gas flow rate F =16.06 *l*/min and Nozzle to plate distance S = 15 mm. This is observed from the figure 5.19.

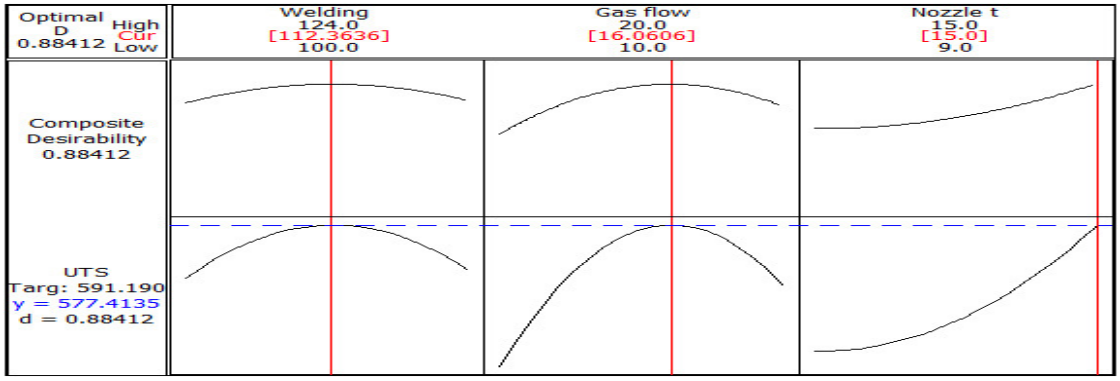

Figure 5.19 Response optimization plot for UTS: 316L Austenitic stainless steel

Confirmatory test

Confirmatory test has been conducted at the optimized parametric setting i.e., Welding current (C) = 112 A, Gas flow rate (F) = 16 *l*/min and Nozzle to plate distance= 15 mm. Results of tensile test of the sample show that UTS of the sample is 570.25 MPa, which is very close to the optimized UTS by RSM. Optimum condition is thus confirmed.

B) SINGLE-OBJECTIVE OPTIMIZATION OF YS BY RSM

The optimized parametric condition for YS by RSM is shown in the figure 5.20. This is obtained by using the observed results given in Table 4.3 of chapter 4 and using the MINITAB 16 software for solving single objective optimization problem using RSM. The optimized YS value is 318.303 MPa with desirability 0.76438. The optimized parametric combination is Welding current C = 124 A, Gas flow rate F =10 *l*/min and Nozzle to plate distance S = 9 mm.

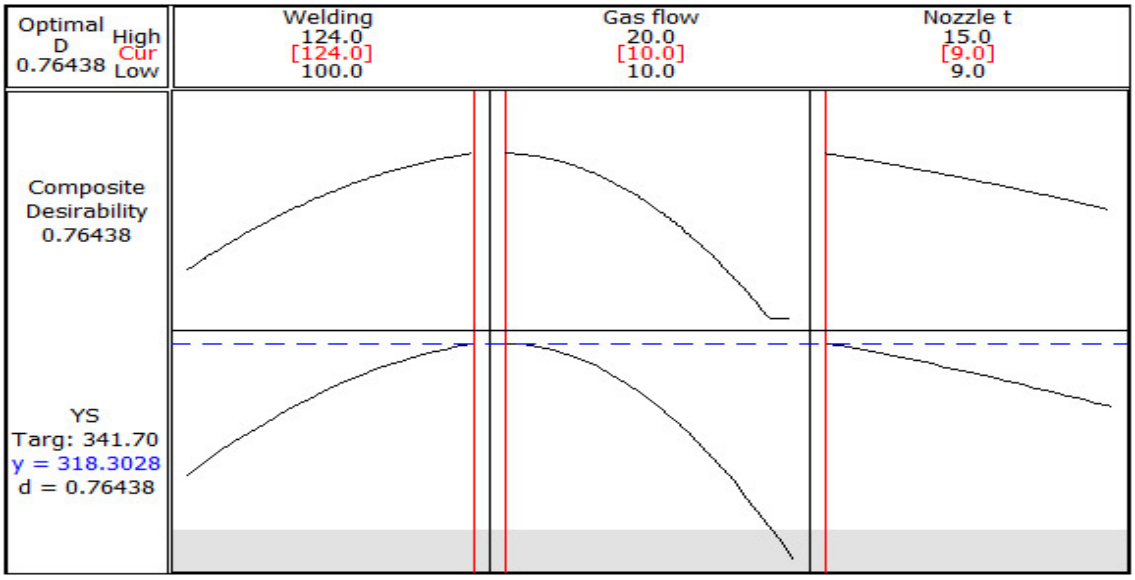

Figure 5.20 Response optimization plot for YS: 316L Austenitic stainless steel

Confirmatory test

Confirmatory test has been conducted at the optimized parametric setting i.e., at Welding current (C)= 124 A, Gas flow rate (F) = 10 l/min and Nozzle to plate distance= 9 mm. Results of tensile test of the sample show that YS of the sample is 313 MPa, which is very close to the optimized YS determined by RSM. Validation of optimum condition is thus obtained.

C) SINGLE-OBJECTIVE OPTIMIZATION OF PE BY RSM

The optimized parametric condition for PE by RSM is shown in figure 5.21. The data contained in Table 4.3, chapter 4 are taken for the purpose. MINITAB 16 software is used, objective being single objective optimization by RSM. The optimized PE is 45% with desirability 1.0000. The optimized parametric combination is Welding current C = 123 A, Gas flow rate F =18 *l*/min and Nozzle to plate distance S = 9 mm. This is as per the results shown in figure 5.21.

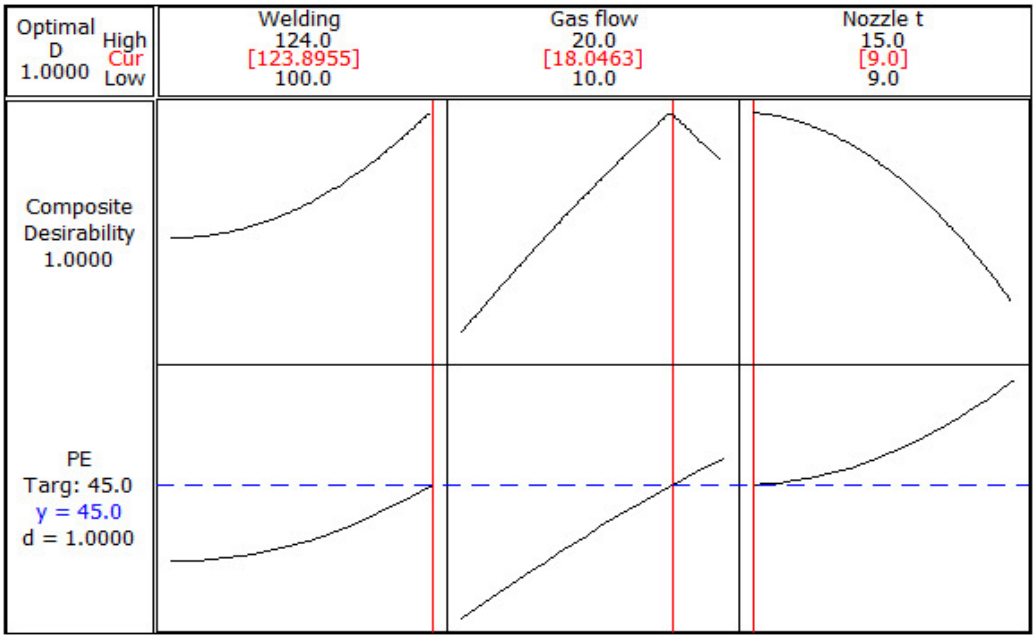

Figure 5.21 Response optimization plot for PE: 316L Austenitic stainless steel

Confirmatory test

A confirmatory test of the welded sample made by using optimum parametric setting i.e. current (C)= 123 A, gas flow rate (F) = 18 *l*/min and Nozzle to plate distance= 9 mm , show that PE of the sample is 43% , which is not much away from the optimized value by RSM. This validates the results of RSM optimization.

5.1.4.2 MULTI-OBJECTIVE OPTIMIZATION BY RSM: 316L AUSTENITIC STAINLESS STEEL

MINITAB 16 software has a toolbox for carrying out multi-objective optimization by RSM. This has been used using the data given in Table 4.3, in chapter 4. Multi-response optimization plot for UTS, YS and PE is shown in figure 5.22. From this figure it is observed that the optimum condition is: current C = 111.8 A, gas flow rate F = 17.17 *l*/min and Nozzle to plate distance= 15mm. The corresponding UTS is 576.0464 MPa with desirability = 0.87263 and YS is 316.6009 MPa with desirability = 0.74724 and PE is 44.91% with desirability =0.99502.

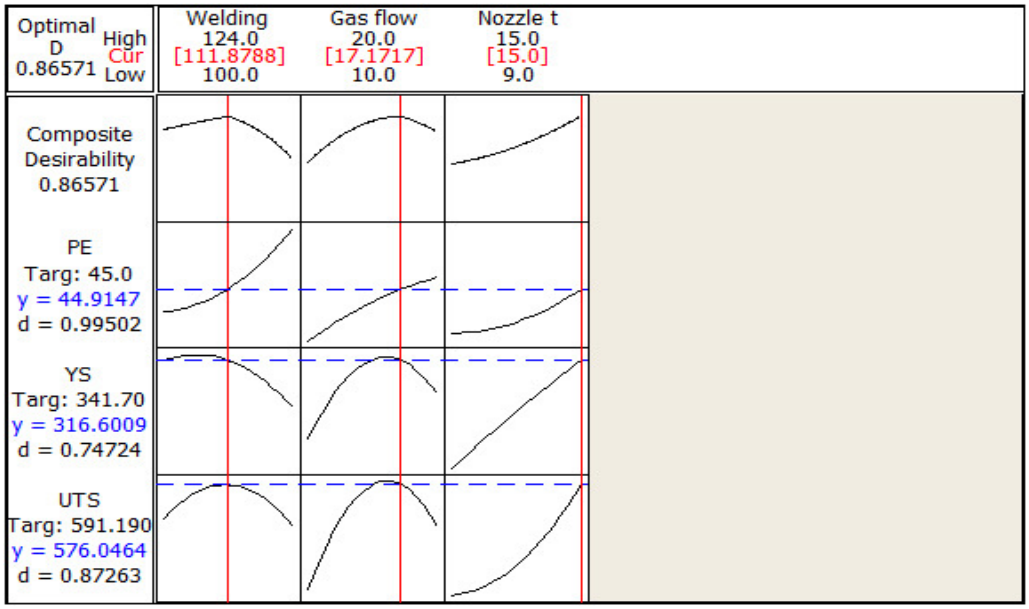

Figure 5.22 Multi-response optimization plot of UTS, Yield strength (YS) and PE: 316L Austenitic stainless steel

Confirmatory test

Confirmatory test done at the optimized parametric combination for UTS, YS and PE i.e., at current (C) = 111.8 A, gas flow rate (F) = 17.2 *l*/min and Nozzle to plate distance = 15 shows that UTS of the sample is 560.02 MPa and YS of the sample is 310 MPa and PE is 41%. These values are very close to the optimized UTS, YS and PE values determined by RSM. Thus optimal condition is confirmed. Confirmatory tensile test diagram is shown in figure 5.23

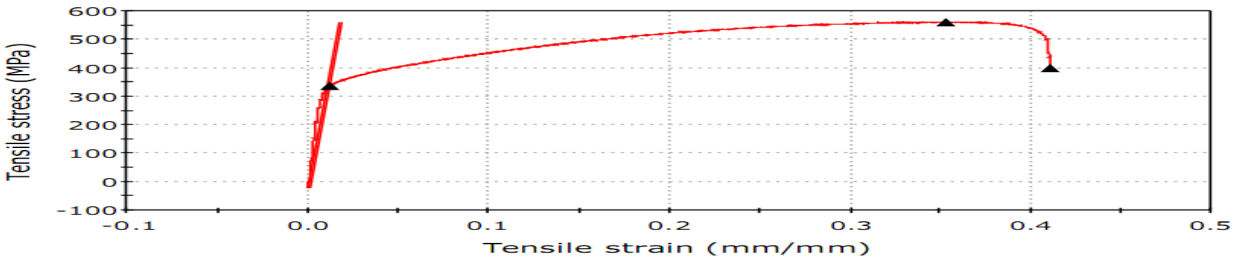

Figure 5.23 Confirmatory tensile test: optimization plot for AISI 316L Austenitic stainless steel as per RSM design of experiment

5.1.5 MULTI – OBJECTIVE OPTIMIZATION BY GREY BASED TAGUCHI METHOD: 316L AUSTENITIC STAINLESS STEEL

Multi-objective optimization has also been done by Grey based Taguchi method. Linear normalization of the experimental data is performed in the range between zero and unity, which is also called Grey relational generating. Experimental data are obtained from Table 4.7, chapter 4. Normalization of experimental data is calculated based on eq. (2.9) ─ larger the better criterion.

Normalization of experimental data is shown in Table 5.4.

Table 5.4 Normalization of experimental data based on L9Taguchi Orthogonal Array design of experiment: 316L Austenitic stainless steel

Sample No.	Yield strength(MPa)	Ultimate tensile strength (MPa)	Percentage of elongation(%)
S1A	0.98216	0.75076	0.35278
S2A	0.94649	0.76289	0.44722
S3A	1.00000	1.00000	1.00000
S4A	0.62207	0.55791	0.40278
S5A	0.19175	0.03699	0.00000
S6A	0.34783	0.33475	0.40556
S7A	0.10479	0.00000	0.02778
S8A	0.15273	0.35597	0.67500
S9A	0.00000	0.14979	0.27500

Grey Relation Coefficients are shown in Table 5.5. Grey Relation coefficients for 316L: L9 Taguchi orthogonal array design of experiment are calculated by using eq. (2.10)

Table 5.5 Grey Relation Coefficients: 316L Austenitic stainless steel as per L9Taguchi Orthogonal Array design of experiment

Sample No.	Grey Relation Coefficient		
	Yield strength (YS)	Ultimate tensile strength (UTS)	Percentage of elongation(%)
S1A	0.96555	0.66734	0.43584
S2A	0.90332	0.67832	0.47493
S3A	1.00000	1.00000	1.00000
S4A	0.56952	0.53074	0.45570
S5A	0.38219	0.34176	0.33333
S6A	0.43396	0.42909	0.45685
S7A	0.35837	0.33333	0.33962
S8A	0.37112	0.43705	0.60606
S9A	0.33333	0.37031	0.40816

After averaging the grey relation coefficients, the grey relational grade γ_i can be computed by using eq. (2.11) . The grey relational grades γ_i are shown in Table 5.6.

Table 5.6 The grey relational grades: 316L Austenitic stainless steel as per L9 Taguchi Orthogonal Array design of experiment

Sample No.	Grey relational grade
S1A	0.68958
S2A	0.68553
S3A	1.00000
S4A	0.51865
S5A	0.35243
S6A	0.43997
S7A	0.34378
S8A	0.47141
S9A	0.37060

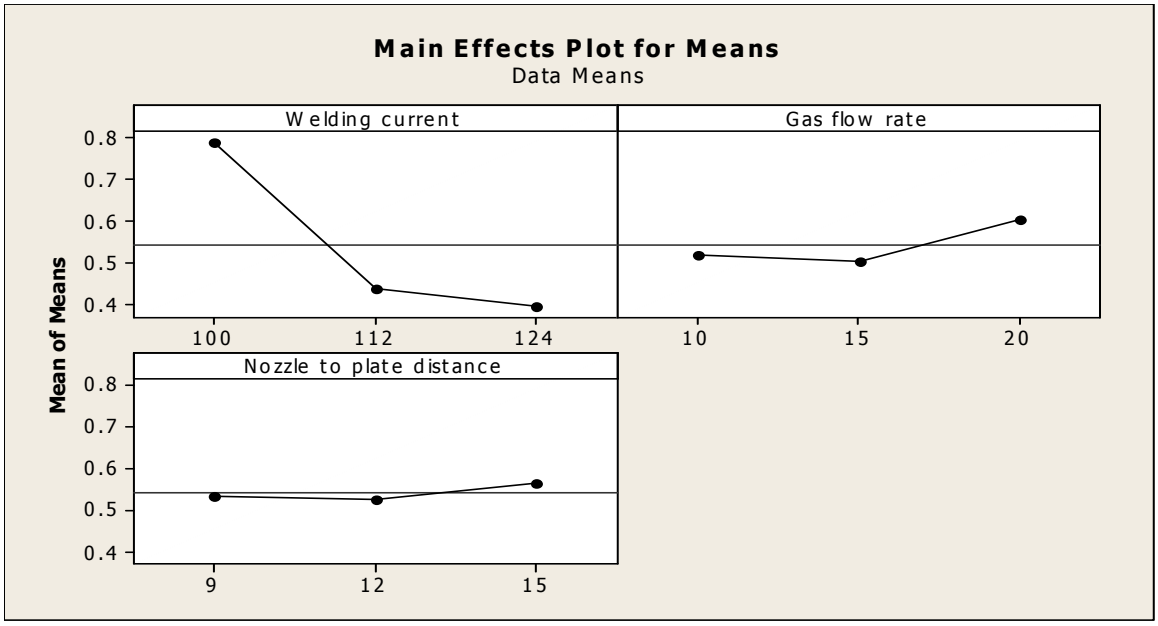

Figure 5.24 Main Effects Plot for mean grey relational grade:316L Austenitic stainless steel

With the help of Main effects plot of the means: grey relational grade (figure 5.24) optimum parametric combination has been determined. The optimal factor setting becomes **C1F3S3** (i.e. welding current = 100 A, Gas flow rate = 20 *l*/min and Nozzle to plate distance =15mm).

Confirmatory test

Confirmatory test has been conducted at the optimized parametric combination for UTS and Yield strength i.e., at Welding current (C) = 100 A, Gas flow rate (F) = 20 *l*/min and Nozzle to plate distance = 15 mm and confirmatory tensile test diagram is shown in figure 5.25. Results of tensile test of the sample show that measured UTS of the sample is 570.34 MPa and YS of the sample is 315 MPa and PE is 42%: all of these values are very close to the optimized UTS, YS and percentage elongation values determined by Grey- Taguchi method. Thus optimal condition is validated.

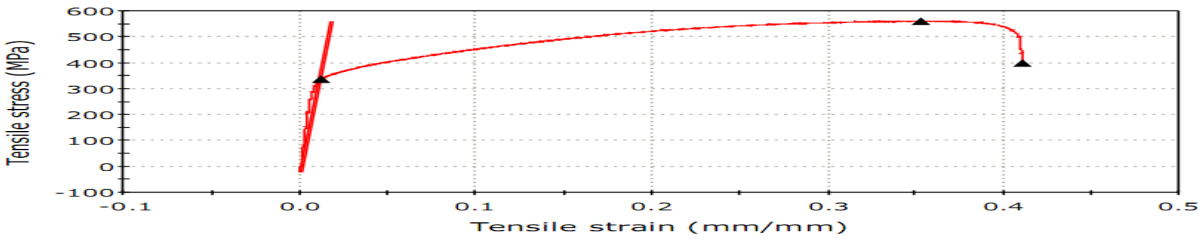

Figure 5.25 Confirmatory tensile test: optimization plot for AISI 316L Austenitic stainless steel as per L9 Taguchi Orthogonal Array design of experiment

Analysis of Variance for overall grey relation grade is shown in Table 5.7.

Table 5.7 Analysis of Variance for overall grey relation grade: 316L Austenitic stainless steel as per L9 Taguchi Orthogonal Array design of experiment

Source	DF	Seq SS	Adj SS	Adj MS	F	P	Percentage of contribution
Welding current	2	0.28471	0.28471	0.14235	4.22	0.192	76.39
Gas flow rate	2	0.01771	0.01771	0.00886	0.26	0.792	4.75
Nozzle to plate distance	2	0.00272	0.00272	0.00136	0.04	0.961	0.72
Error	2	0.06754	0.06754	0.03377			18.14
Total	8	0.37268					

S = 0.183771 R-Sq = 81.88% R-Sq(adj) = 27.51%

Where

DF = Degree of freedom

SS = Sum of squared deviation = $\sum_{i}^{n}(y_i - y)^2$

Where, y_i is the observed S/N ratio value of response, n is the number of observation or experiment number and y is the mean of S/N ratio.

MS = Mean squared deviation = SS/DF

F = Fisher test *(The terms used in all the ANOVA tables are the standard terms with usual significance).*

Pie- Chart and line diagram of Percentage of contribution: 316L Austenitic stainless steel are shown in figures 5.26 and 5.27 respectively.

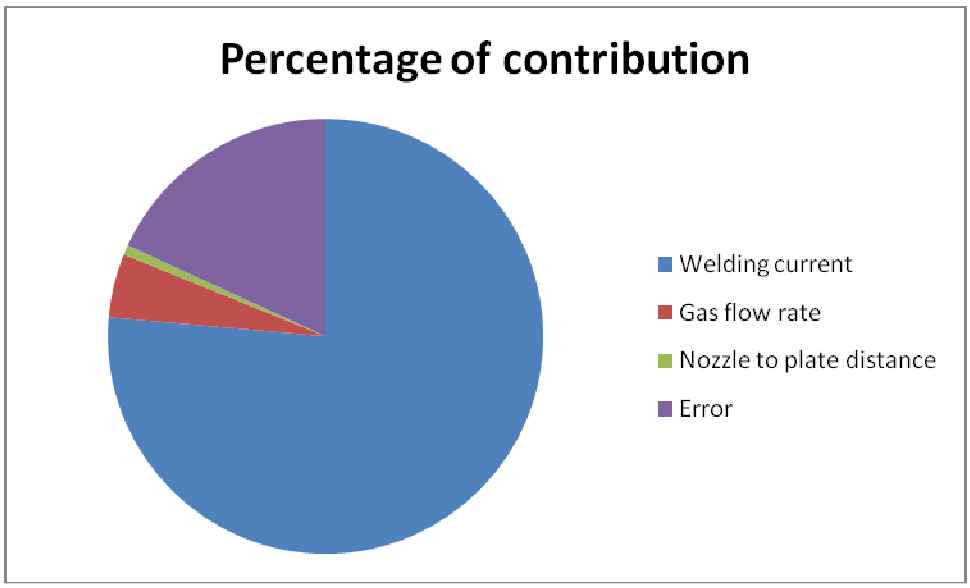

Figure 5.26 Pie Chart of Percentage of contribution: 316L Austenitic stainless steel

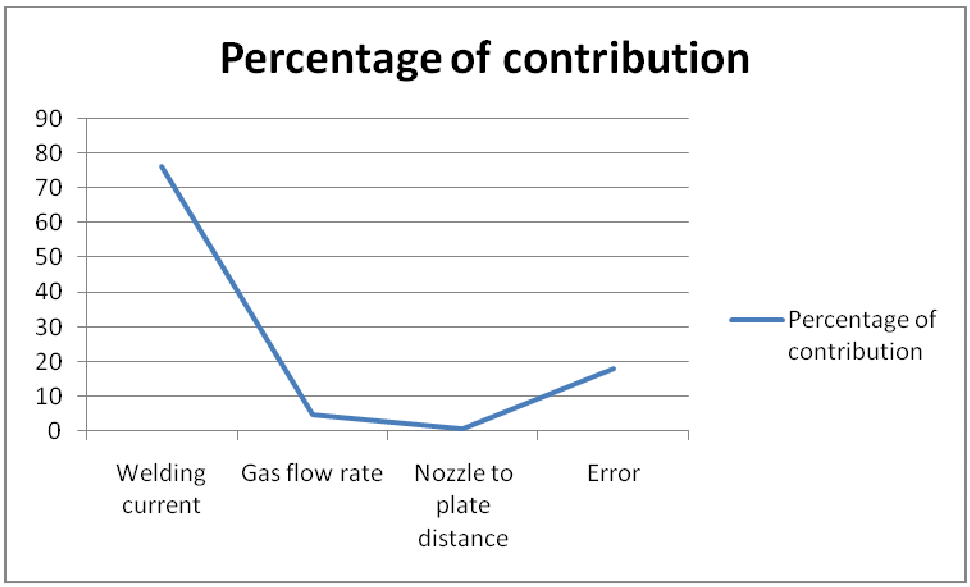

Figure 5.27 Percentage of contribution: 316L Austenitic stainless steel

ANOVA of overall grey relational grade (Table 5.7) has revealed that the most important factor influencing grey relation grade is Welding current (C) as it has the lowest P value (P = 0.192)

and followed by Gas flow rate (F) (P=0.792) and Nozzle to plate distance (S) (P=0.961). These are also identified from figures 5.26 and 5.27.

5.1.6 COMPARISONS OF MULTI OBJECTIVE OPTIMIZATION RESULTS DONE BY GREY-TAGUCHI METHOD AND RSM: 316L AUSTENITIC STAINLESS STEEL

Optimal parametric condition for multi objective optimization has been determined by Taguchi method and RSM method for each of the responses UTS, YS and PE.

By Grey-Taguchi method, the optimal parametric condition is found: Welding current (C) = 100 A, Gas flow rate (F) = 20 *l/*min and Nozzle to plate distance = 15 mm and by RSM, optimized parametric condition is found: Welding current (C) = 111.8 A, Gas flow rate (F) = 17.2 l/min and Nozzle to plate distance = 15. The response values, at optimal parametric condition are shown in Table 5.8.

Table 5.8 Multi-objective optimization values for 316L Austenitic stainless steel by Taguchi and RSM

Technique	UTS (MPa)	YS (MPa)	PE(%)
Response Surface Methodology (RSM)	560.02 MPa	310 MPa	41.0
Grey-Taguchi Method	570.34MPa	315MPa	42.0

Thus, the above observations lead to the fact that the results of multiple objective optimizations may be considered reliable, acceptable. Particularly, the results from Taguchi Method appear to be somewhat more useful as the corresponding UTS, YS and PE values are larger, and these are confirmed by confirmatory test.

5.2 ANALYSIS: RESULTS OF MIG WELDING OF 409 FERRITIC STAINLESS STEEL (2ND SET OF EXPERIMENTS)

The results of MIG welding of 409 Ferritic stainless steel as per RSM design of experiment and L9 Taguchi orthogonal array design of experiment are analyzed, in the following sections.

5.2.1 RESPONSE SURFACE ANALYSIS OF TENSILE TEST FOR YS: 409 FERRITIC STAINLESS STEEL

Through regression analysis, using the data contained in Table 4.10 in chapter 4, a mathematical model for prediction of YS is developed, as a part of RSM. The adequacy of the model has been checked using ANOVA. Surface plots and contour plots for YS have also been drawn.

A) MATHEMATICAL MODELLING

Yield Strength (YS) has been expressed in terms of the process parameters i.e., Welding current (C), Gas flow rate (F) and Nozzle to Plate distance (S) using the following form. The form of equation is already mentioned in eq. (5.1), chapter 5.

$$YS = \beta_0 + \beta_1(C) + \beta_2(F) + \beta_3(S) + \beta_{11}(C*C) + \beta_{22}(F*F) + \beta_{33}(S*S) + \beta_{12}(C*F) + \beta_{13}(C*S) + \beta_{23}(F*S) \quad (5.7)$$

The final mathematical model to estimate per Yield strength is given as

$$Y_{YS} = -1326.07 + 17.61(C) + 6.61(F) + 133.55(S) - 0.08(C*C) + 1.90(F*F) - 7.39(S*S) - 0.48(C*F) + 0.46(C*S) - 1.000(F*S) \quad (5.8)$$

Where Y_{YS} is in MPa, C is in A, F is in *l/min* and S is in mm

B) ANOVA OF THE MODEL

The adequacy of the developed model is checked using ANOVA technique and the results of this analysis are listed in Table 5.9

Table 5.9 ANOVA table for YS: 409 Ferritic stainless steel

Source	DF	Seq SS	Adj SS	
Regression	9	47409.1	47409.1	
Linear	3	20076.4	20076.4	
Welding current	1	13868.2	13868.2	
Gas flow rate	1	1468.9	1468.9	
Nozzle to plate distance	1	4739.3	4739.3	
Square	3	16601.1	16601.1	
Welding current*Welding current	1	2780.1	409.6	
Gas flow rate*Gas flow rate	1	1639.9	6229.7	
Nozzle to plate distance*Nozzle to plate distance	1	12181.1	12181.1	
Interaction	3	10731.6	10731.6	
Welding current*Gas flow rate	1	6745.4	6745.4	
Welding current*Nozzle to plate distance	1	2201.2	2201.2	
Gas flow rate*Nozzle to plate distance	1	1785.0	1785.0	(contd.)

Residual Error	10	9497.1	9497.1
Lack-of-Fit	5	9471.7	9471.7
Pure Error	5	25.3	25.3
Total	19	56906.2	

Source	Adj MS	F	P
Regression	5267.7	5.55	**0.007**
Linear	6692.1	7.05	0.008
Welding current	13868.2	14.60	**0.003**
Gas flow rate	1468.9	1.55	**0.242**
Nozzle to plate distance	4739.3	4.99	**0.050**
Square	5533.7	5.83	0.014
Welding current*Welding current	409.6	0.43	0.526
Gas flow rate*Gas flow rate	6229.7	6.56	**0.028**
Nozzle to plate distance*Nozzle to plate distance	12181.1	12.83	**0.005**
Interaction	3577.2	3.77	0.048
Welding current*Gas flow rate	6745.4	7.10	**0.024**
Welding current*Nozzle to plate distance	2201.2	2.32	0.159
Gas flow rate*Nozzle to plate distance	1785.0	1.88	0.200
Residual Error	949.7		
Lack-of-Fit	1894.3	373.66	0.000
Pure Error	5.1		
Total			

S = 30.8173 PRESS = 64093.8
R-Sq = 83.31% R-Sq(pred) = 0.00% R-Sq(adj) = 68.29%

From Table 5.9, it is seen that P-value of the regression equation is P = 0.007 which is lower than the P value (P = 0.05) corresponding to 95% confidence level. It highly supports the validity of the proposed regression model. From the statistical analysis it is obtained that in so far as the input parameters are considered individually, Welding current is the most significant factor affecting the response: yield strength, having the lowest corresponding P factor (P = 0.003) followed by Nozzle to plate distance (P = 0.050) and Gas flow rate (P = 0.242). Among the inner interaction terms, F-F and S-S have higher significances with P values 0.028 and 0.005 respectively. Among the cross interaction terms, i.e., C-F shows high significance, with P value 0.024. The determination factor (R^2) indicates goodness of fit of the model. The value R^2 of this model is 83.31%. This implies that at least 83.3% of the variability in data for the response can be explained by this model. This indicates that the model is adequate.

C) SURFACE PLOTS AND CONTOUR PLOTS FOR YIELD STRENGTH

Surface plots are shown in figures 5.28-5.30. Interaction effects indicated in figures 5.30 (a-c) are comparatively less significant than those indicated in figures 5.28 (a-c) and 5.29 (a-c). This means interaction among the factors Welding current (C) and Gas flow rate (F) causes lesser influence on the response YS (figures 5.30 a-c) as compared to the interaction among the factors

Gas flow rate (F) and Nozzle to plate distance(S) (figures 5.28 a-c), Welding current (C) and Nozzle to plate distance (S)[figures 5.29(a-c)].

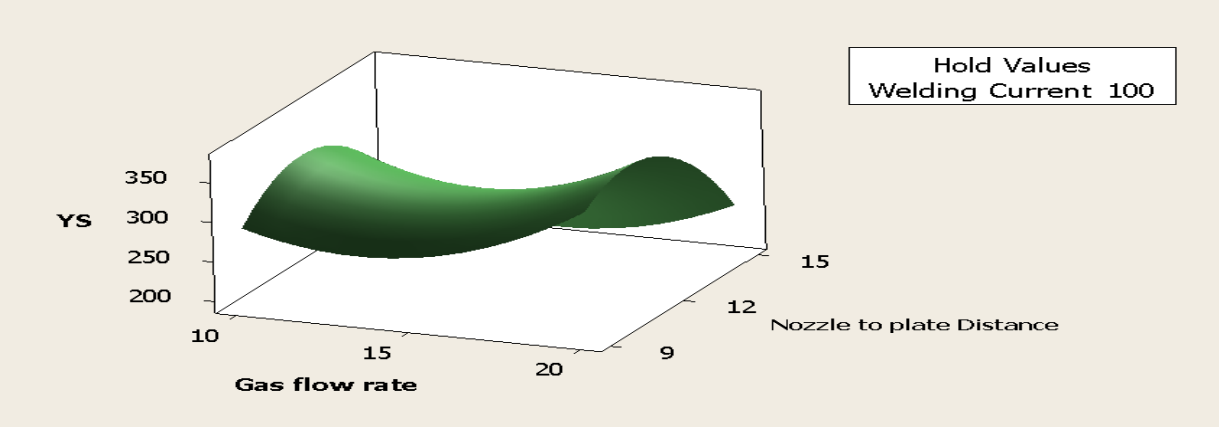

(5.28 a) Welding current(C) is constant at lowest level

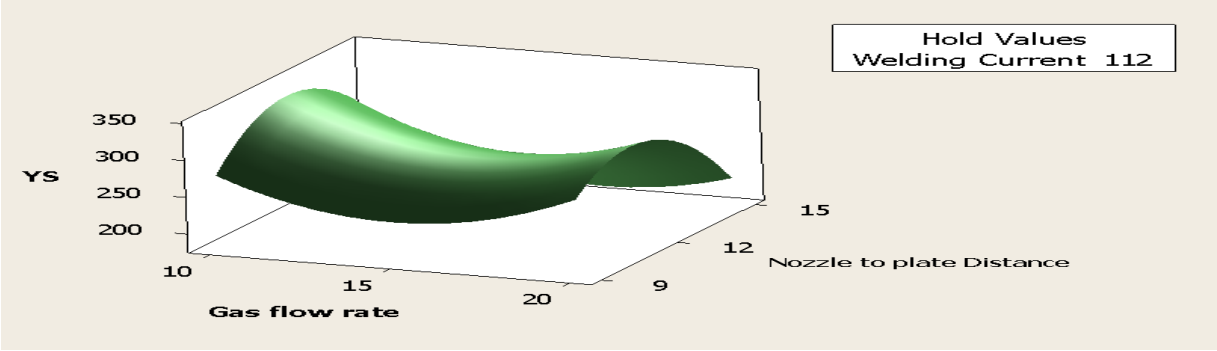

(5.28b) Welding current(C) is constant at middle level

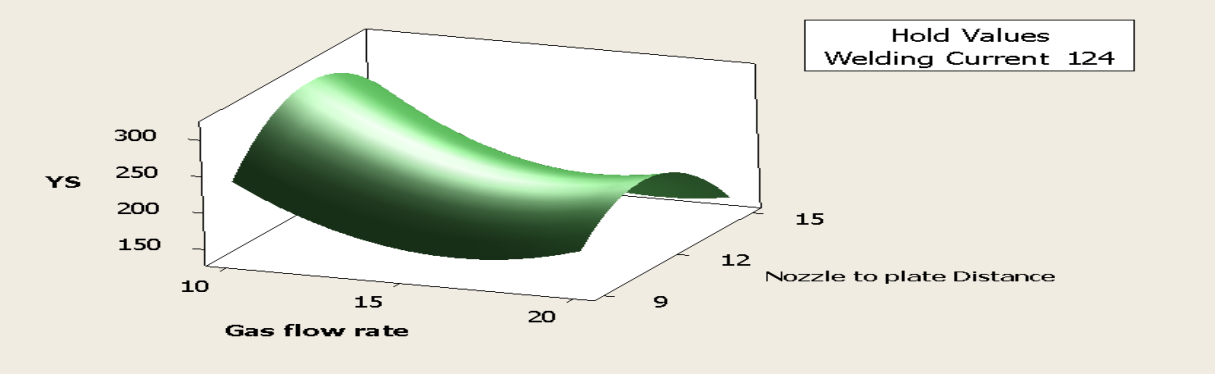

(5.28c) Welding current (C) is constant at highest level

Figure 5.28 Response surface plots showing combined effects of Gas flow rate (F) and Nozzle to plate distance (S) on YS when Welding current(C) is kept constant: 409 Ferritic stainless steel

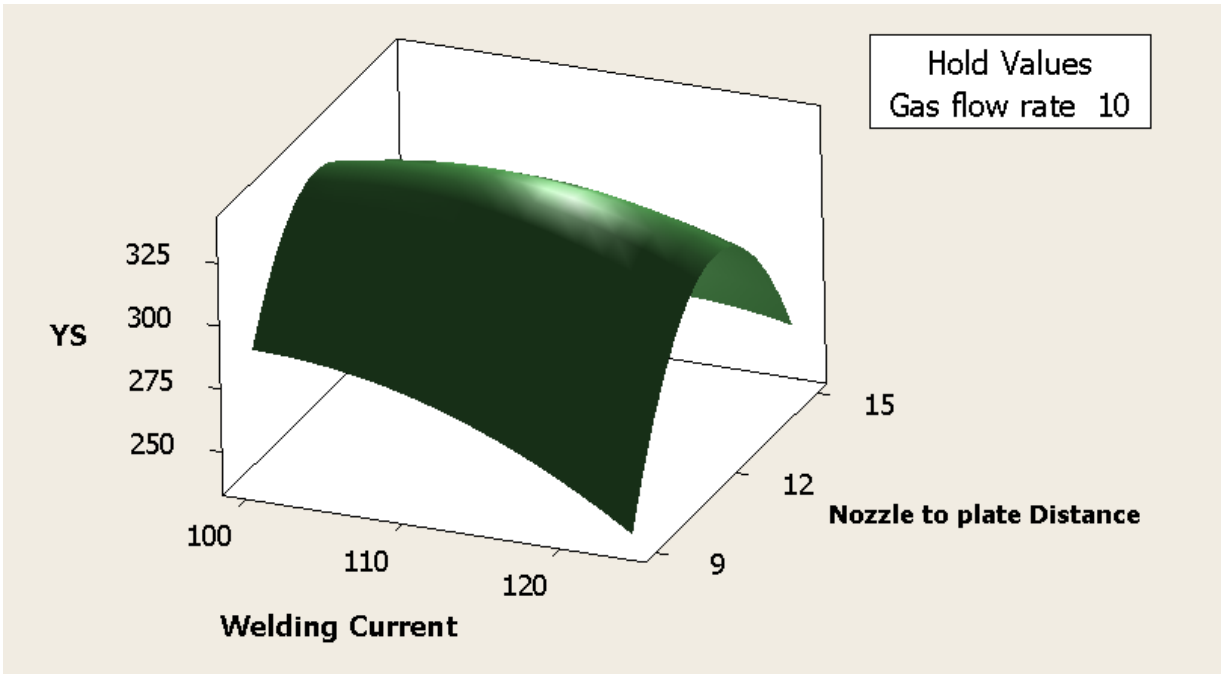

(5.29 a) Gas flow rate (F) is constant at lowest level

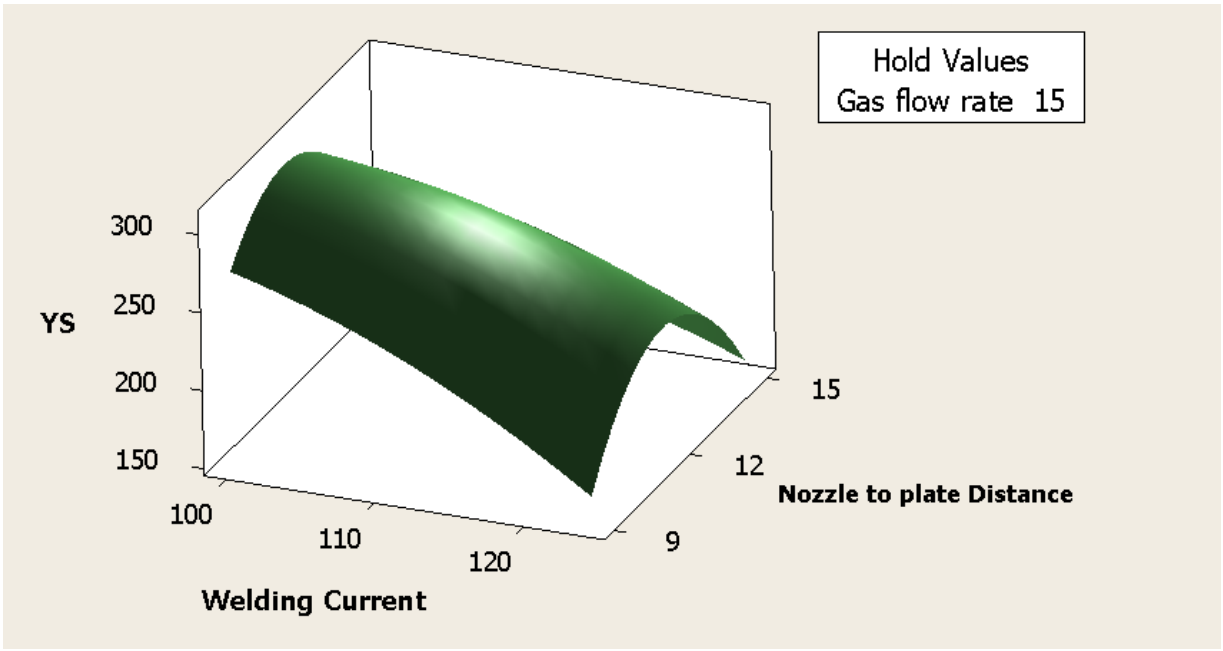

(5.29b) Gas flow rate (F) is constant at middle level

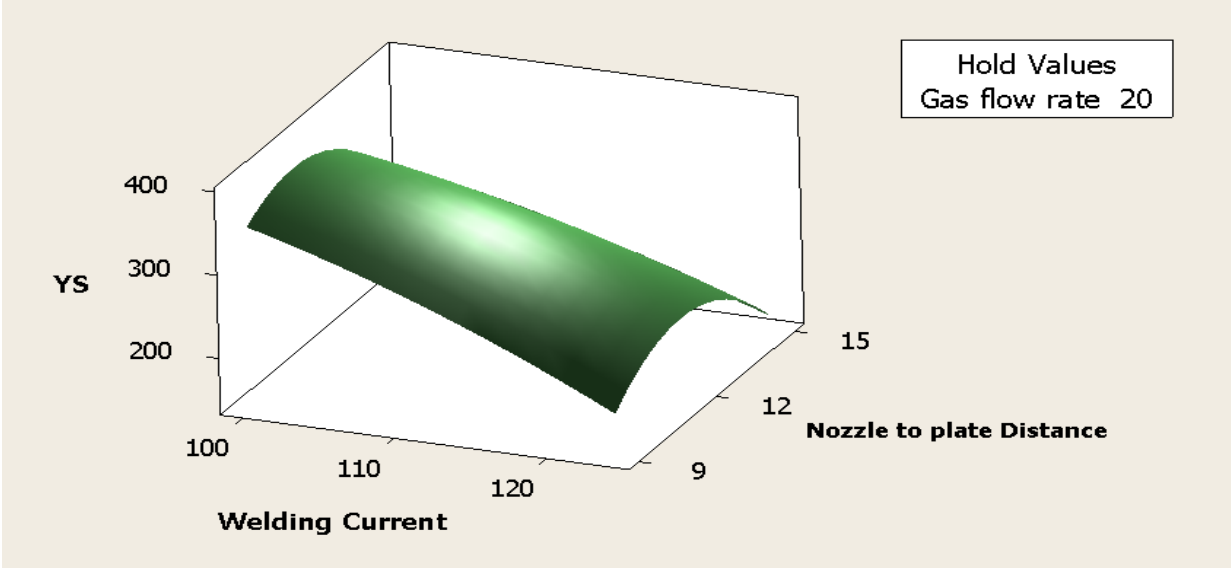

(5.29c) Gas flow rate (F) is constant at highest level

Figure 5.29 Response surface plots showing combined effects of Welding current (C) and Nozzle to plate distance (S) on YS when Gas flow rate (F) is kept constant: 409 Ferritic stainless steel

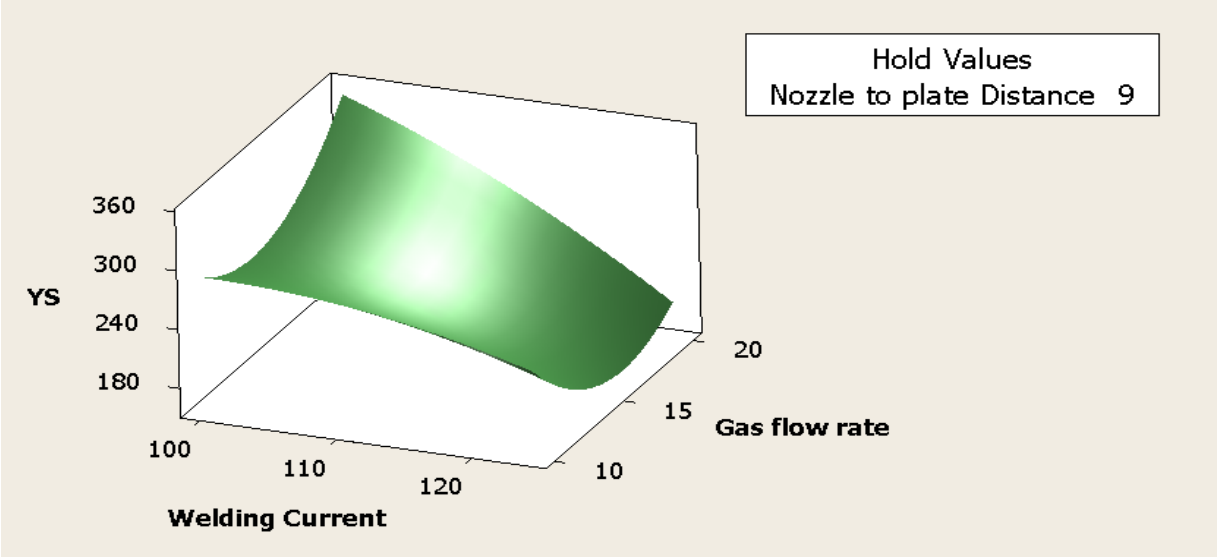

(5.30a) Nozzle to plate distance (S) is constant at lowest level

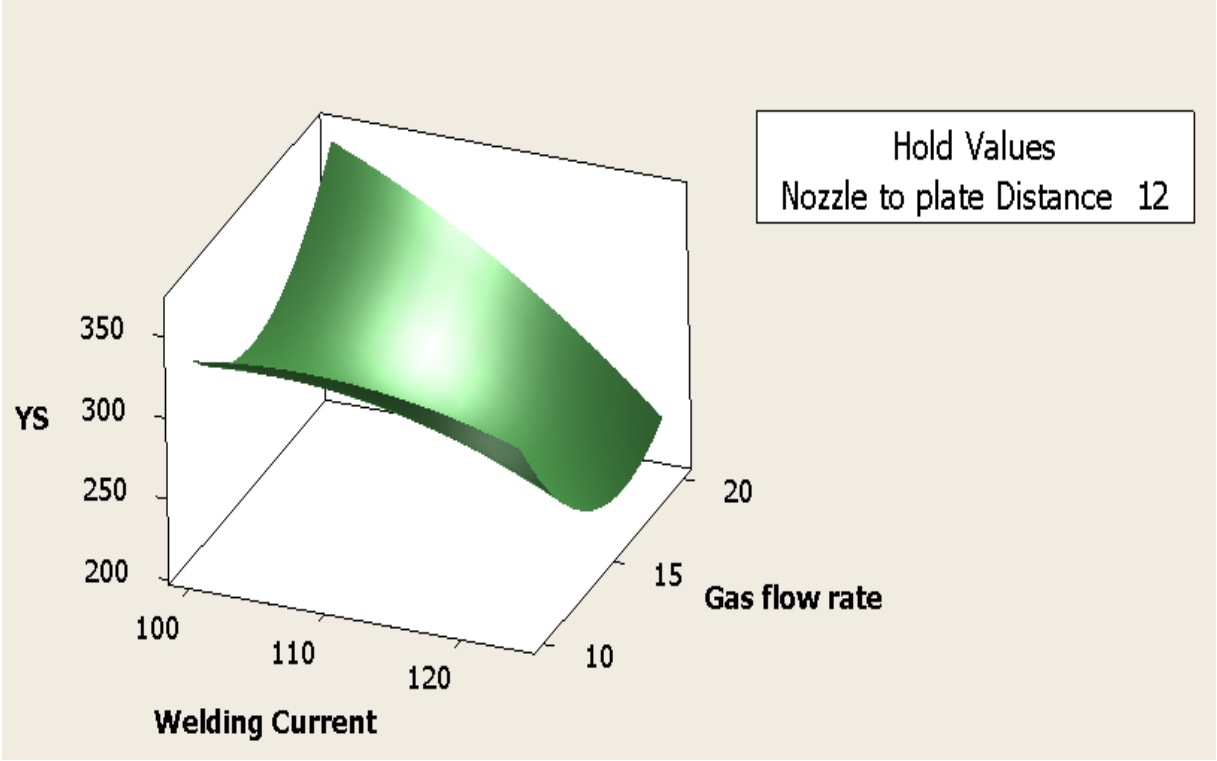

(5.30b) Nozzle to plate distance (S) is constant at middle level

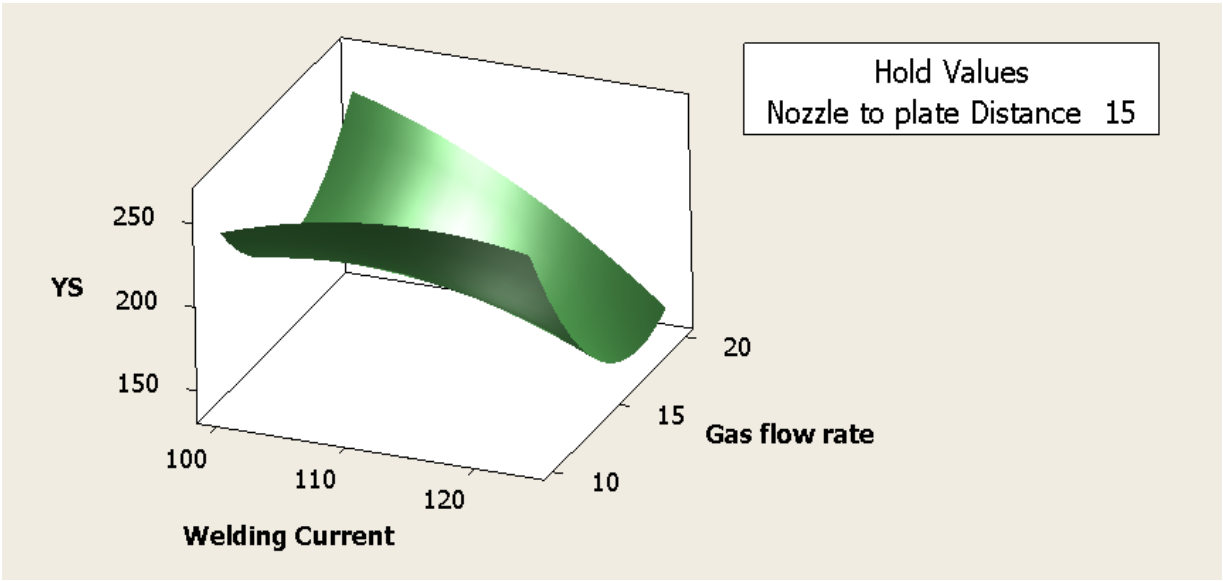

(5.30c) Nozzle to plate distance (S) is constant at highest level

Figure 5.30 Response surface plots showing combined effects of Welding current (C) and Gas flow rate (F) on YS when Nozzle to plate distance (S) is kept constant: 409 Ferritic stainless steel

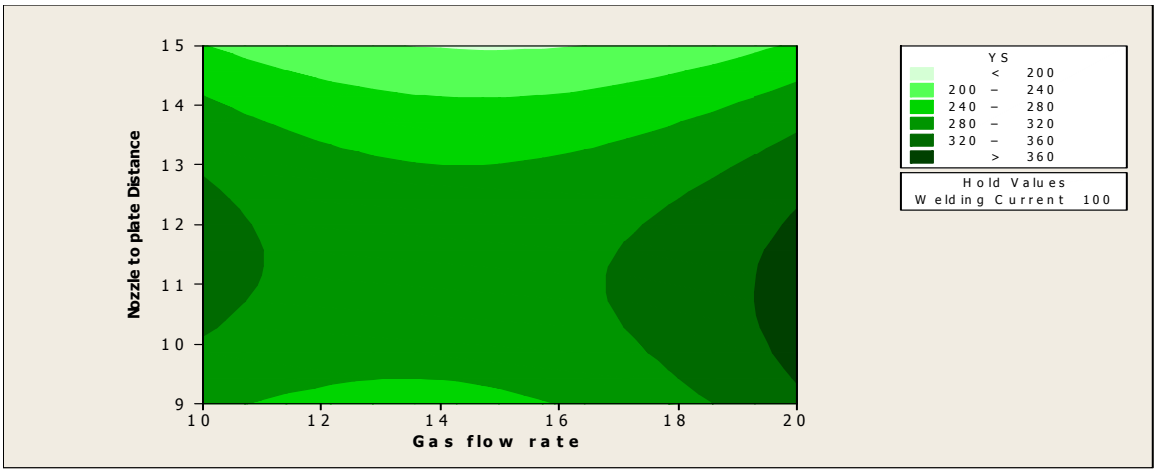

(5.31a) Welding current(C) is constant at lowest level

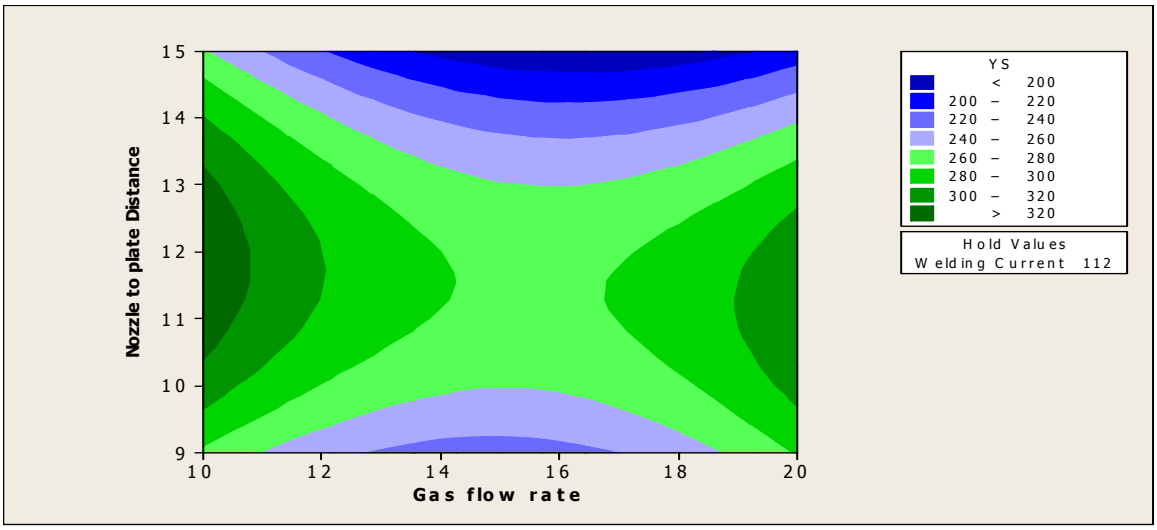

(5.31b) Welding current(C) is constant at middle level

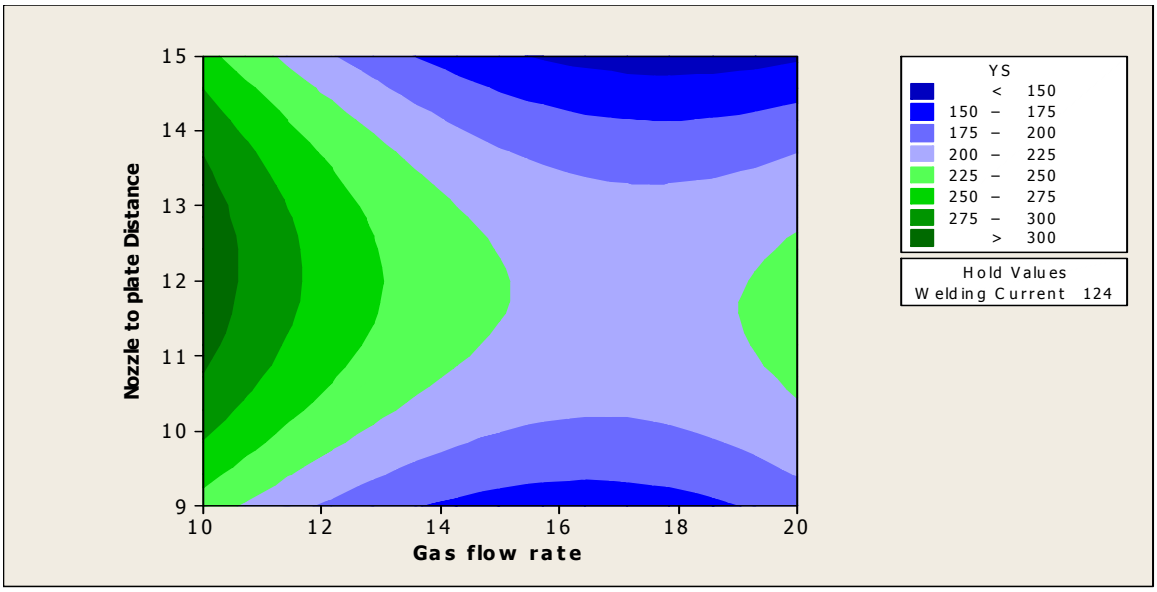

(5.31c) Welding current(C) is constant at highest level

Figure 5.31 Contour plots showing combined effects of Gas flow rate (F) and Nozzle to plate distance(S) on YS when Welding current (C) is kept constant: 409 Ferritic stainless steel

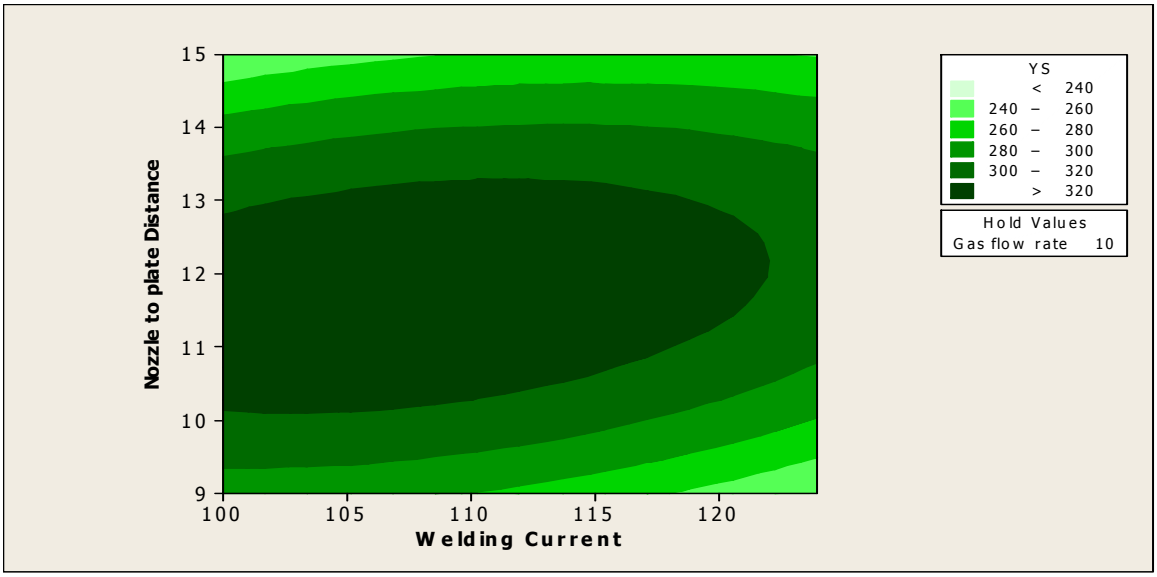

(5.32a) Gas flow rate (F) is constant at lowest level

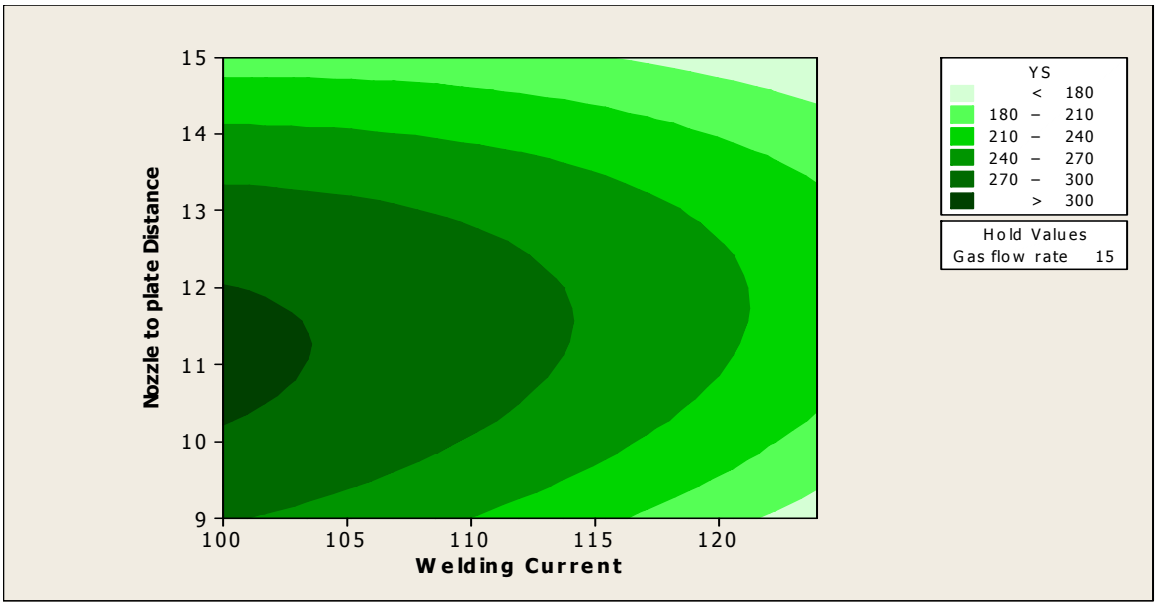

(5.32b) Gas flow rate (F) is constant at middle level

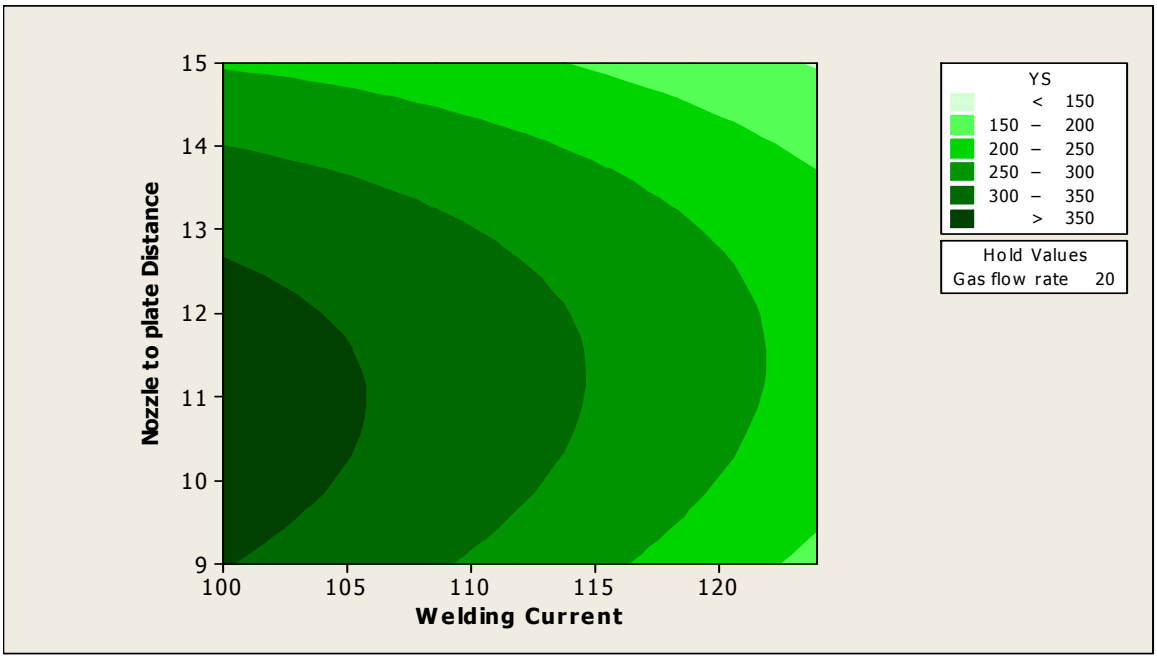

(5.32c) Gas flow rate (F) is constant at highest level

Figure 5.32 Contour plots showing combined effects of Welding current (C) and Nozzle to plate distance(S) on YS when Gas flow rate (F) is kept constant: 409 Ferritic stainless steel

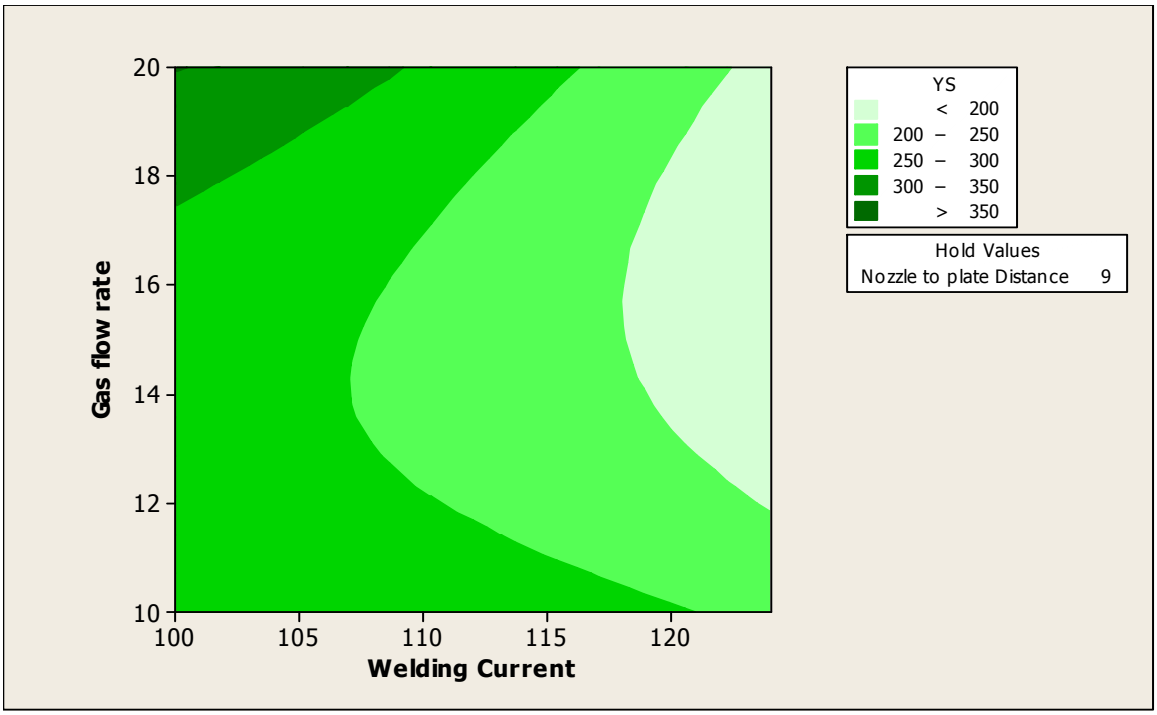

(5.33a) Nozzle to plate distance (S) is constant at lowest level

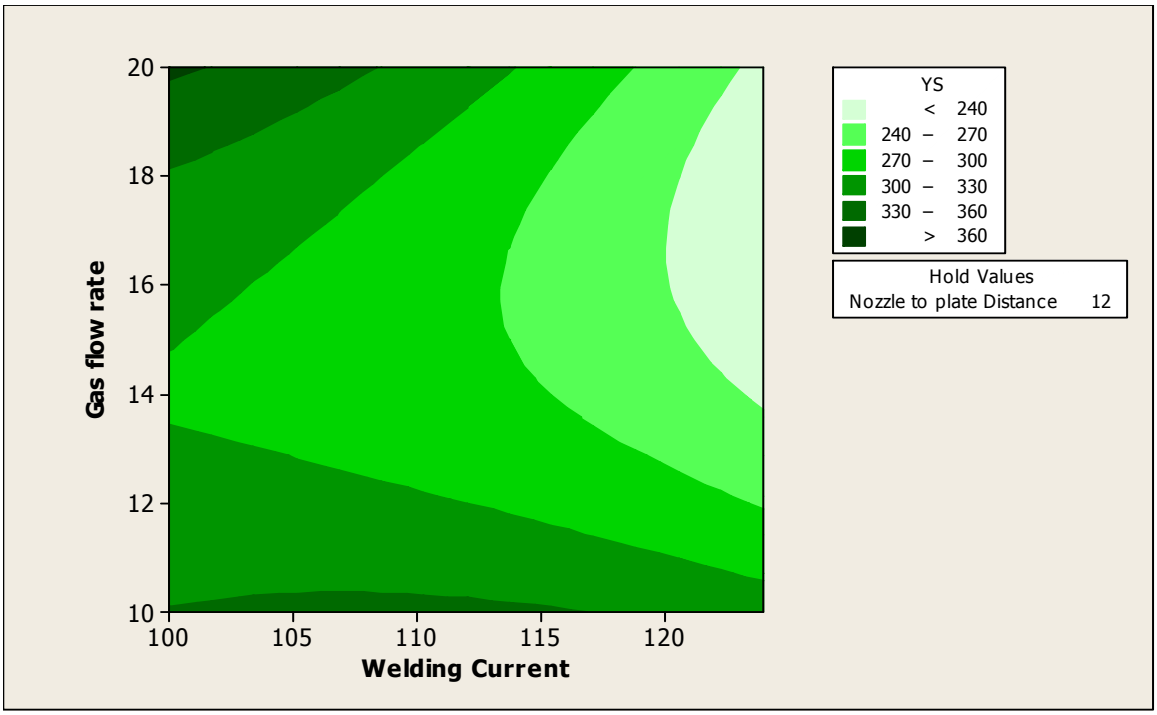

(5.33b) Nozzle to plate distance (S) is constant at middle level

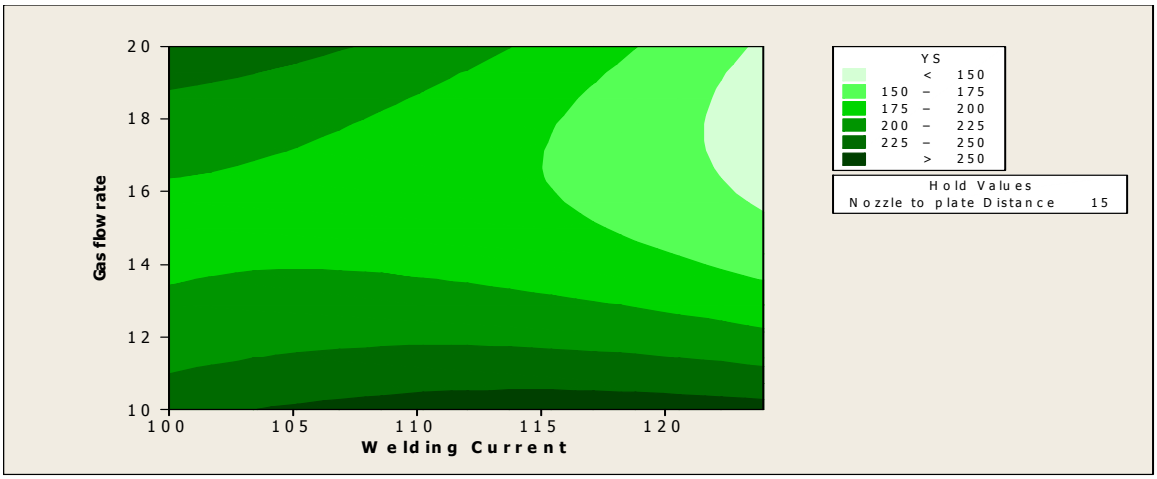

(5.33c) Nozzle to plate distance (S) is constant at highest level

Figure 5.33 Contour plots showing combined effects of Welding current (C) and Gas flow rate (F) on YS when Nozzle to plate distance (S) is kept constant: 409 Ferritic Stainless steel

Contour plots are shown in figures 5.31 – 5.33. The contour lines, with little or no curvature indicate lesser or no interaction effect; whereas bent or circular contours suggest interaction effect to be significant on the response. For example, interaction among the factors Welding current (C) and Nozzle to plate distance (S) is found to be significant in so far as the effect of this interaction on YS is concerned (figures 5.32 a-c).

5.2.2 RESPONSE SURFACE ANALYSIS OF TENSILE TEST FOR UTS: 409 FERRITIC STAINLESS STEEL

In this section, response surface analysis of ultimate tensile strength (UTS) has been done using MINITAB 16 software. At first a mathematical model is developed. ANOVA is carried out. Surface plots and contour plots for UTS have also been presented.

A) MATHEMATICAL MODELLING

Ultimate tensile strength (UTS) has been expressed in terms of the process variables Welding current (C), Gas flow rate (F) and Nozzle to plate distance (S) in the form:

$$UTS = \beta_0 + \beta_1(C) + \beta_2(F) + \beta_3(S) + \beta_{11}(C*C) + \beta_{22}(F*F) + \beta_{33}(S*S) + \beta_{12}(C*F) + \beta_{13}(C*S) + \beta_{23}(F*S) \quad (5.9)$$

The model to estimate UTS in numerical value is given as

$$Y_{UTS} = -2582.18 + 51.54(C) + 18.8\ (F) + 32.19(S) - 0.28(C*C) + 0.92(F*F) - 3.85(S*S) - 0.21(C*F) + \ 0.79(C*S) - 2.00(F*S) \quad (5.10)$$

B) ANOVA OF THE MODEL

The adequacy of the developed model is tested using the analysis of variance (ANOVA) and the results are given in Table 5.10.

Table 5.10 ANOVA table for UTS: 409 Ferritic stainless steel

Source	DF	Seq SS	Adj SS	Adj MS	F	P
Regression	9	49995.9	49995.9	5555.1	7.81	**0.002**
Linear	3	20557.6	20557.6	6852.5	9.64	0.003
Welding current	1	20313.0	20313.0	20313.0	28.57	**0.000**
Gas flow rate	1	82.9	82.9	82.9	0.12	**0.740**
Nozzle to plate distance	1	161.6	161.6	161.6	0.23	**0.644**
Square	3	14480.3	14480.3	4826.8	6.79	0.009
Welding current*Welding current	1	10857.8	4328.3	4328.3	6.09	**0.033**
Gas flow rate*Gas flow rate	1	326.0	1464.5	1464.5	2.06	0.182
Nozzle to plate distance*Nozzle to plate distance	1	3296.5	3296.5	3296.5	4.64	**0.057**
Interaction	3	14957.9	14958.0	4986.0	7.01	0.008
Welding current*Gas flow rate	1	1225.1	1225.1	1225.1	1.72	0.219
Welding current*Nozzle to plate distance	1	6520.8	6520.8	6520.8	9.17	**0.013**
Gas flow rate*Nozzle to plate distance	1	7212.0	7212.0	7212.0	10.14	**0.010**
Residual Error	10	7110.1	7110.1	711.0		
Lack-of-Fit	5	7018.8	7018.8	1403.8	76.87	0.000
Pure Error	5	91.3	91.3	18.3		
Total	19	57106.0				

S = 26.6648 PRESS = 77499.4
R-Sq = 87.55% R-Sq(pred) = 0.00% R-Sq(adj) = 76.34%

From Table 5.10, it is seen that P-value of the regression equation is P = 0.02 which is very close to P = 0.05 (95% confidence level). It supports the validity of the proposed regression model. **F** in Table 5.10 is different from the symbol F used as a nomenclature of gas flow rate. From the statistical analysis it is observed that, Welding current (C) is the most significant factor affecting the response UTS as it has the lowest P value (P = 0.000), followed by Nozzle to plate distance (P = 0.644) and Gas flow rate (P=0.740). The last two factors are not significant at all at 95% confidence level. The value of P less than 0.05 indicates that the corresponding factor is significant at 95% level of confidence in so far as the effect of this factor on response is concerned. Among the others, inner interaction terns, C-C (P= 0.033) and S-S (P = 0.057) have strong significances. Among the cross interaction terms, F-S and C-S are found to be very much significant having P = 0.010 and P = 0.013 respectively. The determination factor (R^2) indicates the goodness of fit of the model. The value of R^2 of this model is 87.55% which is greater than 85 %. This implies that at least 87% of the variability in data for the response is explained by the model. This indicates that the proposed model is adequate, fairly.

C) SURFACE PLOTS AND CONTOUR PLOTS FOR UTS

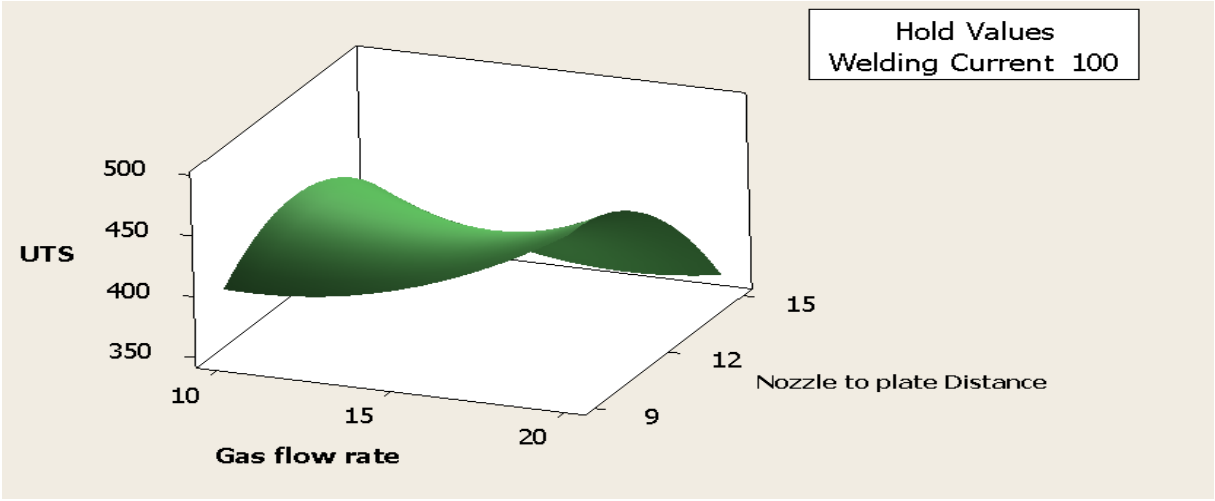

(5.34a) Welding Current (C) is constant at lowest level

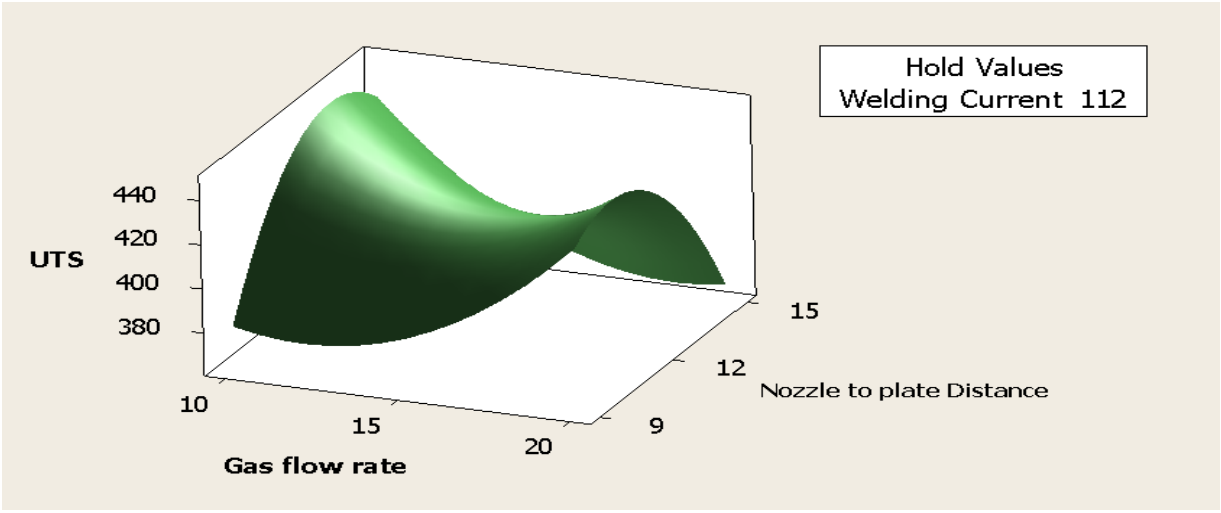

(5.34b) Welding current(C) is constant at middle level

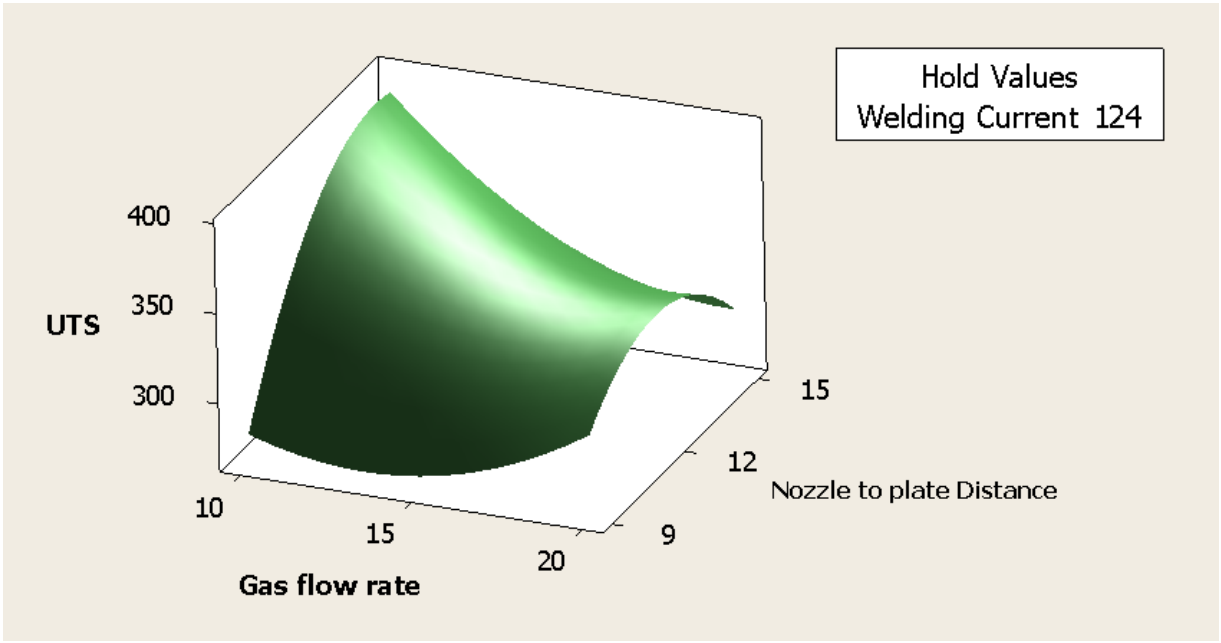

(5.34c)Welding current (C) is constant at highest level

Figure 5.34 Response surface plots showing combined effects of Gas flow rate (F) and Nozzle to plate distance (S) on UTS when Welding current (C) is kept constant:409 Ferritic Stainless steel

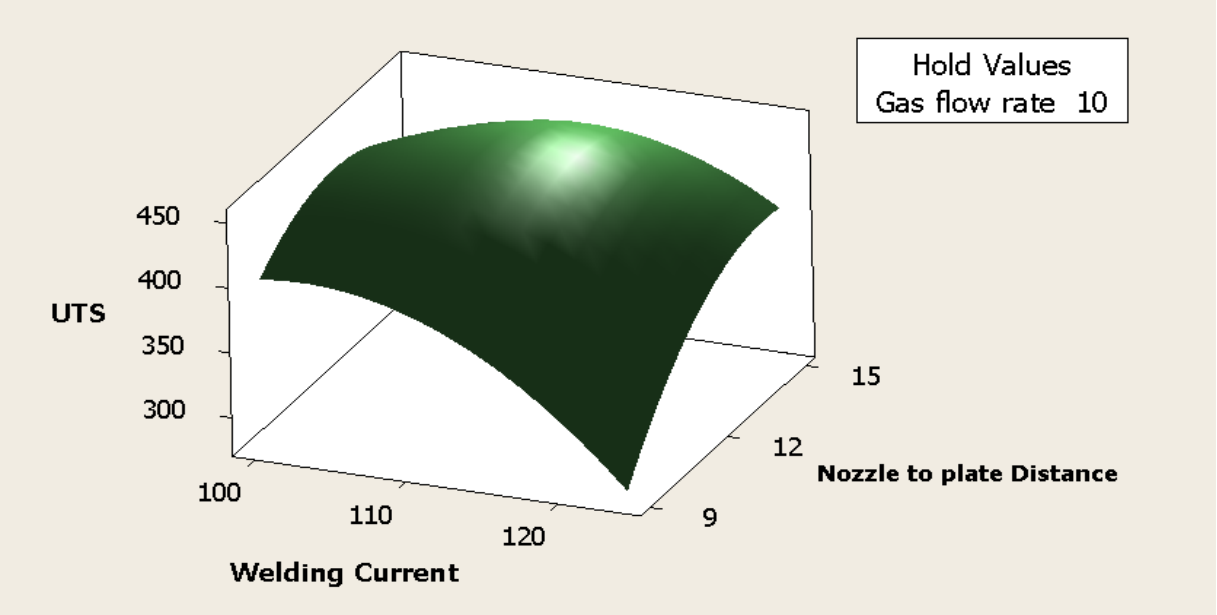

(5.35a) Gas flow rate (F) is constant at lowest level

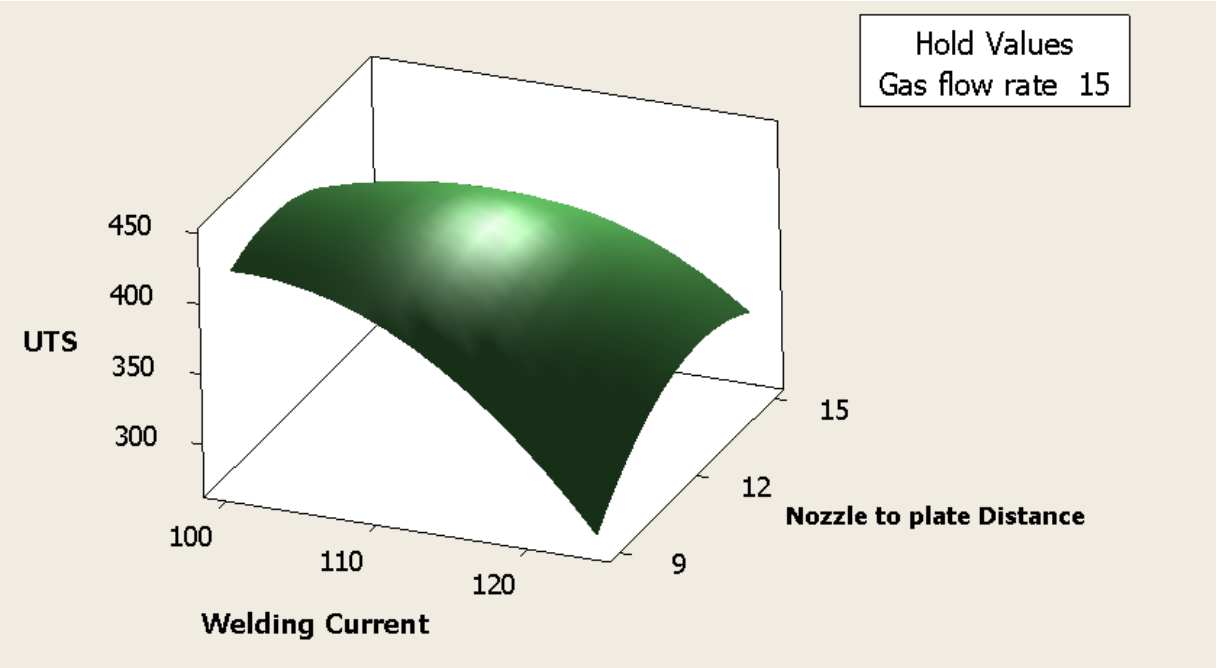

(5.35 b) Gas flow rate (F) is constant at middle level

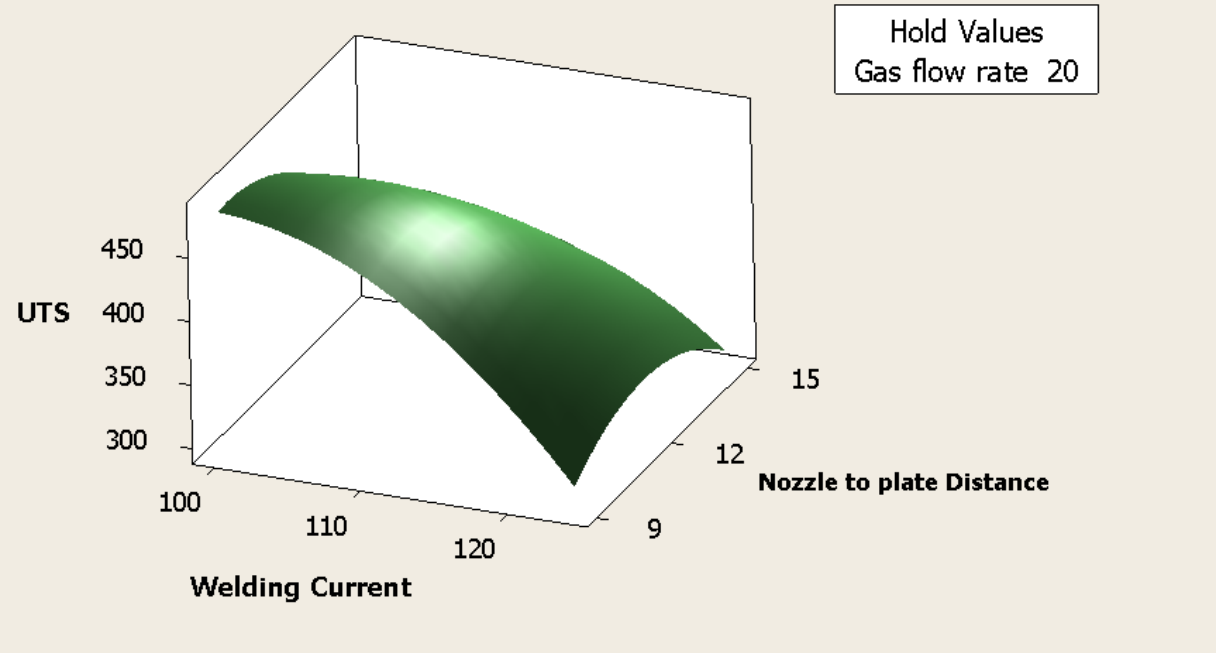

(5.35c) Gas flow rate (F) is constant at highest level

Figure 5.35 Response surface plots showing combined effects of Welding current (C) and Nozzle to plate distance(S) on UTS when Gas flow rate(F) is kept constant: 409 Ferritic stainless steel

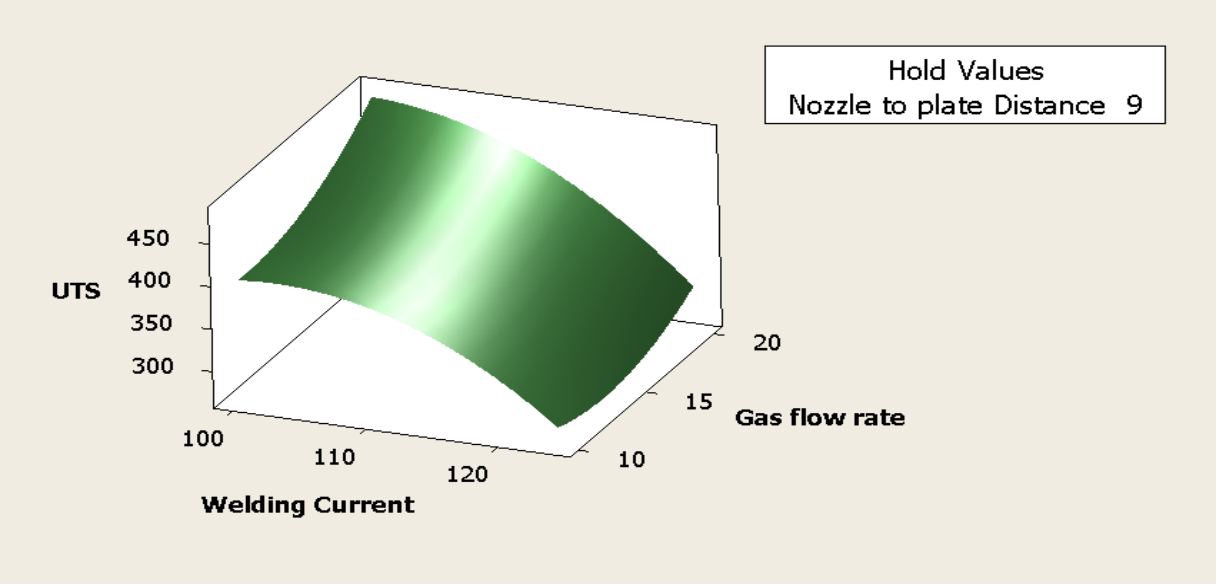

(5.36a) Nozzle to plate distance (S) is constant at lowest level

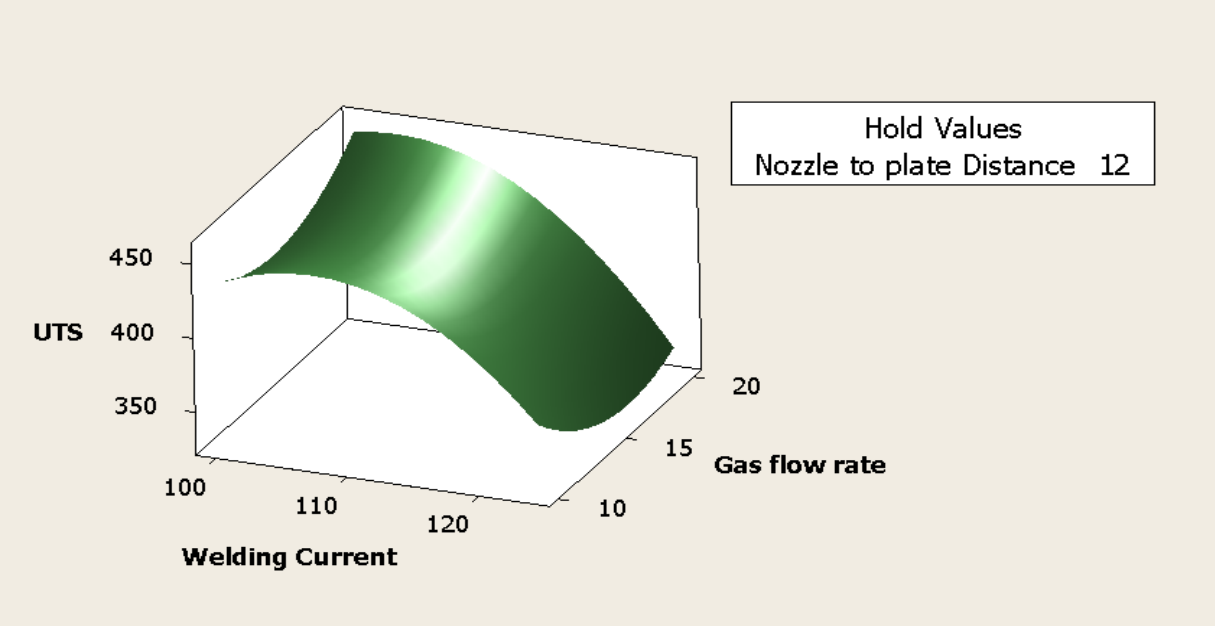

(5.36b)Nozzle to plate distance (S) is constant at middle level

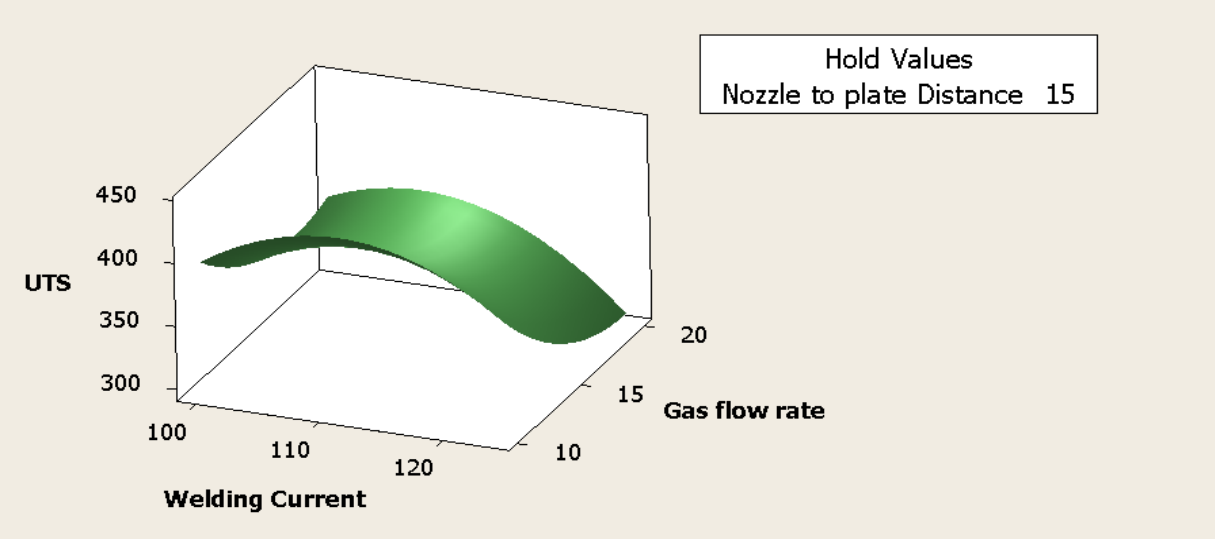

(5.36c) Nozzle to plate distance (S) is constant at highest level

Figure 5.36 Response surface plots showing combined effects of Welding current (C) and Gas flow rate (F) on UTS when Nozzle to plate distance (S) is kept constant: 409 Ferritic stainless steel

Response surface plots are shown in figures 5.34-5.36. Interaction effects found in figures 5.36 (a-c) are comparatively less significant than those observed in the figures 5.34 (a-c) and 5.35 (a-c). It points to the fact that interaction among the factors Welding current (C) and Gas flow rate (F) causes lesser influence on the response UTS (figures 5.36 a-c) as compared to the interaction among the factors Gas flow rate (F) and Nozzle to plate distance(S) (figures 5.34 a-c), Welding current (C) and Nozzle to plate distance (S) [figures 5.35 (a-c)].

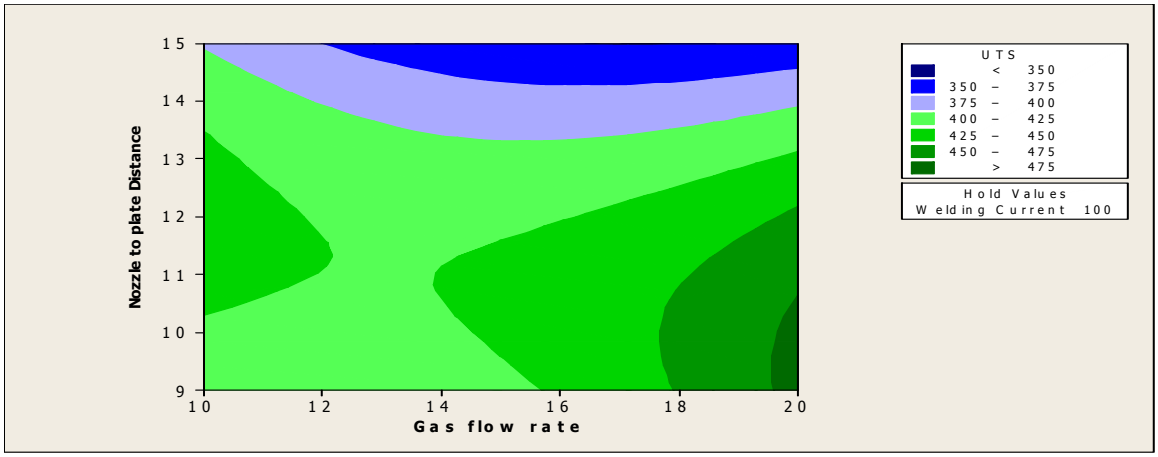

(5.37a) Welding current (C) is constant at lowest level

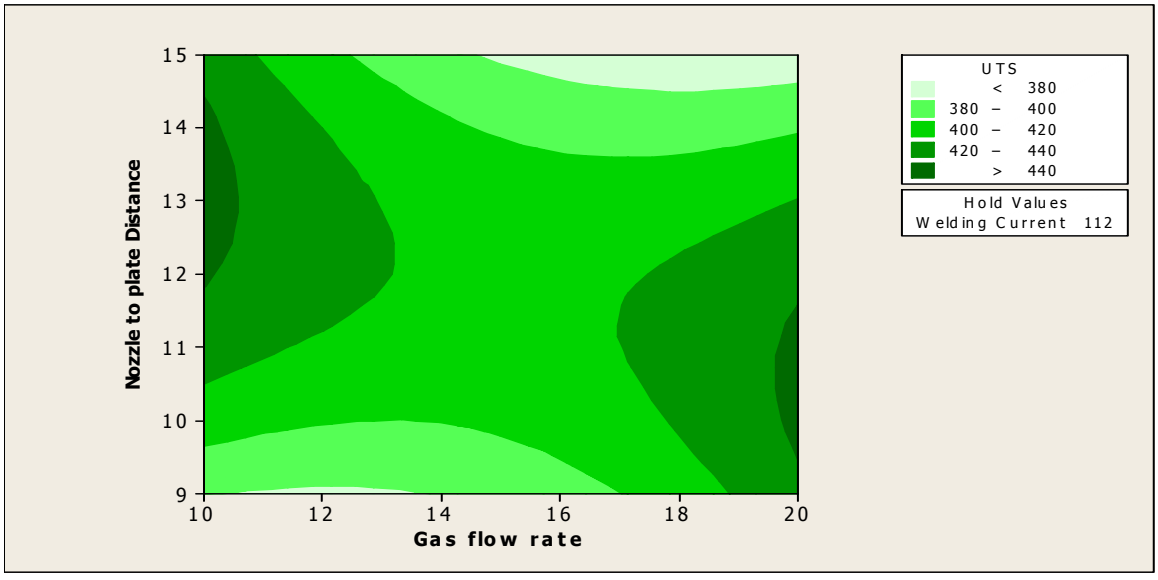

(5.37b) Welding current(C) is constant at middle level

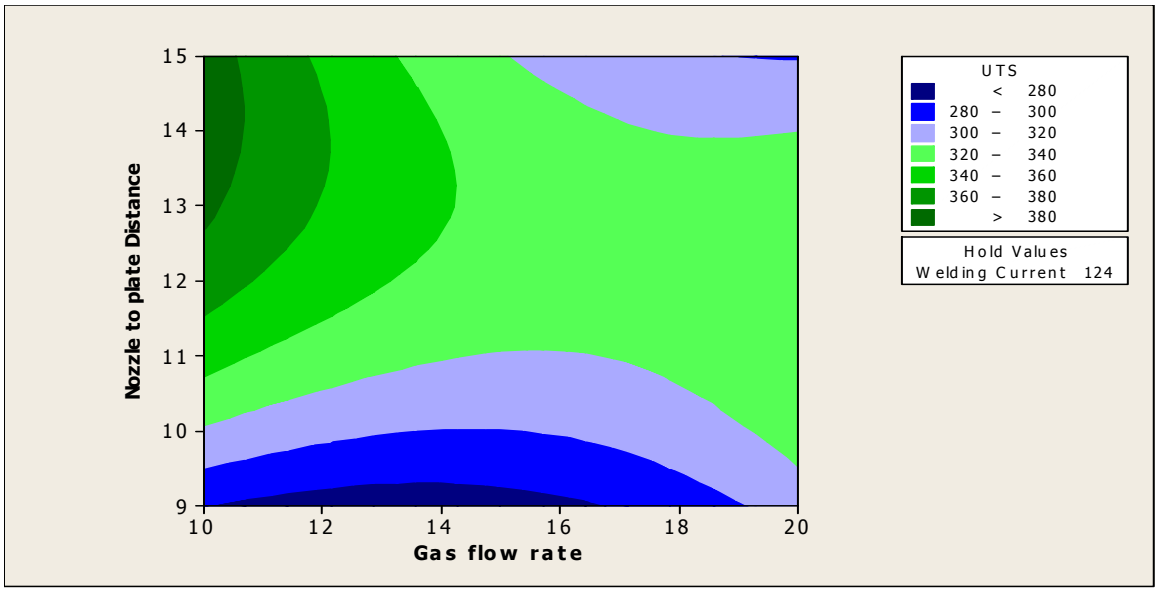

(5.37c) Welding current(C) is constant at highest level

Figure 5.37 Contour plots showing combined effects of Gas flow rate (F) and Nozzle to plate distance (S) on UTS when Welding current (C) is kept constant: 409 Ferritic stainless steel

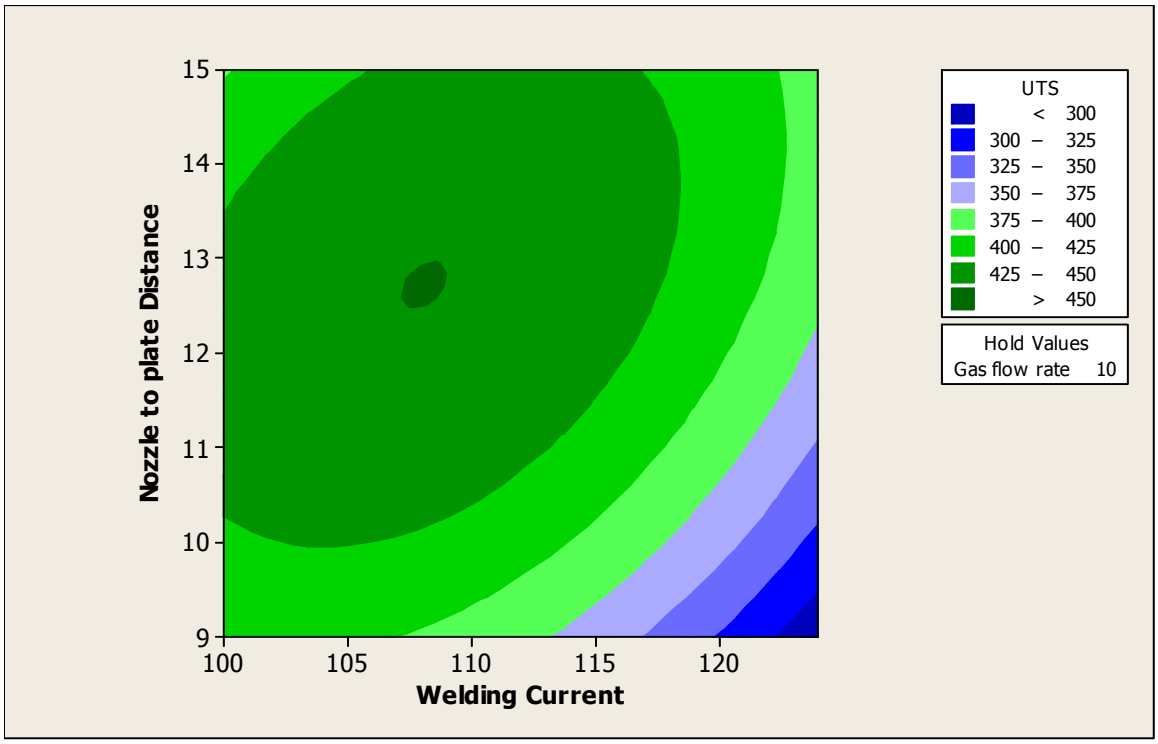

(5.38a) Gas flow rate (F) is constant at lowest level

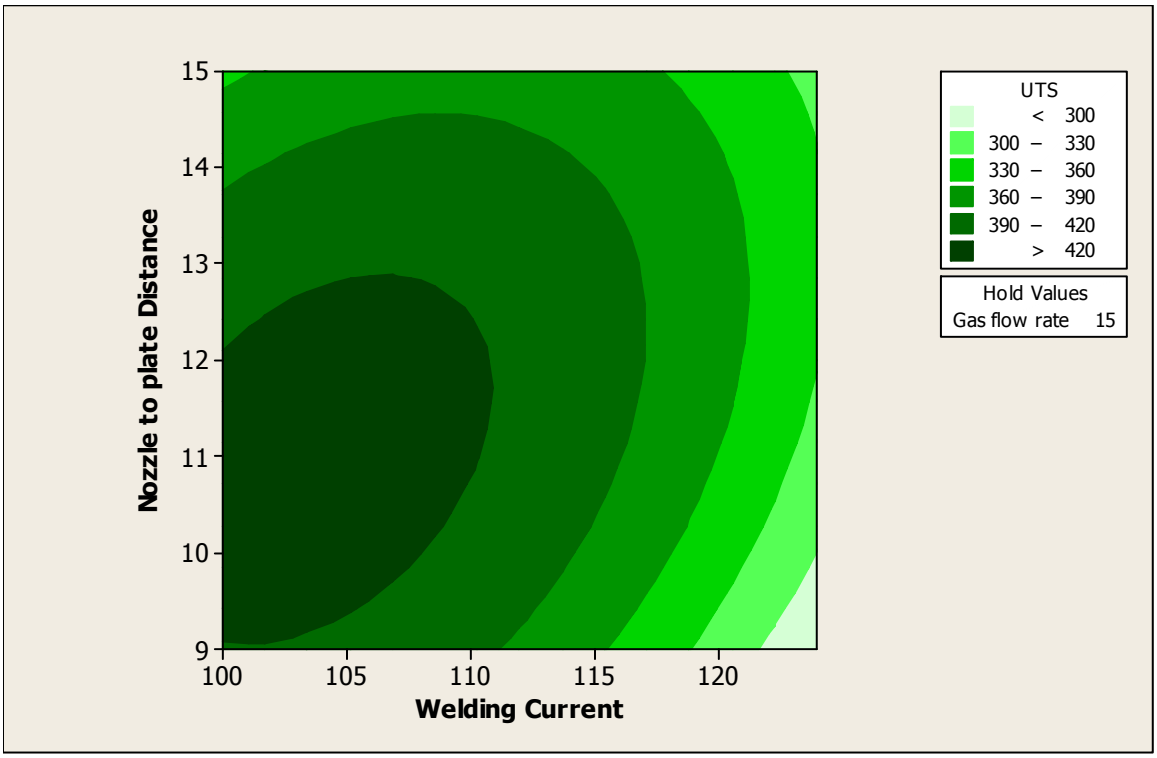

(5.38 b) Gas flow rate (F) is constant at middle level

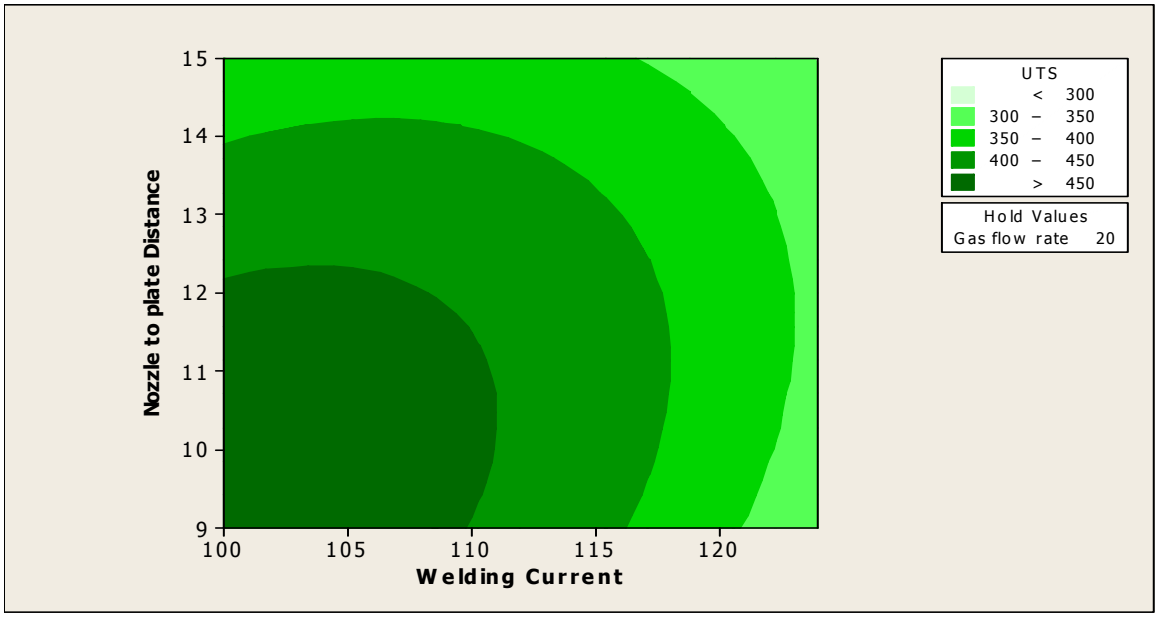

(5.38c) Gas flow rate (F) is constant at highest level

Figure 5.38 Contour plots showing combined effects of Welding current (c) and Nozzle to plate distance (S) on UTS when Gas flow rate (F) is kept constant: 409 Ferritic stainless steel

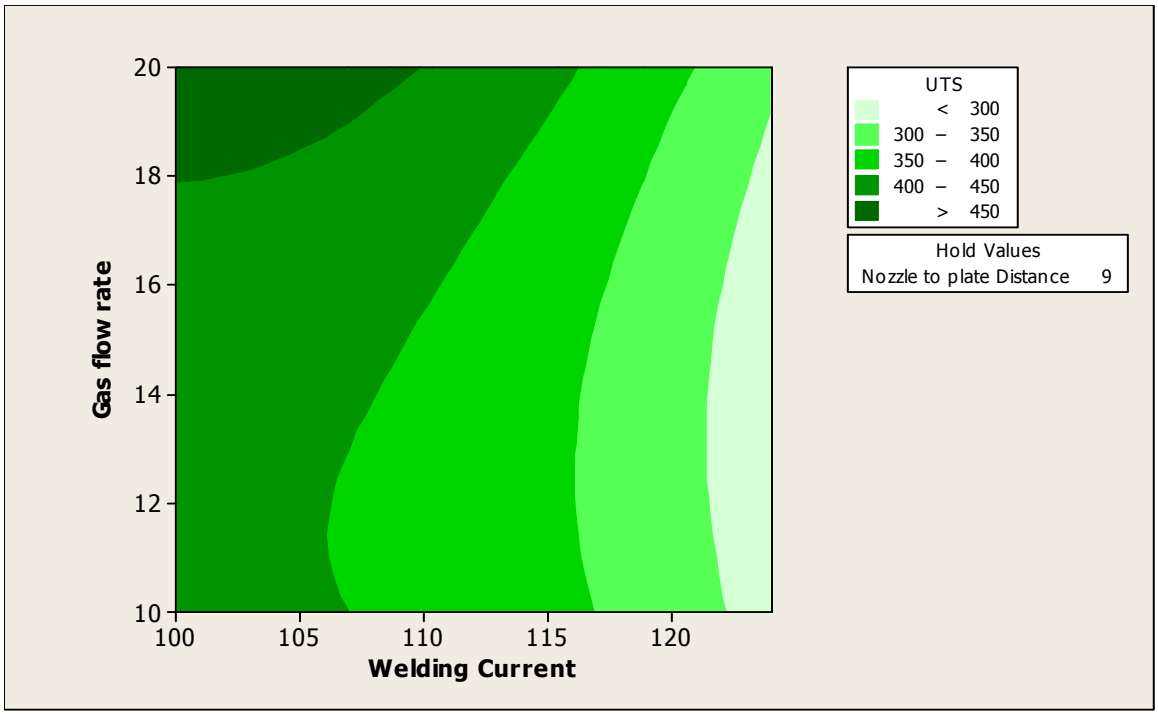

(5.39a) Nozzle to plate distance (S) is constant at lowest level

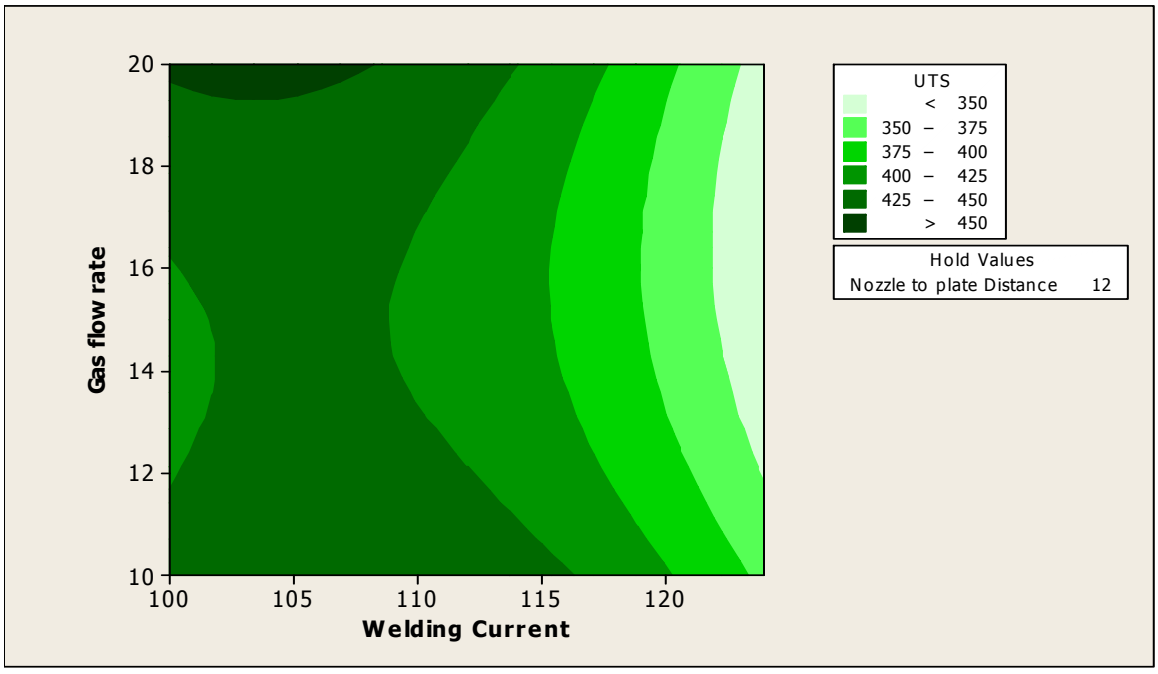

(5.39b) Nozzle to plate distance (S) is constant at middle level

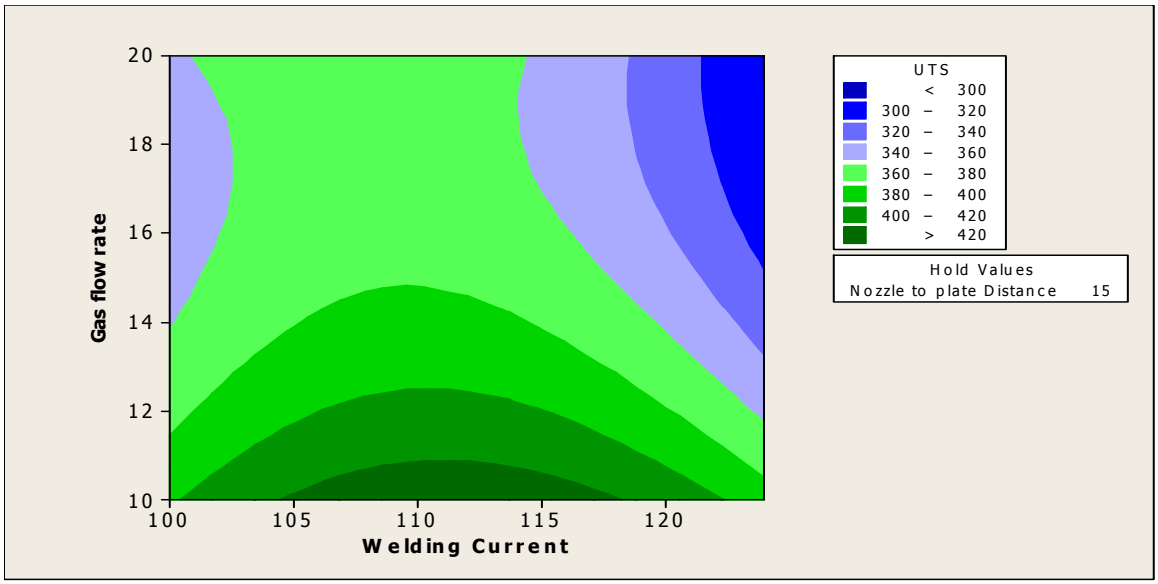

(5.39c) Nozzle to plate distance (S) is constant at highest level

Figure 5.39 Contour plots showing combined effects of Welding current (C) and Gas flow rate (F) on UTS when Nozzle to plate distance (S) is kept constant: 409 Ferritic stainless steel

Contour plots (shown in figures 5.37 – 5.39) also show the combined effects of any two parameters on the response. The contour lines of constant responses can be seen in these plots. Interaction effects can also be examined. For example, interaction among the factors Welding current (C) and Nozzle to plate distance (S) is found to be significant in so far as the effect of this interaction on UTS is concerned (figures 5.38 a-c).

5.2.3 RESPONSE SURFACE ANALYSIS OF TENSILE TEST FOR PE: 409 FERRITIC STAINLESS STEEL

In this section, response surface analysis of percentage elongation (PE) has been done using MINITAB 16 software. At first a mathematical model is developed. The adequacy of the developed model has been tested using ANOVA. Surface plots and contour plots for PE have also been generated and presented.

A) MATHEMATICAL MODELLING

Percentage of elongation (PE) has been expressed in terms of the process variables welding current (C), gas flow rate (F) and nozzle to plate distance (S) in the following form:

$$PE = \beta_0 + \beta_1(C) + \beta_2(F) + \beta_3(S) + \beta_{11}(C*C) + \beta_{22}(F*F) + \beta_{33}(S*S) + \beta_{12}(C*F) + \beta_{13}(C*S) + \beta_{23}(F*S) \quad (5.11)$$

PE (Y_{PE}) can be estimated from the equation which has been arrived at(eq. 5.12), in the above form.

$$Y_{PE} = 135.511 - 0.397(C) - 6.780(F) - 8.723(S) - 0.001(C*C) + 0.021(F*F) + 0.348(S*S) + 0.051(C*F) + 0.007(C*S) + 0.016(F*S) \quad (5.12)$$

B) ANOVA OF THE MODEL

The adequacy of the developed model is tested using the analysis of variance (ANOVA) and the results of the second order response surface model, fitting in the form of variance are given in Table 5.11

Table 5.11 ANOVA table for PE: 409 Ferritic stainless steel

Source	DF	Seq SS	Adj SS
Regression	9	198.664	198.664
Linear	3	66.494	66.494
Welding current	1	19.044	19.044
Gas flow rate	1	13.225	13.225
Nozzle to plate distance	1	34.225	34.225
Square	3	56.236	56.236
Welding current*Welding current	1	19.800	0.126
Gas flow rate*Gas flow rate	1	9.385	0.791
Nozzle to plate distance*Nozzle to plate distance	1	27.051	27.051
Interaction	3	75.934	75.934
Welding current*Gas flow rate	1	75.031	75.031
Welding current*Nozzle to plate distance	1	0.451	0.451
Gas flow rate*Nozzle to plate distance	1	0.451	0.451
Residual Error	10	115.206	115.206
Lack-of-Fit	5	94.557	94.557
Pure Error	5	20.648	20.648
Total	19	313.870	

Source	Adj MS	F	P	
Regression	22.0738	1.92	**0.163**	
Linear	22.1647	1.92	0.190	
Welding current	19.0440	1.65	0.228	(contd.)

Gas flow rate	13.2250	1.15	0.309
Nozzle to plate distance	34.2250	2.97	**0.116**
Square	18.7454	1.63	0.245
Welding current*Welding current	0.1255	0.01	0.919
Gas flow rate*Gas flow rate	0.7911	0.07	0.799
Nozzle to plate distance*Nozzle to plate distance	27.0511	2.35	0.156
Interaction	25.3113	2.20	0.151
Welding current*Gas flow rate	75.0313	6.51	0.029
Welding current*Nozzle to plate distance	0.4512	0.04	0.847
Gas flow rate*Nozzle to plate distance	0.4512	0.04	0.847
Residual Error	11.5206		
Lack-of-Fit	18.9115	4.58	0.060
Pure Error	4.1297		
Total			

S = 3.39420 PRESS = 755.671
R-Sq = 63.30% R-Sq(pred) = 0.00% R-Sq(adj) = 30.26%

From the Table 5.11, it is seen that P-value of the regression equation is P = 0.163 which is very close to P = 0.1 (90% confidence level). It supports the validity of the proposed regression model. **F** in Table 5.11 is different from the symbol F used as a nomenclature of Gas flow rate. Individually, Nozzle to plate distance is found to be the very significant factor (P value is minimum: 0. 116). However, none of the three input parameters, individually, is identified as significant at 95% confidence level. Among the cross interaction terms, C-F is found to be very much significant having P = 0.029. The value of R^2 of this model is 63.30%. This implies that at least 63% of the variability in data for the response is explained by the model. This indicates that the proposed model is not fairly accurate, but roughly acceptable.

C) SURFACE PLOTS AND CONTOUR PLOTS FOR PE

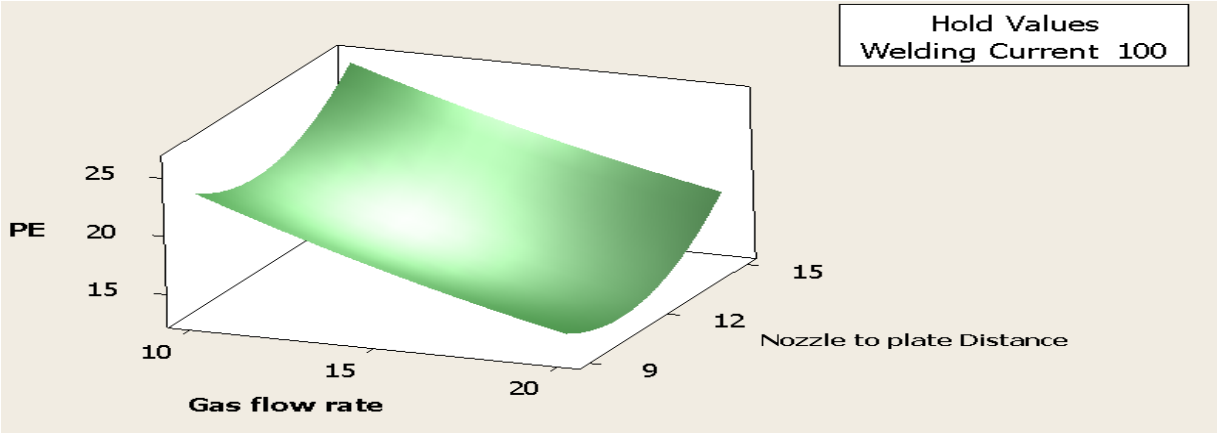

(5.40a) Welding current (C) is constant at lowest level

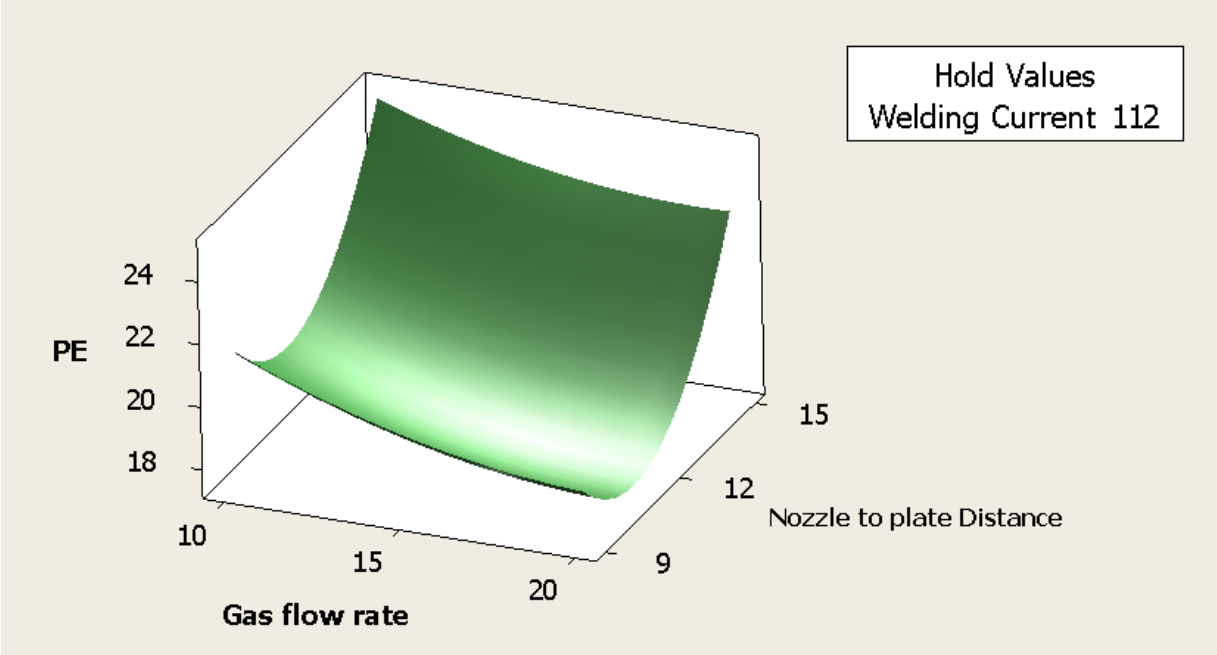

(5.40b) Welding current(C) is constant at middle level

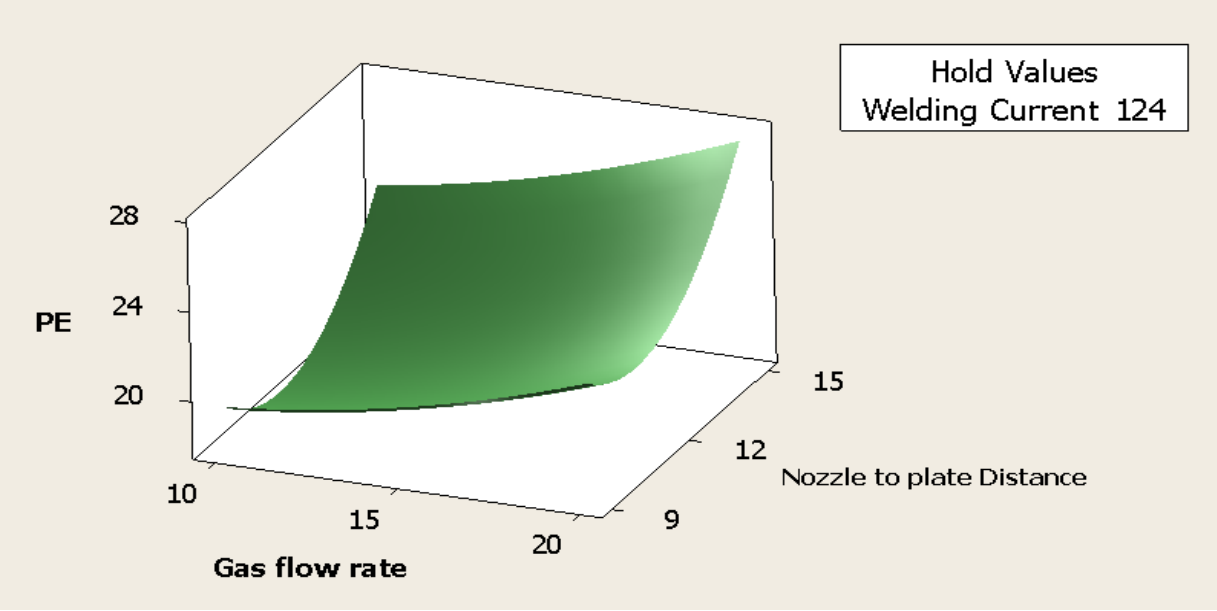

(5.40c) Welding current (C) is constant at highest level

Figure 5.40 Response surface plots showing combined effects of Gas flow rate(F) and Nozzle to plate distance(S) on PE when Welding current (C) is kept constant: 409 Ferritic Stainless steel

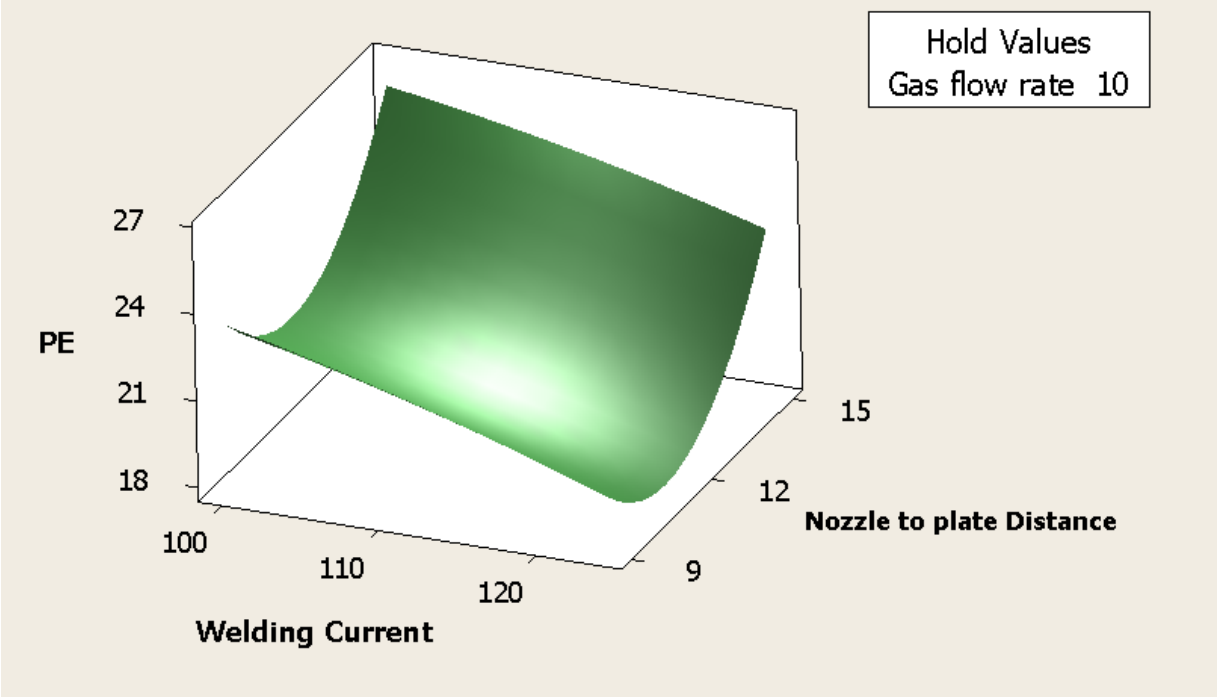

(5.41a) Gas flow rate (F) is constant at lowest level

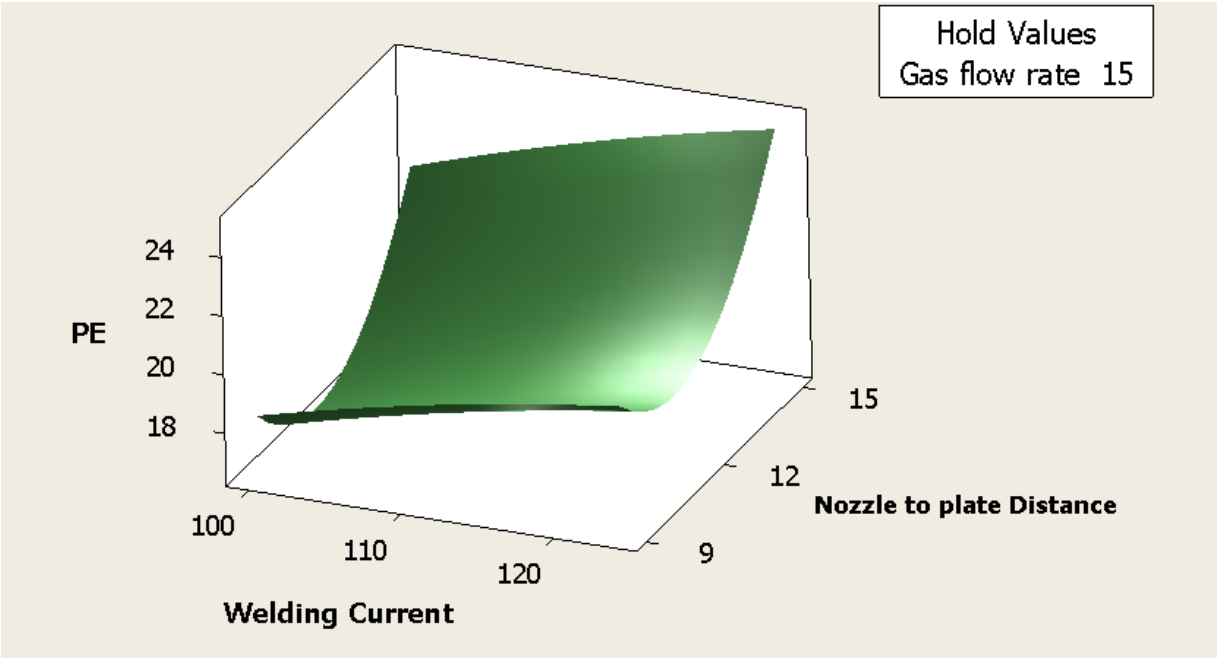

(5.41b) Gas flow rate (F) is constant at middle level

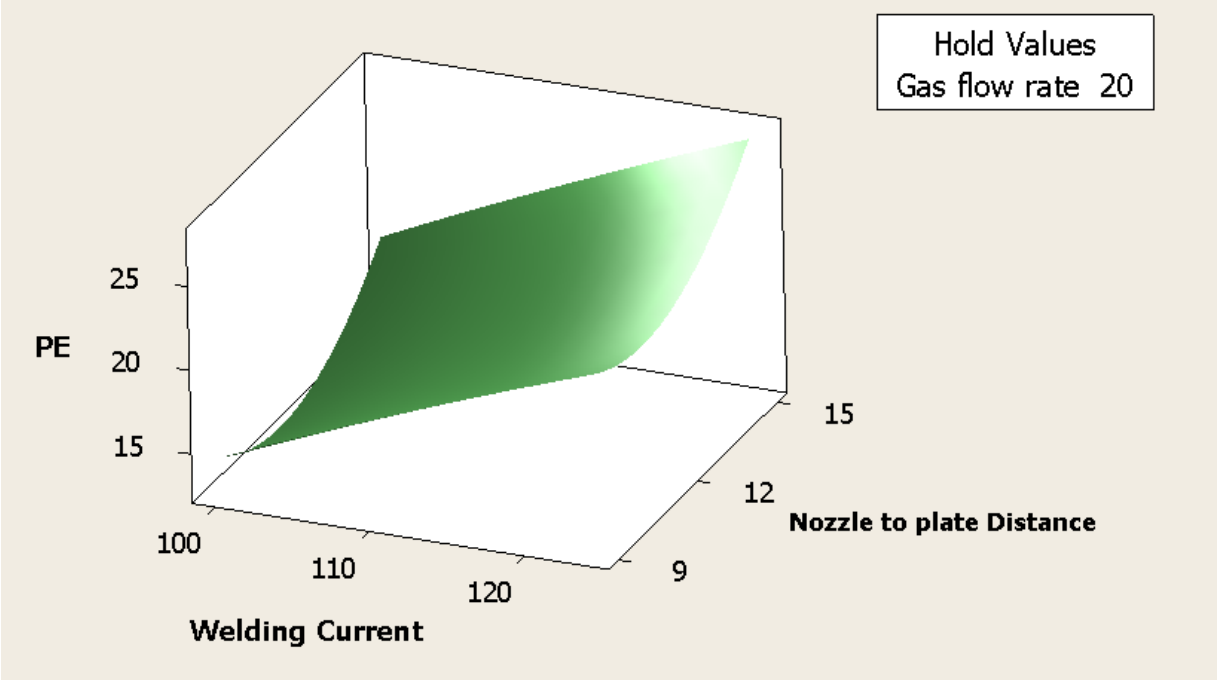

(5.41c) Gas flow rate (F) is constant at highest level

Figure 5.41 Response surface plots showing combined effects of Welding current (C) and Nozzle to plate distance(S) on PE when Gas flow rate (F) is kept constant: 409 Ferritic stainless steel

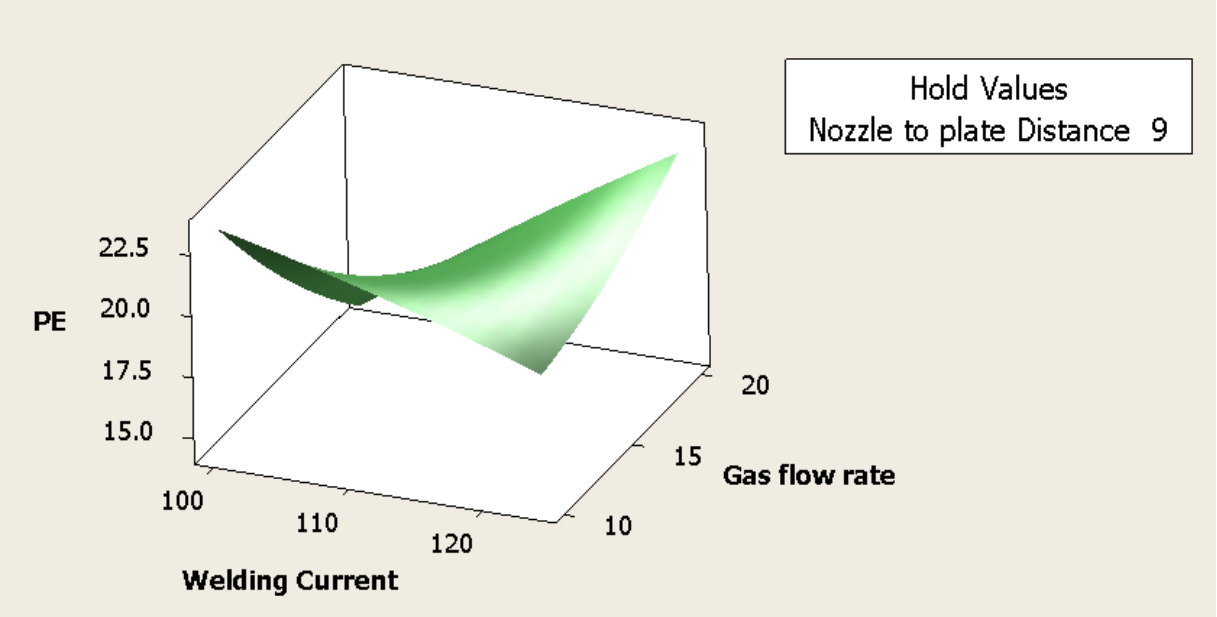

(5.42a) Nozzle to plate distance (S) is constant at lowest level

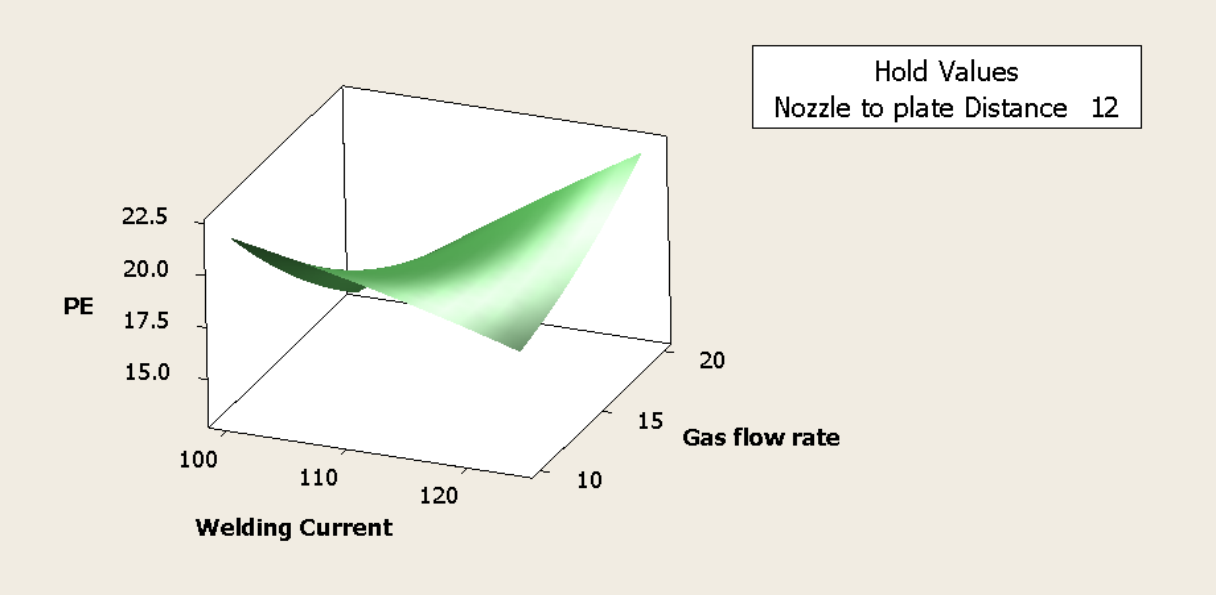

(5.42b) Nozzle to plate distance (S) is constant at middle level

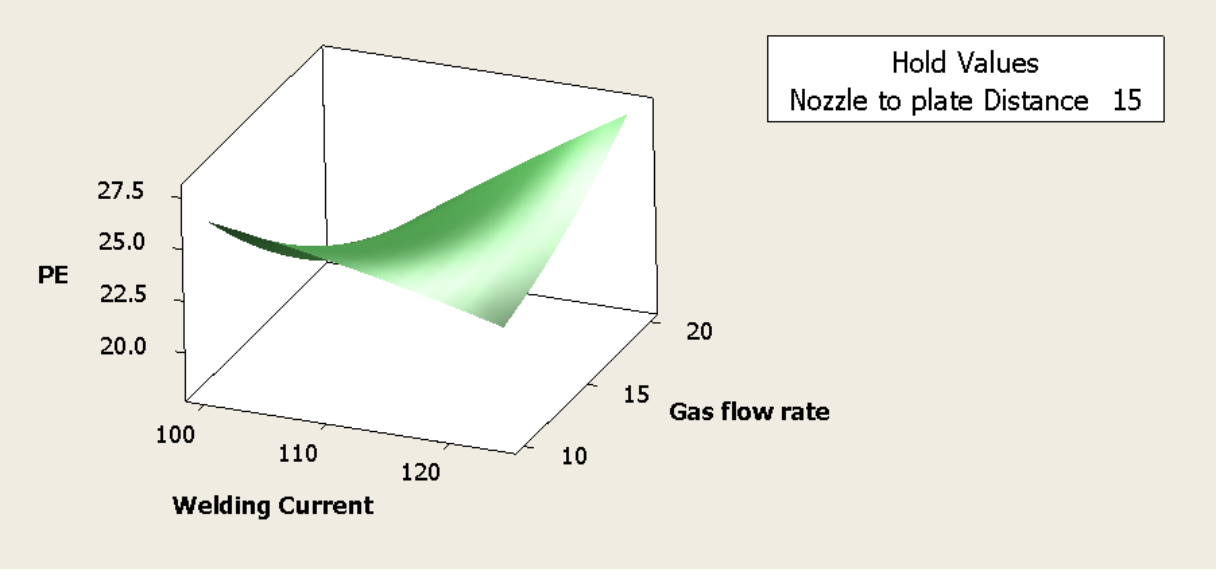

(5.42c) Nozzle to plate distance (S) is constant at highest level

Figure 5.42 Response surface plots showing combined effects of Welding current (C) and Gas flow rate (F) on PE when Nozzle to plate distance(S) is kept constant: 409 Ferritic stainless steel

Surface plots have been made and shown in figure 5.40-5.42. Effects of interaction of the factors shown in 5.40(a-c) and 5.42(a-c) are comparatively more significant than those revealed in the figures 5.41 (a-c). This establishes that interaction among the factors Welding current (C) and Nozzle to plate distance (S) causes lesser influence on the response PE (figures 5.41 a-c) as compared to the interactions among the factors Gas flow rate (F) and Nozzle to plate distance(S) (figures 5.40 a-c), Welding current (C) and Gas flow rate (F) figures 5.42 (a-c).

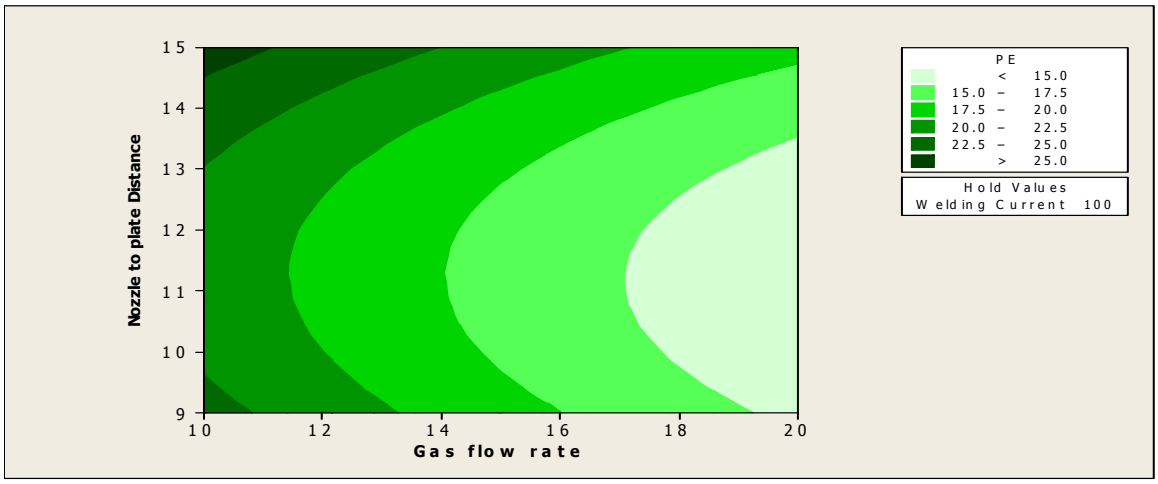

(5.43a) Welding current (C) is constant at lowest level

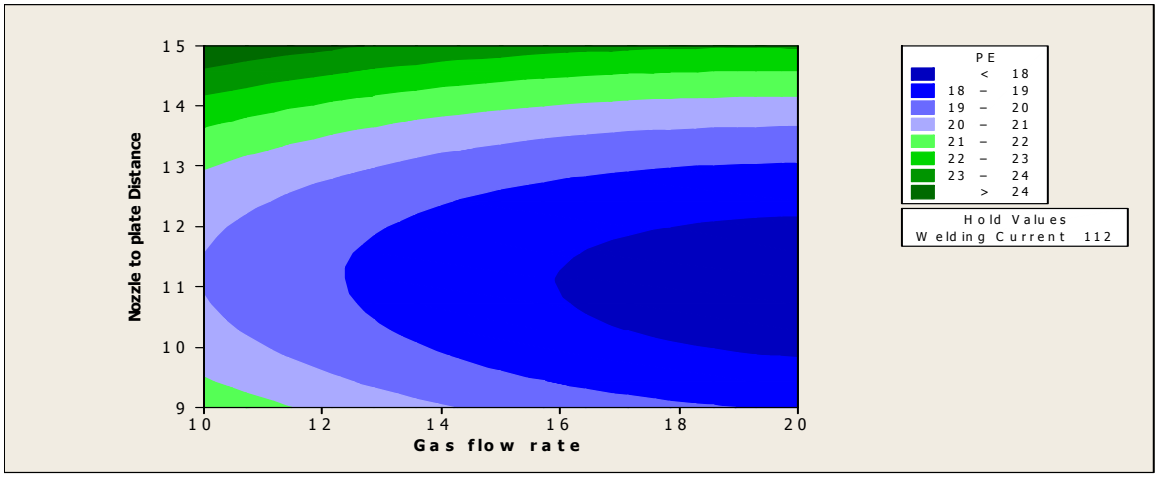

(5.43b) Welding current(C) is constant at middle level

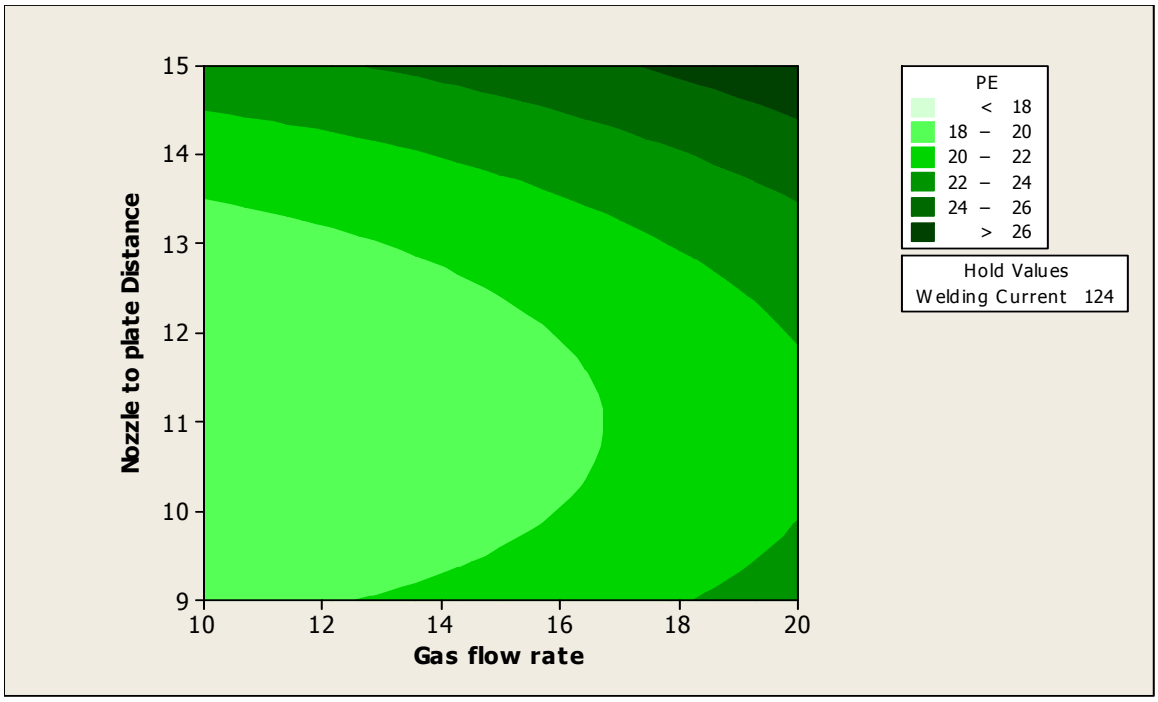

(5.43c) Welding current (C) is constant at highest level

Figure 5.43 Contour plots showing combined effects of Gas flow rate (F) and Nozzle to plate distance (S) on PE when Welding current (C) is kept constant: 409 Ferritic stainless steel

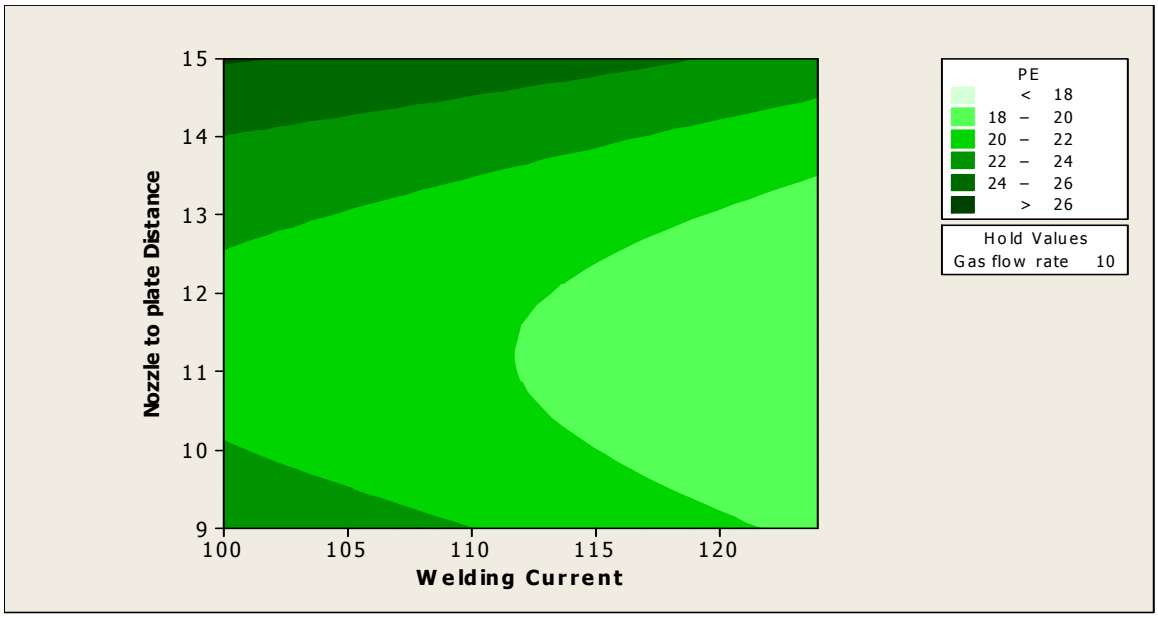

(5.44a) Gas flow rate (F) is constant at lowest level

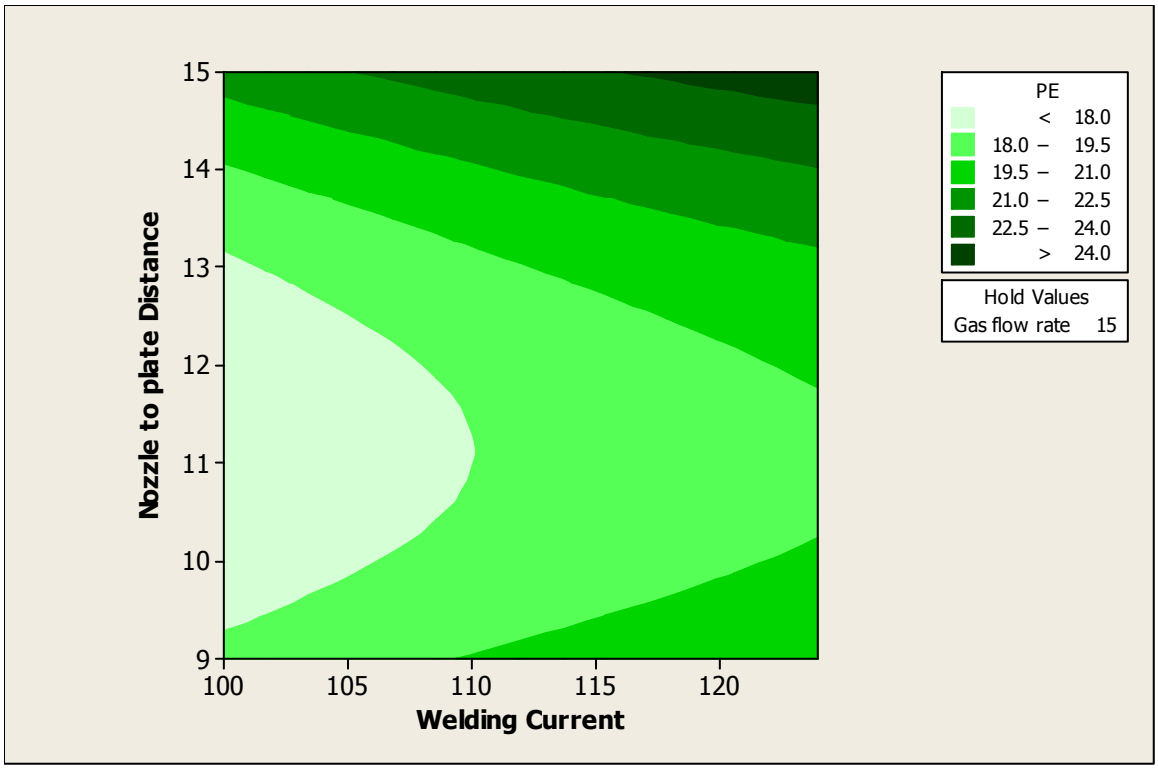

(5.44b) Gas flow rate (F) is constant at middle level

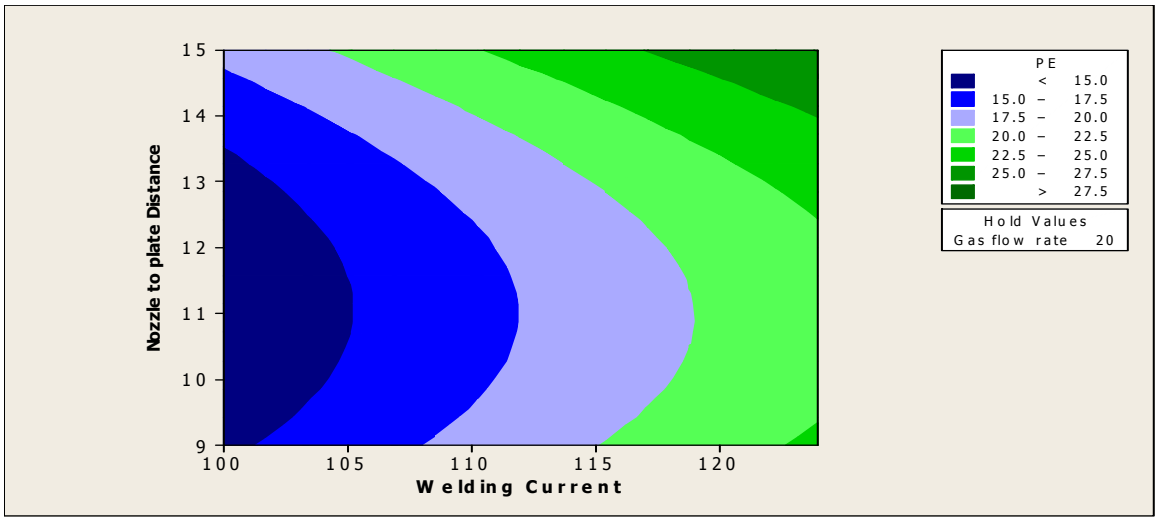

(5.44c) Gas flow rate (F) is constant at highest level

Figure 5.44 Contour plots showing combined effects of Welding current (C) and Nozzle to plate distance (S) on PE when Gas flow rate (F) is kept constant: 409 Ferritic stainless steel

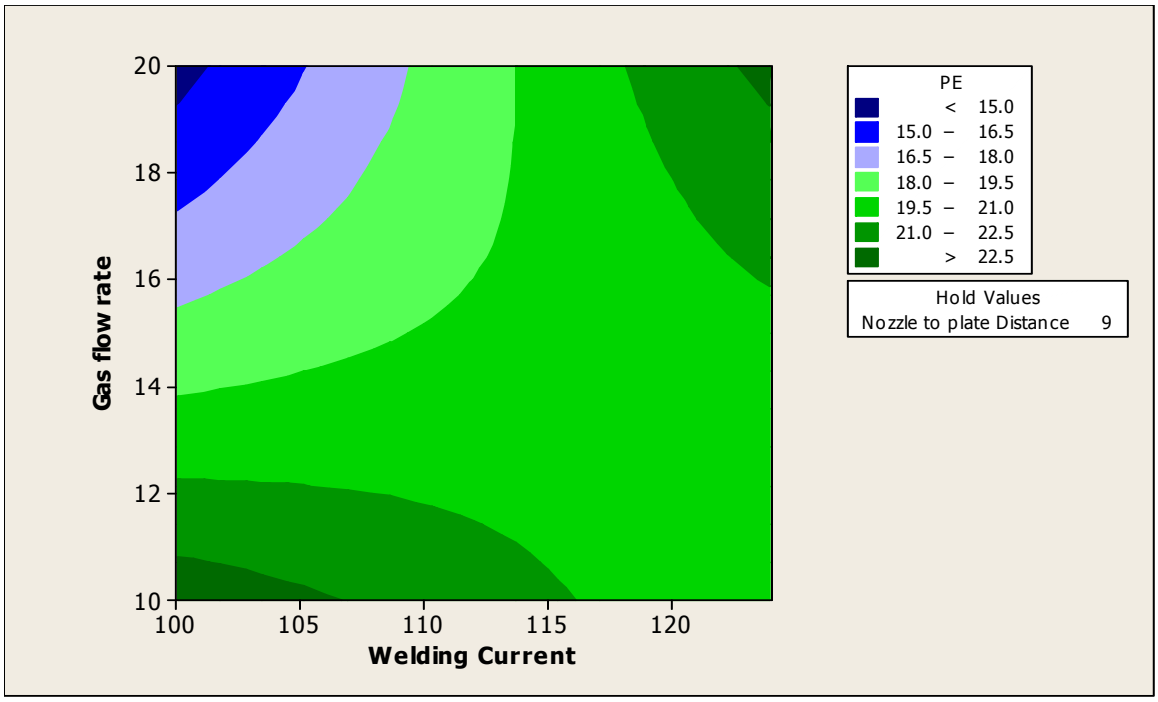

(5.45a) Nozzle to plate distance (S) is constant at lowest level

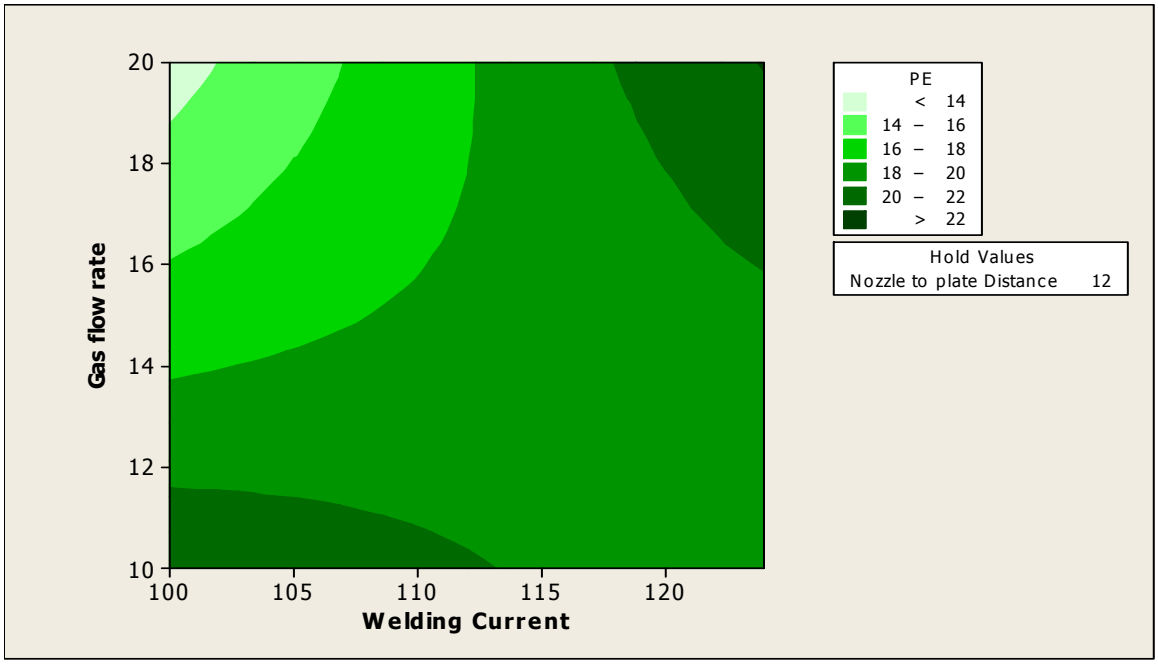

(5.45b) Nozzle to plate distance (S) is constant at middle level

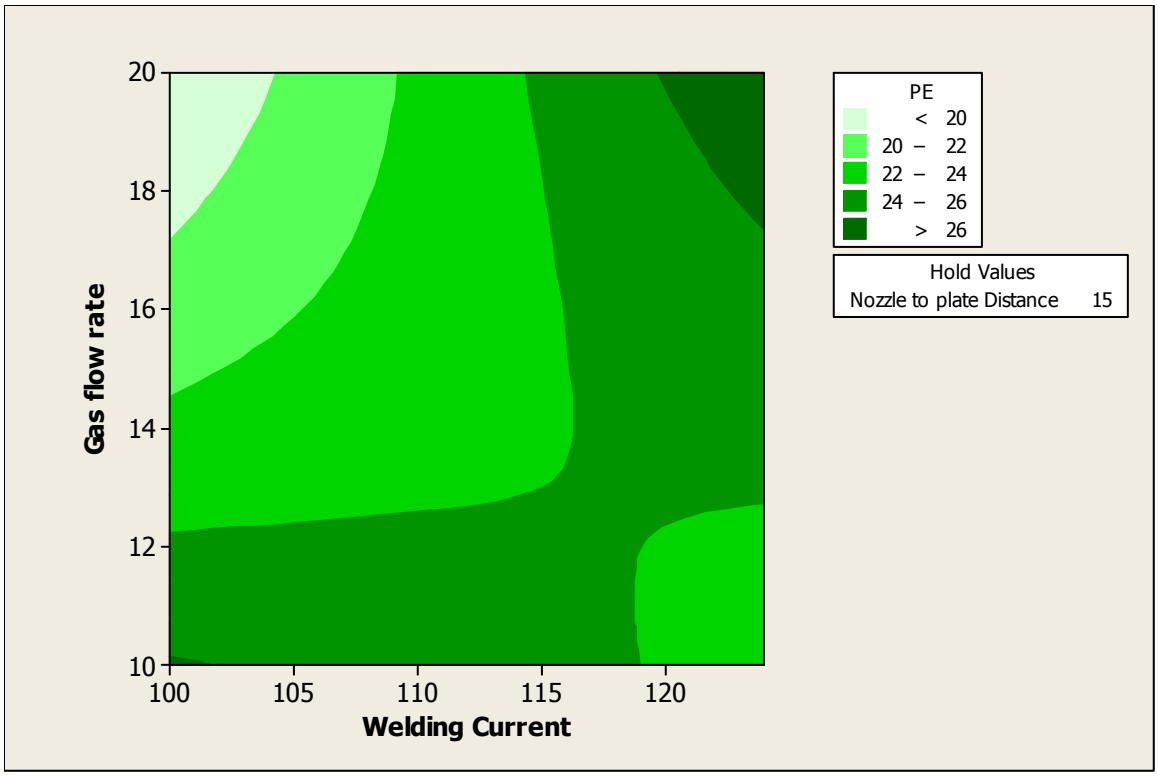

(5.45c) Nozzle to plate distance (S) is constant at its highest level

Figure 5.45 Contour plots showing combined effects of Welding current (C) and Gas flow rate (F) on PE when Nozzle to plate distance (S) is kept constant: 409 Ferritic stainless steel

Contour plots (shown in figures 5.43 – 5.45) give the idea about the combined effects of any two parameters on the response. Further, as stated elsewhere, the contour lines, with little or no curvature indicate lesser or no interaction effect; whereas bent or circular contours suggest interaction effect to be significant on the response. Thus, for example, interaction among the factors Gas flow rate (F) and Nozzle to plate distance (S) is found to be significant in so far as the effect of this interaction on PE is concerned (figures 5.43 a-c).

5.2.4 PROCESS OPTIMIZATION: MIG WELDING OF 409 FERRITIC STAINLESS STEEL

The following sections deal for the second set. Single objective optimization has been carried by RSM philosophy. Multi-objective optimization has been done by two techniques: RSM and Grey based Taguchi Method.

5.2.4.1 SINGLE-OBJECTIVE OPTIMIZATION BY RSM: 409 FERRITIC STAINLESS STEEL

Next, it is important to determine the best parametric condition. Here RSM is used for single-objective optimization for UTS, YS and PE separately.

A) SINGLE-OBJECTIVE OPTIMIZATION OF UTS

The optimized parametric condition for UTS by RSM is shown in the figure 5.46. This is obtained by using the observed results given in Table 4.10 of chapter 4 and using the MINITAB 16 software for solving single objective optimization problem using RSM. The optimized UTS is 472.59 MPa with desirability 1.0000. The optimized parametric combination is Welding current C = 100A, Gas flow rate F =19.4 *l*/min and nozzle to plate distance S = 9 mm. This is from figure 5.47.

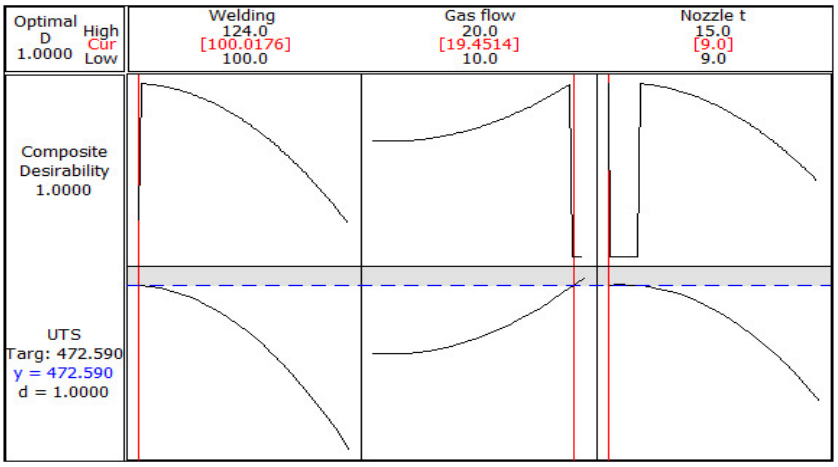

Figure 5.46 Response optimization plot for UTS: 409Ferritic stainless steel

Confirmatory test

Confirmatory test is carried out for the sample made at optimum setting of the parameters i.e. Welding current(C) = 100 A, Gas flow rate (F) = 19 l/min and Nozzle to plate distance= 9 mm. Results of confirmatory test show that UTS of the sample is 468 MPa, which matches fairly with the optimized UTS by RSM. Optimum condition is thus confirmed.

B) SINGLE-OBJECTIVE OPTIMIZATION OF YS

The optimized parametric condition for yield strength YS by RSM is shown in the figure 5.47. This is obtained based on the data given in Table 4.10 of chapter 4 and using the MINITAB 16 software for solving single objective optimization problem using RSM. The optimized YS is 349 MPa with desirability 1.0000. The optimized parametric combination is Welding current C = 100 A, Gas flow rate F =19.8 l/min and Nozzle to plate distance S = 9 mm.

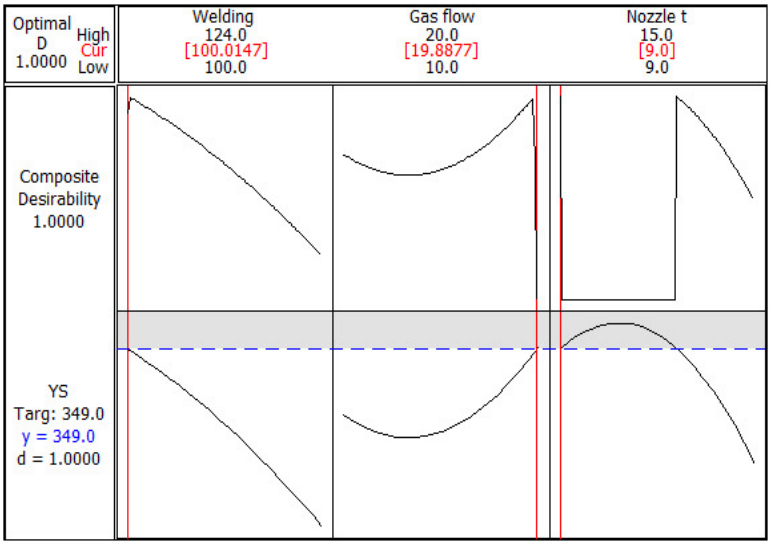

Figure 5.47 Response optimization plot for YS: 409 Ferritic Stainless steel

Confirmatory test

Confirmatory test has been conducted at the optimized parametric setting i.e., at current (C) = 100 A, gas flow rate (F) = 19.8 l/min and Nozzle to plate distance= 9 mm. Results of tensile test of the sample welded at the optimal setting of the parameters show that YS of the sample is 349 MPa, which is very close to the optimized YS by RSM. Validation of optimum condition is thus obtained.

C) SINGLE-OBJECTIVE OPTIMIZATION OF PE

The result of RSM optimization done in this respect is given in figure 5.48. Here also MINITAB software 16 has been used and data are taken from Table 4.10, chapter 4 - which contain the

observed results in this context. The optimized PE, in single objective optimization, is 25% with desirability 1.0000. The optimized parametric combination is Welding current C = 111.3 A, Gas flow rate F =10 *l*/min and Nozzle to plate distance S = 15 mm.

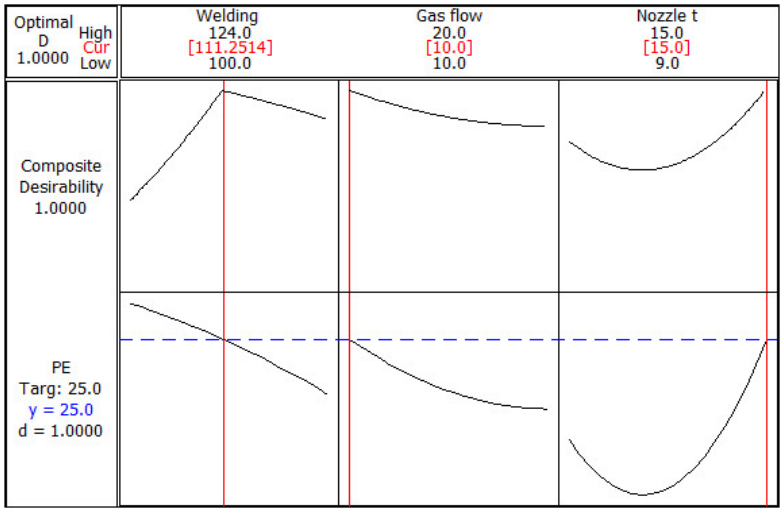

Figure 5.48 Response optimization plot for PE: 409Ferritic stainless steel

Confirmatory test

Test has been conducted at the optimized parametric setting i.e., at Welding current (C) = 111.3 A, Gas flow rate (F) = 10 l/min and Nozzle to plate distance= 15 mm. A sample is obtained by welding at the said setting. Result of tensile test of that sample shows that PE of the sample is 24.5%, which is close to optimized value by RSM. Validation of optimum condition is thus obtained.

5.2.4.2 MULTI-OBJECTIVE OPTIMIZATION BY RSM: AISI 409 FERRITIC STAINLESS STEEL

A toolbox for carrying out multi-objective optimization by RSM is available in MINITAB 16 software. This has been used using the data given in Table 4.10, in chapter 4. Multi-response optimization plot for UTS, YS and PE is shown in figure 5.49. From this figure it is observed that the optimum condition evaluated by RSM is: Welding Current C = 105.8 A, Gas flow rate F = 10 *l*/min and Nozzle to plate distance = 13.1 mm. The corresponding UTS is 447.4392 MPa

with desirability = 0.88343 and YS is 321.2705 MPa with desirability = 0.86920 and PE is 21.9669% with desirability =0.63836. Figure 5.50 is the basis of above findings.

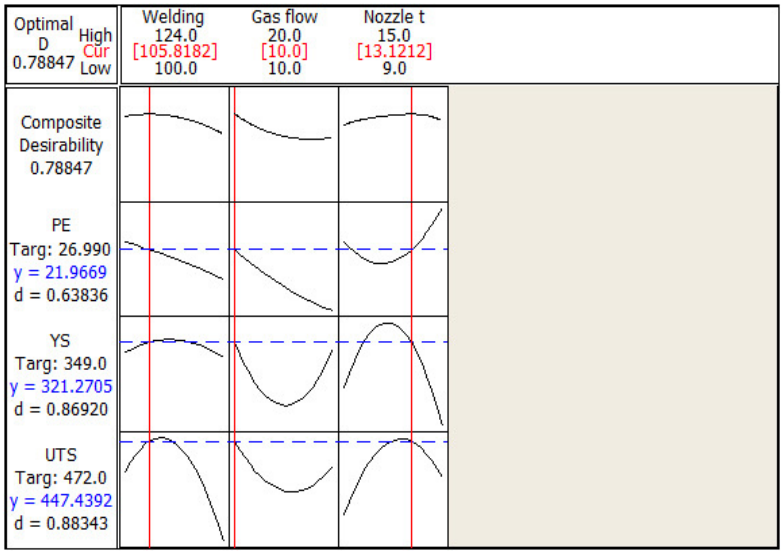

Figure 5.49 Multi-response optimization plot of UTS, Yield strength (YS)and Percentage Elongation (PE)

Confirmatory test

Confirmatory test has been conducted at the optimized parametric combination, i.e., at Welding current (C) = 105.8 A, Gas flow rate (F) = 10 l/min and Nozzle to plate distance = 13 mm. Result of the confirmatory test of the sample prepared at the optimum combination of the parameters as mentioned above, show that measured UTS is 450 MPa and yield strength of the sample is 321.9 MPa , PE is 23.4%; Prediction by RSM matches well with these values. Plot of this test is given in figure 5.50.

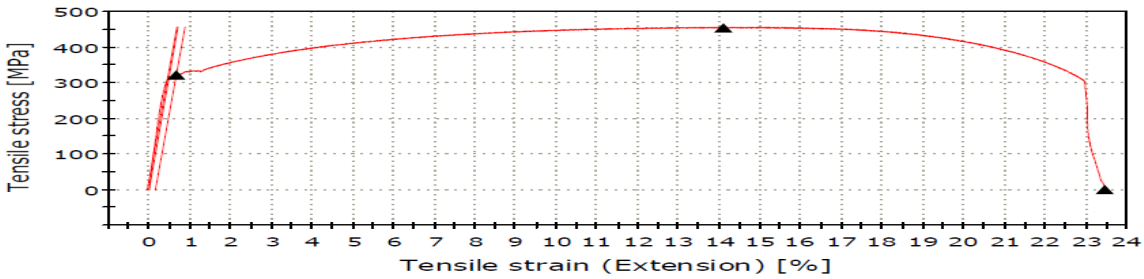

Figure 5.50 Confirmatory tensile test: plot for AISI 409 Ferritic stainless steel

5.2.5 MULTI – OBJECTIVE OPTIMIZATION BY GREY BASED TAGUCHI METHOD: 409 FERRITIC STAINLESS STEEL

Linear normalization of the experimental data of Table 4.14 is performed in the range between zero and unity, which is also called the grey relational generating. Normalization of the experimental data is calculated by using eq. (2.9)

Normalization of experimental data is shown in Table 5.12 (Based on larger the better criterion).

Table 5.12 Normalization of experimental data based on L9Taguchi Orthogonal Array design of experiment: 409 Ferritic stainless steel

Sample No.	Yield strength (MPa)	Ultimate tensile strength (MPa)	Percentage of elongation (%)
S1D	0.70082	0.74209	1.00000
S2D	0.21319	0.09613	0.00000
S3D	0.22379	0.10551	0.33301
S4D	0.62191	0.56624	0.24402
S5D	0.00000	0.00000	0.90431
S6D	0.60071	0.65299	0.1866
S7D	0.70082	0.74209	1.00000
S8D	0.58304	0.64713	0.2823
S9D	1.00000	1.00000	0.79904

Grey Relation Coefficients are listed in Table 5.13. Grey Relation Coefficient is calculated by using eq. (2.10)

Table 5.13 Grey Relation Coefficients: 409 Ferritic stainless steel

Sample No.	Grey Relation Coefficient		
	Yield strength(MPa)	Ultimate tensile strength(MPa)	Percentage of elongation (%)
S1D	0.62564	0.65971	1.00000
S2D	0.38856	0.35616	0.33333
S3D	0.39179	0.35855	0.42845
S4D	0.56942	0.53547	0.39810
S5D	0.33333	0.33333	0.83936
S6D	0.55599	0.59031	0.38069
S7D	0.62564	0.65971	1.00000
S8D	0.54528	0.58626	0.41061
S9D	1.00000	1.00000	0.71331

After averaging the grey relation coefficients, the grey relational grades γ_i . are computed using eq. (2.11)

The grey relational grades γ_i are shown in Table 5.14**.**

Table5.14 The grey relational grades: 409 Ferritic stainless steel

Sample no.	Grey relational grade
S1D	0.761783
S2D	0.359350
S3D	0.392931
S4D	0.500994
S5D	0.502010
S6D	0.508999
S7D	0.761783
S8D	0.514049
S9D	0.904436

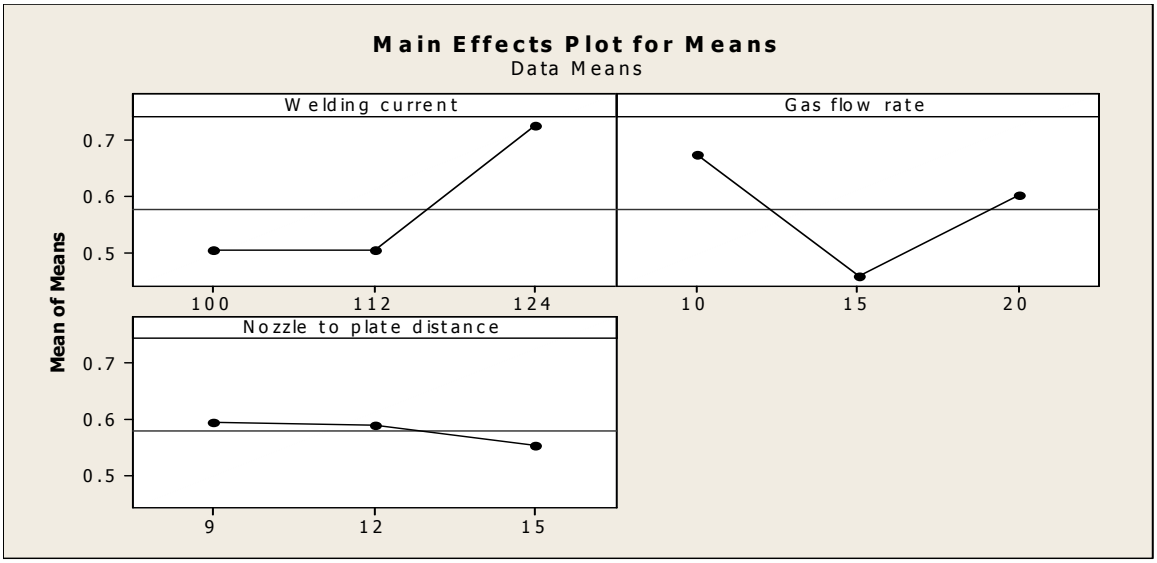

Figure5.51 Main effects plot of the means for grey relational grade: 409 Ferritic stainless steel

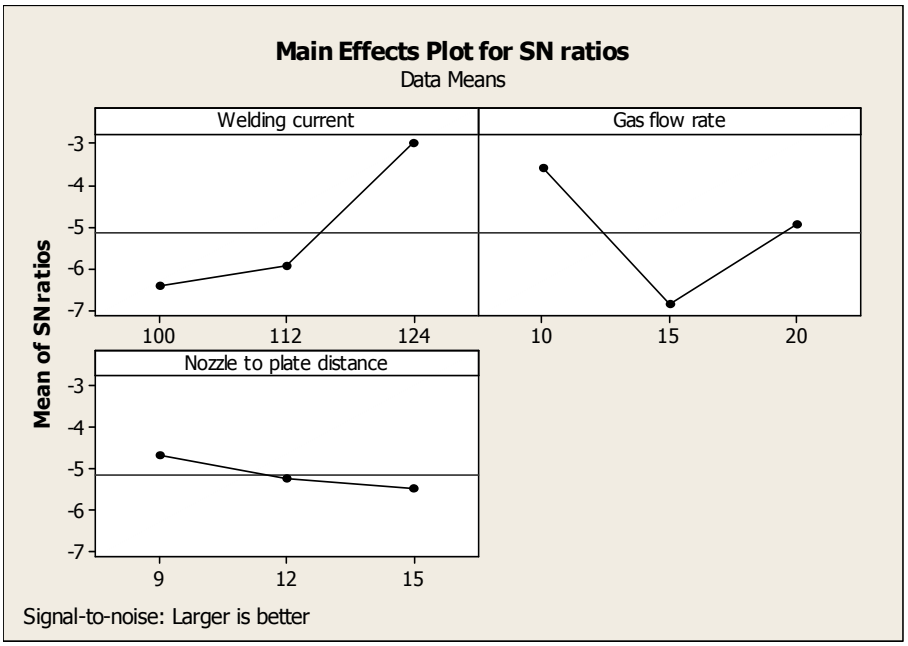

Figure 5.52 S/N ratio Plots for grey relational grade : 409 Ferritic stainless steel

With the help of Main effects plots and S/N ratio plots (figures 5.51 and 5.52) optimum parametric combination has been determined. The optimal factor setting becomes **C3F1S1** (i.e. Welding current = 124 A, Gas flow rate = 10 *l*/min and Nozzle to plate distance = 9 mm).

Analysis of Variance for overall grey relation grade is shown in Table 5.15.

Table 5.15 Analysis of Variance for overall grey relation grade: 409 Ferritic stainless steel

Source	DF	Seq SS	Adj SS	Adj MS	F	P	Percentage of contribution
Welding current	2	0.09893	0.09893	0.04947	0.97	0.507	35
Gas flow rate	2	0.07275	0.07275	0.03637	0.71	0.583	26.09
Nozzle to plate distance	2	0.00317	0.00317	0.00158	0.03	0.970	3.11
Error	2	0.10188	0.10188	0.05094			36.8
Total	8	0.27672					

S = 0.225695 R-Sq = 63.18% R-Sq(adj) = 0.00%

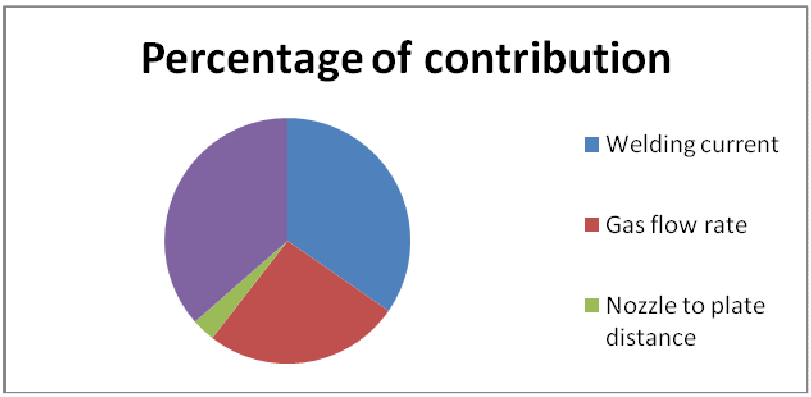

Figure 5.53 Pie Chart of Percentage of contribution: 409 Ferritic stainless steel

Percentage of contribution in case of 409 Ferritic stainless steel is shown in figure 5.53. The Welding current appears to be more significant than other input parameters. The same conclusion can also be derived from Table 5.15, by examining the P-value of each individual input parameter.

Confirmatory test

At the optimized parametric setting i.e., at Welding current = 124 A, Gas flow rate = 10 *l*/min and Nozzle to plate distance = 9 mm, results of tensile test are the following: UTS: 489.3 MPa, YS: 353.6 MPa, PE: 13.2%. Validation of optimum condition is thus obtained. Stress-strain diagram of the test performed on the confirmatory sample is shown in figure 5.54.

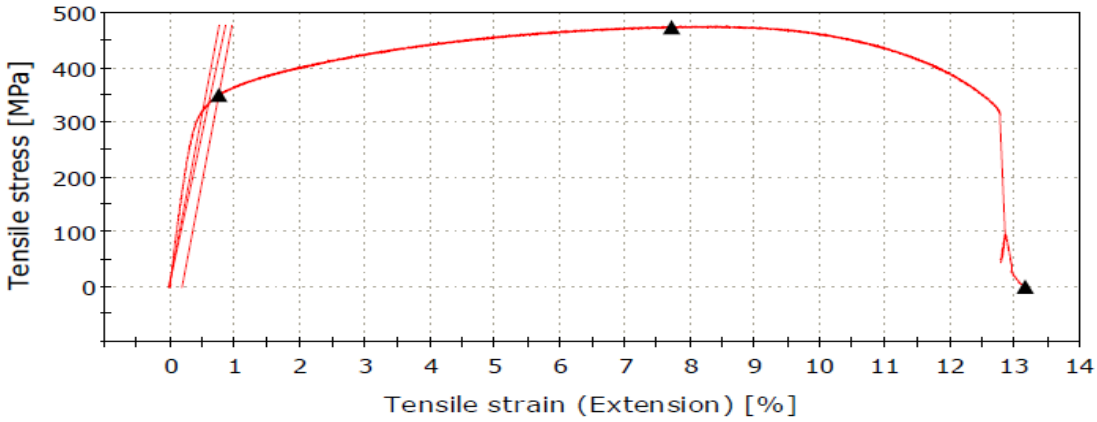

Figure 5.54 Tensile test diagram for confirmatory test: 409 Ferritic stainless steel

5.2.6 COMPARISONS OF MULTI OBJECTIVE OPTIMIZATION RESULTS DONE BY GREY-TAGUCHI METHOD AND RSM: 409 FERRITIC STAINLESS STEEL

Optimal parametric condition for multi objective optimization has been determined by Taguchi method and RSM method for each of the responses UTS, YS and PE.

By the Grey-Taguchi method, the optimal parametric condition is found as: Welding current = 124 A, Gas flow rate = 10 *l*/min and Nozzle to plate distance = 9 mm and by RSM, optimized parametric condition is found to be: Welding current (C) = 105.8 A, Gas flow rate (F) = 10 l/min and Nozzle to plate distance = 13.1 mm. The response values, at optimal parametric condition are shown in Table 5.16.

Table 5.16 Multi-objective optimization values for 409 Ferritic stainless steel by Taguchi and RSM

Technique	UTS (MPa)	YS (MPa)	PE(%)
Response Surface Methodology (RSM)	450MPa	321.9 MPa	23.4
Grey-Taguchi Method	489.3MPa	353.6 MPa	13.2

The response values shown in the Table are not too apart, though not quite close. However, the results of Grey- Taguchi Method appear to be more useful as the corresponding UTS and YS values are larger, at the cost of some ductility indeed.

5.3 ANALYSIS: RESULTS OF MIG WELDING OF 316L AUSTENITIC STAINLESS STEEL TO 409 FERRITIC STAINLESS STEEL (3RD SET OF EXPERIMENTS)

In the following paragraphs the results of MIG welding of 316L Austenitic stainless steel to 409 Ferritic stainless steel are analyzed for multi-objective optimization by Grey-Taguchi method.

5.3.1 MULTI – OBJECTIVE OPTIMIZATION BY GREY BASED TAGUCHI METHOD: 316L AUSTENITIC STAINLESS STEEL TO 409 FERRITIC STAINLESS STEEL

All linear normalization of the experimental data is performed in the range between zero and unity, which is also called grey relational generating. Experimental data are obtained from the Table 4.17.

Normalization of experimental data is shown in Table 5.17. It is done using eq. (2.9) based on larger the better criterion.

Table 5.17 Normalization of experimental data based on L9Taguchi Orthogonal Array design of experiment: 316L Austenitic stainless steel to 409 Ferritic stainless steel

Sample No.	Normalized Values		
	Yield Strength (MPa)	Ultimate Tensile Strength(MPa)	Percentage of Elongation (%)
Ideal	1.00000	1.00000	1.00000
S1C	0.48362	0.44733	0.48358
S2C	0.13701	0.03155	0.90003
S3C	1.00000	1.00000	1.00000
S4C	0.23739	0.18297	0.57679
S5C	0.23396	0.22464	0.39778
S6C	0.59225	0.61196	0.42386
S7C	0.51789	0.46541	0.00000
S8C	0.00000	0.00000	0.27141
S9C	0.68882	0.62641	0.74823

Grey Relation Coefficients calculated by using eq. 2.10, are shown in Table 5.18.

Table 5.18 Grey Relation Coefficients: 316L Austenitic stainless steel to 409 Ferritic stainless steel

Sample No.	Grey relational coefficients (k)		
	Yield Strength(Mpa)	Ultimate Tensile Strength (MPa)	Percentage of Elongation (%)
S1C	0.49194	0.47498	0.49192
S2C	0.36684	0.34049	0.83338
S3C	1.00000	1.00000	1.00000
S4C	0.39601	0.37964	0.54159
S5C	0.39493	0.39205	0.45363
S6C	0.55081	0.56304	0.46462
S7C	0.50911	0.48328	0.33333
S8C	0.33333	0.33333	0.40697
S9C	0.61639	0.57235	0.66510

After averaging the grey relation coefficients, the grey relational grades γ_i -s are determined, using eq. (2.11). The grey relational grades γ_i -s are shown in Table 5.19.

Table 5.19 The grey relational grades: 316L Austenitic stainless steel to 409 Ferritic stainless steel

Sample No.	Grey relational grade
S1C	0.48628
S2C	0.51357
S3C	1.00000
S4C	0.43908
S5C	0.41354
S6C	0.52616
S7C	0.44191
S8C	0.35788
S9C	0.61794

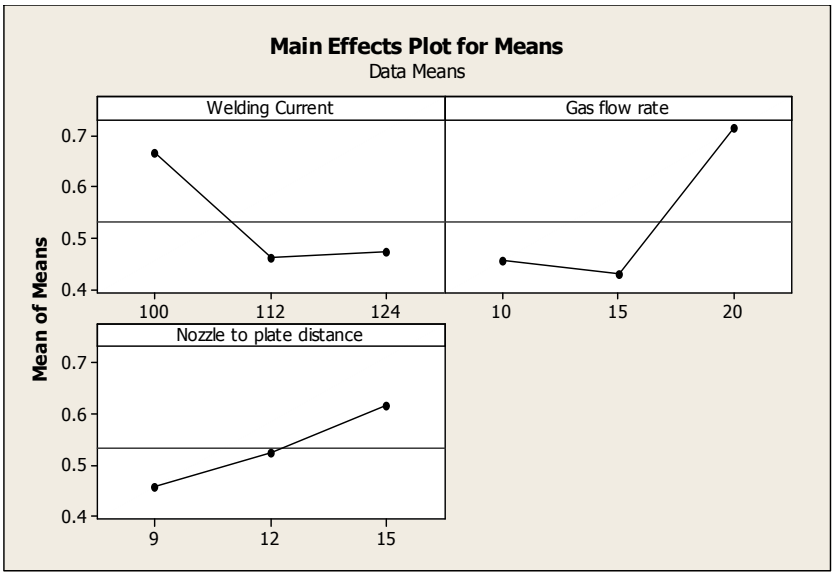

Figure 5.55 Mean Effects Plots for means of grey relational grade: 316L Austenitic stainless steel to 409 Ferritic stainless steel

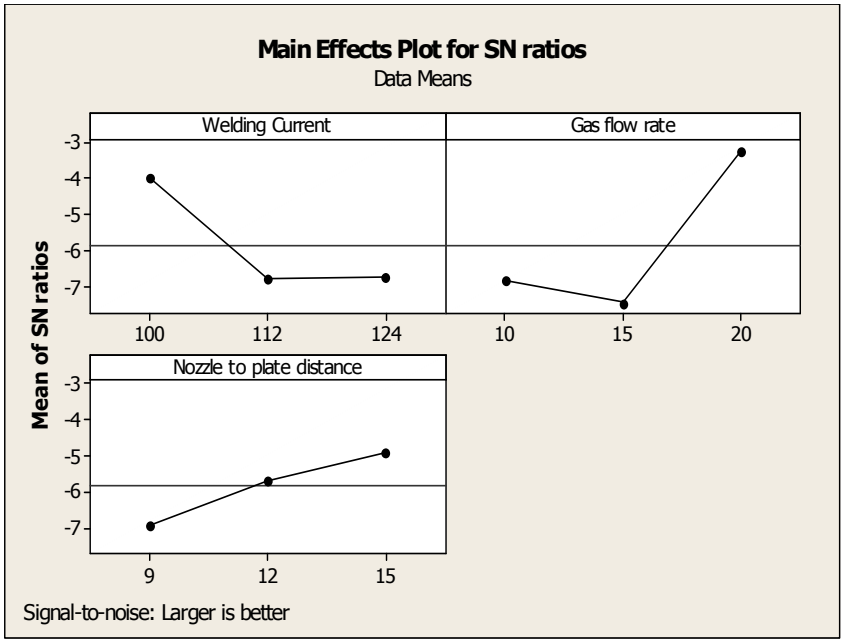

Figure5.56 S/N ratio Plot for grey relational grade: 316L Austenitic stainless steel to 409 Ferritic stainless steel

With the help of Mean main effects plot and S/N ratio plots (figures 5.55 and 5.56) optimum parametric combination has been determined. The optimal factor setting becomes **C1F3S3** (i.e. Welding current = 100A, Gas flow rate = 20*l*/min and Nozzle to plate distance =15mm).

Analysis of Variance for overall grey relation grade is shown in Table 5.20, where it is observed that maximum contribution on overall grey relation grade is from Gas flow rate.

Table 5.20 Analysis of Variance for overall grey relation grade: 316L Austenitic stainless steel to 409 Ferritic stainless steel

Source	DF	Seq SS	Adj SS	Adj MS	F	P	Percentage of contribution(%)
Welding Current	2	0.080679	0.080679	0.040339	4.06	0.197	27.82
Gas flow rate	2	0.149812	0.149812	0.074906	7.55	0.117	51.6
Nozzle to plate distance	2	0.039623	0.039623	0.019811	2.00	0.334	13.6
Error	2	0.019854	0.019854	0.009927			6.8
TOTAL	8	0.289967					

S = 0.0611358 R-Sq = 92.85% R-Sq(adj) = 71.40%

Confirmatory Test

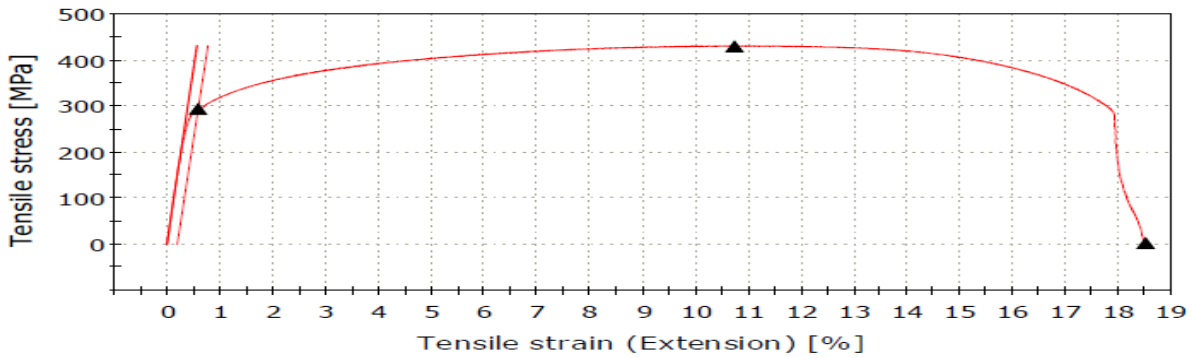

Figure 5.57 Confirmatory Tensile Test Diagram : 316L Austenitic stainless steel to 409 ferritic stainless steel

Confirmatory test has been conducted at the optimized parametric setting i.e., at Welding current (C) = 100 A, Gas flow rate (F) = 20 *l*/min and Nozzle to plate distance = 15 mm and Confirmatory tensile test diagram is shown in figure 5.57. Results of tensile test of the sample

are: UTS: 462 MPa, YS: 293.5 MPa, PE: 18.3%. Thus the results of optimization process appear to be acceptable.

(The symbols/terms used in all the ANOVA tables and optimization plots carry the usual meaning, if not mentioned separately)

Chapter 6

6. CONCLUSIONS AND FUTURE SCOPE OF WORK

6.1 CONCLUSIONS

The present study investigates, first, some perspectives of GMAW of i) Austenitic stainless steel and ii) Ferritic stainless steel, next dissimilar welding between Austenitic stainless steel to Ferritic stainless steel by MIG welding, under varied input parameters (Welding current: 100A, 112A and 124A, Gas flow rate: 10*l*/min, 15 *l*/min and 20 *l*/min and Nozzle to plate distance: 9mm, 12mm and 15mm)

Welding of Austenitic stainless steel by GMAW: Based on the results of investigation and analyses, the following conclusions are made.

- Visual inspection and X-ray radiography test reveals that in few samples defects like porosity, lack of fusion, undercut occur. However, almost defect free joints are also observed, under some parametric conditions.
- Tensile test results are found to be satisfactory, excepting for few samples. The variations in input parameters have influenced the mechanical properties to a certain extent. Ultimate Tensile Strength (UTS) varies from 538 MPa to 591 MPa
- Measurement of hardness at different zones of weldment indicates that hardness in weld metal is more than hardness in HAZ and base metal. HAZ hardness is found to be a little bit smaller than base metal. However, variation in hardness at different zones is not found to be too excessive. The graphical plots show similar pattern for all the samples.
- Pure austenitic structure with significant amount of austenitic twin is found in the microstructure of base metal. No significant difference is observed in the microstructure of HAZ with respect to base metal microstructure. However, grain growth is observed in HAZ. Austenitic twins are also observed in HAZ and equiaxed grain is observed in weld metal. In some samples columnar dendritic growth is also found. Micro structural characteristics are more or less consistent with results of tensile test.

- Optimal condition is determined as Current 111.8A, Gas flow rate 17.2l/min, Nozzle to plate distance 15mm. This is the multi –objective optimization result, done by using RSM for maximizing of UTS, YS and PE simultaneously
- Both the results are validated by confirmatory experiments. Maximum UTS 570.3 MPa, YS 315 MPa and PE 42% is found to be with Grey-Taguchi method.
- Optimum conditions for single objective optimization are also determined for each of the responses separately.
- Mathematical modeling, response surfaces and contour plots are generated. These are found to be useful to predict responses under different combinations of any two parameters, while the third parameter is held constant.
- Significance of each of the factors has been identified through ANOVA. Most significant factor is Welding current. Interaction effects are also determined.

Welding of Ferritic stainless steel by GMAW: Following conclusions are drawn from the observed data and data analysis.

- Some defects like porosity, lack of fusion are observed in some of the samples in visual inspection and X-ray radiography due to change in the level of the input parameter. Defects free joints are also obtained.
- Tensile test results indicate that within the range of input parameters used in the study, some of the samples exhibit fairly good ultimate tensile strength. The variation in the mechanical properties- UTS, YS and PE is also observed. Maximum UTS is found to be 472.6 MPa.
- Hardness in HAZ is of lower value than in weld in most of the cases. Trends in hardness plot are similar irrespective of parametric combinations.
- Base material show typically ferritic matrix which is usual for Ferritic stainless steel. In general, austenitic grains are found to be coarser in HAZ than in base metal. This may be attributed to lower cooling rate in the HAZ region. In some of the portions, precipitated carbide has been found. Dispersed carbide phases are found in HAZ region. Sample no. S10B shows lowest UTS in tensile test.
- Microstructures determine mechanical properties, which are actually influenced by input parameters and other factors.

- Mathematical models showing relationships between input parameters and individual responses are made based on experimental data, response surface methodology and subsequently RSM plots and contour plots are generated which can be utilized for estimation of the response value by setting any two parameters at different combinations, third parameter being fixed at some constant level.
- Multi objective optimization results are the following i) RSM- Current (C) = 105.8 A, Gas flow rate (F) =10l/min and Nozzle to plate distance (S) =13.1mm (ii) Grey Taguchi method: C3F1S1 (Welding current = 124 A, Gas flow rate = 10 *l*/min and Nozzle to plate distance = 9 mm)
- Both the results are validated by confirmatory experiments. Maximum UTS is found to be with Grey-Taguchi method.
- Significance of the factors has been established by ANOVA. Welding current is found to be most significant factor. Next important factor is Gas flow rate.

Welding of Dissimilar welding between Austenitic stainless steel (AISI 316L) and Ferritic stainless (AISI 409) by GMAW: The following conclusions are drawn on the basis of present investigation on dissimilar welding between Austenitic and Ferritic stainless steel under varied input parameters.

- All the results indicate that within the range of the input parameters used in the study, dissimilar welding between Austenitic to Ferritic stainless steel is possible by MIG welding, yielding favourable results. However, at some combination of the input parameters, the results are better than the other combinations of parameters.
- In visual inspection and X-ray radiographic test, through some defects are observed in some samples, defect free joint are also obtained under some conditions.
- In tensile tests, UTS values are found satisfactory in the sense that these values are in between the UTS of Ferritic stainless steel and The UTS of Austenitic stainless steel.
- Hardness in HAZ is of lower value than in weld in most of the cases. Trends in hardness plot are similar irrespective of parametric combinations.
- Grain boundary austenite is found within ferrite matrix. Microstructure of weld metal consists of austenite and δ ferrite, Ferrite shape is lacy and vermicular, primary austenitic grains are clearly seen. Pro-eutectoid and Widmanstatten ferrite on grain boundaries are seen too.

- The optimal factor setting becomes C1F3S3 (i.e. Current =100A, Gas flow rate = 20l/min and Nozzle to plate distance = 15mm). This is obtained by Grey Taguchi method. The result is validated by confirmatory experiments.
- In dissimilar welding Gas flow rate is found to be the most significant factor in the context of multi-objective optimization.

Integrating all these, it is concluded that in the present work, effect of input parameters on output responses has been established; indentifying weld quality and determining optimum parametric condition and this is with reference to each of the three sub sets of the work.

6.2 FUTURE SCOPE OF WORK

- The parameters like voltage, electrode wire diameter and welding speed may also be included as variable input parameters in future study; these parameters have not been considered in the present study
- Experiments may be planned for GMA welding of some other Austenitic stainless steel (304, 309) and Ferritic stainless steel grades (430, 440) etc.
- The data of the present work may be used to build up reliable Artificial Neural Network and Fuzzy logic models for prediction of the responses under given set of input parameters.
- Effect of process parameters with variation in edge preparation may also be studied.
- Change in weld bead geometry with change in process parameters can also be studied.
- Single-objective optimization and multi-objective optimization have been carried out by RSM and Grey-Taguchi method, in the present work. Other techniques of optimization like principal component analysis, simulated annealing, colony optimization etc. may be used in future work with the objective of finding relative usefulness and limitations of the different techniques in the context of the objective and process considered.

REFERENCES

[1] M. Singla, D. Singh and D. Deepak, "***Parametric optimization of gas metal arc welding processes by using factorial design approach"***, Journal of Mineral and Material Characterization and Engineering 9 (2010) pp.353-363.

[2] U. Esme, M. Bayramoglu,Y. Kazancoglu and S. Ozgun, "***Optimization of weld bead geometry in TIG Welding process using grey relation analysis and Taguchi method***", Material and Technology. 43 (2009) pp. 143–149.

[3] S. Datta, G. Nandi, A. Bandyopadhyay and P. K. Pal, "***Application of PCA-based hybrid Taguchi method for correlated multi criteria optimization of submerged arc weld: a case study***", International Journal of Advances Manufacturing Technology 45 (2009) pp. 276–286.

[4] V.V. Satyanarayana, G. M. Reddy and T. Mohandas, "***Dissimilar metal friction welding of austenitic–ferritic stainless steels***", Journal of Material Processing and Technology. 160 (2005) pp. 128–137

[5] B. Weiss and R. Stickler, "***Phase instabilities during high temperature exposure of 316 austenitic stainless steel***", *Metallurgical Transaction* 3 (1972) pp. 851-866.

[6]C. Balaji, S.V.A. Kumar, S. A. Kumar and R. Satish, "***Evaluation of mechanical properties of SS 316 L weldments using tungsten inert gas welding***", International Journal of Engineering Science and Technology 4 (2012) pp. 2053-2057.

[7] G. J. Parr and A. Handson, ***Introduction to stainless steel, American Society for Metals,*** USA (1963).

[8] J.A. Sedriks, ***Corrosion of Stainless Steels***, *Wiley,* New York (1996).

[9] R. M. Molak, K. Paradowski, T. Brynk, L. Ciupinski, Z. Pakiela and K.J. Kurzydlowski, "***Measurement of mechanical properties in a 316L stainless steel welded joint***", International Journal of Pressure Vessels and Piping 86 (2009) pp. 43-47.

[10] H. Shengsun, H. Ruifeng, S. Jungi, H. Jian and X. Haigang, "***Effect of pulse frequency on microstructure of 21% Cr ferritic stainless steel in pulsed gas tungsten arc welding***", Transaction Tianjin University, 19 (2013) pp. 127-129

[11] D. Qizhan, ***Welding of Stainless Steel,*** China Machine Press, China (2009).

[12] S. Afshan and L. Gardner, "***Experimental study of cold-formed ferritic stainless steel hollow sections***", Journal. of Structural Engineering 139 (2013) pp. 717–728

[13] M. Li, H. Shengsun, H. Bao, S. Junqi and W. Yonghui, "***Activating flux design for laser welding of ferritic stainless steel***", Transaction Tianjin University, 20 (2014) pp. 429-434

[14]M. Arivarasu, D. R. Kasinath and A. Natarajan, "***Effect of continuous and pulsed current on the metallurgical and mechanical properties of gas tungsten arc welded AISI 4340 aeronautical and AISI 304 L austenitic stainless steel dissimilar joints***", *Material Research* 18 (2015) pp. 59-77.

[15] J. N. Dupont and C. S. Kusko. Technical note: "***Martensite formation in austenitic/ferritic dissimilar alloy welds***". Welding Journal (2007) pp. 51-54.

[16] R.S. Parmar, "Welding Processes and Technology", 2nd edition, Khanna Publications, New Delhi-1997.

[17] O.P. Khanna, "Welding Technology", Dhanpat Rai & Sons, 1986.

[18] https://me-mechanicalengineering.com/gas-metal-arc-welding-gmaw/dated08.02.2014

[19] A. Ghosh, & A.K. Mallik, "Manufacturing Science", East-West Press Private Limited, New Delhi-2008.

[20] https://www.sciencedirect.com/topics/engineering/gas-metal-arc-welding/ dated 16.02.2014

[21]B. Vijaya Sankar, I. Daniel Lawrence, S. Jayabal, "***Experimental Study and Analysis of Weld Parameters by GRA on MIG Welding***" ,Materials Today: Proceedings, Volume 5, Issue 6, Part 2, 2018, pp. 14309-14316,

[22] K Srinivasan, V Balasubramanian, "***Effect of Heat Input on Fume Generation and Joint Properties of Gas Metal Arc Welded Austenitic Stainless Steel***", Journal of Iron and Steel Research, International, Volume 18, Issue 10, 2011, pp. 72-79

[23] Xiaohui Chen, Jia Li, Xu Cheng, Bei He, Huaming Wang, Zheng Huang, "***Microstructure and mechanical properties of the austenitic stainless steel 316L fabricated by gas metal arc additive manufacturing***", Materials Science and Engineering: A, Volume 703 2017, pp. 567-577

[24] Abbasi. K, Alam. S, Khan. M. I, " ***An experimental study on the effect of increased pressure on MIG welding arc***", International journal of applied engineering research, Dindigul, Vol2, No1,(2011) pp. 22-27

[25] Khanna, P., Maheshwari, S. "***Microhardness analysis in mig welding of stainless steel 409M***", Journal of production engineering (2017) Vol.20 (1) pp. 93-96

[26] Biswajit Das, B. Debbarma, R. N. Rai, S. C. Saha"***Influence of process parameters on depth of penetration of welded joint in mig welding process*****,**" International journal of research in engineering and technology 02 issue: 10 (oct-2013) pp. 220-224, ISSN: 2321-7308

[27] H. H. Na, I.S. Kim, B.Y. Kang and J.Y. Shim "***An experiment study for welding optimization of fillet welded structure***," Journal of achievements in materials and manufacturing engineering vol. 45 Issue 2 (April 2011) pp. 178-187.

[28] A. Hooda, A. Dhingra and S. Sharma "***Optimization of mig welding process parameters to predict maximum yield strength in AISI 1040,***" International journal of mechanical engineering & robotic research, vol. 1, no. 3, October 2012 ISSN 2278 – 0149 pp.203-213

[29] C. N. Patel, S. Chaudhary "***Parametric optimization of weld strength of metal inert gas welding and tungsten inert gas welding by using analysis of variance and grey relational analysis***," International journal of research in modern engineering and emerging technology Vol. 1, issue: 3, (April-2013) (ijrmeet) ISSN: 2320-6586

[30]Gautam Kocher, Sandeep kumar and Gurcharan Singh "***experimental analysis in mig welding with is 2062E250 a steel with various effects***" international journal of advanced engineering technology, april-june, 2012, pp. 158-162

[31] A. R. Bahman and E. Alialhosseini "***change in hardness, yield strength and uts of welded joints produced of st37 grade steel*** " Indian journal of Science and Technology, Dec 2010.

[32] N. Murugan , R. S. Parmar, "***Effect of MIG process parameters on the geometry of the bead in the automatic surfacing of stainless steel***, "Journal of Material Processing Technology, vol.41, pp. 381-398, 1994.

[33] I. Z. Ibrahim, S.A. Mohamat, A. Amir, A. Ghalib, "***The effect of Gas Metal Arc Welding (GMAW) processes on different welding parameters***", Procedia Engineering, 41 (2012), pp. 1502-1506.

[34]K. Sittichai, N. Santirat, and P. Sompong, "***A study of gas metal arc welding affecting mechanical propertie of austenitic stainless steel AISI 304***", World Academy of Science, Engineering and Technology Vol.6 No.1, (2012), pp. 100-103.

[35] S. R. Patil, C. A. Waghmare "***Optimization of MIG Welding parameters for improving strength of welded joints***", International Journal of Advanced Engineering Research and Studies, July-Sept., 2013, pp. 14-16

[36]R.Yilmaz and H.Uzun,“ ***Mechanical properties of austenitic stainless steels welded by GMAW and GTAW***”, Journal of Marmara for Pure and Aplied Sciences, 18 (2002), pp. 97-113.

[37]Pradeep Khanna and, Sachin Maheshwari, “***Residual Stress Analysis in MIG Welding of Stainless Steel 409M***”, Materials Today: Proceedings, Volume 5, Issue 2, Part 1, 2018, pp. 4939-4947,

[38] Jince P Mathew , Dr. Binod Kumar , Dr. A. K. Pathak , Razaullah Khan “***Study of Corrosion Behavior of Tig and Mig Welded Joints of Ferritic Stainless Steel (FSS) (Aisi-430) in Different Environments***”International Journal of Innovative Research in Science, Engineering and Technology, Vol. 6, Issue 3, March 2017

[39] Erdal Karadeniz, Ugur Ozsarac, Ceyhan Yildiz “***The effect of process parameters on penetration in gas metal arc welding Processes***” Journal of Materials and design, Vol. 28, Issue 2, (2007) pp. 649-656.

[40]A. M. Torbati, R. M. Miranda, L. Quintino, S. Williams, D. Yapp “***Optimization procedures for GMAW of bimetal pipes***”. Journal of Materials process technology, Vol. 211, Issue 6 (1 June 2011) pp. 1112-1116.

[41] Ye Ruan, Xiao Ming Qiu, Wen Biao Gong, D.- Q. Sun, Y.P. Li***"Mechanical properties and microstructures of 6082-T6 joint welded by twin wire metal inert gas arc welding with the SiO2 flux"*** March 2012, Materials and Design , 35:pp. 20–24

[42] I .O.Oladele Msc, J.A Omotoyimbo Phd,B.O.Adewuyi Phd “***Study of the effect of welded joints on the mechanical properties of Wrought (6063) aluminum alloy***”, The Pacific journal of science and Technology, Vol 10, (Nov 2009),pp. 120-125

[43]P. J. Modenesi and R.C. de Avelar “***The influence of small variations of wire characteristics on gas metal arc welding process stability,***” Journal of Materials Processing Technology Vol. 86 Issue 1-3(1999) pp. 226–232

[44] Rati Saluja, K M Moeed “***Modeling and Parametric Optimization using Factorial Design Approach of Submerged Arc Bead Geometry for Butt Joint***”. International journal of engineering research and applications2248- 9622, Volume-2, Issue 3, May-June 2012 pp. 505-508

[45] G.Hargopal, P.V.R.Ravindra reddy, “***Parameter design for MIG welding of Al- 65032 alloy using Taguchi technique***”, Journal of Scientific & Industrial research, 0975-1084, Volume-70, October 2011, pp. 844-850

[46] P.K.J. Martikainen, "***Influence of shielding gases in the welding of metals***", Int J Adv Manuf Technol, DOI 10.1007/ s00170–012–4111–6, 2012

[47]H.Y. Huang, "***Effects of activating flux on the welded joint characteristics in gas metal arc welding***", Materials and Design 31 (2010), pp. 2488 – 2495.

[48]D.S. Correia, C.V. Gonclaves, S.S. da Cunha, V.A Ferraresi, "***Comparison between genetic algorithms and response surface methodology in GMAW welding optimization***", Journal of Materials Processing Technology 160 (2005), pp. 70-76.

[49] Hee-Keun Lee, Kwang-San Chun, Sang-Heyon Park, Chung Yun Kang "***A scientific application oriented classification for metal transfer modes in GMAW***," International Journal of Naval Architecture and Open Engineering, vol. 7, issue 4 July 2015, pp. 770-783

[50] Joseph Achebo, William Ejenavi Odinikuku "***Optimization of GMAW process parameters using standard deviation and multi objective optimization on the basis of ratio analysis (MOORA),***" Journal Minerals and Materials Characterization and Engineering.2015,3, pp.298-308

[51] Xiangmeng Meng, Guoliang Qin, Yuhu Su, Banglong Fu, Yang Ji, "***Numerical simulation of large spot laser+MIG arc brazing–fusion welding of Al alloy to galvanized steel***,"Journal of Materials Processing Technology, Volume 222, 2015, pp. 307-314.

[52] Abhishek Prakash & Raju S. S et al,(2016) "***Parametric optimization of metal inert gas welding by using taguchi approach***."International Journal of Research in Engineering and Technology, *Volume: 05 Issue: 02, Feb-2016).*

[53] Diganta Kalita.et al, (2015), "Taguchi ***Optimization of MIG Welding Parameters Affecting Tensile Strength of C20 Welds***."International Journal of Engineering Trends and Technology (IJETT) – Volume 26 Number 1- August 2015. ISSN: 2231-5381

[54] A R Yazdipour, A shafiei M ,H. Jamshidi Aval "***An investigation of the microstructures and properties of metal inert gas and friction stir welds in aluminum alloy 5083***" ,Sadhana ,Vol 36,issue 4,(Aug 2011), pp. 505-514

[55] Rajesh P Verna ,K.N Pandey "***Investigation of fatigue life of 6061-T6 and 5083-O aluminum alloys welded by two welding processes – manual metal arc welding and metal inert***

gas welding" ,International conference on mechanical and industrial engineering (ICMIE) -9th Sept 2012

[56] Anjaneya Prasad. B, Prasanna. P "***Experimental Comparison of the MIG and Friction stir welding processes for AA6061(Al Mg Si Cu) Aluminum alloy***" ,International Journal of Mining, Metallurgy & Mechanical Engineering (IJMMME) Vol. 1,Issue 2(2013) pp. 137-140

[57] J. P. Ganjigatti, Dilip Kumar Pratihar, A. Roy Choudhury "***Global versus cluster-wise regression analyses for prediction of bead geometry in MIG welding process***". Journal of Materials processing and technology, Vol.189, Issues1-3, (6 July 2007) pp. 352-366.

[58] Sukhomay Pal, Surjya K. Pal, Arun K. Samantaray "***Artificial neural network modeling of weld joint strength prediction of a pulsed metal inert gas welding process using arc signals***". Journal of Materials process technology, Vol. 202, Issues 1-3 (20 June 2008) pp. 464- 474.

[59] K. Manikya Kanti, P. Srinivasa Rao "***Prediction of bead geometry in pulsed GMA welding using back propagation neural network***". Journal of Materials process technology, Vol. 200, Issues 1-3 (8 May 2008) pp. 300-305.

[60] Dinesh Mohan Arya, Vedansh Chaturvedi, Jyoti Vimal "***Parametric optimization of mig process parameters using Taguchi and grey Taguchi analysis,***" International journal of research in engineering & applied sciences volume 3, issue 6 (June 2013) pp.1-17, ISSN: 2249-3905

[61]Neha Bhadauria, Prof. R. S. Ojha" ***Optimization of Process Parameters for Weld Bead Penetration of IS2062 Mild Steel for GMAW Process Using Response Surface Methodology***" International Journal of Advanced Research in Computer Science and Software Engineering, October 2012, pp. 349-353

[62] A.S. Shahi., S. Pandey., "***Modeling of the effects of welding conditions on dilution of stainless steel claddings produced by gas metal arc welding procedures,*** " Journal of Materials Processing Technology, 196.,pp. 339–344, 2008.

[63] K. Kishore., P.V.G. Krishna., K. Veladri., S.Q. Ali., "***Analysis of defects in gas shield arc welding of AISI 1040 steel using Taguchi Meth****od,*" ARPN Journal of Engineering and Applied Sciences. Vol. 5. No. 1, January 2010.

[64] S.R. Meshram and N.S.Pohokar "***Optimization of Process Parameters of Gas Metal Arc Welding to Improve Quality of Weld Bead Geometry***". 2321-0613, International Journal for Scientific Research and Development Volume-1, Issue 9, 2013

[65] Bhargav c Patel, Jaivesh Gandhi "***Optimizing and analysis of parameter for pipe welding***". International journal of engineering research and technology, 2278-0181, Volume-2, Issue 10, 2013

[66] Pengcheng Z., Dasen L. (2011) "***Study of the Free Surface Fluctuations in a GMAW Weld Pool with Globular Transfer Mode***". In: Dai M. (eds) Innovative Computing and Information. ICCIC 2011. Communications in Computer and Information Science,vol. 232., pp. 405–413.

[67]M..M. Anzehaee, M. Haeri, "***Estimation and control of droplet size and frequency inprojected spray mode of a gas metal arc welding (GMAW) process***", ISA Transactions, 50 (2011), pp. 409 – 418.

[68]W.U. Chuan-song, Z.O.U. De-gang, GAO Jin-quing, "***Determining the critical transition current for metal transfer in gas metal arc welding (GMAW)***", Frontiers of Materials Science in China, Volume 2, Issue 4, December 2008 , pp. 397–401

[69]I.S. Kim, A. Basu, "***A mathematical model of heat transfer and fluid flow in the gas metal arc welding***", Journals of Materials Processing Technology vol. 77 Issue 1-3(May 1998), pp. 17 -24.

[70]Hakan Ates "***Prediction of gas metal arc welding parameters based on artificial neural***" Journal of Materials and design, Vol. 28, Issue 7 (2007) pp. 2015-2023

[71] Sreeraj, Daniel Ramos-Jaime, Ismael López- Juárez, Pedro Perez, "***Effect of processparameters on GMAW bead area estimation***", Procedia Technology, Volume 7, (2013), pp. 398-405.

[72] Salawadagi Sushant S. & Kumbhar S. B. "***Parametric Optimization of Butt Weld for Minimum Residual Stress***". International Journal on Mechanical Engineering and Robotics (IJMER) ISSN (Print): 2321-5747, Volume-1, Issue-2, 2013

[73] S. Shashi Kumar, N. Murugan, K.K. Ramachandran, "***influence of tool material on mechanical and microstructuralproperties of friction stir welded 316 l austenitic stainless steel butt joints***", International Journal of Refractory Metals and Hard Materials vol. 58, pp.196-205 (2016).

[74]P. Bharath, V.G. Sridhar, M. Senthil kumar, "***Optimization of 316 Stainless Steel Weld Joint Characteristics using Taguchi Technique***" ,Procedia Engineering,Volume 97,2014, pp. 881-891

[75] S. Shashi Kumar, N. Murugan, K.K. Ramachandran, "***Microstructure and mechanical properties of friction stir welded AISI 316L austenitic stainless steel joints***", Journal of Materials Processing Technology, Volume 254, 2018, pp. 79-90,

[76] Danial Kianersi, Amir Mostafaei, Ahmad Ali Amadeh, "***Resistance spot welding joints of AISI 316L austenitic stainless steel sheets: Phase transformations, mechanical properties and microstructure characterizations***", Materials & Design, Volume 61, 2014, pp. 251-263

[77] B.N. Zuma, J.W. van der Merwe, "***Effect of Ru Addition on the Mechanical Properties and Microstructure of 316L Austenitic Stainless Steel Weld Metal***", Procedia Manufacturing, Volume 7, 2017, pp. 2-7

[78] E Ahmadi, AR Ebrahimi "***Welding of 316L austenitic stainless steel with activated tungsten inert gas process***" Journal of materials engineering and performance 24 (2), pp. 1065-1071

[79] M.O.H.Anuda; S. Mridha., 2011 "***Analysis of sensitization profile in Medium Chromium Ferritic stainless steel (FSS) welds***"Journal of Integrated Engineering, Vol. 3 No1 pp.17- 22.

[80] M. L. Greeef., M. du Toit. 2004, "***Looking at the Sensitization of 11–12% Chromium EN 1.4003 Stainless Steels during Welding***", welding journal. pp.243-251

[81]K. Shanmugam, A.K. Lakshminarayanan, V. Balasubramanian, "***Effect of weld metal properties on fatigue crack growth behaviour of gas tungsten arc welded AISI 409M grade ferritic stainless steel joints***" , International Journal of Pressure Vessels and Piping .pp.517–524

[82] E. Taban, E. Deleu, A. Dhooge,E. Kaluc. 2007, "***Gas metal arc welding of modified X2CrNi12 ferritic stainless steel***" Published in Kovove Mater.pp.67-74.

[83] J. Rawlings, Howard M. Kopech, Howard G. Ruz.1997, "***The effect of service temperature on the properties of ferritic p/m stainless steels***" International Conference on Powder Metallurgy & Particulate Materials.pp.1-23.

[84] Emel Taban a, Erdinc Kaluc., Alfred Dhooge 2009, "***Hybrid (plasma + gas tungsten arc) weldability of modified 12% Cr ferritic stainless steel***" ,Materials and Design 30, pp.4236–4242.

[85] A K Lakshminarayanan, K Shanmugam, V Balasubramanian.2009 "***Effect of Welding Processes on Tensile and Impact Properties, Hardness and Microstructure of AISI 409MFSS Fabricated by Duplex Stainless Steel Filler Metal***" journal of iron and steel research, international. pp.66- 72

[86] A K Lakshminarayanan, K Shanmugam, V Balasubramanian.2009, " ***Effect of Autogenous Arc Welding Processes on Tensile and Impact Properties of Ferritic Stainless Steel Joints***" Journal of iron and steel research, internkrional. pp. 62-68.

[87] D F Filho, V A Ferraresi, and A Scotti "Shielding gas influence on the ferritic stainless steel weldability***"Proceedings of the Institution of Mechanical Engineers, Part B: Journal of Engineering Manufacture Vol 224, Issue 6, pp. 951 - 961***

[88]M. Alizadeh-Sh, S.P.H. Marashi, M. Pouranvari, "***Resistance spot welding of AISI 430 ferritic stainless steel: Phase transformations and mechanical properties"***, Materials & Design (1980-2015), Volume 56, 2014, pp. 258-263

[89]Zhang Guang-jun, Yan Zhi-hong, Wu Lin, "***Visual sensing of weld pool in variablepolarity TIG welding of aluminium alloy***", Transaction of Nonferrous Metal Society of China vol.16, issue 3 (june2006), pp.522-526

[90]LEI Yu-cheng, YU Wen-xia, LI Cai-hui, CHENG Xiao-nong, "***Simulation on temperaturefield of TIG welding of copper without preheating***", Transaction Of Nonferrous Metal Society of China vol.16, issue 4(August 2006), pp. 838-842.

[91]A. Dargutlu, "***Experimental investigation of the effect of hydrogen in argon as a shieldinggas on TIG welding of austenitic stainless steel***", Materials and design 25, (2004), pp. 19-23

[92]S. C juang, Y. S. Tarng, "***Process parameter selection for optimizing the weld poolgeometry in the tungsten inert gas welding of stainless steel***", Journal of Materials ProcessingTechnology,122, issue 1(March2002), pp. 33-37.

[93] Y. S. Tarng, H. L. Tsai, S. S. Yeh, "***Modeling, optimization and classification of weldquality in tungsten inert gas welding***", International Journal ofMachine Tool & Manufacture, Vol.39,Issue 9(September1999), pp. 1427-1438.

[94] M. Vasudevan, M. V. Kuppuswamy and A. K. Bhaduri, "***Optimizing Process Parameters for Gas Tungsten Arc Welding of an Austenitic Stainless Steel Using Genetic Algorithm***," Transactions of the Indian Institute of Metals, Vol. 63, No. 3, 2010, pp. 1-10

[95] R. Satish, B. Naveen, P. Nijanthan, K. Arun Vasantha Geethan, Vaddi Seshagiri "***Weldability and process parameter optimization of dissimilar pipe joints using GTAW***".International Journal of Engineering Research and Applications (IJERA) 2525-2530, Vol. 2, Issue 3, May-Jun 2012, pp.2525-2530

[96] G.Padmanaban, V.Balasubramanian, "***Optimization of pulsed current gas tungsten arc welding process parameters to attain maximum tensile strength in AZ31B magnesium alloy***", Transactions of Nonferrous Metals Society of China21, Issue 3 , march 2011, pp. 467-476

[97] Palani. P. K, Saju. M "***Modeling And Optimization Of Process Parameters For Tig Welding Of Aluminium- 65032 Using Response Surface Methodology***" .2248- 9622, Volume-3, Issue 2, 2013.

[98] S. Datta, A. Bandyopadhyay and P. K. Pal "***Grey-based Taguchi method for optimization of bead geometry in submerged arc bead-on-plate welding***," Journal of Advanced Manufacturing Technology vol. 39 , Issue 11-12,(Dec 2008) pp. 1136–1143

[99]K. Y. Benyounis, A. G. Olabi, M. S. J. Hashmi, "***Effect of laser welding parameters on thetensile-shear strength of AISI304 sheet***". In: Published in AMPT2006 proceedings, July 30-August 3, 2006. Athens [OH], USA: Ohio University; (2006).

[100]V. Gunaraj, N. Murugan, "***Application of response surface methodology for predicting weld bead quality in submerged arc welding of pipes***", Journal of Materials Processing Technology, *Vol.* 88 Issue 1-3(April1999). pp. 266-275

[101]T. Mohandas, G. Reddy Madhusudan, N. Mohammad, "***A comparative evaluation of gas tungsten and shielded metal arc welds of a "ferritic" stainless steel***", Journal of Materials Processing Technology, 94 (1999), pp. 133-140

[102]A. K. Lakshminarayanan, V. Balasubramanian, "***Comparison of RSM with ANN inpredicting tensile strength of friction stir welded AA 7039 aluminium alloy joints***", Transaction of Nonferrous Metal Society of China, vol. 19, (2009), pp. 9-18

[103] Bappa Acherjee, Subrata Mondal, Bipan Tudu, Dipten Mishra, "***Application of artificial neural network for predicting weld quality in laser transmission welding of thermo plastics***", Applied Soft Computing, Vol.11, issue 2(2011).pp. 2548-2555

[104] B. josefsson, U. Bergenlid, "***Tensile, low cycle fatigue and fracture toughness behaviour of type 316L steel irradiated to 0.3 dpa***", Journal of Nuclear Materials, Volumes 212-215, part 1,(Sept.1994), pp. 525-529.

[105] Mallaiah Gurram, Kumar Adepu, Ravinder Reddy Pinninti, Madhusudhan Reddy Gankidi "***Effect of copper and aluminium addition on mechanical properties and corrosion behaviour of AISI 430 ferritic stainless steel gas tungsten arc welds***" journal of material research technology 2013;2(3):pp.238–249

[106] P.K. Palani, N. Murugan, "***Selection of process parameters of pulsed current gas metal arc welding***", Journals of Materials Processing Technology, vol.172, issue 1 (20 Feb 2006), pp. 1 -10.

[107] J.Pasupathy, V.Ravisankar "***parametric optimization of TIG welding parameters using taguchi method for dissimilar joint*** " International Journal of Scientific & Engineering Research,Vol.4, november-2013 ISSN 2229-5518

[108] S. R. Patil, C. A. Waghmare "***Optimization of MIG Welding parameters for improving strength of welded joints***", International Journal of Advanced Engineering Research and Studies, July-Sept., 2013, pp. 14-16

[109] M. Aghakhani, E. Mehrdad, and E. Hayati "***Parametric optimization of gas metal arc welding process by Taguchi method on weld dilution***", International journal of modeling and optimization, vol. 1, no. 3, (August 2011) pp. 216-220

[110] T. Senthil Kumar, V. Balasubramanian, M. Y. Sanavullah***"Influences of pulsed current tungsten inert gas welding parameters on the tensile properties of AA 6061 aluminum alloy",*** Journal of Materials and design, Vol. 28, Issue 7 (2007) pp. 2080-2092.

[111] M Bala Chennaiah, P. Nanda Kumar, K. Prahlada Rao "***The numerical simulation of heat transfer during a hybrid laser-MIG welding using equivalent heat source approach***," Procedia Computer Science, vol. 85, pp. 54-61.

[112] Sharmistha Singh, Neha Gupta "***Analysis of Hardness in Metal Inert Gas Welding Of Two Dissimilar Metals, Mild Steel & Stainless Steel***," IOSR Journal of Mechanical and Civil Engineering vol. 13, issue 3, Jun. 2016, pp. 94-113.

[113] Radha Raman Mishra, Visnu Kumar Tiwari and Rajesh Singh (2014) "***A study of tensile strength of MIG and TIG welded dissimilar joints of mild Steel and stainless steel***", International journal of advances in materials science and engineering (IJAMSE), vol.3, no. 2, pp. 23-32.

[114] Vikas Chauhan, R. S. Jadoun (2014) "***Parametric optimization of MIG welding for stainless steel (SS-304) and low carbon steel using Taguchi design method***", International Journal of Advanced Technology & Engineering Research (IJATER), vol. 2, no. 1, pp. 224-229

[115] L. Suresh Kumar, S. M. Verma, P. Radhakrishna Prasad, P. Kirankumar, T. SivaShanker (2011) "***Experimental investigation for welding aspects of AISI 304 & 316 by Taguchi technique for the process of TIG & MIG welding***", International Journal of Engineering Trends and Technology, vol. 2, no. 2, pp. 28-33

[116] Pawan Kumar, B. K. Roy, Nishant (2013) "***Parameters optimization for gas metal arc welding of austenitic stainless steel (AISI 304) & low carbon steel using Taguchi's technique***", International Journal of Engineering and Management Research, vol. 3, no. 4, pp. 18-22.

[117] B. Larsson and L. Berthold, ***Fabrication of ferritic – austenitic stainless steels*.** Material & Design 7 (1986) pp. 81-88.

[118] E. Taban, E. Deleu, A. Dhooge and E. Kaluc, ***Evaluation of dissimilar welds between ferritic stainless steel modified 12% Cr and carbon steel S355***, Welding journal., 87 (2008)pp. 291-297

[119] E.M. Anawa and A.G. Olabi, "***Optimization of tensile strength of ferritic/austenitic laser-welded components***", Optics and Lasers in Engg. 46 (2008) pp. 571– 577

[120] C. Ugur, D. Halil and T. Mustafa, "***Microstructural characteristic of dissimilar welded components (AISI ferritic –AISI 304 austenetic stainless steels) by CO2 laser beam welding***". GU J. Sci, 25 (2012)pp. 35-51.

[121] S. M. Joo, H. S. Bang and S.Y. Kwak, "***Optimization of hybrid CO2 laser-GMA welding parameters on dissimilar materials AH32/STS304L using grey-based Taguchi analysis***", International Journal of Precission Engineering and Manufacturing 15 (2014) pp. 447-454

[122] R. Rudrapati, N. Choudhury and A. Bandyopadhyay, "***Parametric optimization of TIG welding process in butt joining of mild steel and stainless steel***". International journal of Current Engineering and Technology (2016) pp. 144-149.

[123]Sivashanmugam M., Manoharan N., Ananthapadmanaban D., Ravi Kumar S."***Investigation of microstructure and mechanical properties of GTAW &GMAW joints of AA 7075 aluminum alloy***" ,International journal on Design and Manufacturing Technologies ,Vol 3,No2,(July 2009),pp.56-62

[124] D.S. Nagesh and G.L. Datta "***Prediction of weld bead geometry and penetration in shielded metal-arc welding using artificial neural networks***," Journal of Materials Processing Technology vol.123 Issue 2 (April 2002) pp.303–312

[125]D. S. Nagesh, G. L. Datta, "***Genetic algorithm for optimization of welding variables for height to width ratio and application of ANN for prediction of bead geometry for TIG welding process***", Applied soft Computing, Vol. 10 Issue 3(June2010), pp. 897-907.

[126] Mr. Harshal K. Chavan ,Mr. Gunwant D. Shelake ,Dr. M. S. Kadam "***effect of heat input and speed of welding on distortion in MIG welding*** " international journal of industrial engineering research and development (IJIERD)" Vol.3, Issue2, July-December (2012), pp. 42-50

[127]I. Pires, L. Quintino, R.M. Miranda, "***Analysis of the influence of shielding gas mixtures on the gas metal arc welding metal transfer modes and fume formation rate***", Materials and Design 28 (2007), pp. 1623-1631.

[128]D. Kim, S. Rhee, H. Park, "***Modelling and optimization of a GMA welding process genetic algorithm process by genetic algorithm and response surface methodology***", International Journal of Production Research , (2002), vol. 40, No. 7, pp. 1699-1711.

[129]A.D. Tipi, "***Neutralizing the effect of the angle of the variations on the drop detachment in automatic GMAW system***", International Journal of Advances Manufacturing and Technology Vol. 54 Issue1-4 (April 2011), pp. 123-137.

[130]P. Sathiya, S. Aravindan, A. Noorul Haq, K. Paneerselvam**, "*Optimization of friction welding parameters using evolutionary computational techniques*"** journal of materials processing technology, volume 209, issue 5, (1 march 2009), pp. 2576-2584.

[131]M.R. Bosworth, "***Effective heat input in pulsed gas metal arc welding with solid wire electrodes***", Welding Journal 70 (5) (1991), pp. 111-s–117-s.

[132] P. Dutta, D. K. Pratihar, "***Modeling of TIG welding process using conventional regression analysis and neural l network-based approaches***", Journal of Materials Processing Technology, 184, (2007), pp. 56-68

[133]P. Modenesi, E. Âquio R. Apolina Ârio, Iaci M. Pereira, "***TIG welding with single-component fluxes***", Journal of Materials Processing Technology 99, (2000), pp. 260 - 265

[134]Hua-yun Du, Ying-huiWei, Wen-xianWang, Wan-mingLina, Ding Fan, "***Numericalsimulation of temperature and fluid in GTAW-arc under changing process conditions***", journal ofmaterials processing technology, 209, (2009), pp. 3752–3765.

[135]Y. Cai, G. Wang, H. Yang, X. Hua, Y Wu, "***Spatter Rate Estimation of GMAW-S based on Partial Least Square Regression***", Journal of Shanghai Jiaotong University (Science)December 2008, Volume 13, Issue 6, pp 695–701

[136] M.I. Khan, "Welding Science and Technology", New age International Publishers, New Delhi-2007.

[137] G.E. Dieter and L.C. Schmidt, "Engineering Design", 4th Edition, Mc-Graw Hill, New York, 2009.

[138] V.D. Kodgire and S.V. Kodgire, "Material Science and Metallurgy", Everest Publishing House, 2006.

[139] D.C. Montgomery, "Design and analysis of experiments", 7th Edition, Wiley-India

[140] www.aws.org dated12.04.2014

[141] www.lincolnelectric.comdated18.05.2014

[142] https://www.totalmateria.com/dated19.05.2015

[143]https://www.azom.com/article dated 31.10.2019